Computational studies of one and two-dimensional photonic microstructures

Beggs, Daryl M.

University of Durham

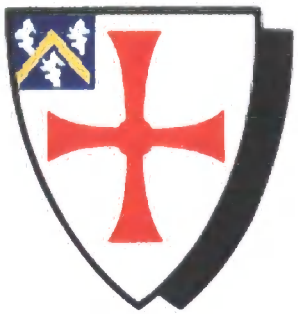

Computational Studies of One and Two-Dimensional Photonic Microstructures

Daryl M. Beggs

Department of Physics

A thesis submitted for

the degree of Doctor of Philosophy

2006

Abstract

This work is concerned with the study of photonic crystals and other topical photonic microstructures, whose optical properties are investigated by solving the Maxwell equations using appropriate theoretical and computational schemes, which are described. The work focuses on the photonic band gap, the existence of which is crucial for most applications of photonic crystals.

Disorder in photonic crystals has been studied. The photonic eigenmodes of an ensemble of a type of disordered one-dimensional photonic crystal are investigated statistically for three different models of disorder and a certain type of disordered two-dimensional photonic crystal has also been studied. It is seen that the disorder introduces photonic modes into the band gap, and the properties of disorder-induced modes localised on random microcavities are discussed for both one and two-dimensional photonic crystals. It is apparent, however, that there is a certain level of disorder below which the probability of finding disorder-induced photonic modes with eigenfrequencies in the centre of the photonic band gap is negligible, and this produces a threshold-like behaviour as a function of the disorder parameter in the transmission properties of the photonic crystals.

Novel designs for two-dimensional photonic crystals based on the deep etching of a Bragg reflector and on a unit cell with local quasicrystalline order are considered. Both are found to possess wide complete photonic band gaps for one polarisation of light over a wide range of geometrical parameters, and the parameters of the structures are investigated in order to optimise the properties of the photonic band gap.

An approach using a simple analytical theory has been developed for the design of multilayered optical bandpass filters based on coupled microcavity layers embedded in an one-dimensional photonic crystal and the parameters of the optimal structure are presented.

A formalism based on non-local dielectric response theory and a Green function technique has been developed to describe the interaction of a quantum well exciton with an evanescent optical mode of a planar waveguide, and the dispersion relations of waveguide polaritons in a planar dielectric waveguide with an embedded quantum well have been calculated.

Work presented in this thesis has contributed to the following publications in peer reviewed journals:

- M. A. Kaliteevski, D. M. Beggs, S. Brand, R. A. Abram and V. V. Nikolaev. *Statistics of the eigenmodes and optical properties of one-dimensional disordered photonic crystals.* Physical Review E (2006), in print.

- M. A. Kaliteevski, D. M. Beggs, S. Brand, R. A. Abram and V. V. Nikolaev. *Stability of the photonic band gap in the presence of disorder.* Physical Review B (2006) **73**, 033106.

- D. T. Roper, D. M. Beggs, M. A. Kaliteevski, S. Brand and R. A. Abram. *Properties of two-dimensional photonic crystals with octagonal quasicrystalline unit cells.* Journal of Modern Optics (2006) **53** (3) 407–416.

- D. M. Beggs, M. A. Kaliteevski, S. Brand, R. A. Abram, D. Cassagne and J. P. Albert. *Disorder induced modification of reflection and transmission spectra of a two-dimensional photonic crystal with an incomplete band-gap.* Journal of Physics: Condensed Matter (2005) **17** 4049–4055.

- D. M. Beggs, M. A. Kaliteevski, S. Brand, R. A. Abram, D. Cassagne and J. P. Albert. *Disorder induced modification of the transmission of light through two-dimensional photonic crystals.* Journal of Physics: Condensed Matter (2005) **17** 1781–1790.

- D. M. Beggs, M. A. Kaliteevski and R. A. Abram. *Etched Bragg reflectors as two-dimensional photonic crystals.* Journal of Physics: Condensed Matter (2004) **16** 8093–8099.

- D. M. Beggs, M. A. Kaliteevski, S. Brand, R. A. Abram, V. V. Nikolaev and A. V. Kavokin. *Interaction of quantum well excitons with evanescent plane electromagnetic waves.* Journal of Physics: Condensed Matter (2004) **16** 3401–3409.

- D. M. Beggs, M. A. Kaliteevski, S. Brand and R. A. Abram. *Optimisation of an optical filter with a square-shaped passband based on coupled microcavities.* Journal of Modern Optics (2004) **51** (3) 437–446.

In addition work from this thesis has contributed to the following peer reviewed conference proceedings:

- D. M. Beggs, M. A. Kaliteevski, S. Brand, R. A. Abram and A. V. Kavokin. *Waveguide polaritons: interaction of a quantum well exciton with an electromagnetic mode of a planar waveguide.* Physica Status Solidi (c) (2005) **2** (2) 787–790.

- D. M. Beggs, M. A. Kaliteevski, S. Brand, R. A. Abram and A. V.Kavokin. *The interaction of quantum well excitons with evanescent EM waves and the spectroscopy of waveguide polaritons.* AIP Conference Proceedings (2004) **772** (B) 1166–1167.

Declaration

The work presented in this thesis was carried out in the Condensed Matter Theory Group in the Department of Physics, University of Durham, between January 2003 and December 2005. The work has not been submitted for any other degree in the University of Durham or elsewhere, and unless stated otherwise, is the original work of the author.

Copyright

Acknowledgements

I would like to acknowledge and thank my supervisors, Prof. Richard Abram and Dr. Mike Kaliteevski, for all their help and the input they have made to the direction of this work, and their careful reading of the draft of this thesis. I would also like to acknowledge the other collaborators in this work, in no particular order: Alexey Kavokin, David Roper, Valitin Nikolaev, David Cassagne, Jean-Paul Albert and Stuart Brand. I would also like to thank Stewart Clark for his useful suggestions and reading of chapter 1.

Contents

List of Figures

List of Tables

Chapter 1

Introduction

It seems to the author that the guiding principle of science is (or should be) understanding. If something is understood, then it stands that it is amenable to control. Thus it has been throughout the history of human progress; understanding leading to control. It is set against this background that the field of photonics attempts to understand the behaviour of light in material systems. If it is understood why or how light acts the way it does, then mankind can invent ways to modify this behaviour to suit our applications for light. One example of this from the telecommunications industry is the optical fibre—it is known that light can be confined by a step in the refractive index, and this is used to guide light through "light tubes" to wherever we want, even across the oceans. Our understanding of the mechanisms involved also allows us to understand the limitations—in the example of the optical fibre, confinement is lost if it is attempted to guide the light around sharp bends.

Microstructures are structures with component parts on the scale of micrometres. Visible light in air has a wavelength of 400 to 700 nm, and so the understanding of how light behaves in photonic microstructures must involve a description of the wave nature of the electromagnetic field of the light.

The aim of the study of the optical properties of photonic microstructures is to understand them and how to control and manipulate light with them. If we were able to guide, store, filter, suppress and create light, then light could be put to all manner of useful purposes. For example, building integrated photonic microchips that used light for all-optical computing and telecommunications. Such all-optical realisations would have many advantages over current (no pun intended) ways of doing things. Since the 1970s, the number of electronic

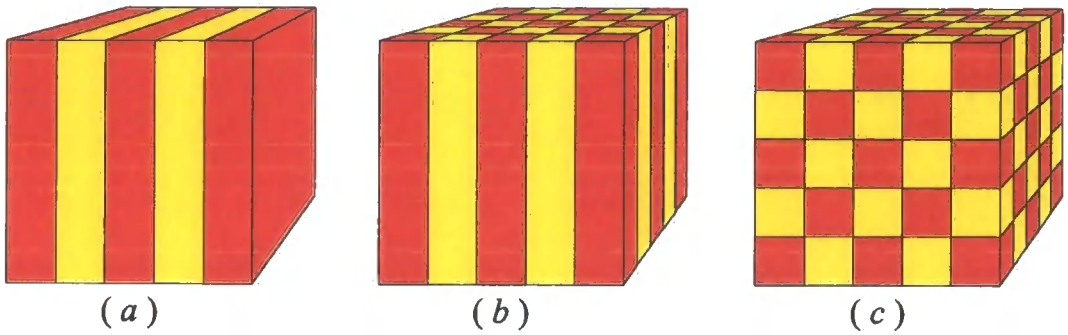

Figure 1.1 An illustration of possible dielectric variations of (a) 1D, (b) 2D and (c) 3D photonic crystals. The structures are piecewise homogeneous, and the red and yellow coloured regions represent two different dielectric materials.

components that can be fitted into a microchip has doubled every 18 months, with a commensurate increase in computer speed. This trend is known as Moore's law, but there are fundamental reasons to suspect that it could be coming to an end, and the top speed at which integrated electronic circuits can perform will level out [1]. Researchers now believe that all optical computer chips could break the speed barriers that integrated electronics seems to be coming up against, but such chips would require the total control of light on micrometre scales. A new class of materials known as photonic crystals [2–7], researched for the last 15 years, has emerged, which promises the potential to be able to control light in the ways discussed.

Photonic crystals are dielectric materials where the refractive index varies periodically, but the segments of the photonic crystal are normally piecewise homogeneous. This periodicity can be in one-, two- or three-dimensions, with the properties being constant in the remaining dimensions, as illustrated in figure 1.1. Thus the structure presents a series of dielectric interfaces to any incident light, and it is well known that at such dielectric interfaces, incident light is partially reflected and partially transmitted. How much the light is reflected or transmitted depends on the refractive index contrast of the two materials and the angle at which the light is incident upon the interface, described by the Fresnel equations. For any photonic structure where the wavelength of the light is similar to the scale of the structure, interference of the reflected waves must be taken into account. For a periodic arrangement of dielectric material, Bragg-like reflection effects occur. This can result in a photonic band gap, a range of frequencies for which no harmonic modes of the electromagnetic field exist due to the destructive interference of waves in the structure. The concepts of photonic crystals were first suggested by Yablonovitch [8] and John [9] in 1987, who both suggested that the prop-

erties of light could be controlled in such a structure. Yablonovitch's main motivation was to engineer the photonic density of states, in order to control the radiative properties of materials inside them, whereas John's idea was to use photonic crystals to effect the localisation and control of light.

Photonic crystals that do possess a photonic band gap are also sometimes called photonic band gap materials. Note, however, that not all photonic crystals necessarily possess a photonic band gap. A photonic crystal might possess no photonic band gaps, or band gaps only for certain directions of propagation within the crystal, or for certain polarisations of light. If a photonic crystal has a band gap for certain directions in the crystal which closes for other directions, then the band gap is said to be incomplete. Only if the photonic crystal has band gaps for all possible directions, and further that these band gaps overlap spectrally, is the photonic band gap said to be complete. If a photonic crystal has complete, overlapping band gaps for all polarisations and directions of propagation in the crystal, then the photonic band gap is said to be absolute. In the latter case, the density of photonic modes drops to zero at frequencies in the absolute band gap. The rate of spontaneous emission of a quantum mechanical emitter, as given (to first order) by Fermi's golden rule, is proportional to the final density of states of the system. Thus spontaneous emission at frequencies in the photonic band gap of a photonic crystal can be suppressed by embedding the emitter in the photonic crystal.

Many authors choose to introduce photonic crystals and the concept of a photonic band gap through an appealing analogy with electrons in crystals [2, 5, 6]. These systems possess a periodic arrangement of positive charges (the (screened) nuclear cores of atoms) which create a periodic total potential. Electron waves obeying the Schröedinger wave equation experience Bragg-like scattering when they interact with this periodic potential, which can lead to forbidden frequency regions in which no electronic states obeying the Schröedinger equation and associated boundary conditions are allowed. An example of this is the forbidden band gap between the valence and conduction bands in a semiconductor. The appeal of this analogy is broadened when one realises that many of the principles and much of the nomenclature is directly transferable between the two cases; it is usual to preface words used in the description of atomic crystals with the word "photonic". Bloch's law/theorem applies equally well for electromagnetic waves in periodic dielectric media as it does for electrons

in a crystalline solid. The notion of Brillouin zones and bands of allowed states are equally used in both cases.

These appealing similarities between the photonic and electronic cases in periodic media arise because both the electric field $\mathbf{E}(\mathbf{r})$ in the photonic case and the wavefunction $\psi(\mathbf{r})$ in the electronic case must obey wave equations, from the Maxwell wave equation for the electric field of angular frequency ω in the former case (see section 1.1)

$$\nabla \times \nabla \times \mathbf{E}(\mathbf{r}) = \varepsilon(\mathbf{r}) \frac{\omega^2}{c^2} \mathbf{E}(\mathbf{r}) \tag{1.1}$$

and the time independent Schröedinger equation for electrons of energy U in a potential $V(\mathbf{r})$ in the latter case

$$-\frac{\hbar^2}{2m} \nabla^2 \psi(\mathbf{r}) + V(\mathbf{r}) \psi(\mathbf{r}) = U \psi(\mathbf{r}) \tag{1.2}$$

However, there are also important differences between the wave equations in equations 1.1 and 1.2. The electromagnetic field in the photonic case is a vector quantity, whereas the electronic wavefunction in the Schröedinger equation is a scalar. Also, the potential $V(\mathbf{r})$ in the time independent Schröedinger equation can be positive or negative, and a potential can therefore exist where $V(\mathbf{r}) > U$ in the local surrounding region. The analogous situation is not possible in the photonic case, as the relative permittivity $\varepsilon(\mathbf{r})$ in non-absorbing linear media has a real positive value. Also, in the second term of equation 1.2, the potential $V(\mathbf{r})$ enters the equation independently from the electronic energy U, whereas, $\varepsilon(\mathbf{r})$ enters in equation 1.1 as a product of ω^2.

Examples of photonic crystals can be found in nature. Opals are minerals consisting of grains of hydrated silica ($SiO_2 \cdot nH_2O$) which are regularly packed in a crystalline lattice. However, the refractive index contrast between the grains and the voids is not sufficient for a complete photonic band gap to form. Rather stop-bands of high reflectivity caused by incomplete band gaps are seen in different frequency ranges when the angle of viewing changes. This photonic crystal property gives the opal its iridescent appearance, which is considered attractive enough for opals to be used as gemstones. In biology, the wings of some butterflies derive their colour from photonic crystal lattices grown naturally. Figure 1.2 shows an opal gemstone and a butterfly with a naturally grown photonic crystal on its wings. Also,

Figure 1.2 Left—a bracelet made from the gemstone opal. Its iridescent colour is due to the incomplete photonic band gaps, which strongly reflect light of certain frequencies, which change with angle of viewing. Right—the Blue Morpho butterfly. Its wings are iridescent in colour due to a natural photonic crystal.

crystalline solids display ultra-thin photonic band gaps at X-ray frequencies, when the wavelength of the electromagnetic radiation is small enough to see the microscopic difference in dielectric constant between atoms on a periodic lattice and the interstitial regions. These photonic band gaps are so thin, as the dielectric contrasts involved are small.

Despite these natural examples of photonic crystals, interest in photonic crystals is so great because of the potential to design completely from first principles and then fabricate artificial photonic crystals for our device needs. However, this is no simple task as the feature sizes of photonic crystals must be similar to the wavelength of light in the crystal at the required frequencies of operation. Two main approaches are used to fabricate photonic crystals for use at visible and near-infrared frequencies—self assembly and nanolithography [10]. Self-assembly techniques involve creating the conditions for components to come together naturally to form a structure that can be used as a photonic crystal. For example, a colloidal suspension of identical spherical grains can be allowed to settle under gravity into an opalline crystalline structure. This already gives a photonic crystal like the one shown in figure 1.3 (a) but for the most commonly used materials the refractive index contrast between the grains and the voids is not sufficient to give a complete photonic band gap, as with natural opals. However, it is possible to fill the voids between the grains with a high refractive index material, and then the grains are selectively etched away, to leave an inverse opal of air voids with a high refractive index shell-like structure (such as the one shown in the inset of figure 1.3 (a)) with a sufficiently high refractive index contrast to produce a photonic band gap in three dimensions [11–16].

The second main method of fabrication is to use nanolithography techniques. Researchers

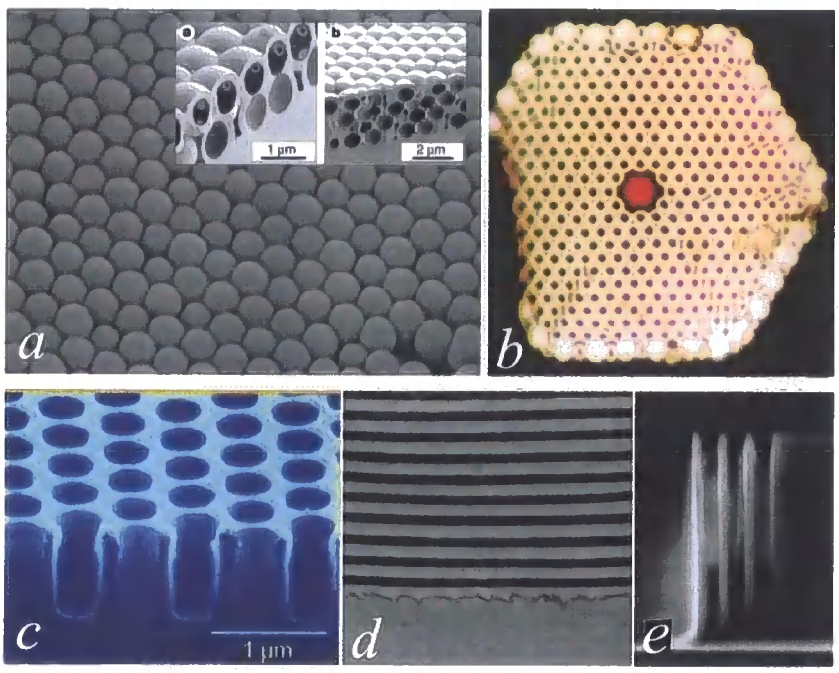

Figure 1.3 (a) SEM images of an artificial opal structure of grains that spontaneously organise on a regular lattice, which is used as a template for the inverse opal structure of silicon shown inset. Reprinted by permission from Macmillan Publishers Ltd: Y. A. Vlasov *et al.* Nature **414** 289–293, copyright 2001. (b) A photonic crystal fibre. Light is guided along the central air region due to the photonic band gap of the 2D photonic crystal of air holes in silica. Reprinted with permission, from P. Russell, Science **299** 358–362. Copyright 2003 AAAS. (c) SEM image of a 2D photonic crystal consisting of a honeycomb-like lattice of air holes in GaAs. (d) Cross-sectional TEM image of a Bragg reflector on a quartz substrate. (e) Three period Bragg reflector etched in GaAs for use in waveguide lasers.

of photonic crystals have a head start here, as many of the methods have already been pioneered and refined in the semiconductor industry. Such methods can be used to make 1D, 2D or 3D photonic crystals. Figure 1.3 (c) shows a 2D photonic crystal created by etching cylindrical air holes on an hexagonal lattice into a dielectric substrate, leaving a honeycomb-like structure. Such a photonic crystal can display an absolute photonic band gap, but only in the plane of the 2D variation of refractive index.

However, due to the complexity of fabricating photonic crystals for use at visible frequencies, many early studies of photonic crystals relied solely on theoretical and computational studies [17–30]. More recently much attention has focused on the experimental realisation of photonic band gap materials for use at visible or near infrared frequencies [31–35]. Today, computational methods for the research of photonic crystals have matured [36–39] and are very valuable for many reasons. First, numerical simulations can be considerably cheaper and more effective than experimental trial and error, and further, are practically exact when

solving the Maxwell equations for photonic crystals. For example, if a new idea on how to construct a photonic crystal for a particular application is thought of, then its properties can be simulated numerically, and the parameters optimised for the desired application, before any attempt to fabricate such a structure is undertaken. Second, the interpretation of experimental results is greatly aided by knowledge of the underlying photonic bandstructure, or the calculated properties of the idealised system. Also, ideas on why any results differ from what is expected can be tested by numerical simulations. Third, numerical simulations can be used as a predictive tool, in much the same way as they were used to predict the first dielectric structures which possessed photonic band gaps.

A large body of research has been conducted into the control and manipulation of light. Point defects can be introduced that support localised defect modes with frequencies in the photonic band gap. Such defects can act as high finesse microcavities [40–46]. The frequencies and line-shapes of modes can be engineered by correctly designing the defect, allowing structures to be designed for many potential applications. For example, photons can tunnel between defects in the photonic crystal, and optical filters can be designed with the line-shapes and frequencies of the photonic defect modes. Or the defects can be aligned in a chain, such that light is guided along the chain by tunnelling from defect to defect; such a structure is known as a coupled cavity waveguide [47–50]. Light at frequencies in the photonic band gap can also be confined along a linear defect within a photonic crystal, in a structure known as a photonic crystal waveguide [51,52]. It is known that both coupled cavity and photonic waveguides should allow for the guiding of light, even around sharp bends, in the waveguide. Such control of light would be required for the realisation of all-optical computer chips. However an all-optical computer chip is a distant possibility, and much research and many innovations will be needed to realise it [53]. However devices based on photonic crystals are already being built. The photonic crystal fibre [54, 55] uses the principle of a photonic band gap to guide light along the fibre, rather than total internal reflection as in a conventional optical fibre. In a photonic crystal fibre, such as the one shown in figure 1.3 (b), a two-dimensionally periodic cladding of air holes and dielectric that possesses a photonic band gap is used to confine light at frequencies in the band gap to a core made up of a defect in the photonic crystal. However, the ability to design and engineer the dispersion and other properties of the photonic crystal fibre offers many advantages over the conventional optical

fibres, and allows their uses in a much more broad range of applications [55]. Also periodic multilayered dielectric stacks [56, 57], such as those shown in figure 1.3 (d) and (e), are examples of one-dimensional photonic crystals, and these structures have found many uses as Bragg reflectors and as high reflectivity mirrors for microcavities for many years.

Most of the applicable properties of photonic crystals rely on the existence of a photonic band gap, and thus most research has been in finding structures that can be made with photonic band gaps and then finding parameters of the structures which optimise properties of the band gap. However, some interesting properties of photonic crystals which could find uses on all-optical microchips, such as the superprism effect [58, 59], or negative effective refractive indices [60], rely not on the photonic band gap but instead on engineering the features in the dispersion curves of the allowed photonic bands.

1.1 The Maxwell equations

In general, the four Maxwell equations relate five vector quantities and one scalar quantity—the electric field vector $\mathbf{E}$; the magnetic induction vector $\mathbf{B}$; the electric displacement $\mathbf{D}$; the magnetic vector $\mathbf{H}$; the current density $\mathbf{J}$; and the charge density ρ. In addition to the Maxwell equations, the constitutive relations (or material equations) are needed to relate the fields $\mathbf{D}$ and $\mathbf{B}$ to the fields $\mathbf{E}$ and $\mathbf{H}$, and also the generalised Ohm's law relating $\mathbf{J}$ to $\mathbf{E}$ and $\mathbf{B}$, in the material system being considered. In general, these constitutive relations can be complicated, involving the polarisation or magnetisation of materials, non-linear and anisotropic effects and history-dependent (hysteresis) behaviour [57, 61].

However, when considering photonic crystals composed of good dielectric media, it is usual to make a number of simplifications. The dielectric materials are considered to have no free charges or associated currents so that $\mathbf{J} = \mathbf{0}$ and $\rho = 0$, and the Maxwell equations can be written as

$$\nabla \times \mathbf{H} = \frac{\partial \mathbf{D}}{\partial t} \tag{1.3}$$

$$\nabla \times \mathbf{E} = -\frac{\partial \mathbf{B}}{\partial t} \tag{1.4}$$

$$\nabla \cdot \mathbf{D} = 0 \tag{1.5}$$

$$\nabla \cdot \mathbf{B} = 0 \tag{1.6}$$

The materials are considered to be a continuum where it is sufficient to consider the spatially averaged fields, and no knowledge of the particular microscopic structure is required. This is a very reasonable model for light at visible or near-infra-red frequencies as the wavelength of the electromagnetic radiation is large on the atomic scale. For many photonic crystals it is fair to assume that they are constructed from materials that are isotropic and that the dielectric response is linear and lossless. These assumptions mean that $\mathbf{D}$ and $\mathbf{E}$ can be related by a real scalar factor, called the relative permittivity $\varepsilon(\mathbf{r})$, and the fields $\mathbf{B}$ and $\mathbf{H}$ can similarly be related by the magnetic permeability $\mu(\mathbf{r})$

$$\mathbf{D}(\mathbf{r}) = \varepsilon(\mathbf{r})\,\varepsilon_0 \mathbf{E}(\mathbf{r}) \tag{1.7}$$

$$\mathbf{B}(\mathbf{r}) = \mu(\mathbf{r})\,\mu_0 \mathbf{H}(\mathbf{r}) \tag{1.8}$$

Most photonic crystals are made up of non-magnetic materials for which $\mu(\mathbf{r}) = 1$ while $\varepsilon(\mathbf{r})$ varies piecewise periodically. It is also usual to assume that $\varepsilon(\mathbf{r})$ is independent of the frequency of light in the spectral range of interest.

Common candidate materials for the construction of photonic crystals for use at optical or near infrared frequencies are semiconductors such as gallium arsenide (GaAs) [31,34,62–65], gallium aluminium arsenide ($Ga_xAl_{1-x}As$) [31, 62, 63, 65] and silicon (Si) [11, 15, 32, 35, 66–68], or amorphous materials such as silicon dioxide (silica, SiO_2) [18, 54, 67, 69–74] or titanium dioxide (titania, TiO_2) [16]. These are only examples, and many other materials have been used [14, 42, 73, 75–81]. A natural question that arises is how well do these materials meet the model assumptions described above. Semiconductor materials can only be used at frequencies below their absorption edge—this is the frequency corresponding to the width of the electronic forbidden gap between the valence and conduction bands of the semiconductor, above which the semiconductor absorbs light by the promotion of charge carriers from the valence to the conduction band. The absorption edge occurs at frequencies corresponding to $\hbar\omega \sim 1.4\,\text{eV}$ in GaAs [82, 83], $\hbar\omega \sim 2.2\,\text{eV}$ in AlAs [82, 84, 85] (note that AlAs is one end point of the $Ga_xAl_{1-x}As$ system, but is chemically unstable) and $\hbar\omega \sim 1.1\,\text{eV}$ in Si [82], but below these frequencies the approximation of no absorption of light is a good one [83–85]. The refractive index of GaAs varies from 3.7 at a wavelength of 1000 nm ($\hbar\omega \sim 0.8\,\text{eV}$) to 3.4 at a wavelength of 400 nm ($\hbar\omega \sim 3.0\,\text{eV}$) [83]; that of AlAs

varies from 3.0 at 1000 nm to 4.2 at 400 nm [84]. Thus the assumption of constant refractive index is a good one in GaAs, but not so good in AlAs. Ref. [83] and [84] provide reviews of the properties of GaAs and $Ga_xAl_{1-x}As$ respectively. The amorphous SiO_2 and TiO_2 also conform to the assumptions outlined above. For example TiO_2 has a very small absorption coefficient, especially for light at wavelengths longer than 550 nm, and its refractive index varies from 2.45 at 750 nm to 2.75 at 400 nm [86].

Before considering the solution of the Maxwell equations in photonic crystals it is instructive to consider briefly a linear, isotropic, homogeneous medium with relative permittivity ε and relative permeability μ. Taking the curl of equation 1.3 and 1.4 and using the constitutive relations in equation 1.7 and 1.8 gives the wave equations for the electric and magnetic fields

$$\nabla \times \nabla \times \mathbf{E} - \varepsilon\mu\varepsilon_0\mu_0 \frac{\partial^2 \mathbf{E}}{\partial t^2} = 0 \tag{1.9}$$

$$\nabla \times \nabla \times \mathbf{H} - \varepsilon\mu\varepsilon_0\mu_0 \frac{\partial^2 \mathbf{H}}{\partial t^2} = 0 \tag{1.10}$$

In the vacuum, $\varepsilon = \mu = 1$, and the speed of the electromagnetic wave is

$$c = \frac{1}{\sqrt{\varepsilon_0\mu_0}} \tag{1.11}$$

whereas in a dielectric medium, the wave is slowed by a factor of the refractive index n, where

$$n = \sqrt{\varepsilon\mu} \tag{1.12}$$

For photonic crystals, which are non-magnetic and piecewise homogeneous, the refractive index as a function of position $n(\mathbf{r})$ is related to the relative permittivity $\varepsilon(\mathbf{r})$ by

$$n(\mathbf{r}) = \sqrt{\varepsilon(\mathbf{r})} \tag{1.13}$$

The time dependence of the electromagnetic fields can always be separated out from the spatial dependence in the wave equations (equation 1.9 and 1.10), and as such it is possible to speak of harmonic modes with a time dependence $e^{-i\omega t}$, where ω is the angular frequency of the harmonic mode. Of course, any solutions of the Maxwell equations can be built from an appropriate combination of these harmonic modes.

Now consider the solution of the Maxwell equations for a photonic crystal. Considering a harmonic time dependence $e^{-i\omega t}$ in equations 1.3 and 1.4 gives

$$\nabla \times \mathbf{H}(\mathbf{r}) = -i\omega\varepsilon(\mathbf{r})\varepsilon_0\mathbf{E}(\mathbf{r}) \tag{1.14}$$

$$\nabla \times \mathbf{E}(\mathbf{r}) = i\omega\mu_0\mathbf{H}(\mathbf{r}) \tag{1.15}$$

and using equation 1.14 to eliminate $\mathbf{E}(\mathbf{r})$ from equation 1.15 leads to

$$\nabla \times \left[\frac{1}{\varepsilon(\mathbf{r})}\nabla \times \mathbf{H}(\mathbf{r})\right] = \frac{\omega^2}{c^2}\mathbf{H}(\mathbf{r}) \tag{1.16}$$

Equation 1.16 casts the solution of the Maxwell equations into an eigenvalue problem. This equation can be solved to find the bandstructure and electromagnetic field profiles of the eigenmodes given the form of the dielectric function $\varepsilon(\mathbf{r})$. Of course solutions of equation 1.16 solve the first two Maxwell equations (equations 1.3 and 1.4) for harmonic modes. However, we must ensure that the second two Maxwell equations (equations 1.5 and 1.6) are also satisfied. Equations 1.5 and 1.6 have a simple physical interpretation—there are no point sources or sinks of the displacement or magnetic fields in the media and mathematically they require the electromagnetic fields are transverse. Thus equations 1.5 and 1.6 can be satisfied by explicitly enforcing the transversality requirement in the solutions of equation 1.16.

Consider a dielectric function $\varepsilon'(\mathbf{r})$ that is merely a scaled version of $\varepsilon(\mathbf{r})$—that is $\varepsilon'(\mathbf{r}) = \varepsilon(\mathbf{r}/s)$ for some scale factor s. Then, if the eigenfrequencies ω_n and field profiles $\mathbf{H}_n(\mathbf{r})$ are known for the dielectric function $\varepsilon(\mathbf{r})$, the equivalent quantities for the scaled system are ω_n/s and $\mathbf{H}(\mathbf{r}/s)$. This can be seen by making the change of variables $\mathbf{r} \rightarrow \mathbf{r}/s$ and $\nabla \rightarrow s\nabla$ in equation 1.16 to give

$$\nabla \times \left[\frac{1}{\varepsilon'(\mathbf{r})}\nabla \times \mathbf{H}(\mathbf{r}/s)\right] = \frac{\omega^2}{s^2c^2}\mathbf{H}(\mathbf{r}/s) \tag{1.17}$$

In essence there is no fundamental length scale inherent in the Maxwell equations and the frequencies and electromagnetic field profiles of the eigenmodes of the scaled structure are just scaled versions of those for the original structure. Thus once the bandstructure and electromagnetic field profiles are known for a given structure, they can be found for a structure scaled up by a factor s by increasing the length scale of the field functions and scaling down

the frequencies by the same factor s (assuming the refractive indices do not change). This scaling property is very useful; photonic crystals can be built with length scales of centimetres and experimentally tested at microwave frequencies [5, 87–93], in the full knowledge that results obtained are in principle scalable to any other frequency regime. In this regime, a photonic crystal can be produced by mechanical drilling of a suitable dielectric material, followed by infilling if required, and the first photonic crystals built where in the microwave regime, owing to the difficulty in achieving suitable dielectric structures at the micrometre length scales used for visible wavelengths.

1.2 Description of the work

As already noted, many of the useful properties of photonic crystals rely on the existence of a photonic band gap, and so the work in this thesis chooses to focus on the creation, properties and potential destruction of the photonic band gap.

It follows from the definition of a photonic crystal given above that a one-dimensional photonic crystal is a multilayered dielectric stack, of the kind that have been studied since long before the phrase photonic crystal was coined [56, 57]. Probably the best known example of this is a Bragg reflector, which consists of a number of quarter-wave layers of alternating dielectric materials. Chapter 2 focuses on periodic multilayered dielectric structures and the concepts of them as one-dimensional photonic crystals. Also, after a discussion of one-dimensional photonic crystals, and Bragg reflectors in particular, chapter 2 focuses on microcavities in 1D layered media, which can be considered as defect layers in one-dimensional photonic crystals, which can add photonic modes into the band gap. Finally chapter 2 ends with a study on how the line shape of the photonic modes in the band gap, created by coupling together these microcavities, can be optimised in the design of an optical filter with a square-shaped passband.

Chapter 3 looks at two-dimensional photonic crystals. Firstly it outlines the two key computational methods used in this thesis when studying the properties of 2D photonic crystals. The first of these key methods is a plane wave method, where equation 1.16 is solved by employing a suitable unit cell with periodic boundary conditions appropriate for the crystal being studied, and expanding $\varepsilon(\mathbf{r})$ and the electromagnetic eigenmodes for the structure as

a linear combination of plane waves. The second method is a transfer matrix method, which is used in this thesis for the calculation of the reflection and transmission from finite slabs of photonic crystals. Chapter 3 then studies the mode structure, density of states and transmission properties of a new type of 2D photonic crystal—the etched Bragg reflector—with the aim of finding the parameters of the structure for which a photonic band gap exists and providing the parameters of the structure which optimise the properties of the bandstructure and density of states.

Photonic crystals ideally have a periodic arrangement of their dielectric materials. However, it is technologically impossible to realise photonic crystals without some deviation from this ideal. Thus all real photonic crystals will display disorder to some greater or lesser extent. Since many potential applications rely on the photonic band gap of photonic crystals, a natural question arises—how will disorder in photonic crystals affect the photonic band gap? Chapter 4 studies the effect of disorder on the band gaps of 1D and 2D photonic crystals, using the methods detailed in chapter 2 and chapter 3. For 1D photonic crystals, it is possible to calculate directly the eigenfrequencies and lifetimes of an ensemble made up of thousands of random realisations of the disordered 1D photonic crystals. The statistics of the eigenmodes of the disordered 1D photonic crystals can then be calculated, and how these relate to the experimentally measurable transmission is examined. For disordered 2D photonic crystals, the greater computational resources required means that the properties of only a few tens of random disordered structures can be calculated. Nevertheless, results from the 1D case can be used to help guide the conclusions from the properties of these disordered 2D photonic crystals.

The properties of a 2D photonic crystal with a unit cell based on a quasicrystalline tiling are studied in chapter 5. Quasicrystals are not periodic, but do display long range order and can display non-crystallographic symmetries. In particular, they can display rotational degrees of symmetry beyond six (the maximum possible for a periodic crystal) which should allow for the formation of a more isotropic band gap than is possible in other photonic crystals. The properties of modes with frequencies in the band gap and localised on microcavities in a photonic quasicrystal are also calculated.

The light-matter interaction in a photonic structure is introduced in chapter 6. Quantum wells can be embedded in layered dielectric media, and quantum well excitons will then

interact with the electric field of incident light through their polarisation. The interaction of light with the polarisation of the quantum-well exciton gives rise to a part-light part-exciton quasi-particle, known as an exciton polariton. Usually the quantum well is embedded within a microcavity enclosed by two Bragg reflectors. If a quantum well exciton has a resonance within the 1D photonic band gap of the Bragg reflectors, the optical confinement provided can be used to enhance the coupling between the exciton and the light in the cavity, such that the so-called strong-coupling regime is realised [94, 95]. Exciton-polaritons are thus usually studied in the context of microcavities and referred to as cavity polaritons [96]. However, a waveguide in the waveguiding regime of light can also provide optical confinement, and chapter 6 describes studies of the properties of waveguide polaritons. Firstly the interactions of quantum well excitons with evanescent plane waves, such as are present in the cladding of waveguides, are studied, before the dispersion relation of a waveguide polariton is calculated.

Chapter 2

One dimensional multilayered dielectric structures

One-dimensional dielectric multilayer structures [56], have found use in many optical devices as, for example, anti-reflection coatings, Bragg reflectors and microcavities. In general they are stratified media, with a constant relative permittivity or refractive index in every layer perpendicular to some fixed direction along which the dielectric properties vary. A Bragg reflector is a well known example of a multilayer structure, where the refractive index varies periodically along the direction of stratification. A Bragg reflector can be considered to be a one-dimensional photonic crystal [2, 3], a structure which can possess a so called photonic band gap due to the interference of electromagnetic waves within the structure. A Bragg reflector usually consists of two types of layers, A and B, and the thickness of each type of layer is arranged such that all layers have equal optical thickness—interference of waves reflected from the various dielectric boundaries in the structure then meet the Bragg condition for reflection the optical thickness of the layers is one quarter of the wavelength of the incident light. The layer structure of a quarter-wave Bragg reflector (sometimes known as a quarter-wave stack or distributed Bragg reflector) is then $(\mathrm{AB})^N$, where N is the number of periods contained in the Bragg reflector, and each letter represents one quarter-wave layer. The photonic band gap (PBG) is a spectral band in which no electromagnetic states exist in the infinite structure. Thus light incident on a Bragg reflector at frequencies within the PBG are highly reflected if there are a sufficient number of quarter-wave layers, and this region is also known as the stop-band of the Bragg reflector.

Bragg reflectors and other multilayered structures can be fabricated by epitaxial growth methods, such as molecular beam epitaxy, metal-organic vapour-phase deposition and atomic layer epitaxy, or other techniques, such as conventional or reactive evaporation and sputtering [86, 97]. Although construction of such structures for use at infrared (optical telecommunications) or visible frequencies is non-trivial, such techniques are mature technologies, with layer thickness control reaching the nanometre scale. Materials for their construction must be non-absorbing (see ref. [98] for discussion of absorption effects in Bragg reflectors) over the range of frequencies of operation of the Bragg reflector. Bragg reflectors can be fabricated from epitaxial semiconductors [63, 72, 75, 81] or organic materials [78, 79], and recently air has been used as one of the dielectric materials by etching a semiconductor substrate to leave "walls" of high refractive index contrast to the air [64, 80]. Bragg reflectors find their main use in providing optical confinement as high reflectivity mirrors in high finesse microcavities or in vertical cavity surface emitting lasers (VCSELs) [73, 75, 81, 99], and as high reflection surface coatings.

A microcavity can be constructed by enclosing a dielectric layer between two Bragg reflectors. The microcavity layer could be a homogeneous layer of any non-absorbing dielectric material, but more usually is a material of the type A or B, used in the layers of the surrounding Bragg reflectors. If constructed to contain an active region or regions (such as semiconductor quantum wells), the microcavity can be used as a laser cavity (as in the vertical-cavity surface-emitting laser (VCSEL) [73, 75, 81, 99]). The cavity usually has an optical thickness of an integer number of half wavelengths of light at the Bragg reflection condition. Such a microcavity layer can be considered as an isolated defect layer in a one-dimensional photonic crystal [2, 3, 49].

For the theoretical and computational studies of Bragg reflectors and microcavities in this chapter, the refractive indices of the two types of layers A and B are chosen to be $n_1 = 1.45$ and $n_2 = 2.3$ respectively, which correspond to the materials SiO_2 and TiO_2 respectively, at a wavelength of 700 nm. If 700 nm is chosen to correspond to the wavelength where the condition for Bragg reflection is met, then the two types of layers must have thicknesses of d_1 =76.1 nm and d_2 =120.7 nm to be quarter-wave layers. The parameters of TiO_2 and SiO_2 have been used in past theoretical studies conducted by other authors [100], and are an experimentally feasible pair of materials for the construction of multilayers for use at optical

wavelengths [86, 97].

The multilayered structures present a series of dielectric interfaces to light incident upon them. Fresnel reflection is known to occur at such interfaces [57] and when the optical thicknesses of the layers are similar to the wavelength of light propagating through the structure, the interference of the electromagnetic waves reflected and re-reflected from the dielectric boundaries must be taken into account to properly describe the optical properties of the structure. This can be most conveniently achieved by solving the Maxwell equations for the electromagnetic fields in a single isotropic homogeneous layer, and using a transfer matrix formalism to propagate the fields through each layer and dielectric interface consecutively.

This chapter begins with a description of a transfer matrix techniques in stratified dielectric media, which can be used to calculate the reflection and transmission properties, or the eigenfrequencies and eigenmodes, of any arbitrary multilayered structure by imposing suitable boundary conditions. The method is well known, and described in many textbooks (e.g. [56, 57]), and is presented here as it is used throughout the remainder of the chapter and also in chapter 3 in the study of disordered one-dimensional photonic crystals and chapter 6 in the study of waveguide polaritons.

The transfer matrix method is then applied in two simple examples—an isolated dielectric boundary, where the Fresnel formulae for reflection and transmission at such a boundary are derived, and a thin dielectric film, where expressions for the lifetime of the Fabry-Perot modes and the reflection and transmission spectra of the structure are derived.

In section 2.4 the optical properties of Bragg reflectors are discussed. First Bloch's theorem is used to derive the dispersion relation from the transfer matrix of the infinite Bragg reflector (a true one-dimensional photonic crystal), and then the reflection and transmission properties are studied. Section 2.5 studies the change in the optical properties of the quarter-wave Bragg reflector when a half-wave cavity layer is introduced into the layer structure. The splitting of the cavity mode through the coupling together two or more microcavities is then studied in section 2.6. Finally, section 2.7 presents a method of optimising the design of square-shaped passband optical filters based on a chain of coupled microcavities.

2.1 The transfer matrix method for a multilayered structure

In this section we introduce a transfer matrix method to describe the propagation of the electromagnetic field through a general multilayer dielectric structure with N layers, where the relative permittivity $\varepsilon(z)$ and relative permeability $\mu(z)$ can take any real value but are constant within each layer. For example, for the structure illustrated in figure 2.1

$$\varepsilon(z) = \begin{cases} \varepsilon_1 & z_0 \leq z < z_1 \\ \varepsilon_2 & z_1 \leq z < z_2 \\ \vdots & \vdots \\ \varepsilon_i & z_{i-1} \leq z < z_i \\ \vdots & \vdots \\ \varepsilon_{N-1} & z_{N-2} \leq z < z_{N-1} \\ \varepsilon_N & z_{N-1} \leq z < z_N \end{cases} \tag{2.1}$$

$$\mu(z) = \begin{cases} \mu_1 & z_0 \leq z < z_1 \\ \mu_2 & z_1 \leq z < z_2 \\ \vdots & \vdots \\ \mu_i & z_{i-1} \leq z < z_i \\ \vdots & \vdots \\ \mu_{N-1} & z_{N-2} \leq z < z_{N-1} \\ \mu_N & z_{N-1} \leq z < z_N \end{cases} \tag{2.2}$$

and the layers have thicknesses $d_i = z_i - z_{i-1}$. The transfer matrix is derived here for arbitrary values of μ_i, but its use in the thesis is limited to the case of $\mu = 1$.

Consider the propagation of a time harmonic electromagnetic wave through the multilayered structure. Any arbitrary polarised plane wave can be resolved into two independent components—a transverse electric (TE) polarisation, where the electric field is perpendicular to the plane of incidence; and a transverse magnetic (TM) polarisation, where the magnetic field is perpendicular to the plane of incidence. If the plane of incidence is taken to be the xy-plane, then the electric field is $\mathbf{E} = (0, E_y, 0)$ in the TE-polarisation and $\mathbf{E} = (E_x, 0, E_z)$ in the TM-polarisation. The symmetry of the Maxwell equations for dielectric media mean

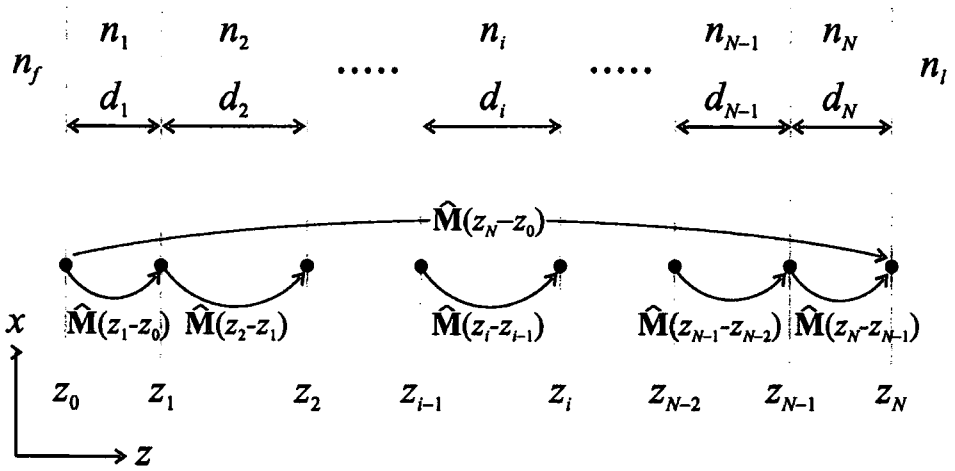

Figure 2.1 An illustration of the multilayer structure under consideration. The transfer matrix of the whole structure can be found from the matrix multiplication of the transfer matrix for each layer, as discussed in the text, and illustrated here by the arrows.

that any formula derived for one polarisation can be generalised to the other polarisation by making the substitutions $\mathbf{H} \leftrightarrow \mathbf{E}$ and $\mu \leftrightarrow -\varepsilon$ [57].

In the derivations for the TE-polarisation that follow, the quantity p is defined as

$$p = \sqrt{\frac{\varepsilon\varepsilon_0}{\mu\mu_0}} \cos\theta = n\cos\theta \tag{2.3}$$

where θ is the angle of propagation to the normal and ε and μ are the relative permittivity and relative permeability of the medium respectively. Due to the substitution rule outlined above, all the results derived for the TE-polarisation can be generalised to the TM-polarisation by replacing the quantity p by its equivalent for the TM polarisation

$$p = \sqrt{\frac{\mu\mu_0}{\varepsilon\varepsilon_0}} \cos\theta = \frac{\cos\theta}{n} \tag{2.4}$$

The parameter n is the refractive index of the medium when the medium is non-magnetic ($\mu = 1$), as is the case in this thesis.

2.1.1 Transfer matrix through a single layer

For a linear, isotropic, homogeneous material of relative permittivity ε and relative permeability μ

$$\mathbf{B} = \mu\mu_0\mathbf{H} \tag{2.5}$$

$$\mathbf{D} = \varepsilon\varepsilon_0\mathbf{E} \tag{2.6}$$

and the Maxwell equations

$$\nabla \times \mathbf{E} = -\frac{\partial \mathbf{B}}{\partial t} \tag{2.7}$$

$$\nabla \times \mathbf{H} = \frac{\partial \mathbf{D}}{\partial t} \tag{2.8}$$

can be written as

$$\nabla \times \mathbf{E} = i\omega\mu\mu_0\mathbf{H} \tag{2.9}$$

$$\nabla \times \mathbf{H} = -i\omega\varepsilon\varepsilon_0\mathbf{E} \tag{2.10}$$

for time-harmonic waves of angular frequency ω. In the TE-polarisation, there is only one non-zero component of the electric field, E_y. Thus equation 2.9 gives

$$-\frac{\partial E_y}{\partial z} = i\omega\mu\mu_0 H_x \tag{2.11}$$

$$0 = i\omega\mu\mu_0 H_y \tag{2.12}$$

$$\frac{\partial E_y}{\partial x} = i\omega\mu\mu_0 H_z \tag{2.13}$$

and it is apparent that the magnetic field has two non-zero components, H_x and H_z. Equation 2.10 becomes

$$\frac{\partial H_x}{\partial z} - \frac{\partial H_z}{\partial x} = -i\omega\varepsilon\varepsilon_0 E_y \tag{2.14}$$

$$\frac{\partial H_x}{\partial y} = 0 \tag{2.15}$$

$$\frac{\partial H_z}{\partial y} = 0 \tag{2.16}$$

showing that the magnetic field is constant in the y direction. Substitution of equations 2.14 to 2.16 into equations 2.11 to 2.13 gives the wave equation for the electric field

$$\frac{\partial^2 E_y}{\partial z^2} + \frac{\partial^2 E_y}{\partial x^2} + k^2 E_y = 0 \tag{2.17}$$

where $k = n\omega/c$ and $n = \sqrt{\varepsilon\mu}$ is the refractive index of the layer. This can be solved by a separation of variables, to give

$$E_y = E_{0,y}(z)\, e^{ik_x x - i\omega t} \tag{2.18}$$

and using equations 2.11 to 2.13

$$H_x = H_{0,x}(z)\, e^{ik_x x - i\omega t} \tag{2.19}$$

$$H_z = H_{0,z}(z)\, e^{ik_x x - i\omega t} \tag{2.20}$$

where the relationships between $E_{0,y}(z)$, $H_{0,x}(z)$ and $H_{0,z}(z)$ are

$$\frac{dH_{0,x}(z)}{dz} - ik_x H_{0,z}(z) = -i\omega\varepsilon\varepsilon_0 E_{0,y}(z) \tag{2.21}$$

$$\frac{dE_{0,y}(z)}{dz} = -i\omega\mu\mu_0 H_{0,x}(z) \tag{2.22}$$

$$ik_x E_{0,y}(z) = i\omega\mu\mu_0 H_{0,z}(z) \tag{2.23}$$

Eliminating $H_{0,z}(z)$ from equations 2.21 and 2.23 gives

$$\frac{dH_{0,x}(z)}{dz} = \left(\frac{ik_x^2}{\omega\mu\mu_0} - i\omega\varepsilon\varepsilon_0\right) E_{0,y}(z) \tag{2.24}$$

Differentiating equations 2.22 and 2.24 with respect to z leads to

$$\frac{d^2H_{0,x}(z)}{dz^2} = \left(\frac{ik_x^2}{\omega\mu\mu_0} - i\omega\varepsilon\varepsilon_0\right)\frac{dE_{0,x}(z)}{dz} \tag{2.25}$$

$$\frac{d^2E_{0,y}}{dz^2} = -i\omega\mu\mu_0\frac{dH_{0,y}(z)}{dz} \tag{2.26}$$

Substituting equation 2.24 and equation 2.22 into these gives

$$\frac{d^2E_{0,y}}{dz^2} + k_z^2 E_{0,y}(z) = 0 \tag{2.27}$$

$$\frac{d^2H_{0,x}}{dz^2} + k_z^2 H_{0,x}(z) = 0 \tag{2.28}$$

Equation 2.27 has the general solution

$$E_{0,y}(z) = A\sin(k_z z) + B\cos(k_z z) \tag{2.29}$$

where A and B are constants. Using equation 2.22, the solution of equation 2.28 is

$$H_{0,x}(z) = \frac{k_z A}{i\omega\mu\mu_0}\cos(k_z z) - \frac{k_z A}{i\omega\mu\mu_0}\sin(k_z z) \tag{2.30}$$

Now, to simplify the solution of the Maxwell equations in the TE polarisation, we can construct a two-component column vector, whose components are the tangential components of the electric and magnetic fields

$$\Theta(z) = \begin{bmatrix} E_{0,y}(z) \\ H_{0,x}(z) \end{bmatrix} \tag{2.31}$$

The electromagnetic fields can then be coupled between any two planes of constant z within the layer by applying the solutions of the Maxwell equations

$$\Theta(z) = \hat{\mathrm{M}}\Theta(z_0) \tag{2.32}$$

Due to the substitution rule for transforming between the two independent polarisations, the vector for the TM polarisation must be constructed as

$$\Theta(z) = \begin{bmatrix} H_{0,y}(z) \\ E_{0,x}(z) \end{bmatrix} \tag{2.33}$$

and the fields are coupled in the same way as the TE polarisation, by using equation 2.32.

Here $\hat{\mathrm{M}}$ is the transfer matrix to propagate the electromagnetic fields from z_0 to z. When z_0 and z are the boundaries of a layer in a dielectric multilayer structure, $\hat{\mathrm{M}}$ is known as the characteristic matrix of the layer. To find the form of the matrix elements M_{ij}, we consider the two cases when $\Theta(z_0) = [1, 0]$, and $\Theta(z_0) = [0, 1]$, which will give four conditions with which to specify M_{11}, M_{12}, M_{21} and M_{22}. Applying the boundary condition $E_{0,x}(z_0) = 1$

and $H_{0,y}(z_0) = 0$ gives $A = \sin(k_z z_0)$ and $B = \cos(k_z z_0)$ and

$$M_{11} = \cos(k_z(z - z_0)) \tag{2.34}$$

$$M_{21} = ip\sin(k_z(z - z_0)) \tag{2.35}$$

where p is given by equation 2.3 (and equation 2.4 for the TM polarisation). Applying the boundary condition $E_{0,x}(z_0) = 0$ and $H_{0,y}(z_0) = 1$ gives

$$M_{12} = \frac{i}{p}\sin(k_z(z - z_0)) \tag{2.36}$$

$$M_{22} = \cos(k_z(z - z_0)) \tag{2.37}$$

Therefore, when z and z_0 are the coordinates of the two boundaries of an isotropic homogeneous layer, the characteristic transfer matrix of the layer is

$$\hat{\mathrm{M}} = \begin{bmatrix} \cos(k_z d) & i\frac{1}{p}\sin(k_z d) \\ ip\sin(k_z d) & \cos(k_z d) \end{bmatrix} \tag{2.38}$$

where $d = z - z_0$ is the thickness of the layer, $k_z = (n\omega/c)\cos\theta$ is the z-component of the wavevector and n is the refractive index of the layer. p is given in equation 2.3 for the TE-polarisation and equation 2.4 for the TM polarisation.

2.1.2 Characteristic transfer matrix of dielectric multilayers

For a multilayered dielectric structure consisting of N isotropic, homogeneous layers, where the i^{th} layer has boundaries at $z = z_{i-1}$ and $z = z_i$, the formula

$$\Theta(z_i) = \hat{\mathrm{M}}(z_i - z_{i-1})\,\Theta(z_{i-1}) \tag{2.39}$$

relates the tangential components of the electromagnetic fields at the layer boundaries. The tangential components of the electric and magnetic fields at any dielectric boundary must be continuous, so if the fields at the external boundary are known, the characteristic transfer

matrix of successive layers can be applied to propagate the fields through the structure. Thus

$$\Theta(z_N) = \hat{\mathrm{M}}(z_N - z_0)\,\Theta(z_0) \tag{2.40}$$

where the characteristic transfer matrix for the entire multilayer structure $\hat{\mathrm{M}}(z_N - z_0)$ is the product of the matrices for each layer

$$\hat{\mathrm{M}}(z_N - z_0) = \hat{\mathrm{M}}(z_N - z_{N-1}) \ldots \hat{\mathrm{M}}(z_i - z_{i-1}) \ldots \hat{\mathrm{M}}(z_1 - z_0) \tag{2.41}$$

where

$$\hat{\mathrm{M}}(z_j - z_{j-1}) = \begin{bmatrix} \cos(k_{z,j} d_j) & i\frac{1}{p_j}\sin(k_{z,j} d_j) \\ i p_j \sin(k_{z,j} d_j) & \cos(k_{z,j} d_j) \end{bmatrix} \tag{2.42}$$

where the subscripts j label the layers. Thus the electromagnetic fields can be propagated through the entire structure, as long as the boundary conditions are known. The situation is illustrated in figure 2.1.

2.1.3 Reflection and transmission

Now consider a multilayer dielectric structure, surrounded by two semi-infinite media of relative permittivity ε_f and ε_l and relative permeabilities μ_f and μ_l, as shown in figure 2.1. The characteristic transfer matrix of the multilayer can be calculated as $\hat{\mathrm{M}}$, and this couples the fields at the left and right boundaries of the multilayer. The general solution to the Maxwell equations in the homogeneous, isotropic semi-infinite boundary media can be written as

$$E_{0,y}(z) = \begin{cases} A' e^{i k_{z,f} z} + B' e^{-i k_{z,f} z} & z < z_0 \\ C' e^{i k_{z,l} z} + D' e^{-i k_{z,l} z} & z > z_N \end{cases} \tag{2.43}$$

$$H_{0,x}(z) = \begin{cases} i k_{z,f} A' e^{i k_{z,f} z} - i k_{z,f} B' e^{-i k_{z,f} z} & z < z_0 \\ i k_{z,l} C' e^{i k_{z,l} z} - i k_{z,l} D' e^{-i k_{z,l} z} & z > z_N \end{cases} \tag{2.44}$$

These equations describe an incident plane wave from the left of the multilayer structure with a complex amplitude A'. The incident wave is partially reflected by the multilayer to give a left-travelling wave in the region $z < z_0$ of complex amplitude B'. It is also be partially transmitted through the structure, to give a right-travelling wave in the region

$z > z_N$ of amplitude C'. However, since there is no left-travelling wave in the region $z > z_N$, $D' = 0$. The reflection coefficient is given by the ratio of the amplitudes $r = B'/A'$ and the transmission coefficient by $t = C'/A'$. Then the reflectivity is $R = |r|^2$, and the transmissivity is $T = |t|^2 p_l/p_f$, which describe the proportions of the power reflected by and transmitted through the structure respectively. The fields at the left and right boundaries are coupled by the characteristic transfer matrix, so

$$\hat{\mathrm{M}} \begin{bmatrix} 1+r \\ p_f\,(1-r) \end{bmatrix} = \begin{bmatrix} t \\ p_l t \end{bmatrix} \tag{2.45}$$

and thus the reflection coefficient is given by

$$r = \frac{M_{11} + M_{12}p_f - M_{21}/p_l - M_{22}p_f/p_l}{M_{12}p_f + M_{21}/p_l - M_{22}p_f/p_l - M_{11}} \tag{2.46}$$

and the transmission coefficient is

$$t = \frac{2\,(M_{11}M_{22} - M_{12}M_{21})\,p_f/p_l}{M_{11} + M_{22}p_f/p_l - M_{12}p_f - M_{21}/p_l} \tag{2.47}$$

Note that conservation of energy requires $M_{11}M_{22} - M_{12}M_{21} = 1$ for the characteristic transfer matrix of any multilayer where there is no absorption of light (i.e. all the refractive indices are real, non-complex values).

2.1.4 Eigenfrequencies

The eigenfrequencies of the electromagnetic modes of the structure can be found by considering the structure with no incident electromagnetic fields. The condition of no incident electromagnetic fields corresponds to a boundary condition of outgoing waves, or simply only a left-travelling wave in the region $z < z_0$ and a right-travelling wave in the region $z > z_N$ giving $A' = D' = 0$ in equations 2.43 and 2.44. It follows

$$\hat{\mathrm{M}} \begin{bmatrix} 1 \\ -p_f \end{bmatrix} = \mathcal{A} \begin{bmatrix} 1 \\ p_l \end{bmatrix} \tag{2.48}$$

where $\mathcal{A}$ is a constant. Eliminating the constant $\mathcal{A}$ from the two equations that result from equation 2.48 gives the formula

$$M_{11}(\omega) - M_{12}(\omega) p_f - M_{21}(\omega) \frac{1}{p_l} + M_{22}(\omega) \frac{p_f}{p_l} = 0 \tag{2.49}$$

The values of ω which are the roots of the above equation are the eigenfrequencies of the multilayered system. These eigenfrequencies will be complex, as the electromagnetic fields within the structure decay, with a lifetime related to the imaginary part of the eigenfrequencies, $\tau = 1/\mathrm{Im}(\omega)$.

2.1.5 Electromagnetic field profiles

The electromagnetic fields in a multilayered dielectric structure result from the interference of waves due to multiple reflections and transmissions at the the various dielectric boundaries that make up the structure. Hence the electromagnetic field profile can be very complicated, even for a structure with just a few layers.

The transfer matrix $\hat{\mathrm{M}}(z' - z)$ can be used to relate the fields at any two points within the structure. The method for calculating the electromagnetic field throughout the structure consists of dividing each layer into a series of slices, and applying the transfer matrix of a slice to propagate the fields from one slice to the next. Hence, if the electric and magnetic fields are known at one external boundary (or at any other point in the structure), the complete electromagnetic field profile for the structure can be calculated.

2.1.6 Transfer matrix in a basis of propagating waves

This section has so-far detailed transfer matrix methods using a basis of the tangential components of the electric and magnetic fields. However, sometimes it is useful to recast the transfer matrix method into a basis of left and right propagating plane waves. The general solution of the Maxwell equations within the i^{th} layer of a multilayered structure

$$E_{0,x}(z) = a_i e^{ik_{z,i}z} + b_i e^{-ik_{z,i}z} \qquad z_{i-1} < z < z_i \tag{2.50}$$

for the TE-polarisation. We can construct a two-component column vector consisting of the complex amplitudes of the left and right propagating plane waves

$$\Phi(z) = \begin{bmatrix} a(z) \\ b(z) \end{bmatrix} \tag{2.51}$$

Matrices can then be constructed to propagate the fields across a layer in the structure

$$\hat{\mathrm{M}}^{(l)} = \begin{bmatrix} e^{-i\phi_i} & 0 \\ 0 & e^{+i\phi_i} \end{bmatrix} \tag{2.52}$$

where ϕ_i is the change in the phase associated with propagation across the layer. At the dielectric interfaces between the layers, reflection and transmission of the plane waves takes place. In the transfer matrix formalism with a plane wave basis, this is described by the so-called dynamical matrices [56]

$$\hat{\mathrm{M}}_i^{(d)} \Phi_i(z_i) = \hat{\mathrm{M}}_i^{\prime(d)} \Phi_i'(z_i) \tag{2.53}$$

where $\Phi_i(z_i)$ and $\Phi_i'(z_i)$ are the amplitudes of the fields at the left and right boundaries of the i^{th} dielectric interface respectively. The dynamical matrices are given by

$$\hat{\mathrm{M}}_i^{(d)} = \begin{bmatrix} 1 & 1 \\ n_i \cos\theta_i & -n_i \cos\theta_i \end{bmatrix} \tag{2.54}$$

for TE-polarised waves and

$$\hat{\mathrm{M}}_i^{(d)} = \begin{bmatrix} \cos\theta_i & \cos\theta_i \\ n_i & -n_i \end{bmatrix} \tag{2.55}$$

for TM-polarised waves.

Ref. [56] includes a derivation of the transfer matrix in the basis of the left and right propagating plane waves, and also a discussion of the properties of the transfer matrix. The most important result for this thesis is that the transfer matrix of any structure can be written

in terms of the reflection and transmission coefficients, r and t, of the structure

$$\hat{\mathrm{M}} = \frac{1}{t}\begin{bmatrix} 1 & -r \\ r & t^2 - r^2 \end{bmatrix} \tag{2.56}$$

2.2 Fresnel equations for reflection and transmission at a dielectric interface

The Fresnel formula give the reflection from and transmission through a dielectric interface. These formulae are derived by considering the boundary conditions on the electric and magnetic fields at such an interface [57]. These state that the tangential component of the electric and magnetic field must be continuous at any dielectric interface. The Fresnel formula can be obtained in the transfer matrix formalism by writing the characteristic transfer matrix of a single interface, bounded by the two semi-infinite media with refractive indexes n_1 and n_2, and using equations 2.46 and 2.47 for the reflection and transmission coefficients. Consider a plane wave incident upon the interface from the first medium. The wave will be partially reflected from the interface, and partially transmitted through the interface into the second medium. The continuity of the tangential components of the electric and magnetic fields can formally be described by the transfer matrix through the interface which is just the 2×2 unity matrix,

$$\hat{\mathrm{M}} = \begin{bmatrix} 1 & 0 \\ 0 & 1 \end{bmatrix} \tag{2.57}$$

Thus, from equation 2.46 the reflection coefficient is

$$r = \frac{p_1 - p_2}{p_1 + p_2} \tag{2.58}$$

and from equation 2.47 the transmission coefficient is

$$t = \frac{2p_1}{p_1 + p_2} \tag{2.59}$$

Snell's law can be used to express the Fresnel equations in terms of the angles of incidence and refraction only (see, for example, ref. [57], page 40).

Thus the reflectivity and transmissivity are given by

$$R = |r|^2 = \left(\frac{p_1 - p_2}{p_1 + p_2}\right)^2 \tag{2.60}$$

$$T = \frac{p_2}{p_1}|t|^2 = \frac{4p_1p_2}{(p_1 + p_2)^2} \tag{2.61}$$

respectively.

2.3 Thin films

A thin film can be considered as a dielectric multilayer with only one layer (or as two dielectric interfaces). Let this layer have a refractive index of $n_2 = \sqrt{\varepsilon_2}$ ($\mu = 1$) and a width d_2, so that the characteristic transfer matrix through the thin film is

$$\hat{\mathbf{M}} = \begin{bmatrix} \cos(k_{2,z}d_2) & \frac{i}{p_2}\sin(k_{2,z}d_2) \\ ip_2\sin(k_{2,z}d_2) & \cos(k_{2,z}d_2) \end{bmatrix} \tag{2.62}$$

where $p_2 = n_2\cos\theta_2$ for TE-polarised waves, and $p_2 = \cos\theta_2/n_2$ for TM-polarised waves. Consider now the symmetric case, where the film is bounded on both sides by the same material, of refractive index n_1. From equation 2.46 the reflection coefficient is given by

$$r = \frac{M_{11} + M_{12}p_1 - M_{21}/p_1 - M_{22}}{M_{12}p_1 + M_{21}/p_1 - M_{22} - M_{11}} \tag{2.63}$$

or, inserting the form of the matrix elements from equation 2.62

$$r = \frac{i\left(\frac{p_1}{p_2} - \frac{p_2}{p_1}\right)\sin(k_{2,z}d_2)}{i\left(\frac{p_1}{p_2} + \frac{p_2}{p_1}\right)\sin(k_{2,z}d_2) - 2\cos(k_{2,z}d_2)} \tag{2.64}$$

Alternatively, this formula can be derived from consideration of the multiple reflections within the film which occur at the dielectric boundaries (known as an Airy summation—see, for example, [56], chapter 4). Equation 2.64 leads to the spectral form of the Fabry-Perot

oscillations in the reflection spectrum

$$R = \frac{4r_1^2 \sin^2(k_{2,z}d_2)}{(1-r_1^2)^2 + 4r_1^2 \sin(k_{2,z}d_2)} \tag{2.65}$$

where r_1 is the reflection coefficient of the dielectric interfaces, given by the Fresnel equations as $r_1 = (p_1 - p_2)/(p_1 + p_2)$. The eigenfrequencies of the thin film can be found by application of outgoing wave boundary conditions, as discussed in section 2.1.4. The eigenfrequencies are given by the equation

$$2\cos(k_{2,z}d_2) + i\left(\frac{p_1}{p_2} + \frac{p_2}{p_1}\right)\sin(k_{2,z}d_2) = 0 \tag{2.66}$$

or, after rearrangement

$$\tan(k_{2,z}d_2) = \frac{2ip_1p_2}{p_1^2 + p_2^2} \tag{2.67}$$

For TE-polarised waves, $p_{1,2} = n_{1,2}\cos\theta_{1,2}$, so

$$\tan(k_{2,z}d_2) = \frac{2ik_{1,z}k_{2,z}}{k_{1,z}^2 + k_{2,z}^2} \tag{2.68}$$

For TM-polarised wave, $p_{1,2} = \cos\theta_{1,2}/n_{1,2}$, so

$$\tan(k_{2,z}d_2) = \frac{2ik_{1,z}k_{2,z}}{(n_2/n_1)^2 k_{1,z}^2 + (n_1/n_2)^2 k_{2,z}^2} \tag{2.69}$$

is the eigenvalue equation for TM-polarised modes in the thin film. Due to the symmetry of the structure under consideration, the electromagnetic field profiles of the eigenmodes must be either symmetric or antisymmetric; two different classes of solutions of equation 2.68 and equation 2.69 give the eigenfrequencies of the symmetric and antisymmetric modes. Equations 2.68 and 2.69 can also be derived by directly considering the symmetric and antisymmetric fields that are the solutions of the Maxwell equations in the three regions which the thin film comprises.

In equation 2.67, we can write the tangent function in terms of complex exponentials, and rearrange to give

$$e^{ik_{2,z}d_2} = \pm\frac{p_1 - p_2}{p_1 + p_2} = \pm r_1 \tag{2.70}$$

Using the positive sign on the right hand side leads to the eigenfrequencies of the symmetric

modes, while the negative sign leads to the eigenfrequencies for the antisymmetric modes. The eigenfrequencies are thus given by

$$\omega = \frac{m\pi c}{n_2 \cos\theta_2 d_2} - i\frac{c}{n_2 \cos\theta_2 d_2} \ln r_1 \tag{2.71}$$

where even values of the integer m give the eigenfrequencies of the symmetric modes, and odd values give the eigenfrequencies of the antisymmetric modes. The eigenfrequencies are complex and the time dependence of the electromagnetic field is $e^{-i\omega t} = e^{-i\mathrm{Re}(\omega)t}e^{\mathrm{Im}(\omega)t}$. Hence the fields oscillate at an angular frequency given by the real part of the complex eigenfrequencies and decay in exponentially in time by a factor $e^{\mathrm{Im}(\omega)t}$ where $\mathrm{Im}\,(\omega)$ is negative. This exponential decay of the fields within the structure is due to the outgoing wave boundary conditions—light can escape and leak out of the external boundaries, but no light is incident on the thin film. If τ is the lifetime of the eigenmodes of the thin film, defined by the time taken for the fields to decay by a factor of e, then

$$\tau = \frac{1}{\mathrm{Im}\,(\omega)} \tag{2.72}$$

From equation 2.71, it can be seen that the frequencies of the modes depends only on the properties of the film, specifically on the phase change of light as it propagates through the film. The lifetime, however, depends on the properties of both the film and the bounding medium. Specifically the lifetime is dependent on the reflection coefficient of the bounding dielectric interfaces.

2.4 Bragg reflectors

A Bragg reflector is a dielectric multilayer that has a periodic refractive index profile along the direction of stratification. Usually consisting of two types of layer, A and B, of refractive indices n_1 and n_2 and layer thicknesses d_1 and d_2, they ideally have equal optical thickness, such that $n_1 d_1 = n_2 d_2$. In such a structure, the transfer matrix for one period is

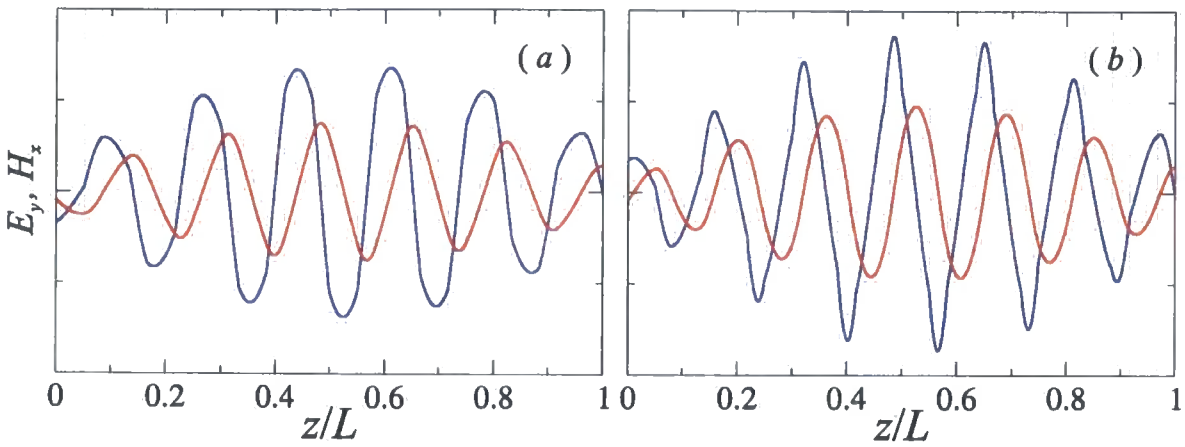

Figure 2.2 Tangential components of the electric (red) and magnetic (blue) fields of the eigenmodes below (a) and above (b) the PBG of a 12 period Bragg reflector. The complex eigenfrequencies of the modes are (a) $\omega/\omega_0 = 0.836 - i2.95 \times 10^{-3}$ and (b) $\omega/\omega_0 = 1.164 - i2.95 \times 10^{-3}$.

given by the matrix multiplication of the transfer matrices for the two layers

$$\hat{\mathrm{M}}^{(P)} = \begin{bmatrix} \cos(k_{2,z}d_2) & \frac{i}{p_2}\sin(k_{2,z}d_2) \\ ip_2\sin(k_{2,z}d_2) & \cos(k_{2,z}d_2) \end{bmatrix} \begin{bmatrix} \cos(k_{1,z}d_1) & \frac{i}{p_1}\sin(k_{1,z}d_1) \\ ip_1\sin(k_{1,z}d_1) & \cos(k_{1,z}d_1) \end{bmatrix} \tag{2.73}$$

For N such periods, the total transfer matrix across the Bragg reflector is $\left[\hat{\mathrm{M}}\right]^N$. From the transfer matrix, the reflection and transmission spectrum can be calculated.

2.4.1 Dispersion relation

Figure 2.2 shows the electric and magnetic fields of the eigenmodes immediately below (a) and above (b) the PBG. Using Bloch's theorem for periodic media, the electromagnetic fields in the structure can be written as

$$\Theta(z) = e^{iKz}\Theta^{(0)}(z) \tag{2.74}$$

where $D = d_1 + d_2$ is the period of the Bragg reflector, and K is the Bloch wavevector. The vector $\Theta^{(0)}$ has the periodicity of the Bragg reflector, $\Theta^{(0)}(z) = \Theta^{(0)}(z + D)$. If z is at a dielectric interface, then the fields at z and $z + D$ are related through the transfer matrix for one period

$$\Theta(z + D) = \hat{\mathrm{M}}^{(P)}\Theta(z) \tag{2.75}$$

where $\hat{\mathbf{M}}^{(P)}$, given by equation 2.73, is the transfer matrix for one period in the Bragg reflector. Therefore

$$\hat{\mathbf{M}}^{(P)}\Theta(z) = e^{iKD}\Theta(z) \tag{2.76}$$

which is an eigenvalue equation, where e^{iKD} are the eigenvalues of the transfer matrix $\hat{\mathbf{M}}^{(P)}$. The eigenvalues are found from the secular equation $\det\left(\hat{\mathbf{M}}^{(P)} - \hat{\mathbf{I}}e^{iKD}\right) = 0$, where $\hat{\mathbf{I}}$ is the 2×2 identity matrix. Therefore

$$\cos(KD) = \frac{1}{2}\left(M_{11}(\omega) + M_{22}(\omega)\right) \tag{2.77}$$

gives the dispersion relation for the infinite periodic multilayer structure with period D and transfer matrix through one period $\hat{\mathbf{M}}^{(P)}$. For the Bragg reflector,

$$\cos(KD) = \frac{(p_1+p_2)^2}{4p_1p_2}\cos(k_{1,z}d_1 + k_{2,z}d_2) - \frac{(p_1-p_2)^2}{4p_1p_2}\cos(k_{1,z}d_1 - k_{2,z}d_2) \tag{2.78}$$

or, in terms of the reflectivity, R_1, and transmissivity, T_1, of the dielectric interfaces that make up the Bragg reflector,

$$\cos(KD) = \frac{1}{T_1}\cos(k_{1,z}d_1 + k_{2,z}d_2) - \frac{R_1}{T_1}\cos(k_{1,z}d_1 - k_{2,z}d_2) \tag{2.79}$$

Equation 2.79 can be solved numerically, and it is found that band gaps appear in the dispersion relation of the Bragg reflector. These photonic band gaps are spectral regions for which no real solutions exist for the Bloch wavevector K, since $|\cos(KD)| > 1$. Thus the band gap edges are at $\cos(KD) = \pm 1$, or values of K which correspond to the centre and edges of the first Brillouin zone. For normal incidence ($\theta = 0$), the PBG appears for any arbitrary values of the refractive indices of the layers as long as $n_1 \neq n_2$, and regardless of how small the refractive index contrast between the two types of layer is. However, the transfer matrix, and therefore the dispersion relation, is dependent on the angle of propagation of light within the Bragg reflector. The angles in each type of layer are related by Snell's law $n_1 \sin\theta_1 = n_2 \sin\theta_2$. If the angle in the higher index medium exceeds the critical angle for total internal reflection from the high index medium to the low index medium, then the fields will be evanescent in the low index medium and propagation will be perpendicular to the direction of stratification ($\theta = \pi/2$). In this case, the system is in effect an infinite chain

of coupled waveguides, and the band gaps in the dispersion relation will have disappeared, as the light is guided along the direction of constant refractive index.

Now, consider the case for which the optical lengths of the two types of layer are identical, such that $n_1 d_1 = n_2 d_2$, and normal incidence, $\theta = 0$. Then, $k_{1,z} d_1 = k_{2,z} d_2 = kd$ for all frequencies, and the dispersion relation is given by

$$\cos(KD) = 1 - \frac{2}{T_1^{(0)}} \sin^2(kd) \tag{2.80}$$

where $T_1^{(0)} = 4n_1 n_2 / (n_1 + n_2)^2$ is the Fresnel transmissivity through the interfaces in the Bragg reflector at normal incidence.

At the centre of the Brillouin zone, $KD = 0, 2\pi, 4\pi, \ldots$, and $\cos(KD) = 1$, and

$$\frac{2}{T_1^{(0)}} \sin^2(kd) = 0 \tag{2.81}$$

Therefore there is only a doubly degenerate solution $kd = m\pi$ for each value of the integer m, and thus no band gap is formed at the centre of the Brillouin zone when $n_1 d_1 = n_2 d_2$. This degeneracy is lifted when $n_1 d_1 \neq n_2 d_2$. At the edge of the first Brillouin zone, $\cos(KD) = -1$, and the allowed frequencies in the dispersion relation are given by

$$\sin^2(kd) = T_1^{(0)} \tag{2.82}$$

Thus the edges of the photonic band gap are at angular frequencies

$$\omega_1 = \frac{c}{nd} \arcsin\left(\sqrt{T_1^{(0)}}\right) \tag{2.83}$$

and

$$\omega_2 = \frac{\pi c}{nd} - \frac{c}{nd} \arcsin\left(\sqrt{T_1^{(0)}}\right) \tag{2.84}$$

and the centre of the band gap, called the Bragg frequency, is given by $\omega_0 = (\omega_1 + \omega_2)/2$,

$$\omega_0 = \frac{\pi c}{\langle n \rangle D} \tag{2.85}$$

where $\langle n \rangle$ is the mean refractive index in the Bragg reflector. The width of the band gap is

given by $\Delta\omega = \omega_2 - \omega_1$,

$$\Delta\omega = \frac{2\pi c}{\langle n \rangle D} - \frac{4c}{\langle n \rangle D} \arcsin\left(\sqrt{T_1^{(0)}}\right) \tag{2.86}$$

and the width of the band gap relative to its centre frequency is

$$\frac{\Delta\omega}{\omega_0} = 2 - \frac{4}{\pi} \arcsin\left(\sqrt{T_1^{(0)}}\right) \tag{2.87}$$

In the PBG, the Bloch wavevector is complex. The physical meaning of this complex wavevector can be seen by examining the form of equation 2.74.

$$\Theta(z) = e^{i\mathrm{Re}(K)z} e^{-\mathrm{Im}(K)z} \Theta^{(0)}(z) \tag{2.88}$$

The real part of the Bloch wavevector K describes the periodicity of the envelope function of the oscillatory electromagnetic field. However when K is complex, the envelope function also describes how the incident field decays exponentially with distance into the Bragg reflector. The attenuation length of the electromagnetic fields, defined as the distance over which the envelope of the electromagnetic fields decays by a factor of e, is given by the reciprocal of the imaginary part of the complex wavevector $(1/\mathrm{Im}(K))$. At the centre of the band gap, the transfer matrix for one period of the Bragg reflector is

$$\hat{\mathbf{M}} = \begin{bmatrix} -n_1/n_2 & 0 \\ 0 & -n_2/n_1 \end{bmatrix} \tag{2.89}$$

and therefore

$$e^{iKD} \begin{bmatrix} E_x(z) \\ H_y(z) \end{bmatrix} = \begin{bmatrix} -\frac{n_1}{n_2} E_x(z) \\ -\frac{n_2}{n_1} H_y(z) \end{bmatrix} \tag{2.90}$$

when $\omega = \omega_0$. For the electric field, the Bloch wavevector is given by $e^{iKD} = -n_1/n_2$, so

$$K = \frac{\pi}{D} - i\frac{1}{D} \ln\left(\frac{n_1}{n_2}\right) \tag{2.91}$$

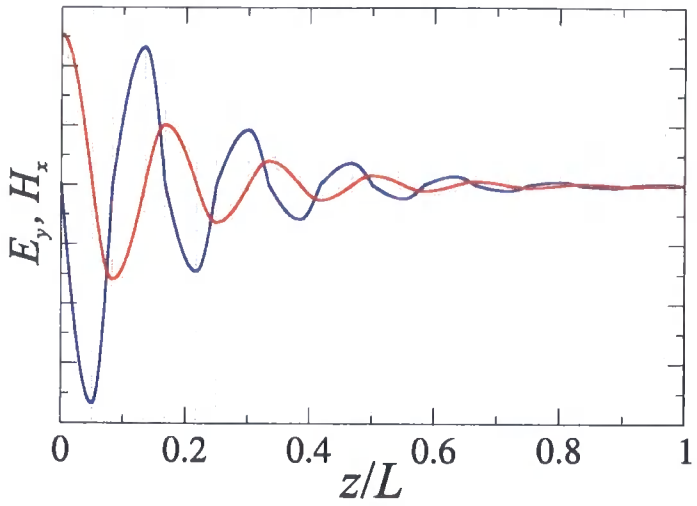

Figure 2.3 Tangential components of the electric (red) and magnetic (blue) fields when a plane wave is incident from the left of a 12 period Bragg reflector at the Bragg frequency ($\omega = \omega_0$).

and for the magnetic field, $e^{iKD} = -n_2/n_1$, so

$$K = \frac{\pi}{D} - i\frac{1}{D}\ln\left(\frac{n_2}{n_1}\right) \tag{2.92}$$

Therefore the attenuation per period of the Bragg reflector is dependent on the ratio of the refractive indices of the two layers. As an example, figure 2.3 shows the electric and magnetic fields of a plane wave incident on a 12-period Bragg reflector from the left at the Bragg frequency.

2.4.2 Reflection and transmission

The reflection and transmission spectra can be calculated from the transfer matrix by application of equation 2.46 and equation 2.47. Figure 2.4 shows the reflection and transmission spectra of a Bragg reflector with parameters $n_1 = 1.45$, $n_2 = 2.3$, $d_1 = 120.7\,\text{nm}$, $d_2 = 76.1\,\text{nm}$, and with $N = 3$ periods, 6 periods or 12 periods. There is a band of high reflectivity in the spectral region of the PBG. This is known as the stop-band of the Bragg reflector. At the Bragg frequency ω_0, the transfer matrix (for normal incidence) is

$$\hat{\mathbf{M}}(\omega_0) = \begin{bmatrix} \left(-\frac{n_1}{n_2}\right)^N & 0 \\ 0 & \left(-\frac{n_2}{n_1}\right)^N \end{bmatrix} \tag{2.93}$$

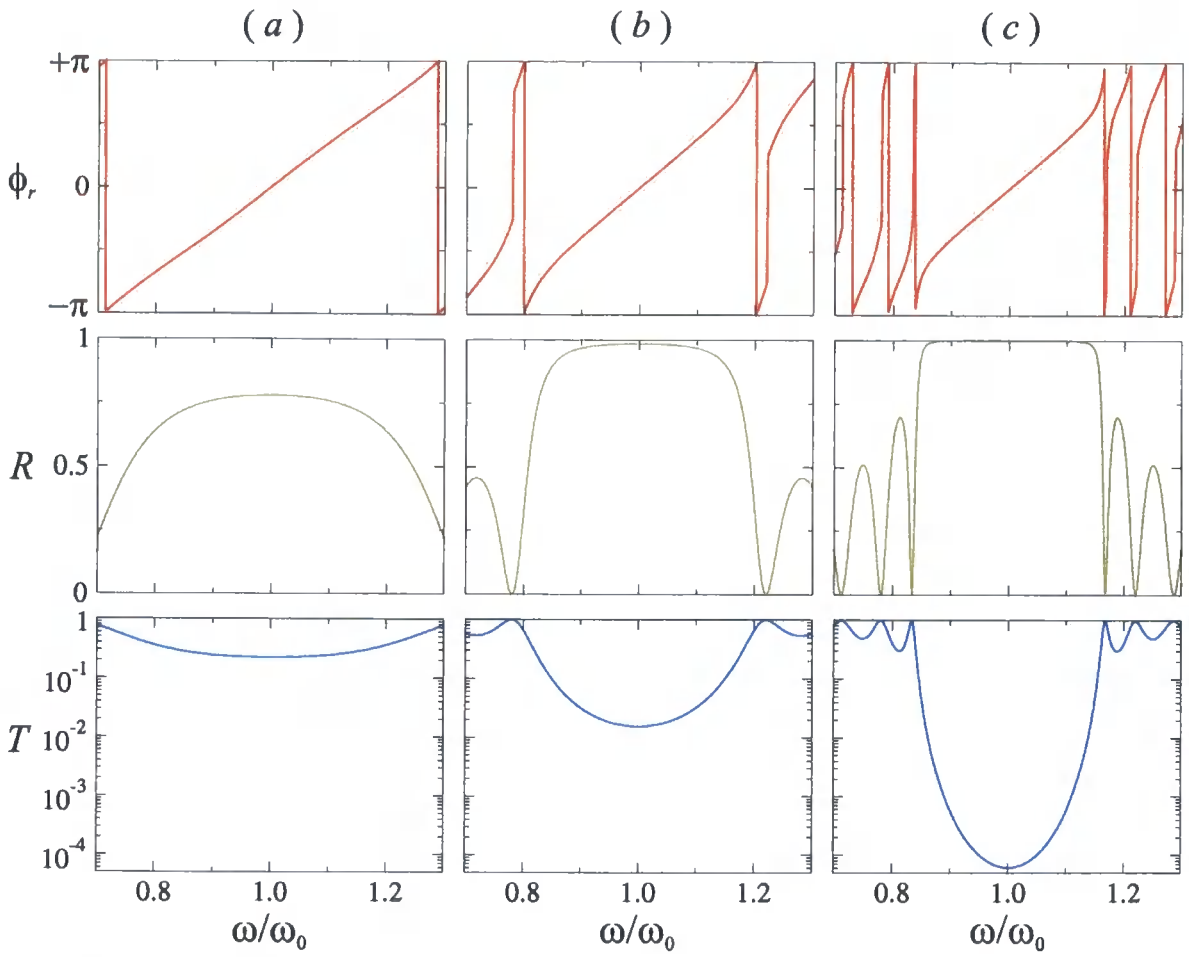

Figure 2.4 Phase change on reflection (top), reflectivity R (middle) and transmission T through a Bragg reflector with $n_1 = 1.45$, $n_2 = 2.3$, $d_1 = 120.7$ nm, $d_2 = 76.1$ nm, and $N = 3$ periods (a), $N = 6$ periods (b) and $N = 12$ periods (c).

for a Bragg reflector of N periods. The reflection coefficient at the Bragg frequency can be calculated from the transfer matrix, and for a Bragg reflector in air,

$$r(\omega_0) = \frac{(n_2/n_1)^{2N} - 1}{(n_2/n_1)^{2N} + 1} \tag{2.94}$$

Thus the phase change on reflection from the Bragg reflector at the Bragg frequency is either 0 (for $n_2 > n_1$) or π (for $n_2 < n_1$). In the spectral region of the stop-band, the phase change upon reflection is approximately a linear function of the frequency, as can be seen in figure 2.4. The maximum reflection (at $\omega = \omega_0$) from the Bragg reflector increases as the number of periods in the Bragg reflector is increased, and also the band of high reflectivity becomes more square. In the transmission spectrum, there is a dip in the region of the PBG, centred on the Bragg frequency ω_0.

2.5 Microcavities

Microcavities are structures that are typically made up of a pair of quarter-wave Bragg reflectors enclosing a central layer of half a wavelength (at the Bragg frequency condition) or more in thickness. The Bragg reflectors essentially act as high reflectivity dielectric mirrors (for frequencies in the stop-band of the Bragg reflector) enclosing the central layer, thus creating a Fabry-Perot type cavity, as illustrated in figure 2.5.

The eigenfrequencies of the microcavity can be found from its transfer matrix by application of outgoing wave boundary conditions. This is most conveniently done by searching for the roots of equation 2.49 numerically. However, an estimate can be made by assuming some simplifications. Using a basis of left and right travelling plane waves, the fields inside the cavity boundaries can be coupled by the matrix equation

$$\mathcal{A}\begin{bmatrix} r_1' \\ 1 \end{bmatrix} = \begin{bmatrix} e^{-i\phi} & 0 \\ 0 & e^{+i\phi} \end{bmatrix}\begin{bmatrix} 1 \\ r_2 \end{bmatrix} \tag{2.95}$$

where r_1' is the reflection coefficient of the left Bragg reflector and r_2 is the reflection coefficient of the right Bragg reflector as seen from the cavity (see figure 2.5), and $\mathcal{A}$ is a constant. r_1' and r_2 are dependent on the frequency (see figure 2.4). Eliminating the constant $\mathcal{A}$ from the two equations that result from equation 2.95 gives

$$r_1' r_2 e^{2i\phi} = 1 \tag{2.96}$$

where ϕ is the phase change associated with propagation across the cavity layer.

If it is assumed that the bounding Bragg mirrors are identical mirror images of each other, so that the layer sequence of the total multilayered structure is $(\mathrm{AB})^N\mathrm{AA}(\mathrm{BA})^N$, then $r_1' = r_2$ and

$$r_2^2 e^{2i\phi} = 1 \tag{2.97}$$

The reflection coefficient of the Bragg reflectors can be written as $r_2 = |r_2|\, e^{i\varphi}$. In the region of the Bragg reflector's stop-band, the magnitude of the reflection coefficient is approximately constant, so we can assume

$$|r_2| \approx |r_2(\omega_0)| \tag{2.98}$$

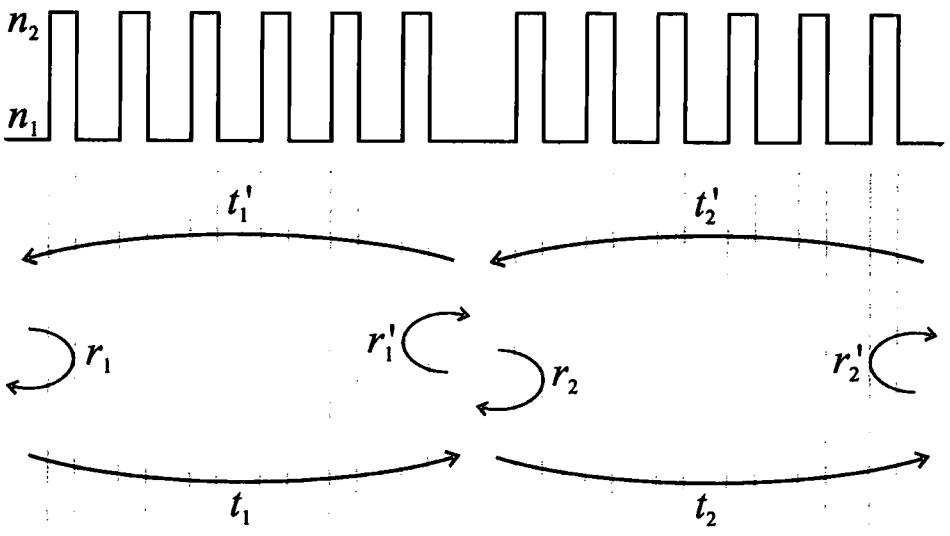

Figure 2.5 A typical refractive index profile of a microcavity bounded by two Bragg reflectors. Vertical grey lines represent dielectric boundaries in the structure. r_1, r_2, t_1 and t_2 are the reflection and transmission coefficients of the left and right Bragg reflectors respectively, when light is incident from the left; dashed values are the equivalent for light incident from the right, as shown by the arrows.

and its phase is approximately a linear function of the frequency, given by [98]

$$\varphi \approx \frac{\pi n_1 n_2}{(n_2 - n_1)\, n_c} \frac{\omega - \omega_0}{\omega_0} \tag{2.99}$$

Solving equation 2.97 for the eigenfrequency using the above approximations gives

$$\omega = \omega_0 - i\frac{\omega_0}{\pi} \frac{(n_2 - n_1)\, n_c}{(n_2 - n_1)\, n_c + n_1 n_2} \ln\left(\frac{1}{|r_2|}\right) \tag{2.100}$$

Figure 2.6 shows the electric (red line) and magnetic (blue line) fields of the cavity mode of a half-wave microcavity enclosed by Bragg reflectors with $N = 6$ periods. It can be seen that the fields are localised on the microcavity layer, as the envelope function of the fields decay exponentially with distance away from the microcavity layer into the two Bragg mirrors.

Thus there is a state localised on the microcavity with an eigenfrequency at the centre of the band gap of the Bragg reflectors and a width which depends on the magnitude of the reflection coefficient of the Bragg reflectors. At the frequency $\omega = \omega_0$, the transfer matrices

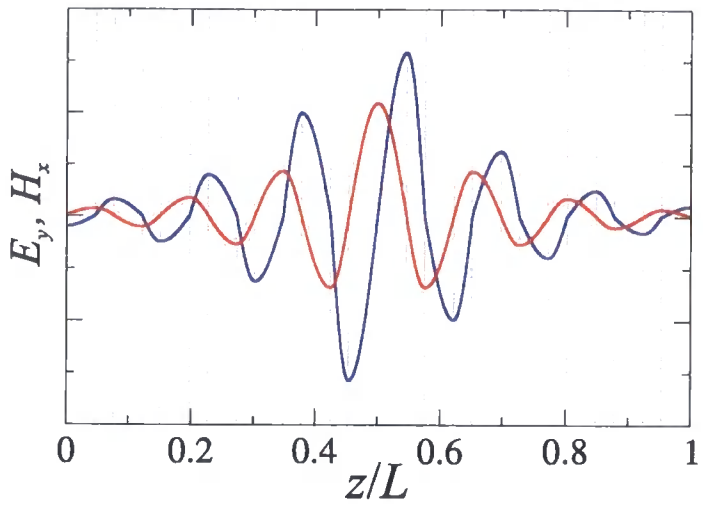

Figure 2.6 Tangential components of the electric (red) and magnetic (blue) field profiles for the cavity eigenmodes of a microcavity with $N = 6$ periods in the enclosing Bragg reflectors. The complex eigenfrequency of the mode is $\omega/\omega_0 = 1.00 - i1.36 \times 10^{-3}$.

for the left and right Bragg mirrors are

$$\hat{\mathbf{M}}(\omega_0) = \begin{bmatrix} (-n_1/n_2)^N & 0 \\ 0 & (-n_2/n_1)^N \end{bmatrix} \tag{2.101}$$

and

$$\hat{\mathbf{M}}(\omega_0) = \begin{bmatrix} (-n_2/n_1)^{N'} & 0 \\ 0 & (-n_1/n_2)^{N'} \end{bmatrix} \tag{2.102}$$

respectively, where N is the number of periods in the left Bragg reflector and N' the number in the right reflector. The transfer matrix of the single cavity layer at the Bragg frequency of the bounding mirrors is

$$\hat{\mathbf{M}}(\omega_0) = \begin{bmatrix} \cos\left(\frac{n_c d_c}{nd}\frac{\pi}{2}\right) & \frac{i}{n_c}\sin\left(\frac{n_c d_c}{nd}\frac{\pi}{2}\right) \\ i n_c \sin\left(\frac{n_c d_c}{nd}\frac{\pi}{2}\right) & \cos\left(\frac{n_c d_c}{nd}\frac{\pi}{2}\right) \end{bmatrix} \tag{2.103}$$

where $nd = n_1 d_1 = n_2 d_2$ is the optical thickness of the layers in the quarter-wave Bragg reflector, and n_c and d_c are the refractive index and thickness of the cavity layer. Therefore the transfer matrix of the whole structure at the Bragg frequency of the mirrors is

$$\hat{\mathbf{M}}(\omega_0) = \begin{bmatrix} (-n_1/n_2)^{N-N'}\cos\left(\frac{n_c d_c}{nd}\frac{\pi}{2}\right) & (-n_2/n_1)^{N+N'}\frac{i}{n_c}\sin\left(\frac{n_c d_c}{nd}\frac{\pi}{2}\right) \\ (-n_1/n_2)^{N-N'} i n_c \sin\left(\frac{n_c d_c}{nd}\frac{\pi}{2}\right) & (-n_2/n_1)^{N-N'}\cos\left(\frac{n_c d_c}{nd}\frac{\pi}{2}\right) \end{bmatrix} \tag{2.104}$$

Choosing the cavity to be a half-wave layer ($n_c d_c = 2nd$) means that the transfer matrix simplifies to

$$\hat{\mathrm{M}}(\omega_0) = \begin{bmatrix} (-n_1/n_2)^{N-N'} & 0 \\ 0 & (-n_2/n_1)^{N-N'} \end{bmatrix} \tag{2.105}$$

It follows that the reflection coefficient is

$$r(\omega_0) = \frac{1-(n_1/n_2)^{2(N'-N)}}{1+(n_1/n_2)^{2(N'-N)}} \tag{2.106}$$

and the reflectivity is

$$R(\omega_0) = \left(\frac{1-(n_1/n_2)^{2(N'-N)}}{1+(n_1/n_2)^{2(N'-N)}}\right)^2 \tag{2.107}$$

as long as the two bounding media are the same (i.e. $n_f = n_l$). Hence the introduction of a microcavity mode at the centre frequency of the stop-band of the Bragg reflectors results in the reflection at the centre of the PBG of the Bragg reflectors is reduced from approximately unity to some significantly smaller value given by equation 2.107. Indeed, if the two Bragg mirrors are identical ($N = N'$), the transfer matrix through the entire structure reduces to the 2×2 identity matrix and the reflectivity $R(\omega_0) = 0$. Hence there is perfect transmission of light at the centre frequency of the stop-band as a result of the introduction of the half-wave cavity.

The frequency dependence of the reflection and transmission properties of a microcavity can also be found by considering the multiple reflections that occur within the cavity layer. To see this take r_1 and t_1 as the reflection and transmission coefficients of the left Bragg mirror when light is incident from the left, and r_1' and t_1' as the equivalent when light is incident from the right. Similar definitions for the right Bragg mirror are also made, as shown in figure 2.5. The total reflection from the entire structure, r, is made up of the first reflection r_1, followed by multiple reflections in the cavity, taking into account the phase shift ϕ on propagation across the cavity layer. Thus

$$r = r_1 + r_2 t_1 t_1' e^{2i\phi} \sum_{n=0}^{\infty} \left(r_2 r_1' e^{2i\phi}\right)^n \tag{2.108}$$

Now using

$$\sum_{n=0}^{\infty} x^n = \frac{1}{1-x} \qquad \text{for} \qquad |x| \leq 1 \tag{2.109}$$

gives

$$r = \frac{r_1 + r_2 \left(t_1 t_1' - r_1 r_1'\right) e^{2i\phi}}{1 - r_2 r_1' e^{2i\phi}} \tag{2.110}$$

Treating the total transmission in a similar way,

$$t = \frac{t_1 t_2 e^{i\phi}}{1 - r_2 r_1' e^{2i\phi}} \tag{2.111}$$

It must be remembered that the reflection and transmission coefficients of the two Bragg mirrors are themselves complex, strongly frequency dependent functions. Therefore, to proceed, make the following simplifications. Assume that the left and right Bragg mirrors are identical "mirror" images of each other, such that $r_1 = r_2'$, $r_2 = r_1'$, $t_1 = t_2'$ and $t_2 = t_1'$. Also assume that the cavity and bounding media have the same refractive index as one of the layers of the Bragg reflector, n_1. In this case $r_1 = r_2$, and $t_1 = t_2$. Thus equation 2.111 simplifies to

$$t = \frac{t_1^2 e^{i\phi}}{1 - r_2^2 e^{2i\phi}} \tag{2.112}$$

The transmissivity is then

$$T = |t|^2 = \frac{(1 - R_1)^2}{(1 - R_1)^2 + 4R_1 \sin^2(\phi + \varphi)} \tag{2.113}$$

for normal incidence, where the reflection coefficient of the Bragg reflectors is written as $r_1 = |r_1| e^{i\varphi}$ and $R_1 = |r_1|^2$. The reflectivity is similarly obtained and is

$$R = |r|^2 = \frac{4R_1 \sin^2(\phi + \varphi)}{(1 - R_1)^2 + 4R_1 \sin^2(\phi + \varphi)} \tag{2.114}$$

In the spectral region of the photonic band gap the magnitude and phase of the reflection coefficient of a Bragg reflector can be approximated by equations 2.98 and 2.99 respectively. At the Bragg frequency ω_0, the phase change for light propagating across the half-wave cavity is $\phi = \pi$, and the phase change upon reflection from the two Bragg reflectors is $\varphi = 0$. Thus from equations 2.113 and 2.114, $R(\omega_0) = 0$ and $T(\omega_0) = 1$, as expected. Also, the FWHM of the transmission spectrum can be estimated as

$$\Delta_{\text{FWHM}} = \frac{c}{nd(1 + n_2)} \frac{1 - R_1}{2\sqrt{R_1}} \tag{2.115}$$

where $1 - R_1$ is assumed to be much smaller than unity. Thus the width of the transmission resonance introduced into the stop-band of the Bragg reflector by the microcavity can be controlled by engineering the reflectivity of the bounding Bragg mirrors.

2.6 Coupled microcavities

Two or more microcavities can be coupled together in a chain, separated by intermediate Bragg mirrors. The system is then a set of coupled oscillators, which will lead to the splitting of frequencies of the the cavity modes, in much the same way as for a set of mechanical oscillators or resonant electrical circuits coupled together. In this section we begin by looking at the splitting of the mode frequencies for a pair of coupled microcavities, as shown in figure 2.7. Then, employing Bloch's theorem for periodic media and using one of the coupled cavities and Bragg mirror as a supercell, the dispersion relation of an infinite chain of coupled microcavities is calculated. It will be seen that the split cavity modes form a photonic miniband in the former PBG when the number of coupled cavities is large enough to be considered essentially infinite.

2.6.1 Cavity mode splitting

Consider a system of two microcavities, bound on either side by Bragg mirrors of reflection coefficient r_1 and r_2, and coupled through an intermediate Bragg mirror of reflectivity r_3. Let the outer Bragg mirrors have N periods, and the intermediate Bragg reflector have $P + 1/2$ periods, as illustrated in figure 2.7, and let the two cavities have refractive indices n_c, and lengths l_1 and l_2 respectively, such that the phase change across a cavity for light incident normally is

$$\phi_{1,2} = \frac{n_c l_{1,2} \omega}{c} \tag{2.116}$$

Using a basis of left- and right-travelling waves, the field at the left boundary of cavity 1 and the right boundary of cavity 2 can be related by

$$\mathcal{A} \begin{bmatrix} r_1 \\ 1 \end{bmatrix} = \begin{bmatrix} e^{-i\phi_1} & 0 \\ 0 & e^{i\phi_1} \end{bmatrix} \begin{bmatrix} \frac{1}{t_3} & -\frac{r_3}{t_3} \\ \frac{r_3}{t_3} & \frac{t_3^2 - r_3^2}{t_3} \end{bmatrix} \begin{bmatrix} e^{-i\phi_2} & 0 \\ 0 & e^{i\phi_2} \end{bmatrix} \begin{bmatrix} 1 \\ r_2 \end{bmatrix} \tag{2.117}$$

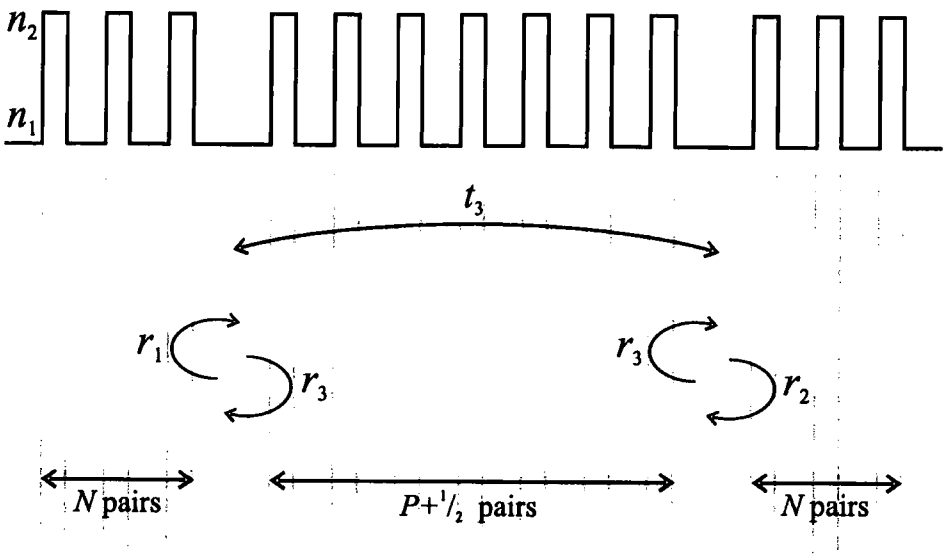

Figure 2.7 Refractive index profile of two coupled microcavities. In general there are Q coupled microcavities; outer Bragg reflectors consist of N pairs of quarter-wave layers while the central Bragg reflectors consist of $P + 1/2$ pairs of layers, as shown. Hence here $N = 3$, $P = 6$ and $Q = 2$. The grey vertical lines represent the dielectric boundaries in the structure, and the outer Bragg reflectors have reflection coefficients r_1 and r_2, as shown. Also the central Bragg reflector has reflection coefficient r_3 and transmission coefficient t_3.

where $\mathcal{A}$ is a constant. Performing the matrix multiplication, and eliminating the constant $\mathcal{A}$ yields

$$r_1 r_2 \left(t_3^2 - r_3^2\right) e^{i(\phi_1+\phi_2)} - e^{-i(\phi_1+\phi_2)} + r_3 \left(r_1 e^{i(\phi_1-\phi_2)} + r_2 e^{-i(\phi_1-\phi_2)}\right) = 0 \qquad (2.118)$$

The solutions of equation 2.118 are the complex eigenfrequencies of the system of coupled microcavities. To proceed, we simplify the problem by considering only symmetric structures, so that $\phi_1 = \phi_2 = \phi$, and $r_1 = r_2$. Thus equation 2.118 becomes

$$r_1^2 \left(t_3^2 - r_3^2\right) e^{2i\phi} - e^{-2i\phi} + 2 r_1 r_3 = 0 \qquad (2.119)$$

which factorises as

$$\left(r_1 \left(r_3 - t_3\right) e^{2i\phi} - 1\right) \left(r_1 \left(r_3 + t_3\right) e^{2i\phi} - 1\right) = 0 \qquad (2.120)$$

It is clear that there are two distinct solutions for the eigenmodes of the system of two coupled microcavities, and that the modes of the two isolated cavities in the stop-band have been split in frequency. The size of this splitting, $\Delta\omega$, is the difference between the two roots

of equation 2.120.

As in section 2.5, the reflection coefficient of the outer Bragg mirrors can be written as $r_1 = |r_1| e^{i\varphi}$ where the magnitude $|r_1|$ and phase φ can be approximated by equations 2.98 and 2.99 in the PBG. Hence the solutions of equation 2.120 can be approximated as

$$\omega = \frac{\frac{\pi n_1 n_2}{(n_2 - n_1) n_c} + i \ln\left(|r_1|\left(r_3 \pm t_3\right)\right)}{\frac{2 n_c l}{c} + \frac{\pi n_1 n_2}{(n_2 - n_1) n_c \omega_0}} \tag{2.121}$$

and the size of the mode splitting is

$$\Delta\omega = \frac{i \ln\left(\frac{r_3 - t_3}{r_3 + t_3}\right)}{\frac{2 n_c l}{c} + \frac{\pi n_1 n_2}{(n_2 - n_1) n_c \omega_0}} \tag{2.122}$$

Assuming that the central Bragg mirror has a sufficient number of periods, then $t_3/r_3 \ll 1$ in the stop-band of the Bragg reflector and the Maclaurin series for the logarithm on the right hand side of equation 2.122 is

$$\ln\left(\frac{r_3 - t_3}{r_3 + t_3}\right) = \ln\left(\frac{1 - t_3/r_3}{1 + t_3/r_3}\right) = -2\frac{t_3}{r_3} - \frac{2}{3}\left(\frac{t_3}{r_3}\right)^3 - \frac{2}{5}\left(\frac{t_3}{r_3}\right)^5 - \ldots \tag{2.123}$$

and only the linear term in t_3/r_3 on the right need be retained in an approximate solution of equation 2.122. It should also be noted that for a symmetric structure, the central Bragg mirror must have an odd number of layers, and hence the phase difference between its transmission coefficient t_3 and its reflection coefficient r_3 will always be $\pi/2$. Thus

$$\frac{t_3}{r_3} = i\frac{|t_3|}{|r_3|} \tag{2.124}$$

and equation 2.122 becomes

$$\Delta\omega = \frac{\omega_0 |t_3|}{\frac{2 n_c l \omega_0}{c} + \frac{\pi n_1 n_2}{(n_2 - n_1) n_c}} \tag{2.125}$$

It is apparent that the size of the mode splitting is directly proportional to the magnitude of the transmission coefficient of the central Bragg mirror.

Two separate, distinct coupling regimes can be realised. In the strong coupling regime, the size of the cavity mode splitting is larger than the width of the cavity modes. In this

case, the transmission spectrum contains two distinct Lorentzian resonances, centred on the eigenfrequencies of the split cavity modes. However, in the weak coupling regime, the size of the cavity mode splitting is smaller than the width of the cavity modes. In this case the two resonances merge into one, such that the transmission spectrum recovers its Lorentzian shape, but with a peak transmission of less than unity.

In section 2.5, it was seen that the width of the cavity modes depends on the magnitude of the reflection coefficient of the bounding Bragg mirrors (equation 2.115), and in this section it has been shown that the cavity mode splitting depends on the magnitude of the transmission through the intermediate Bragg mirror. Hence, to realise the strong coupling regime requires high values of N and low values of P. The opposite is required to realise the weak coupling regime. Figure 2.8 (a) to (e) show several coupled microcavities with various thicknesses of the outer and central mirrors. The central mirrors have $P + 1/2$ periods, and the outer mirrors have $N = 3$ periods (blue lines) and $N = 6$ periods (red lines). We can see that the strong coupling regime is realised for all the red curves. This is because the outer mirrors have a high reflectivity ($\sim 98\%$), and thus the width of the cavity modes is small enougth so that it is always smaller than the size of the cavity mode splitting. For the blue curves, the outer mirrors have a lower reflectivity ($\sim 78\%$), and the cavity modes are wider. Hence for high transmission coupling Bragg mirrors (as in figure 2.8 (d) and (e)), the strong coupling regime can still be realised, but for lower transmission coupling mirrors (figure 2.8 (a) and (b)), the splitting is small and hence the weak coupling regime pertains. In figure 2.8 (c), the blue curve represents the threshold between weak and strong coupling, when the mode splitting and width are equal.

Figure 2.9 shows the electric and magnetic fields of the lower (a) and upper (b) split eigenmodes, calculated by the transfer matrix method described in section 2.1 for a pair of coupled cavities with $N = 6$ and $P = 6$. The fields decay exponentially into the outer Bragg mirrors, and are localised on the microcavity layers. However, there is a substantial overlap of the electromagnetic fields in the intermediate Bragg reflector, and this situation corresponds to the strong coupling regime. Indeed, it is the amount of overlap of the electromagnetic fields from the coupled Bragg reflectors that physically determines the splitting of the cavity modes, and this overlap is related to the transmission through the intermediate Bragg mirror and how far apart the microcavities are.

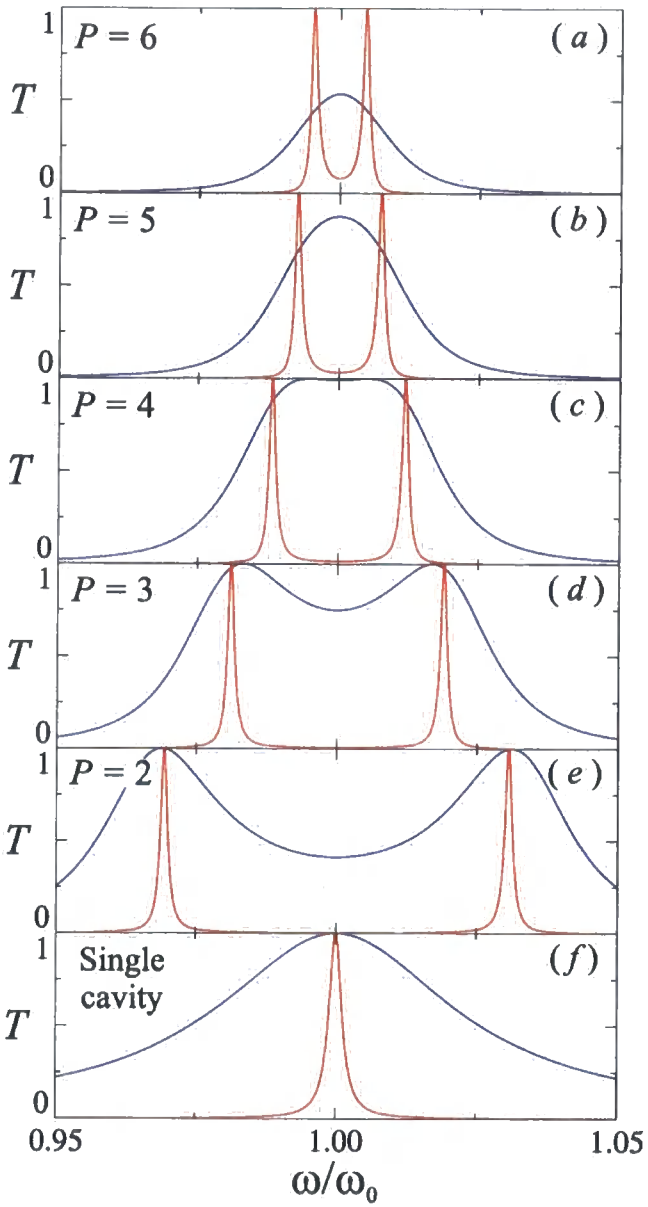

Figure 2.8 (a)–(e) Transmission spectra for two coupled microcavities ($Q = 2$) with varying thicknesses of the intermediate Bragg reflector: $P = 2$, 3, 4, 5, and 6, as indicated. The red lines correspond to an outer Bragg reflector with $N = 6$, and the blue lines correspond to $N = 3$. The spectra for a single cavity is also shown in (f) for comparison.

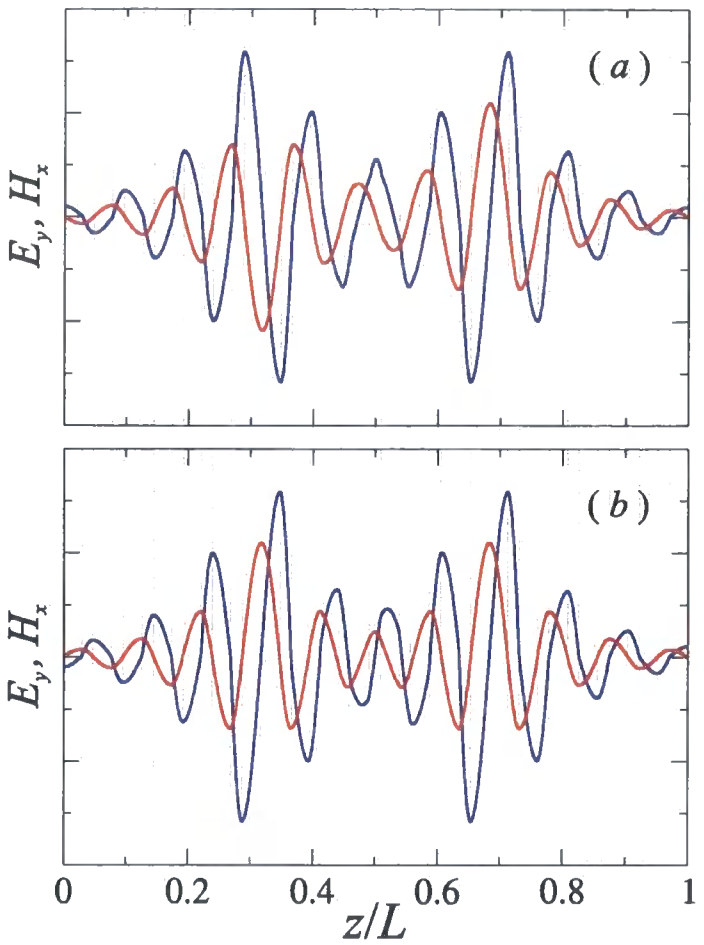

Figure 2.9 The tangential components of the electric (red) and magnetic (blue) field profiles for the lower (a) and upper (b) split cavity eigenmodes of a pair of coupled microcavities ($Q = 2$) with $P = 6$ and $N = 6$. The complex eigenfrequencies of the modes are (a) $\omega/\omega_0 = 0.836 - i2.95 \times 10^{-3}$ and (b) $\omega/\omega_0 = 1.164 - i2.95 \times 10^{-3}$.

2.6.2 Formation of photonic miniband

We have seen in section 2.6.1 that coupling two microcavities through a central Bragg mirror leads to a splitting of the cavity mode which is proportional to the transmission coefficient of the coupling mirror. Now consider what happens when more microcavities are coupled in a chain. Coupling Q microcavities leads to the Q-fold splitting of the cavity mode shown in figure 2.10. For large Q, a quasi-continuous miniband of modes forms in the stop-band of the Bragg reflectors. Figure 2.11 (a) shows the calculated dispersion relation for an infinite chain of coupled microcavities with $P = 4$ and the photonic miniband introduced into the former photonic band gap, centred on $\omega = \omega_0$ is highlighted. The width of this miniband is related to the transmission coefficient of the coupling Bragg mirrors as shown in figure 2.11 (b), which shows the allowed bands for several infinite chains of microcavities

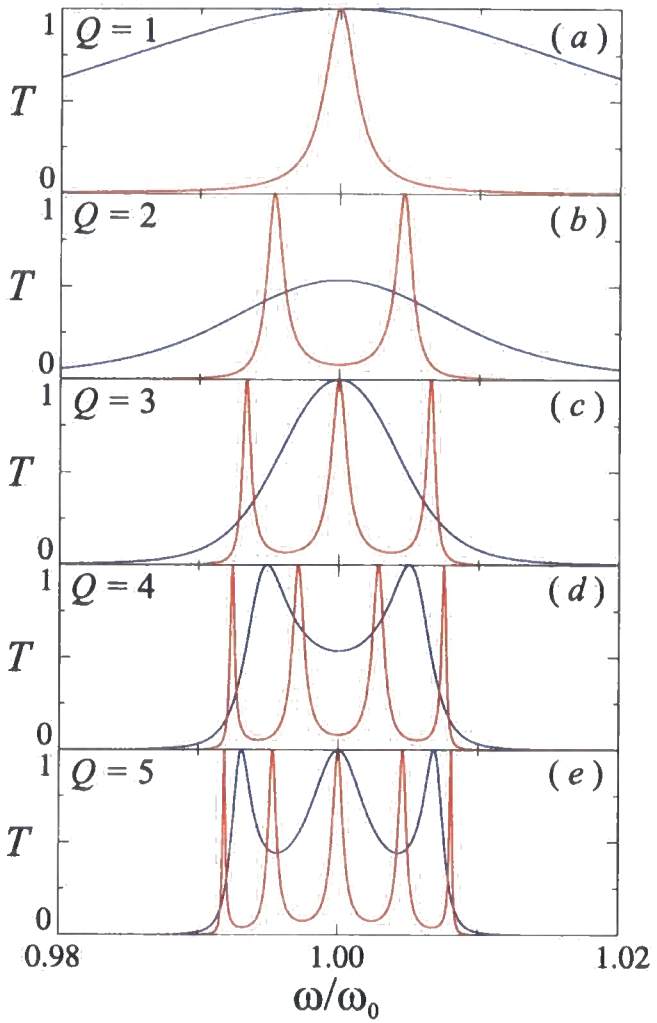

Figure 2.10 Transmission spectra for chains of $Q = 1, 2, 3, 4$, and 5 coupled microcavities, as indicated, with $P = 6$ pairs of layers in the intermediate Bragg reflectors. The red lines correspond to a strong coupling case with outer Bragg reflectors with $N = 6$, and the blue lines correspond to a weak coupling case with $N = 3$.

with varying transmission through the coupling mirrors. It can be seen that microcavities coupled through intermediate mirrors with higher transmission (i.e. smaller P) have thinner minibands, as the photonic states are more localised to a specific microcavity, and less overlap of the electric fields from neighbouring microcavities takes place.

An infinite chain of microcavities can be considered, by considering a single microcavity as a periodically repeating supercell. The dispersion relation of the infinite structure can be derived from the trace of the characteristic transfer matrix of the supercell using Bloch's theorem, in a similar way to the derivation of the dispersion relation for a Bragg reflector, as

$$\cos(KD) = \frac{1}{2}\left(T_{11}(\omega) + T_{22}(\omega)\right) \tag{2.126}$$

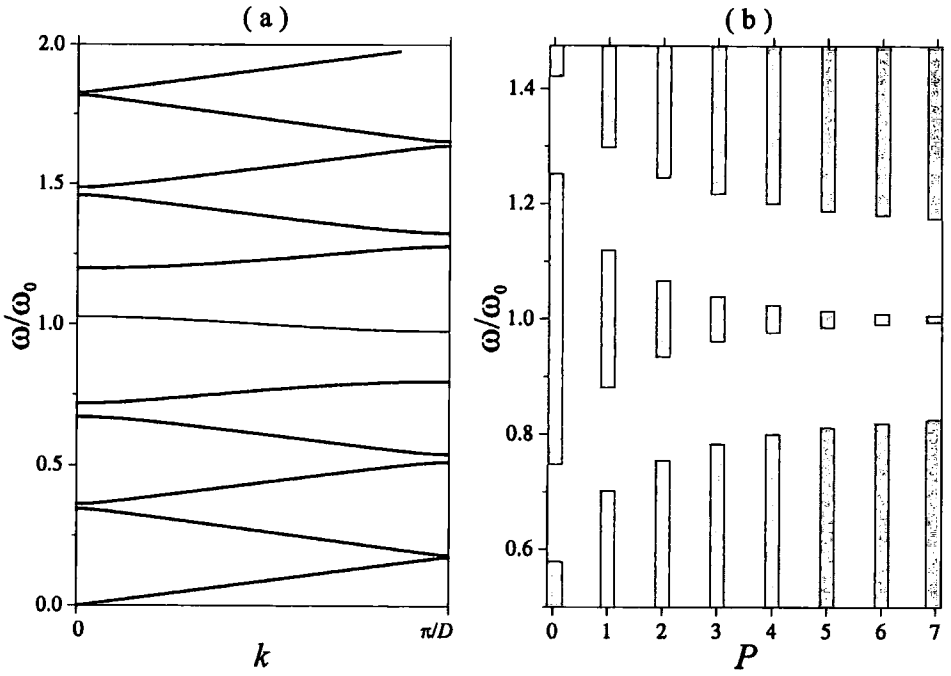

Figure 2.11 (a) The dispersion relation for an infinite array of coupled microcavities, with $4\frac{1}{2}$ periods in the intermediate Bragg reflectors ($P = 4$). (b) Allowed frequency bands (grey) for infinite arrays of coupled microcavities with varying P.

but where D is now the length of the supercell containing the microcavity and Bragg mirror. The dispersion relation can then be calculated numerically, and photonic band gaps occur for frequencies for which $|\cos(KD)| > 1$. In figure 2.11, it can be seen that there is a photonic miniband centred on the Bragg frequency of the bounding mirrors.

2.7 Optical filters based on coupled microcavities

An ideal bandpass optical filter should allow complete transmission of light in some narrow spectral range, with zero transmission outside that range; in other words, the transmission spectrum should possess a square shape.

Optical filters based on absorbing materials [97] generally exhibit smooth and wide transmission profiles. However, a more promising approach could be to design a filter based on the resonant transmission through a multilayered dielectric structures. Such structures have for a long time been used in various optical devices for anti-reflection coatings and Bragg reflectors, and it has been seen in this chapter that the introduction of microcavities into the layer structure of a quarter-wave Bragg reflector can lead to the introduction of a transmission resonance with unit peak transmission in the centre of their stop-band.

It is the aim of this section to describe the design of a type of optical filter based on coupled microcavities that provides the optimal near square transparency band at the centre of the stop-band of the Bragg reflectors. Chains of coupled microcavities have been used previously for the production of "square-top multicavity bandpass filters" [97, 101, 102], but existing examples of such filters exhibit a peak transmission of significantly smaller than unity, and a substantial variation of the transmission in the spectral region that is supposed to correspond to the "square-top". The optical properties of the complicated multilayered structures are usually calculated using transfer matrix techniques that considers the structure as a whole. However, to optimise the design of such structures, an analytical approach would be better, which describes separately the component parts of the filter with a clear insight into their physical significance.

The component parts of a multilayered optical filter based on coupled microcavities are as follows: two Bragg reflector "mirrors", each consisting of N quarter-wave pairs of layers bounding Q half-wave microcavity layers separated and coupled through $Q-1$ intermediate Bragg reflectors, each consisting of $P+1/2$ quarter-wave pairs of layers. Thus the layer structure of the optical filter is $(\mathrm{AB})^N(\mathrm{AA}(\mathrm{BA})^P\mathrm{B})^{Q-1}\mathrm{AA}(\mathrm{BA})^N$, where each letter describes one quarter-wave layer.

As discussed in section 2.6, the coupling of Q microcavities in a chain will lead to the Q-fold splitting of the cavity mode and two distinct regimes—the strong coupling and weak coupling regimes. The nearest to a square-shaped transparency band with unit transmission at its centre is provided at the threshold between the strong and weak-coupling regimes, when the width of the cavity modes equals their splitting.

It was shown in section 2.5 that the width of the cavity modes depends on the magnitude of the reflection coefficient of the outer Bragg mirrors, and it was shown in section 2.6.1 that the splitting of the cavity modes depends on the magnitude of the transmission coefficient in the intermediate Bragg reflectors. These values can be engineered by adjusting the number of layers, N and P, that the Bragg reflectors possess. For the structure considered in section 2.6.1 it is clear from figure 2.8 that this condition is most closely satisfied in the structure with $N=3$ and $P=4$.

The spectral shape of the passband depends on the number of microcavities in the chain, Q. Figure 2.12 shows the transmission spectra for structures with $N=3$, $P=4$, and

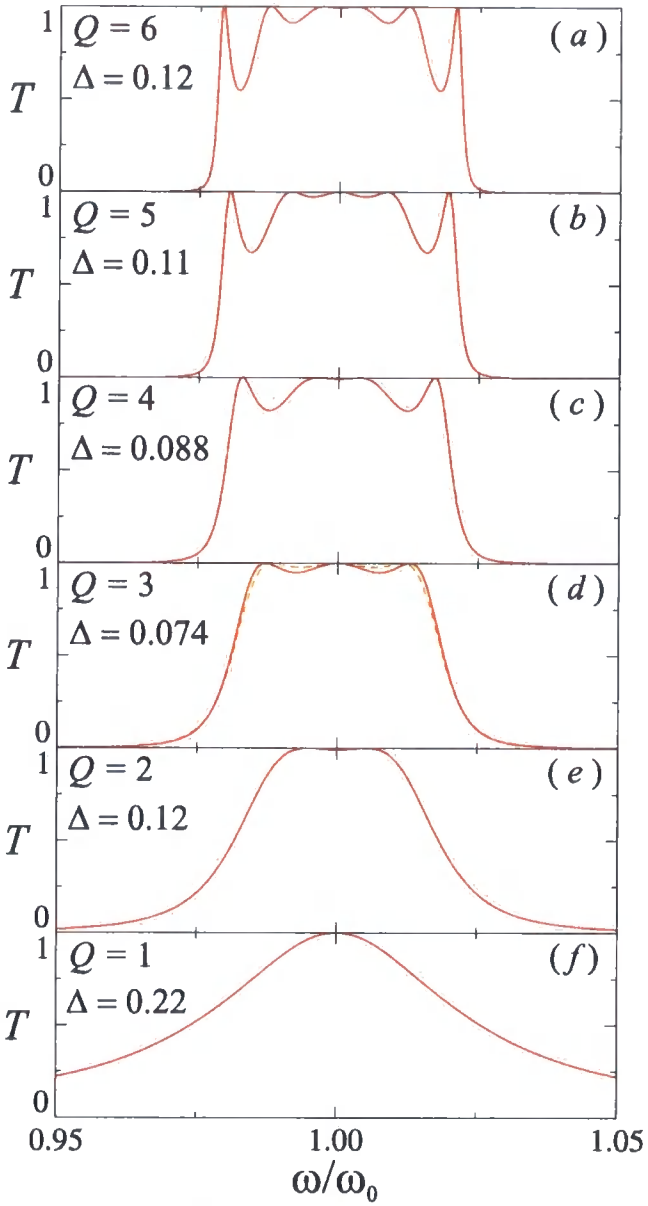

Figure 2.12 Transmission spectra for chains of $Q = 1$, 2, 3, 4, 5, and 6 coupled microcavities, as indicated, with $N = 3$ and $P = 4$ for the outer and intermediate Bragg reflectors (which corresponds to the threshold between weak and strong coupling). Also indicated as the values of the mean deviation away from square within the transparency band, Δ, as defined in equation 2.127. The orange dotted line in (d) is the transmission spectrum for an optimised optical filter with fine-tuning of the reflection in the outer Bragg mirrors applied, as described in the text.

Q = 2, 3, 4, 5, and 6, as indicated. It can be seen that an increase of Q above 2 leads to the introduction of unwanted fringes in the transparency band, degrading the flatness of the top, but also an increase in the slope on the edge of the transparency band, increasing the squareness of its shape. In order to quantify the most square-shaped passband and compare the performance of different structures, the averaged deviation Δ of the transmission within the transparency band

$$\Delta = \frac{1}{W}\int_{\nu_1}^{\nu_2} \frac{T_{max} - T(\nu)}{T_{max}} d\nu \tag{2.127}$$

and the gradient at the edge of the transparency band, characterised by the value

$$S = \frac{1}{W}\frac{\partial \nu}{\partial T}\bigg|_{\nu=\nu_1} \tag{2.128}$$

were calculated for each structure from their transmission spectra. In equations 2.127 and 2.128, $W = T(\nu_2) - T(\nu_1)$ is the width of the transparency band, and $\nu = \omega/\omega_0$ is a dimensionless frequency. ν_1 and ν_2 are the frequencies at the edge of the transparency band, defined as $T(\nu_1) = T(\nu_2) = 1/2$. For an ideal, square-shaped transparency band, $\Delta = 0$ and $S = 0$. W, S and Δ are shown in figure 2.13 as a function of the number of microcavities in the chain, Q, for structure with $N = 3$ and $P = 4$. The width of the transparency band is a minimum for $Q = 2$, and, as Q is increased, the width asymptotically approaches the width of the photonic miniband for the infinite structure with the same value of P. The value of S decreases for increasing Q, as the slope at the edge of the transparency band gets steeper as more microcavities are included in the chain. The parameter Δ is a minimum when $Q = 3$, and this is the situation corresponding to the optimum square-shaped passband. Hence the optimum structure is one with $N = 3$, $P = 4$ and $Q = 3$.

Varying the number of layers in the Bragg reflectors alters their reflection and transmission coefficient in a discrete way. Hence the condition that the width of the cavity modes must equal their splitting can only be approximately met by altering the parameters N and P alone. In order to "fine-tune" the structure to meet this condition exactly, the reflection coefficient of the outer Bragg reflectors must be adjusted in a continuous fashion. The inset of figure 2.13 shows the dependence of Δ on the reflection of the outer Bragg mirrors for the optimum structure. The circle represents the best that can be achieved by altering N and P alone, as described above. It can be seen that a more square-shaped passband can

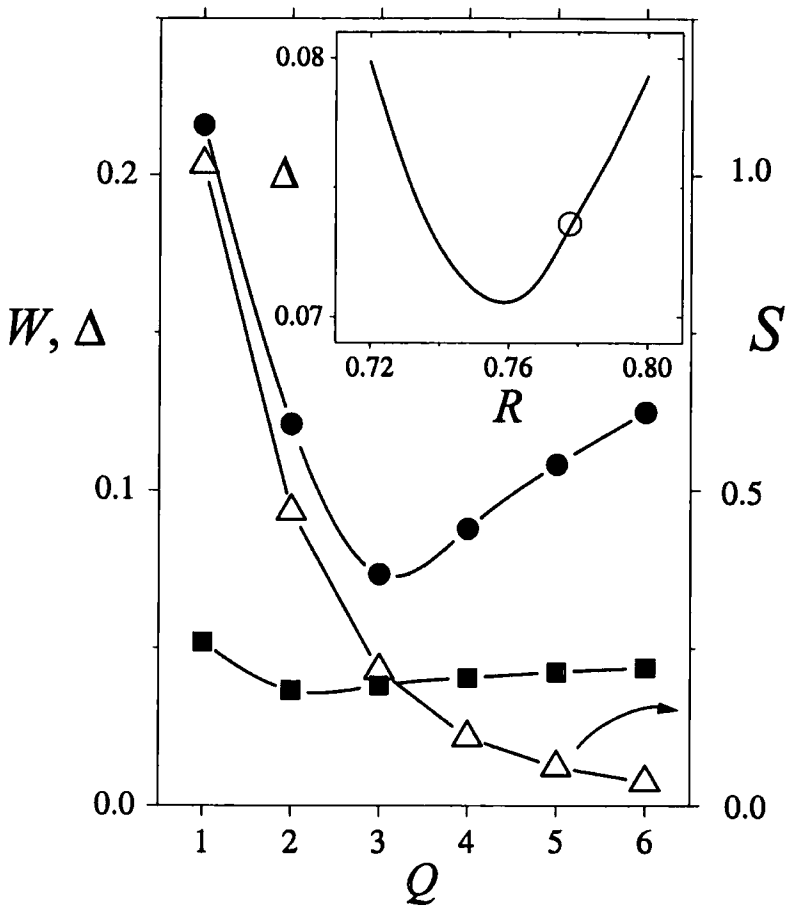

Figure 2.13 Calculated values of the width W of the transparency band (squares) and the average deviation Δ within the transparency band (circles on the left scale, and a value S characteristic of the slope at the edge of the transparency band (open triangles) on the right scale, as a function of the number of microcavities in the chain, Q. The outer and intermediate Bragg reflectors have values of $N = 3$ and $P = 4$ respectively. (Inset) The dependence of the average deviation Δ as a function of the reflection coefficient of the outer Bragg reflectors. The circle indicates the reflection coefficient and deviation when $N = 3$, $P = 4$, and $Q = 3$.

be achieved by fine-tuning the reflection in the outer Bragg mirrors. This fine-tuning of the reflection in the outer Bragg mirrors can be achieved by detuning their Bragg frequency from the Bragg frequency of the intermediate reflectors that couple the microcavity layers by adjusting the thickness of one or both types of layers in the outer Bragg mirrors. The dotted line in figure 2.12 (d) shows the transmission spectrum of such a fine-tuned structure, and it can be seen that a more square-shaped passband has indeed been achieved.

Figure 2.14 shows the electromagnetic fields of the three split cavity modes in the optimal structure. The central split cavity mode is at the Bragg frequency of the Bragg reflectors, and maintains the frequency of the eigenmode of a single cavity. As can be seen, the eigenmode has very little interaction of the electromagnetic fields of the left and right microcavities,

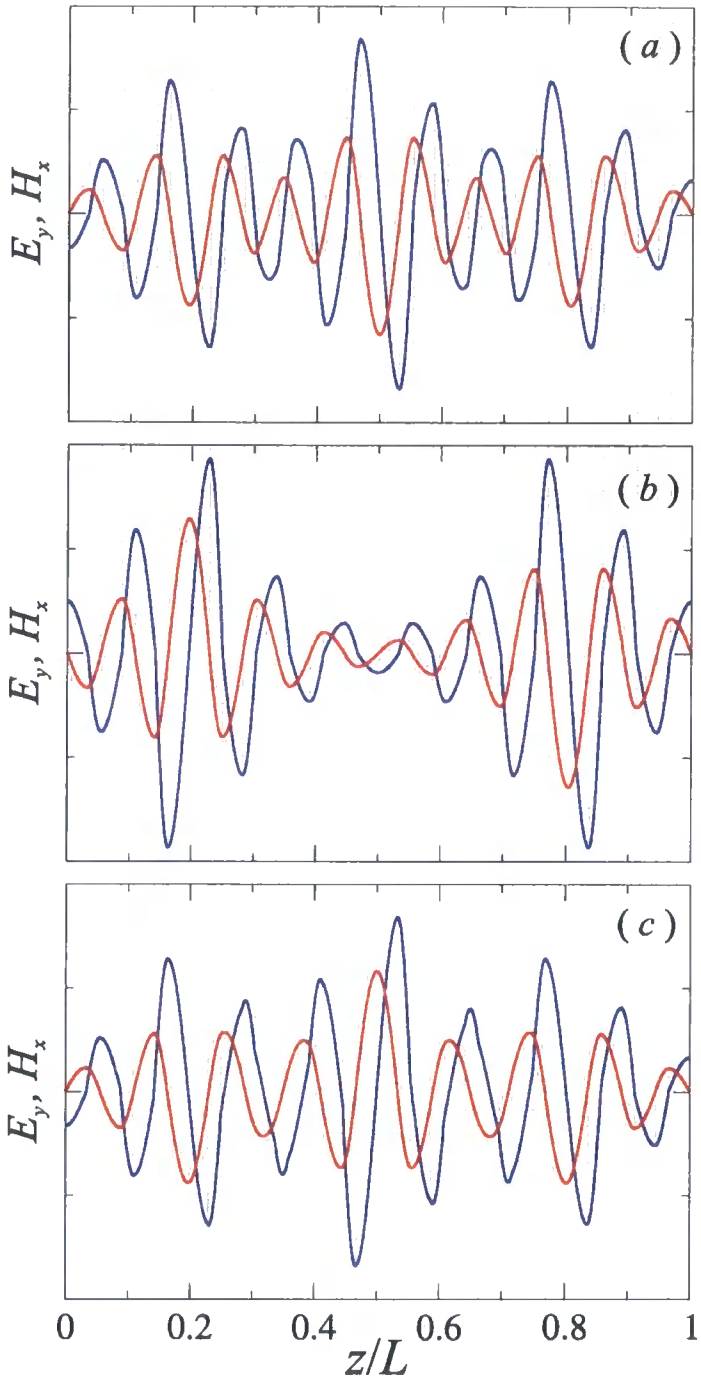

Figure 2.14 The electric (red) and magnetic (blue) field profiles for the upper (a), middle (b) and lower (c) split cavity eigenmodes of the optimal structure to give a near square-shaped passband, as discussed in the text. The parameters are $Q = 3$ with $P = 4$ and $N = 3$. The complex eigenfrequencies of the modes are (a) $\omega/\omega_0 = 1.0165 - i6.012 \times 10^{-3}$, (b) $\omega/\omega_0 = 1.0000 - i11.70 \times 10^{-3}$ and (c) $\omega/\omega_0 = 0.9835 - i6.012 \times 10^{-3}$.

where the field amplitude is concentrated. The fields are small in the central microcavity, and comparing with figure 2.6, the system acts like a set of two decoupled independent cavities at this frequency. The lower and upper split cavity modes however have a large overlap of the electromagnetic fields between adjacent microcavities.

2.8 Conclusions

This chapter has presented a transfer matrix method for solving the Maxwell equations for the electromagnetic fields in arbitrary multilayered dielectric structures. Equations for the reflection and transmission coefficients and the eigenfrequencies of the structures are given in term of the transfer matrix elements.

The transfer matrix methods were then applied to the study of the optical properties of periodic multilayer systems—Bragg reflectors. The Bragg reflector was considered as a one-dimensional photonic crystal, and its band structure calculated. It was seen that there is a band of frequencies for which no states of the electromagnetic fields exist—the photonic band gap—and that an electromagnetic wave incident at these frequencies decay into the Bragg reflector. The physical origin of the photonic band gap is the interference of waves from the multiple reflections from the dielectric interfaces in the structure, and the Bragg condition is met at the centre of the band gap. Light incident at frequencies in the band gap is thus strongly reflected, and this spectral region is the stop-band of the Bragg reflector.

It was then shown how the introduction of a microcavity layer into the Bragg reflector allows the introduction of an electromagnetic state in the photonic band gap. The state causes a Lorentzian transmission resonance with a width related to the reflectivity of the bounding Bragg reflector mirrors. The microcavity layer can be considered as an isolated defect in the one-dimensional photonic crystal.

Microcavities coupled through intermediate Bragg reflectors were then considered. It was shown that coupling together two microcavities causes the splitting of the microcavity mode proportional to the magnitude of the transmission coefficient through the intermediate Bragg reflector. For a large number of coupled microcavities, the system can be considered as a photonic superlattice of cavities, and the dispersion relation of such lattices have been calculated. A photonic miniband of allowed states in the photonic band gap results from the

coupling of the microcavities.

Finally, an analytical approach to the design and optimisation of optical bandpass filters based on coupled microcavities was considered. It is shown that the situation corresponding to the weak-coupling strong-coupling threshold for the coupled microcavities produces the most square-shaped transparency band.

Chapter 3

Two-dimensional photonic crystals

Two-dimensional photonic crystals are dielectric structures in which the dielectric properties, such as the refractive index, varies periodically in two-dimensions, and is constant in the third dimension across the thickness of the sample. As photonic crystals are normally artificial structures, their form is limited only by the available methods of fabrication on the spatial scale required, the materials available for use, and the imagination of the engineers and scientists designing them.

Many of the proposed uses of photonic crystals require operation at visible or near infrared frequencies. Techniques to fabricate dielectric structures on the required spatial scale are almost invariably based on epitaxial growth and lithography of semiconductors. The majority of photonic crystals reported in the literature consist of circular air cylinders etched into semiconductor substrates or semiconductors etched to leave circular cylindrical rods in air [2, 4, 21–24, 26, 103]. Rods/holes with cross-sections other than circular have also been studied theoretically [23, 26, 104], but the nature of the etching techniques used tends to lead to rounded features. Many different schemes for the design of 2D photonic crystals have been proposed and studied theoretically—hexagonal structures with interstitial voids [71], boron or graphite hexagonal structures [19], rods or voids of square or triangular cross-section [23, 26] and dielectric veins [2] are representative. As well as being studied theoretically several 2D photonic crystals have been realised for use at visible or near infrared frequencies [31–33, 62, 65].

2D photonic crystals designed for use at other frequencies have also been reported. In particular, those constructed at the centimetre scale for use at microwave frequencies [87,

88,91–93] are often used to test the theory in proof of concept experiments and to optimise structures, owing to the scaling properties of the Maxwell equations and the relative ease of fabrication compared with fabrication on the micrometre scale.

Experimental methods of measuring the bandstructure of a photonic crystal naturally rely on studies of their optical properties. By plotting the transmission spectrum at different angles of incidence, particular features of the bandstructure such as band gaps can be observed. However, certain modes or photonic bands can be totally missed in this way, experimental resolution notwithstanding. Robertson *et al.* were the first to realise that some modes do not couple to the external incident electromagnetic fields due to their symmetry, and so the radiation is reflected from the photonic crystal at the frequencies corresponding to the uncoupled modes, despite the presence of the photonic band [31, 88, 103]. Thus it is vital to use bandstructure calculations to complement and interpret correctly the experimentally measured spectra.

This chapter outlines the two main computational methods used in this thesis for the study of 2D photonic crystals. The first of these methods is a Fourier plane wave method [17,21,24,25,105], which has been used for the calculation of the bandstructure and density of states of 2D photonic crystals. The second is a transfer matrix method due to Pendry and co-workers [20, 106, 107] and has been used for the calculation of the transmission and reflection spectra of 2D photonic structures.

Section 3.4 then describes studies of a new design of 2D photonic crystal consisting of deep air grooves etched into a Bragg reflector perpendicular to its growth direction. The methods outlined in section 3.2 and 3.3 are applied to this new type of structure to study its bandstructure, density of states and transmission properties, with the aim of providing the parameters of the structure that optimise the properties of the etched Bragg reflector.

3.1 Two-dimensional crystals

The elements of crystallography relevant to 2D photonic crystals are covered in many textbooks. They are reviewed in books about photonic crystals (for example, the appendix in ref. [2]), but more detailed accounts of the relevant material can generally be found in solid state textbooks, for example refs. [108, 109].

The square lattice, illustrated in figure 3.1 (a) is generated by the primitive lattice vectors

$$\mathbf{a}_1 = a\hat{\mathbf{j}}, \quad \mathbf{a}_2 = a\hat{\mathbf{k}} \tag{3.1}$$

such that the translation vectors of the lattice are $\mathbf{T} = n_1\mathbf{a}_1 + n_2\mathbf{a}_2$. a is the distance between neighbouring points in the lattice, and is called the lattice constant. The reciprocal lattice is generated by the primitive reciprocal lattice vectors

$$\mathbf{g}_1 = \frac{2\pi}{a}\hat{\mathbf{j}}, \quad \mathbf{g}_2 = \frac{2\pi}{a}\hat{\mathbf{k}} \tag{3.2}$$

such that the reciprocal lattice vectors are $\mathbf{G} = n_1\mathbf{g}_1 + n_2\mathbf{g}_2$. The reciprocal lattice is illustrated in figure 3.1 (c), which also shows the construction of the first Brillouin zone and its special points of high symmetry, Γ, X and M.

The hexagonal lattice is generated by the primitive lattice vectors

$$\mathbf{a}_1 = \frac{a}{2}\hat{\mathbf{j}} + \frac{a\sqrt{3}}{2}\hat{\mathbf{k}}, \quad \mathbf{a}_2 = \frac{a}{2}\hat{\mathbf{j}} - \frac{a\sqrt{3}}{2}\hat{\mathbf{k}} \tag{3.3}$$

and its reciprocal lattice is generated by the primitive reciprocal lattice vectors

$$\mathbf{g}_1 = \frac{2\pi}{a}\hat{\mathbf{j}} + \frac{2\pi}{a\sqrt{3}}\hat{\mathbf{k}}, \quad \mathbf{g}_2 = \frac{2\pi}{a}\hat{\mathbf{j}} - \frac{2\pi}{a\sqrt{3}}\hat{\mathbf{k}} \tag{3.4}$$

An illustration of the direct space lattice and reciprocal lattice are shown in figure 3.1 (b) and figure 3.1 (d) respectively.

3.2 Plane wave method

The plane wave method is used to solve the Maxwell equations for a photonic crystal by expanding the electromagnetic field and relative permittivity $\varepsilon(\mathbf{r})$ in terms of Fourier series or linear superpositions of plane waves.

It was shown in chapter 1 that the Maxwell equations can be combined to form the wave equation

$$\nabla \times \left[\frac{1}{\varepsilon(\mathbf{R})}\nabla \times \mathbf{H}(\mathbf{R})\right] = \frac{\omega^2}{c^2}\mathbf{H}(\mathbf{R}) \tag{3.5}$$

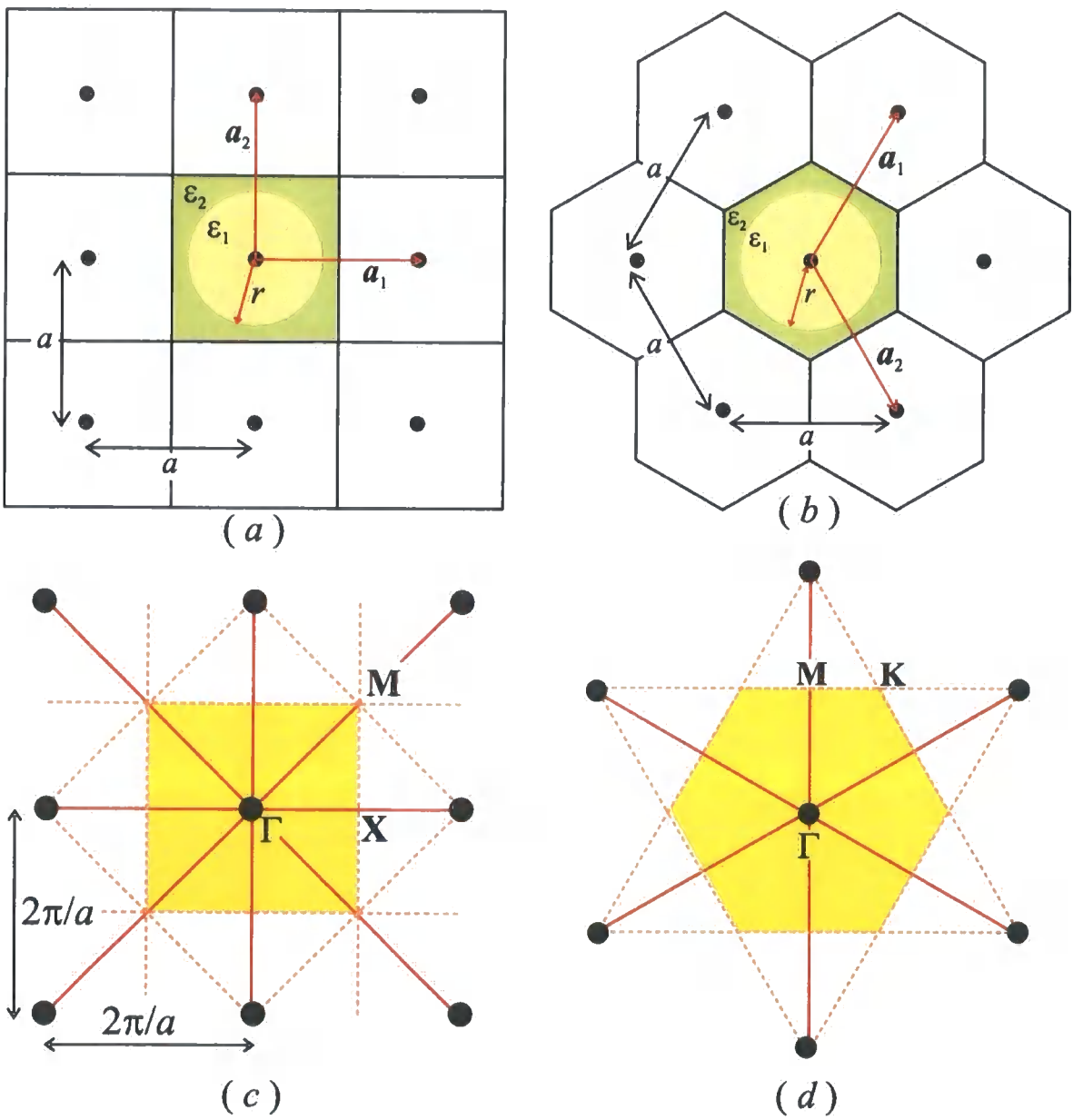

Figure 3.1 The square (a) and hexagonal (b) Bravais lattices. In each case, the primitive Wigner-Seitz unit cells are shown, and the centre cell illustrates the basis used when modelling photonic crystals made up of cylindrical rods/air holes, as described in the text. The reciprocal lattice of (a) and (b) are illustrated in (c) and (d) respectively. The first Brillouin zone is indicated in yellow (the dashed lines are construction lines) and the points of high symmetry are labelled.

which is the basis of our calculational method. For a 2D photonic crystal, $\varepsilon(\mathbf{r})$ varies in a plane and is constant along the third direction. Thus it is convenient to introduce a 2D position vector $\mathbf{R}$ in the plane of refractive index variation. Let the plane of refractive index variation be the yz-plane, so that $\mathbf{R} = (y, z)$, and the direction of constant refractive index is the x direction. In a similar manner, we can define a 2D reciprocal lattice vector as $\mathbf{K} = (k_y, k_z)$.

Light in the plane of a 2D photonic crystal can be separated into two independent and orthogonal polarisations, and solutions of equation 3.5 can always be found for each of these. The transverse electric (TE) polarisation has its electric field polarised in the plane of refractive index variation and its magnetic field polarised out of this plane, whereas the electric and magnetic fields are exchanged in the transverse magnetic (TM) polarisation.

3.2.1 Bloch's law and periodic boundary conditions

If a primitive unit cell of a crystal is considered, the complete crystal structure can be built by applying periodic boundary conditions to the basis within the unit cell and

$$\varepsilon(\mathbf{R}) = \varepsilon(\mathbf{R} + \mathbf{T}) \tag{3.6}$$

where $\mathbf{T}$ is a translation vector of the Bravais lattice. $\varepsilon(\mathbf{r})$, or $\varepsilon^{-1}(\mathbf{r})$ which appears in equation 3.5, can be expanded as a Fourier series in plane waves that satisfy the periodic boundary conditions, which are the reciprocal lattice vectors, $\mathbf{G}$. The plane wave expansion of $\varepsilon^{-1}(\mathbf{r})$ is

$$\frac{1}{\varepsilon(\mathbf{R})} = \sum_{\mathbf{G}'} \varepsilon^{-1}_{\mathbf{G}'} e^{i\mathbf{G}'\cdot\mathbf{R}} \tag{3.7}$$

where $\varepsilon^{-1}_{\mathbf{G}'}$ are the relevant Fourier coefficients.

The magnetic field is also expanded in the basis of plane waves, but in general, $\mathbf{H}(\mathbf{R})$ does not share the periodicity of the Bravais lattice, which is governed by Bloch's law for periodic media (see, for example [108, 109]). Thus the Fourier expansion of the magnetic field is of the form

$$\mathbf{H}(\mathbf{R}) = \sum_{\mathbf{G}} \mathbf{H}_{\mathbf{G}} e^{i(\mathbf{K}+\mathbf{G})\cdot\mathbf{R}} \tag{3.8}$$

where $\mathbf{K}$ is a wavevector within the first Brillouin zone of the reciprocal lattice and $\mathbf{H}_{\mathbf{G}}$ are

the relevant Fourier coefficients. Bloch's law gives the periodicity of the eigenmodes of the photonic crystal such that

$$\mathbf{H}(\mathbf{R}+\mathbf{T}) = \mathbf{H}(\mathbf{R})\, e^{i\mathbf{K}\cdot\mathbf{T}} \tag{3.9}$$

where $\mathbf{K}$ is a Bloch wavevector in the first Brillouin zone.

3.2.2 Transverse electric polarisation

In the chosen coordinate system, the electromagnetic fields for the TE polarisation have the components

$$\mathbf{E} = (0, E_y, E_z) \tag{3.10}$$

$$\mathbf{H} = (H_x, 0, 0) \tag{3.11}$$

Thus the magnetic field vector has only one component out of the plane of refractive index variation and this can be expanded as a Fourier series. Applying periodic boundary conditions and using Bloch's law for periodic media, the magnetic field can be expanded as

$$H_x(\mathbf{R}) = \sum_{\mathbf{G}} H_{\mathbf{G}} e^{i(\mathbf{K}+\mathbf{G})\cdot\mathbf{R}} \tag{3.12}$$

where $\mathbf{K}$ is the Bloch wavevector and $\mathbf{G}$ are the set of reciprocal lattice vectors. The expansions in equation 3.12 and equation 3.7 can be substituted into equation 3.5, and after some algebra gives [17,21,24,25,105]

$$\sum_{\mathbf{G}'} H_{\mathbf{G}'} \varepsilon^{-1}_{\mathbf{G}-\mathbf{G}'} (\mathbf{K}+\mathbf{G}) \cdot (\mathbf{K}+\mathbf{G}') = \frac{\omega^2}{c^2} H_{\mathbf{G}} \tag{3.13}$$

Equation 3.13 can be cast as a matrix eigenvalue equation, where the set of Fourier coefficients $H_{\mathbf{G}}$ are the eigenvectors and ω^2/c^2 the eigenvalues. For real scaler values of the relative permittivity, the matrix in equation 3.13 is Hermitian, which ensures real and positive eigenvalues. Also, the numerical routines used to diagonalise the matrix can be made more efficient be taking advantage of the symmetries of the Hermitian matrix.

3.2.3 Transverse magnetic polarisation

In the chosen coordinate system, the electromagnetic fields in the TM polarisation are of the form

$$\mathbf{E} = (E_x, 0, 0) \tag{3.14}$$

$$\mathbf{H} = (0, H_y, H_z) \tag{3.15}$$

For the TM polarisation, the magnetic field vector has two non-zero components. Thus the Fourier coefficients are also 2D vectors

$$\mathbf{H}(\mathbf{R}) = \sum_{\mathbf{G}} \mathbf{H}_{\mathbf{G}} e^{i(\mathbf{K}+\mathbf{G})\cdot\mathbf{R}} \tag{3.16}$$

If the Fourier coefficients, $\mathbf{H}_{\mathbf{G}}$, are 2D vectors, then in which direction do they point? $\mathbf{H}(\mathbf{R})$ always lies in the yz-plane, as this is the definition of the TM polarisation. Also, $\mathbf{H}(\mathbf{R})$ is perpendicular to the direction of the electric field vector, $\mathbf{E}(\mathbf{R})$, which lies along the x-direction. Further, each plane wave in the expansion must have its magnetic field perpendicular to the direction of propagation of the plane wave. Thus $\mathbf{H}_{\mathbf{G}}$ is in the direction of the unit vector

$$\hat{\mathbf{e}}_{\mathbf{G}} = \frac{(\mathbf{K}+\mathbf{G}) \times \hat{\mathbf{i}}}{|\mathbf{K}+\mathbf{G}|} \tag{3.17}$$

where $\hat{\mathbf{i}}$ is the unit vector along the x direction. The two expansions in equation 3.7 and equation 3.16 are substituted into equation 3.5, and after some algebra [17, 21, 24, 25, 105] we obtain

$$\sum_{\mathbf{G}'} H_{\mathbf{G}'} \varepsilon^{-1}_{\mathbf{G}-\mathbf{G}'} |\mathbf{K}+\mathbf{G}| \, |\mathbf{K}+\mathbf{G}'| = \frac{\omega^2}{c^2} H_{\mathbf{G}} \tag{3.18}$$

As was the case for the TE polarisation in section 3.2.2, equation 3.18 is an Hermitian eigenvalue problem, and the matrix can be diagonalised to give the eigenvalues ω^2/c^2.

The electric field can also be expanded as a Fourier series. In the TM polarisation there is only one non-zero component to consider,

$$E_x = \sum_{\mathbf{G}} E_{\mathbf{G}} e^{i(\mathbf{K}+\mathbf{G})\cdot\mathbf{R}} \tag{3.19}$$

However, the plane wave method outlined above gives the Fourier coefficients for the mag-

netic field vector (the $H_{\mathbf{G}}$s). Thus, it would be useful to know how the Fourier coefficients for the electric field relate to those of the magnetic field. The Maxwell equation relating the magnetic field vector and the electric field vector in photonic crystals is equation 1.15, which after substitution of the expansions in equations 3.16 and 3.19 gives

$$E_{\mathbf{G}} = \frac{\omega\mu_0}{|\mathbf{K}+\mathbf{G}|} H_{\mathbf{G}} \tag{3.20}$$

3.2.4 Calculating the Fourier coefficients

The Fourier coefficients of $\varepsilon^{-1}(\mathbf{R})$ in equation 3.7 are given by

$$\varepsilon_{\mathbf{G}}^{-1} = \frac{1}{A}\int_{\text{unit cell}} \varepsilon^{-1}(\mathbf{R})\, e^{-i\mathbf{G}\cdot\mathbf{R}} d^2\mathbf{R} \tag{3.21}$$

For rods of circular cross section, an analytical method of performing the integral is available [21,26]. It is even possible to extend this method to circular rods coated with a third dielectric material [59]. However, for a more general basis, numerical integration is required.

Several methods exist for carrying out the numerical integration in equation 3.21, ranging from simple trapezoidal rules, Simpson-type rules and Gaussian quadrature. In terms of numerical accuracy for the least computational effort, more complex methods such as Gaussian quadrature give the best performance. However, in this work, a simple trapezoidal rule was adopted. Once a set of Fourier coefficients have been calculated for a given structure, they can be saved, and a library of the Fourier coefficients of different structures maintained for easy use whenever required.

Once the Fourier coefficients have been calculated, a useful check on them is to use equation 3.7 to reproduce the crystal structure. Figure 3.2 shows reproductions of square and hexagonal lattices of air cylinders of radius $r = 0.4a$ in a GaAs background. The calculations used 1951 plane waves in the expansion of $\varepsilon^{-1}(\mathbf{R})$. Evidence of the Gibbs phenomenon can be seen at the edges of the rods.

3.2.5 Convergence

The theory of the plane wave method considers the electromagnetic fields and $\varepsilon^{-1}(\mathbf{R})$ to be expanded over an infinite basis set. The infinite set of plane waves is complete, and

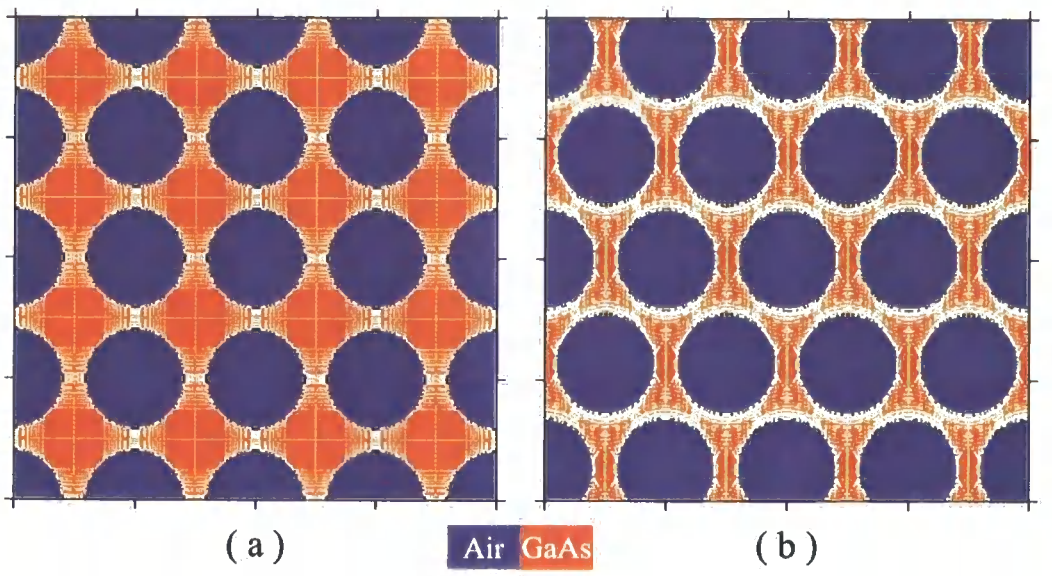

Figure 3.2 Recreations of the photonic crystal of cylindrical air holes in a GaAs background from the calculated Fourier coefficients using equation 3.7. (a) shows the square lattice and (b) shows the hexagonal lattice.

therefore any function can be exactly reproduced by a linear superposition of them. Thus, the methods described in section 3.2.2 and 3.2.3 for the solution of the Maxwell equations are, in principle, exact. However, equations such as equation 3.5 must be solved by numerical computation and the infinite basis set must be truncated. If N plane waves are included in the basis set, equation 3.13 and equation 3.18 require a $N \times N$ Hermitian matrix to be diagonalised for the computation of its eigenvalues and eigenvectors. The number of operations required to diagonalise a $N \times N$ matrix is $O(N^3)$, so doubling the size of the basis set leads to a eight-fold increase in the computation time. More pertinently, the amount of computer memory required scales as N^2, and in practice the maximum size of the truncated basis set is constrained by computer memory resources. Thus a practical question to be answered is how many plane waves need to be used in the calculation? Ideally, the eigenvalues obtained should be as accurate as possible but in practice the number of plane waves used in a calculation is a trade-off between computer resources available and the accuracy of the calculation. A percentage difference between the values obtained with a given number of plane waves and the values of a test case calculated with a very high number of plane waves is often quoted as a measure of the accuracy (or convergence) of the plane wave calculations.

Figure 3.3 shows the calculated eigenfrequencies as a function of the number of plane waves used in the truncated basis set at the Γ point in reciprocal space for the 2D photonic

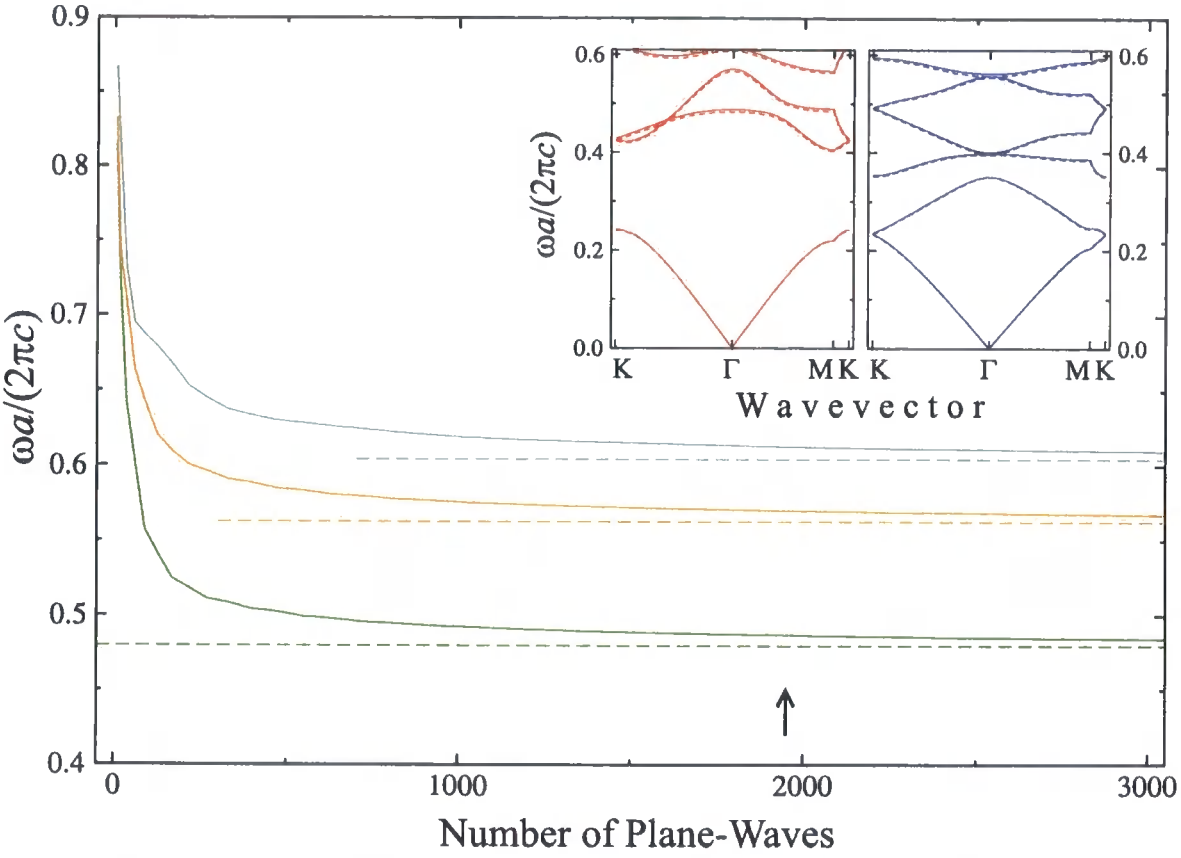

Figure 3.3 Calculated TE-polarised eigenfrequencies at the Γ-point in reciprocal space for the hexagonal lattice of air rods in a GaAs background as a function of the number of plane waves used in the basis set. The three colours refer to the second (green), third (orange) and forth (turquoise) photonic bands, and the horizontal dashed lines indicate the value calculated for 9421 plane waves. The arrow indicates 1951 plane waves. (Inset) A comparison of the bandstructure of the same photonic crystal when 1951 plane waves (solid line) and 4921 plane wave are used in the calculation. Red and blue lines are the TE- and TM-polarised modes respectively.

crystal consisting of air rods of radius $r = 0.4a$ etched into a GaAs background on an hexagonal lattice. The three coloured lines refer to the second, third and fourth photonic bands, and the horizontal dashed lines indicate the relevant eigenfrequency when calculated with 9421 plane waves. It can be seen that below ~ 500 plane waves the eigenfrequencies are not converged but a small increase in the size of the basis set leads to a large increase in the accuracy of the calculation. Above 500 plane waves, there are diminishing returns, and increases in the size of the basis set lead to relatively small increases in the accuracy of the calculation. When $N = 1951$ (indicated by the arrow in figure 3.3), the eigenfrequencies are converged to within 1.5% of their values when $N = 9421$. The inset to figure 3.3 compares the bandstructure calculated using a basis set of 1951 planes-wave (solid lines) with one

calculated using 4921 plane waves (dashed lines). The latter basis set is a factor of ~ 2.5 larger than the former, and so the computer memory and time resources required for the calculation are more than six and 15 times greater respectively. Yet despite this extra effort, the calculated bandstructure is very little different.

3.2.6 Density of states

The density of photonic states or modes can be calculated using the plane wave method described in section 3.2. The basic idea is to calculate the eigenfrequencies (by diagonalising the matrices given by equation 3.13 and equation 3.18) for a sample of wavevectors in the first Brillouin zone of the 2D photonic crystal, and count the eigenfrequencies that lie in a set of frequency "bins". As long as the bin widths are small, and a large enough sample of wavevectors is taken in reciprocal space, this "histogram method" gives us the density of states of the photonic crystal. The histogram method defines the density of states as

$$\rho(\omega) = \sum_{n} \sum_{\mathbf{k}} \delta(\omega - \omega_n(\mathbf{k})) \tag{3.22}$$

where n labels the number of the photonic band, and the k sum is over a sample of wavevectors in the first Brillouin zone.

Computational savings can be made by taking advantage of any symmetries within the first Brillouin zone. For example, for the structures made up of circular rods shown in figure 3.1 (a) and (b), the "irreducible Brillouin zone" is the set of wavevectors within a triangle joining the Γ, X and M points and Γ, M and K points in figure 3.1 (c) and (d) respectively.

The density of states of a photonic crystal can be compared to the density of states of a uniform medium characterised by the same averaged value of the photonic crystal to gauge the influence of periodic dielectric structure. The dispersion relation of photons in a uniform dielectric medium is

$$k = \frac{n\omega}{c} \tag{3.23}$$

and this leads to the density of states for a 2D uniform system of refractive index n as

$$\rho(\omega) = \frac{dN}{d\omega} = \frac{L^2 n^2}{\pi c^2}\omega \tag{3.24}$$

3.3 Transfer matrix methods

In many ways, transfer matrix methods for the calculation of properties of 2D photonic crystals resemble their counterparts for 1D photonic crystals. Certain boundary conditions are assumed at one boundary (dependent upon the type of problem being solved) and the 2D structure is broken down into 2D "slices" through the structure. A transfer matrix is then calculated that propagates the electromagnetic fields from one slice to the next, until the far edge of the structure is reached. The derivation of an individual transfer matrix to propagate the electromagnetic field from those known electromagnetic fields at the previous slice can be achieved by finite difference, analytical, or other methods.

Transfer matrix methods can be applied to calculate the bandstructures of 2D photonic crystals. In fact, unlike the plane wave method previously described in section 3.2, the transfer matrix method described in this section is particularly apt for calculation of bandstructures where the dielectric function is a strong function of frequency (for example, if the structure contains metallic components).

The transfer matrix method described in this section was developed by Pendry and coworkers at Imperial College, London in 1991/2. They developed a publicly available computer code [20, 106, 107], a modified version of which is used in this thesis for the calculation of reflection and transmission spectra of 2D photonic crystals. The method is a direct solution of the Maxwell equations on a discretized mesh of points. Only a brief description is given here but full details can be found in refs. [20], [106] and [107].

Let the mesh have dimensions $\widetilde{a}$, and let the plane of the slices be the xy-plane. Also let $\widetilde{a}$ be the the distance between slices, as shown in figure 3.4. The electromagnetic fields are then propagated by a transfer matrix from one slice to the next. The Maxwell equations for photonic crystals (equation 1.3 and 1.4) and the material equations (equation 1.7 and 1.8, with $\mu(\mathbf{r}) = 1$) are Fourier transformed to give

$$\mathbf{k} \times \mathbf{E} = \omega \mu_0 \mathbf{H} \tag{3.25}$$

$$\mathbf{k} \times \mathbf{H} = -\omega \varepsilon_0 \varepsilon(\mathbf{r}) \mathbf{E} \tag{3.26}$$

Performing the cross products in equations 3.25 and 3.26 and writing the x, y and z compo-

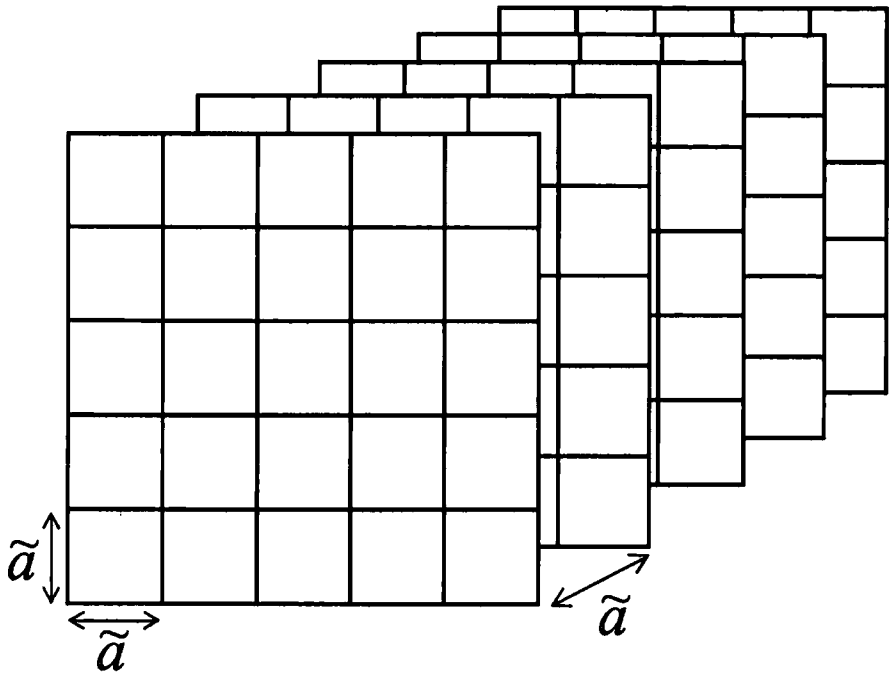

Figure 3.4 An illustration of the mesh upon which the Maxwell equations are discretized and solved in the transfer matrix method.

nents separately gives the six equations

$$k_y E_z - k_z E_y = \omega \mu_0 H_x \tag{3.27}$$

$$k_z E_x - k_x E_z = \omega \mu_0 H_y \tag{3.28}$$

$$k_x E_y - k_y E_x = \omega \mu_0 H_z \tag{3.29}$$

$$k_y H_z - k_z H_y = -\omega \varepsilon_0 \varepsilon(\mathbf{r}) E_x \tag{3.30}$$

$$k_z H_x - k_x H_z = -\omega \varepsilon_0 \varepsilon(\mathbf{r}) E_y \tag{3.31}$$

$$k_x H_y - k_y H_x = -\omega \varepsilon_0 \varepsilon(\mathbf{r}) E_z \tag{3.32}$$

where E_i, H_i, and k_i are the i^{th} components of the relevant vectors.

Next, the main approximations in the method are applied, before transforming the equations back into real space. Using the series expansion of the exponential function one can write

$$e^{ik_x\tilde{a}} = 1 + ik_x\tilde{a} - \frac{k_x^2\tilde{a}^2}{2} + \ldots, \qquad |ik_x\tilde{a}| \ll 1 \tag{3.33}$$

with similar equations for k_y and k_z. Keeping only first order terms and rearranging gives

the approximations for $\mathbf{k}$ in equations 3.27 to 3.29,

$$k_x \approx \frac{e^{ik_x\widetilde{a}} - 1}{i\widetilde{a}}, \qquad k_x\widetilde{a} \ll 1 \tag{3.34}$$

$$k_y \approx \frac{e^{ik_y\widetilde{a}} - 1}{i\widetilde{a}}, \qquad k_y\widetilde{a} \ll 1 \tag{3.35}$$

$$k_z \approx \frac{e^{ik_z\widetilde{a}} - 1}{i\widetilde{a}}, \qquad k_z\widetilde{a} \ll 1 \tag{3.36}$$

Similarly for $e^{-ik_i\widetilde{a}}$,

$$-k_x \approx \frac{e^{-ik_x\widetilde{a}} - 1}{i\widetilde{a}}, \qquad k_x\widetilde{a} \ll 1 \tag{3.37}$$

$$-k_y \approx \frac{e^{-ik_y\widetilde{a}} - 1}{i\widetilde{a}}, \qquad k_y\widetilde{a} \ll 1 \tag{3.38}$$

$$-k_z \approx \frac{e^{-ik_z\widetilde{a}} - 1}{i\widetilde{a}}, \qquad k_z\widetilde{a} \ll 1 \tag{3.39}$$

The conditions $k_x\widetilde{a} \ll 1, \ldots$ amount to a condition that the dimensions of the mesh on which the Maxwell equations are discretized and solved must be small compared with the wavelength of the radiation being considered. Thus for any particular calculation, this condition is better met at low frequencies, and becomes less accurate for higher frequencies. The approximations are invalid when $\widetilde{a} \sim \lambda$, and so the mesh size must be made small compared with the wavelength of light at the frequency range of interest. Thus the smaller the mesh size that the Maxwell equations are discretized upon, the more accurate the calculation will be. However, for a mesh with $N \times N$ points, the number of operations required to compute the transfer matrix of a slice, and thus the computational time required, is of order N^2. Thus, as usual, there is a trade off between the accuracy of the calculation to the computing time taken.

The approximations from equations 3.34 to 3.36 are inserted into equations 3.27 to 3.29, and those from equations 3.37 to 3.39 are inserted into equations 3.30 to 3.32, and the resulting equations are Fourier transformed back into real space

$$E_z(\mathbf{r} + \widetilde{a}\hat{\mathbf{j}}) - E_z(\mathbf{r}) - E_y(\mathbf{r} + \widetilde{a}\hat{\mathbf{k}}) + E_y(\mathbf{r}) = i\widetilde{a}\omega\mu_0 H_x(\mathbf{r}) \tag{3.40}$$

$$E_x(\mathbf{r} + \widetilde{a}\hat{\mathbf{k}}) - E_x(\mathbf{r}) - E_z(\mathbf{r} + \widetilde{a}\hat{\mathbf{i}}) + E_z(\mathbf{r}) = i\widetilde{a}\omega\mu_0 H_y(\mathbf{r}) \tag{3.41}$$

$$E_y(\mathbf{r} + \widetilde{a}\hat{\mathbf{i}}) - E_y(\mathbf{r}) - E_x(\mathbf{r} + \widetilde{a}\hat{\mathbf{j}}) + E_x(\mathbf{r}) = i\widetilde{a}\omega\mu_0 H_z(\mathbf{r}) \tag{3.42}$$

$$H_z(\mathbf{r}-\tilde{a}\hat{\mathbf{j}}) - H_z(\mathbf{r}) - H_y(\mathbf{r}-\tilde{a}\hat{\mathbf{k}}) + H_y(\mathbf{r}) = -i\tilde{a}\omega\varepsilon_0\varepsilon(\mathbf{r})E_x(\mathbf{r}) \tag{3.43}$$

$$H_x(\mathbf{r}-\tilde{a}\hat{\mathbf{k}}) - H_x(\mathbf{r}) - H_z(\mathbf{r}-\tilde{a}\hat{\mathbf{i}}) + H_z(\mathbf{r}) = -i\tilde{a}\omega\varepsilon_0\varepsilon(\mathbf{r})E_y(\mathbf{r}) \tag{3.44}$$

$$H_y(\mathbf{r}-\tilde{a}\hat{\mathbf{i}}) - H_y(\mathbf{r}) - H_x(\mathbf{r}-\tilde{a}\hat{\mathbf{j}}) + H_x(\mathbf{r}) = -i\tilde{a}\omega\varepsilon_0\varepsilon(\mathbf{r})E_z(\mathbf{r}) \tag{3.45}$$

Substituting the z-components of the electromagnetic fields from equations 3.42 and 3.45 into equations 3.40 to 3.45 gives the electromagnetic fields in the plane of points $z+\tilde{a}$ in terms of the fields in the plane of points z.

$$\begin{aligned} E_x(\mathbf{r}+\tilde{a}\hat{\mathbf{k}}) &= E_x(\mathbf{r}) + i\tilde{a}\omega\mu_0 H_y(\mathbf{r}) \\ &- \frac{H_y(\mathbf{r}-\tilde{a}\hat{\mathbf{i}}) - H_y(\mathbf{r}) - H_x(\mathbf{r}-\tilde{a}\hat{\mathbf{j}}) + H_x(\mathbf{r})}{i\tilde{a}\omega\varepsilon_0\varepsilon(\mathbf{r})} \\ &+ \frac{H_y(\mathbf{r}) + H_y(\mathbf{r}+\tilde{a}\hat{\mathbf{i}}) - H_x(\mathbf{r}+\tilde{a}\hat{\mathbf{i}}-\tilde{a}\hat{\mathbf{j}}) + H_x(\mathbf{r}+\tilde{a}\hat{\mathbf{i}})}{i\tilde{a}\omega\varepsilon_0\varepsilon(\mathbf{r}+\tilde{a}\hat{\mathbf{i}})} \end{aligned} \tag{3.46}$$

$$\begin{aligned} E_y(\mathbf{r}+\tilde{a}\hat{\mathbf{k}}) &= E_y(\mathbf{r}) - i\tilde{a}\omega\mu_0 H_x(\mathbf{r}) \\ &- \frac{H_y(\mathbf{r}-\tilde{a}\hat{\mathbf{i}}) - H_y(\mathbf{r}) - H_x(\mathbf{r}-\tilde{a}\hat{\mathbf{j}}) + H_x(\mathbf{r})}{i\tilde{a}\omega\varepsilon_0\varepsilon(\mathbf{r})} \\ &+ \frac{H_y(\mathbf{r}-\tilde{a}\hat{\mathbf{i}}+\tilde{a}\hat{\mathbf{j}}) - H_y(\mathbf{r}+\tilde{a}\hat{\mathbf{j}}) - H_x(\mathbf{r}) + H_x(\mathbf{r}+\tilde{a}\hat{\mathbf{j}})}{i\tilde{a}\omega\varepsilon_0\varepsilon(\mathbf{r}+\tilde{a}\hat{\mathbf{j}})} \end{aligned} \tag{3.47}$$

$$\begin{aligned} H_x(\mathbf{r}+\tilde{a}\hat{\mathbf{k}}) &= H_x(\mathbf{r}) - i\tilde{a}\omega\varepsilon_0\varepsilon(\mathbf{r}+\tilde{a}\hat{\mathbf{k}})E_y(\mathbf{r}+\tilde{a}\hat{\mathbf{k}}) \\ &- \frac{E_y(\mathbf{r}+\tilde{a}\hat{\mathbf{k}}) - E_y(\mathbf{r}-\tilde{a}\hat{\mathbf{i}}+\tilde{a}\hat{\mathbf{k}}) + E_x(\mathbf{r}-\tilde{a}\hat{\mathbf{i}}-\tilde{a}\hat{\mathbf{j}}+\tilde{a}\hat{\mathbf{k}}) + E_x(\mathbf{r}-\tilde{a}\hat{\mathbf{i}}+\tilde{a}\hat{\mathbf{k}})}{i\tilde{a}\omega\mu_0} \\ &+ \frac{E_y(\mathbf{r}+\tilde{a}\hat{\mathbf{i}}+\tilde{a}\hat{\mathbf{k}}) - E_y(\mathbf{r}+\tilde{a}\hat{\mathbf{k}}) - E_x(\mathbf{r}+\tilde{a}\hat{\mathbf{j}}+\tilde{a}\hat{\mathbf{k}}) + E_x(\mathbf{r}+\tilde{a}\hat{\mathbf{k}})}{i\tilde{a}\omega\mu_0} \end{aligned} \tag{3.48}$$

$$\begin{aligned} H_y(\mathbf{r}+\tilde{a}\hat{\mathbf{k}}) &= H_y(\mathbf{r}) - i\tilde{a}\omega\varepsilon_0\varepsilon(\mathbf{r}+\tilde{a}\hat{\mathbf{k}})E_x(\mathbf{r}+\tilde{a}\hat{\mathbf{k}}) \\ &- \frac{E_y(\mathbf{r}+\tilde{a}\hat{\mathbf{i}}-\tilde{a}\hat{\mathbf{j}}+\tilde{a}\hat{\mathbf{k}}) - E_y(\mathbf{r}-\tilde{a}\hat{\mathbf{j}}+\tilde{a}\hat{\mathbf{k}}) - E_x(\mathbf{r}+\tilde{a}\hat{\mathbf{k}}) + E_x(\mathbf{r}-\tilde{a}\hat{\mathbf{j}}+\tilde{a}\hat{\mathbf{k}})}{i\tilde{a}\omega\mu_0} \\ &+ \frac{E_y(\mathbf{r}+\tilde{a}\hat{\mathbf{i}}+\tilde{a}\hat{\mathbf{k}}) - E_y(\mathbf{r}+\tilde{a}\hat{\mathbf{k}}) - E_x(\mathbf{r}+\tilde{a}\hat{\mathbf{j}}+\tilde{a}\hat{\mathbf{k}}) + E_x(\mathbf{r}+\tilde{a}\hat{\mathbf{k}})}{i\tilde{a}\omega\mu_0} \end{aligned} \tag{3.49}$$

Hence, knowing $\mathbf{E}(\mathbf{r})$ and $\mathbf{H}(\mathbf{r})$ for all $\mathbf{r}$ in a slice, equations 3.46 to 3.49 allows for the calculation of the electromagnetic fields in the next slice of points, i.e. $\mathbf{E}(\mathbf{r}+\tilde{a}\hat{\mathbf{k}})$ and $\mathbf{H}(\mathbf{r}+\tilde{a}\hat{\mathbf{k}})$ for all $\mathbf{r}+\tilde{a}\hat{\mathbf{k}}$. Therefore a transfer matrix that propagates the fields from one

slice to the next can be defined by

$$\mathbf{F}(z+\widetilde{a}) = \mathbf{M}(z)\,\mathbf{F}(z) \tag{3.50}$$

where

$$\mathbf{F}(z) = \begin{bmatrix} E_x(\mathbf{r}) \\ E_y(\mathbf{r}) \\ H_x(\mathbf{r}) \\ H_y(\mathbf{r}) \end{bmatrix} \tag{3.51}$$

and the matrix elements $M_{ij}(\mathbf{r}, \mathbf{r}')$ are found from equations 3.46 to 3.49.

If the structure under study is infinite in extent in all directions, then periodic boundary conditions can be set, and Bloch's law used to write the solutions as Bloch waves. Then the transfer matrix through the unit cell can be diagonalised to give the eigenfrequencies and therefore the bandstructure of the periodic array. However, in this thesis, the transfer matrix method is used for the calculation of reflection and transmission coefficients—something that is unobtainable by the Fourier plane wave method described in section 3.2.

3.3.1 Transmission and reflection coefficients

The strategy to obtain the transmission and reflection coefficients of a finite thickness of a 2D photonic crystal is as follows. First, a unit cell is identified, and periodic boundary conditions applied in the direction parallel to the plane of incidence. Then a mesh of points is defined, upon which the Maxwell equations can be discretized and solved, by multiplication of the transfer matrices of individual slices. Once the total transfer matrix that propagates the electromagnetic fields across the sample is known, the transfer matrix is transformed from its basis in electromagnetic fields, $\mathbf{M}$, to a plane wave basis, $\tilde{\mathbf{M}}$. The transmission and reflection coefficients can be extracted from $\tilde{\mathbf{M}}$. Moreover, the angular dependence of the transmission and reflection can be obtained, from the different eigenvalues of the plane wave basis transfer matrix.

Following ref. [106], consider the situation in free space, where $\varepsilon = 1$. In this case, the transfer matrix is independent of z, and the eigenvalues of equation 3.50 are plane waves in free space. However, $\tilde{\mathbf{M}}$ is not an Hermitian matrix, and so the left and right eigenvectors,

$\mathbf{F}_{lj}$ and $\mathbf{F}_{rj}$, defined by

$$\mathbf{M}^{(0)}\mathbf{F}_{rj}^{(0)}(z) = \mathbf{F}_{rj}^{(0)}(z+\widetilde{a}) = e^{ik_j^{(0)}\widetilde{a}}\mathbf{F}_{rj}^{(0)}(z) \tag{3.52}$$

$$\mathbf{F}_{lj}^{(0)}(z)\,\mathbf{M}^{(0)} = \mathbf{F}_{lj}^{(0)}(z+\widetilde{a}) = e^{ik_j^{(0)}\widetilde{a}}\mathbf{F}_{lj}^{(0)}(z) \tag{3.53}$$

are distinct. A unitary transformation into this plane wave basis is then defined as

$$\mathbf{S} = \sum_j \mathbf{F}_{rj}^{(0)}(z)\,\mathbf{F}_{lj}^{(0)}(z) \tag{3.54}$$

where $\mathbf{F}_{li}^{(0)}(z)\cdot\mathbf{F}_{rj}^{(0)}(z) = \delta_{ij}$ provided the vectors are normalised. In this basis of plane waves

$$\tilde{\mathbf{M}}^{(0)} = \mathbf{S}\mathbf{M}^{(0)}\mathbf{S}^{-1} = \begin{bmatrix} e^{ik_1^{(0)}\widetilde{a}} & & & & \\ & e^{ik_2^{(0)}\widetilde{a}} & & 0 & \\ & & \cdots & & \\ & 0 & & e^{-ik_1^{(0)}\widetilde{a}} & \\ & & & & e^{-ik_1^{(0)}\widetilde{a}} \end{bmatrix} \tag{3.55}$$

The same transformation is applied to the transfer matrix in the case where the dielectric function is allowed to vary.

3.3.2 Multiple scattering

In principle, the transmission and reflection coefficients can be obtained by applying the above transformation on the transfer matrix through the entire structure being considered. This is found from consecutive application of the transfer matrix from one slice to the next. Unfortunately, the transfer matrix method can suffer from numerical instability. When many slices have been added to the transfer matrix, some components of the electromagnetic fields can grow exponentially with thickness and overwhelm the calculation with rounding errors and overflows. Thus, there is a finite thickness to which the transfer matrix method described above can be applied for the calculation of transmission and reflection coefficients whilst still retaining the necessary numerical accuracy. The exact thickness at which the calculation becomes unstable is highly dependent upon the details of the calculation and structure being investigated [20, 106, 107].

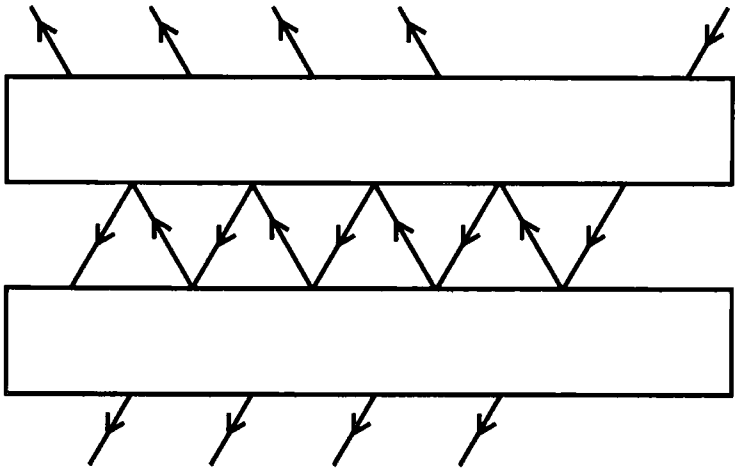

Figure 3.5 An illustration of the multiple scattering technique, used to assemble "slabs" of 2D photonic crystals in transmission and reflection calculations.

Fortunately, there is another method of adding further slices to the structure. Consider two "slabs" of material, each consisting of as many slices as numerical stability in the transfer matrix method will allow. Once the transmission and reflection from each of these slabs is known, the transmission and reflection from the composite structure can be calculated by a multiple scattering method. The situation is summarised in figure 3.5. The details of this method can be found in ref. [106]. The disadvantage of adding slices via this multiple scattering method is that it takes $O(N^3)$ operations to achieve, as opposed to the $O(N^2)$ operations required to add a slice to the transfer matrix. Thus, a combination of transfer matrix and multiple scattering methods are used in any calculations of the reflection and transmission coefficients. As many slices as possible are added to the transfer matrix as numerical stability will allow, after which slices are added using the multiple scattering method.

3.4 Etched Bragg reflectors as two-dimensional photonic crystals

The best known example of a one-dimensional photonic crystal is the Bragg reflector, as studied in chapter 2, which can be used to provide optical confinement in certain systems, such as vertical cavity surface emitting lasers (VCSELs) [73, 75, 81, 99]. Recently, Bragg reflectors made with deep etching of air grooves through a planar waveguide have been employed to enhance the properties of a semiconductor laser [64]. The idea is to use the

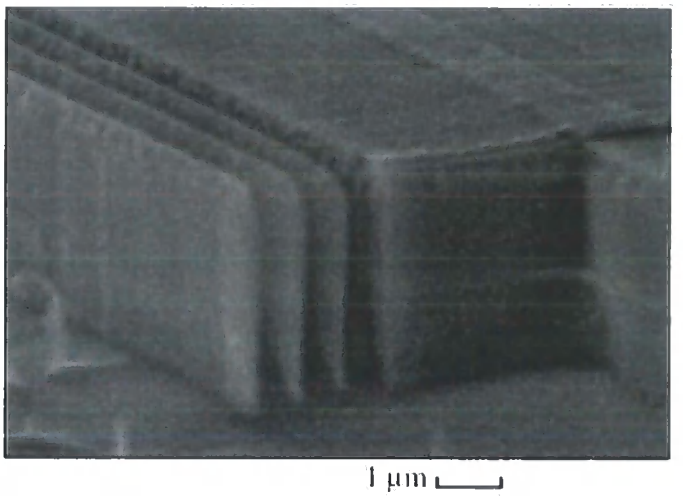

Figure 3.6 Scanning electron microscope image of an deeply etched air/semiconductor Bragg reflector. Reproduced from Maximov *et al.*, "Edge-emitting InGaAs/GaAs lasers with deeply etched semiconductor/air distributed Bragg reflector mirrors", October 2002, IOP Publishing Ltd.

Bragg reflector to improve the optical confinement of the laser cavity. A SEM image of the laser cavity and three period Bragg reflector mirror studied in ref. [64] is shown in figure 3.6. The one-dimensional Bragg reflector provides optical confinement in one direction only. To take the idea further, two- or three-dimensional photonic crystals could be used to provide optical confinement in the laser cavity along two- or three-directions.

A photonic crystal, however, must possess a PBG at the lasing frequency for it to provide appropriate enhanced optical confinement. An attempt to design a technologically feasible 3D photonic crystal was made recently [36] by considering a structure of circular cylindrical air holes etched along the growth direction of a Bragg reflector. Although no complete PBG was reported, some structures did display a reduction in the density of photonic states by a factor of three when compared to a uniform medium with the same average dielectric constant. Therefore, etched Bragg reflectors provide a promising basis from which to try and design photonic crystals providing PBGs suitable for technological applications.

The aim of this section is to study the mode structure of a 2D photonic crystal in the form of a Bragg reflector with straight air grooves parallel to the growth direction, as shown in figure 3.7. Such a structure could be fabricated by the etching of deep air trenches (similar to those described in ref. [64]) in a quarter-wave Bragg stack, which itself can be fabricated by molecular beam or gas-phase epitaxy. In such a structure there is the potential for optical confinement in both the vertical direction, and one of the lateral directions, and it could

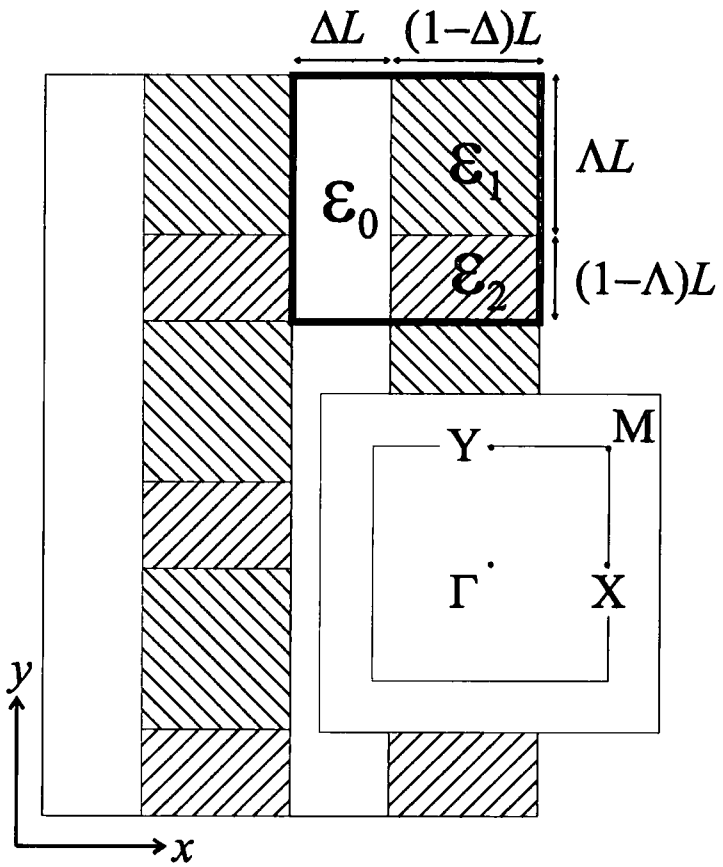

Figure 3.7 Schematic diagram of the structure of the etched Bragg reflector under consideration. The reflector can be constructed by taking the unit cell shown within the square box, and repeating on a square lattice of points in the xy-plane. (Inset) An illustration of the first Brillouin zone of the photonic crystal. The symmetry points are shown, and are located in k-space as follows – Γ: $\mathbf{K} = (0, 0)$; X: $\mathbf{K} = (\pi/L, 0)$; Y: $\mathbf{K} = (0, \pi/L)$; and M: $\mathbf{K} = (\pi/L, \pi/L)$.

be used to improve the optical confinement in certain laser cavities. The unit cell of the structure is represented by a square with sides of length L, divided into three rectangular areas with relative permitivitties ε_0, ε_1 and ε_2; the sizes of the three rectangles are described by two dimensionless parameters Δ and Λ, as shown in figure 3.7. Thus the structure consists of "walls" made from materials with relative permittivities ε_1 and ε_2 separated by uniform grooves with relative permittivity ε_0.

Two-dimensional photonic crystals are usually made by etching air holes in a uniform substrate; the resulting structure is similar to either a honeycomb or a periodic array of solid rods in air. However, structures based on square or rectangular elements similar to the etched Bragg reflectors considered in this section have also been studied, and PBGs reported—for TM-polarised modes when the photonic crystal is made up of a lattice of

square dielectric rods [26], and for TE-polarised modes when the photonic crystal is made up of a connected lattice of dielectric veins [2, 23], which could be constructed by etching air holes of square cross-section on a square lattice of points. The structures studied in refs. [2] and [23] possess the four-fold rotational symmetry of the square Bravais lattice. In contrast, the etched Bragg reflector structure under study in this section possesses no rotational symmetry, and the symmetry points X and Y (see figure 3.7) in the first Brillouin zone are not equivalent.

To obtain a sizeable PBG, one should provide a sufficiently large contrast of the refractive index along both the Γ-X direction (perpendicular to the grooves) and Γ-Y direction (along the grooves). The air grooves have a relative permittivity equal to unity, and thus "walls" made of any semiconductor material achieve the high refractive index contrast along the Γ-X direction automatically. Achieving the high refractive index contrast in Γ-Y direction is a challenging, but feasible, task. A promising pair of materials are GaAs ($\varepsilon_2 = 14.44$) and oxidised AlAs ($\varepsilon_1 = 2.25$).

3.4.1 TM-polarised band gaps

In the etched Bragg reflector, PBGs occur for TM-polarised modes for certain values of the geometric parameters Δ and Λ defined in figure 3.7, but a PBG for TE-polarised modes does not appear. Figure 3.8 shows the ratio of the width of the PBG ($\Delta\omega$) to the centre gap frequency (ω_0) as a function of Δ and Λ for TM-polarised modes. The maximum relative width of the PBG is equal to 34%, and occurs when $\Delta = 0.55$ and $\Lambda = 0.65$. Figure 3.9 shows dispersion relations, density of TM-polarised and TE-polarised photonic modes and transmission spectra for such an optimised structure, and a large band gap for all 2D directions occurs for the TM-polarisation, centred around $\omega L/(2\pi c) = 0.3$ is seen. No such band gap is observed for the TE-polarisation. The density of photonic modes reduces to zero for the TM-polarisation, and there are pronounced stop-bands in the transmission spectrum for both the Γ-X and Γ-Y directions. In contrast, the transmission coefficient for light incident in the Γ-Y direction for TE-polarised modes is close to one, no reduction of the density of TE-polarised modes occurs, and the reduction of the total density of photonic states ρ (which is the sum of the densities of TM-polarised and TE-polarised photonic modes) compared to the density of states of an effective medium ρ_{eff} (characterised by the average

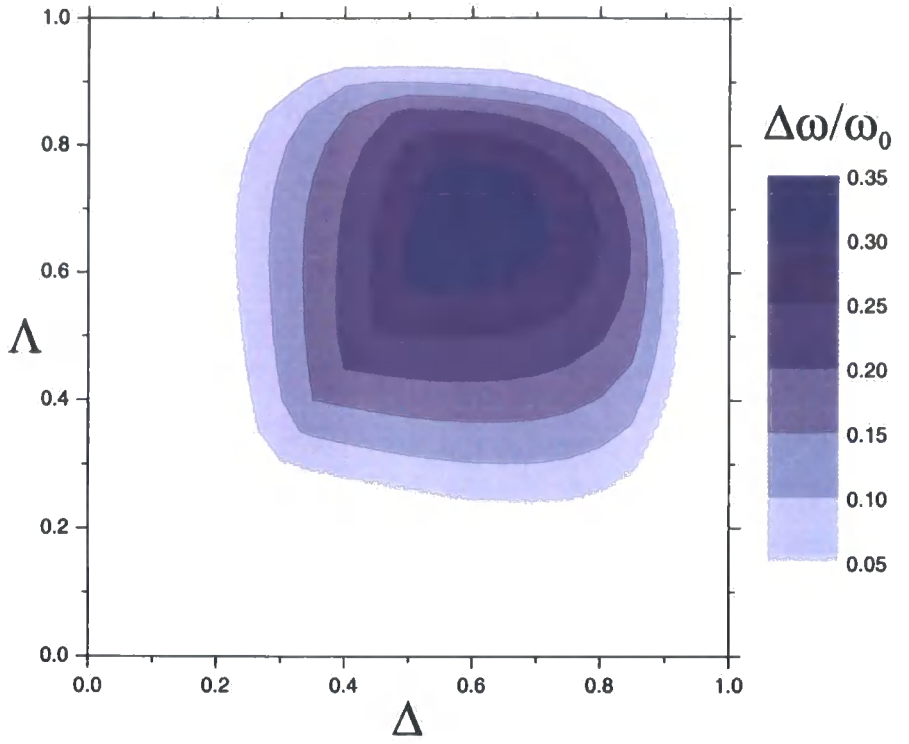

Figure 3.8 A "gap-map" showing the calculated complete 2D photonic band gap between the first and second TM-polarised bands for etched Bragg reflectors with $\varepsilon_0 = 1.0$ (air), $\varepsilon_1 = 2.25$ (oxidised AlAs) and $\varepsilon_2 = 14.44$ (GaAs). The size of the photonic band gap is shown as a ratio between the width of the gap and the centre gap frequency. The largest such band gap is $\Delta\omega/\omega_0 = 0.338$ for the parameters $\Delta = 0.55$ and $\Lambda = 0.65$.

dielectric constant of the structure) is not substantial.

The range of parameters Δ and Λ for which the widest PBGs in the TM-polarisation can be found for the etched Bragg reflectors is interesting. The widest band gaps appear when both Δ and Λ are greater than 0.5; that is when the etched Bragg reflector resembles a square lattice of isolated high-ε "rods" in a low-ε background, albeit rods with a square cross-section and a background made up of two different materials. However, this is in accordance with the rule-of-thumb given by Joannopulos *et al.* in ref. [2], that TM band gaps are favoured when the structure is made up of isolated regions of high-ε material.

3.4.2 "Near-gaps"

Although the etched Bragg reflector structure fails to provide a complete PBG for all directions and polarisations, the density of photonic states do possess an interesting feature near $\omega L/(2\pi c) = 0.5$. Figure 3.9 reveals a band of substantially reduced density of states when compared with the density of states for an effective uniform medium characterised by

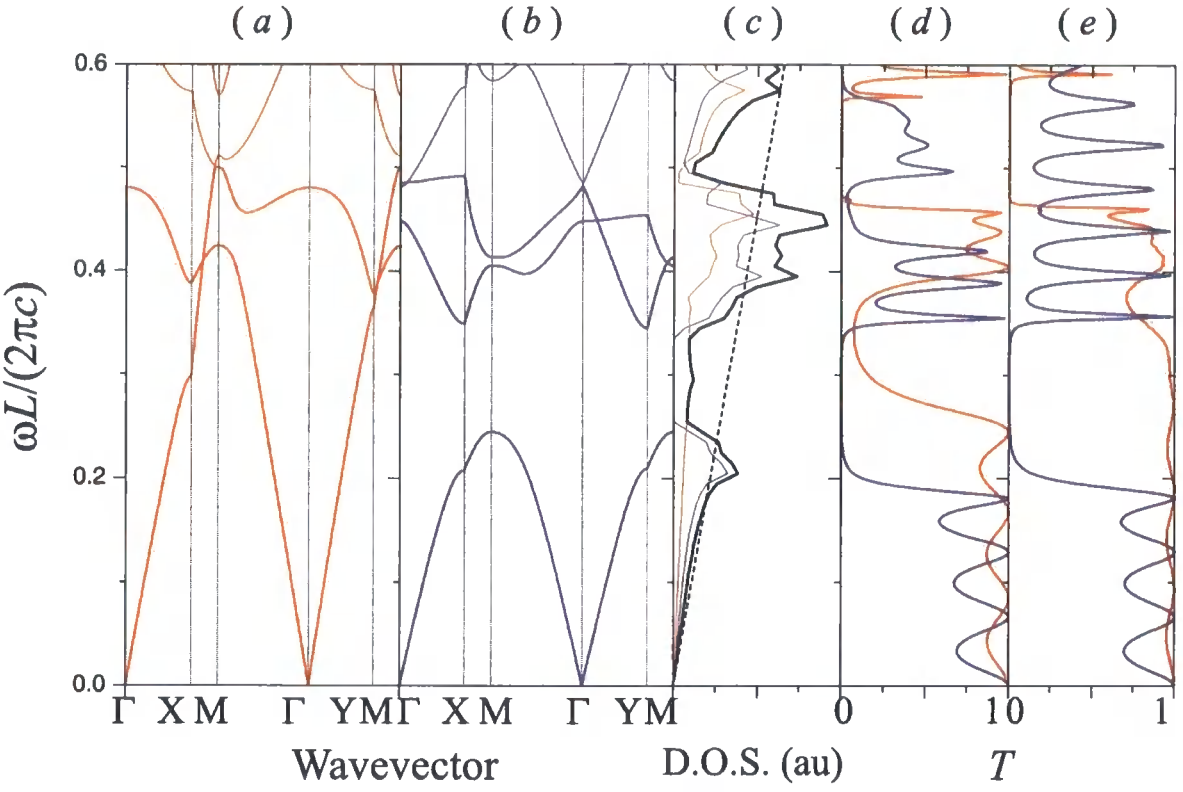

Figure 3.9 Calculated bandstructure for the TE-polarisation (a) and TM-polarisation (b), for the etched Bragg reflector with parameters $\varepsilon_0 = 1.0$ (air), $\varepsilon_1 = 2.25$ (oxidised AlAs) and $\varepsilon_2 = 14.44$ (GaAs), $\Delta = 0.55$ and $\Lambda = 0.65$. (c) The calculated density of states for the same structure. The red line shows the density of TE-polarised states; the blue line the density of TM-polarised states; the black line the total density of states; and the dashed line the density of states for a uniform medium with the same average dielectric constant as the etched Bragg reflector. (d) and (e) The calculated transmission spectra for light incident upon eight periods of the etched Bragg reflector in the Γ-X and Γ-Y directions respectively. The two lines show the calculations for TE-polarised light incident (red line) and TM-polarised light (blue line).

the same average relative permittivity as the etched Bragg reflector around this frequency. The rate of spontaneous emission of a quantum mechanical source inside the structure is given in time-dependent perturbation theory by Fermi's golden rule [110–112] and is proportional to the total density of photonic modes, and a substantial decrease of the spontaneous emission rate, rather than a total absence caused by an absolute PBG, could be of value in certain device applications.

Varying the parameters Δ and Λ, we can change the position, width, and depth of this feature in the density of photonic states. Figure 3.10 shows the relative decrease of the density of states $\eta = \rho/\rho_{eff}$ as a function of Δ and Λ for the band of reduced density of states mentioned above. For $\Delta = 0.55$ and $\Lambda = 0.60$, the band of reduced density of states is

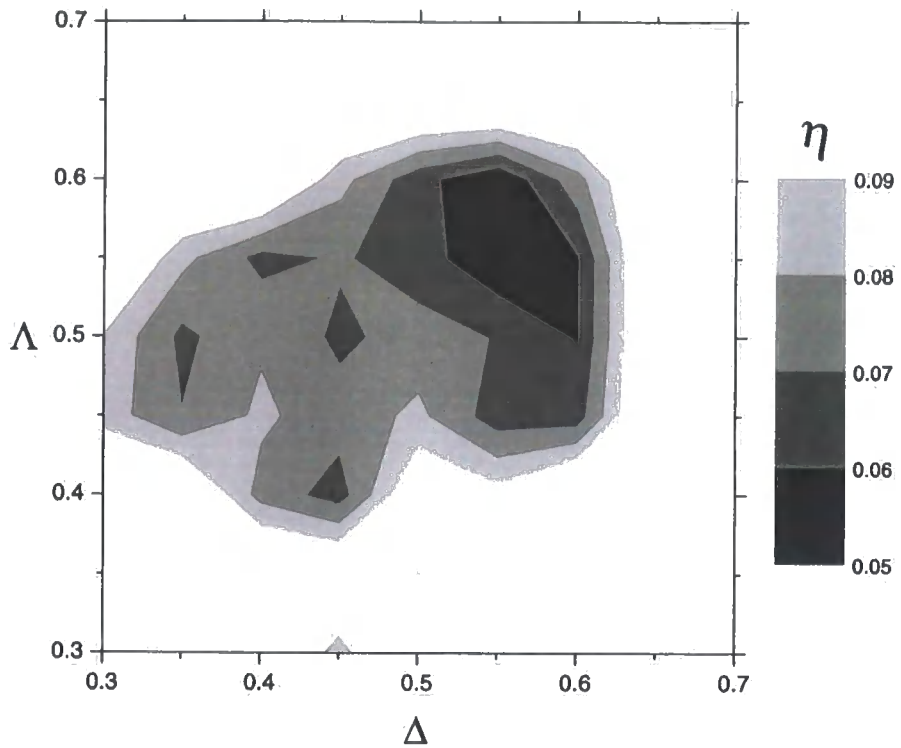

Figure 3.10 Graph showing the maximum relative reduction of the density of states of the feature near $\omega L/(2\pi c) = 0.5$ as a function of the parameters within the unit cell (i.e. $\rho(\Delta, \Lambda)$ in the text) for etched Bragg reflectors with $\varepsilon_0 = 1.0$ (air), $\varepsilon_1 = 2.25$ (oxidised AlAs) and $\varepsilon_2 = 14.44$ (GaAs).

centred near $\omega L/(2\pi c) = 0.5$. The relative reduction (η) becomes as small as 1/20, and the width of the band is 18% of its centre frequency. Although not a true PBG, such a substantial reduction in the density of photonic states provides a "near-gap", and could be of use in some optoelectronic devices that rely on PBG materials.

Figure 3.11 shows the bandstructure, density of states, and transmission spectra for an etched Bragg reflector with $\Delta = 0.5$ and $\Lambda = 0.5$. For this structure, the relative width of the region of the reduced density of states centred near $\omega L/(2\pi c) = 0.5$ reaches 0.23, while the relative reduction $\eta \approx 1/14$. Such a sizeable "near-gap" originates from a complete 2D band gap for the TM-polarisation and band gaps along the Γ-Y and Γ-X directions for the TE-polarisation. In fact, in such a structure, only TE-polarised light can propagate, and then only within a small angle near the Γ-M direction, if at a frequency corresponding to this near gap. The calculated transmission spectra for light propagating in the Γ-X and Γ-Y directions (shown in figure 3.11 (d) and (e)) exhibit near zero transmission coefficients for the spectral region of reduced density of states.

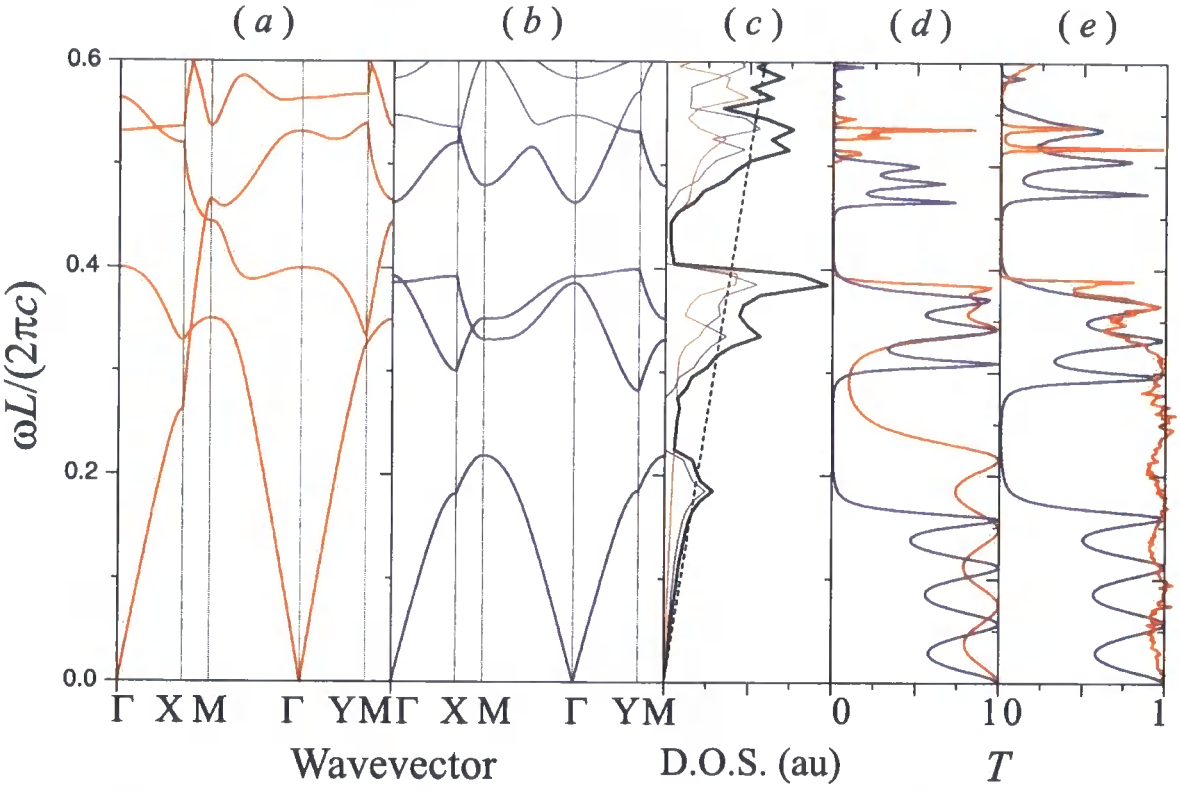

Figure 3.11 Calculated bandstructure for the TE-polarisation (a) and TM-polarisation (b), for the etched Bragg reflector with parameters $\varepsilon_0 = 1.0$ (air), $\varepsilon_1 = 2.25$ (oxidised AlAs) and $\varepsilon_2 = 14.44$ (GaAs), $\Delta = 0.50$ and $\Lambda = 0.50$. (c) The calculated density of states for the same structure. The red line shows the density of TE-polarised states; the blue line the density of TM-polarised states; the black line the total density of states; and the dashed line the density of states for a uniform medium with the same average dielectric constant as the etched Bragg reflector. (d) and (e) The calculated transmission spectra for light incident upon eight periods of the etched Bragg reflector in the Γ-X and Γ-Y directions respectively. The two lines show the calculations for TE-polarised light incident (red line) and TM-polarised light (blue line).

3.4.3 Approximate rotational symmetry

Although the etched Bragg reflectors possess no rotational symmetry, the structures considered in figure 3.10 (with parameters $\Delta \approx 0.5$ and $\Lambda \approx 0.5$) do possess a near rotational symmetry. This near symmetry arises due to the fact that two of the materials which constitute the Bragg reflector have similar relative permitivitties, i.e. $\varepsilon_0 \approx \varepsilon_1$. The near rotational symmetry manifests itself in an almost isotropic dispersion, especially for the low frequency TM-polarised bands (see figures 3.9 (b) and 3.11 (b)). It also results in very similar transmission spectra for the TM-polarised modes in both the Γ-X and Γ-Y directions. For example, the TM-polarised modes for the structure with $\Delta = 0.5$ and $\Lambda = 0.5$ (blue lines in figure 3.11 (d) and (e)) both have near zero transmission for the spectral regions centred on

$\omega L/(2\pi c) \approx 0.23$ and $\omega L/(2\pi c) \approx 0.42$. The corresponding transmission spectra for TE-polarised light differ for low frequencies, as there is no band gap in the Γ-Y direction, and thus no stop-band appears in the spectrum.

3.4.4 Absolute photonic band gap

Whilst no absolute photonic band gaps have been found for both polarisations between low lying photonic bands, certain values of the parameters Δ and Λ do give absolute band gaps between higher frequency photonic bands, but these gaps are very narrow (typically about 2–3% of the mid-gap frequency) and only occur for highly restrictive values of Δ and Λ. For example, the structure with $\Delta = 0.30$ and $\Lambda = 0.35$ has a complete band gap for TE-polarised modes between the 6th and 7th photonic bands, and a complete band gap for TM-polarised modes between the 8th and 9th photonic bands (see figure 3.12 for the bandstructure and density of states). These band gaps overlap each other to give an absolute 2D PBG for both polarisations with a width of 2.8% of the gap centre frequency. Although these band gaps are narrow, the result demonstrates that an etched Bragg reflector structure is capable of supporting absolute PBGs, and that if materials with a greater refractive index contrast were used, these band gaps could open up to a more technologically useful size.

3.4.5 Complementary structures

The etched Bragg reflectors considered so far in this section, with $\varepsilon_0 = 1.0$ (air), $\varepsilon_1 = 2.25$ (oxidised AlAs) and $\varepsilon_2 = 14.44$ (GaAs), give a complete PBG in the TM-polarised bandstructure when the structure resembles isolated "rods" of high-ε material in a low-ε background. This section considers a complementary structure, in which there are connected regions of high-ε material in a low-ε background. According to the rule-of-thumb formulated by Joannopoulos *et al.* [2], it should be possible to find band gaps in the TE-polarised bandstructure of this complementary etched Bragg reflector.

Firstly, consider the etched Bragg reflector structure in which the air grooves are filled in with some dielectric material of high relative permittivity—say with AlAs ($\varepsilon_0 = 9.0$). Then the structure has $\varepsilon_0 = 9.0$, $\varepsilon_1 = 2.25$ and $\varepsilon_2 = 14.44$. However, these values for the three dielectrics fail to provide sufficient dielectric contrast, and no 2D band gaps are found for either polarisation for any values of the parameters Δ and Λ.

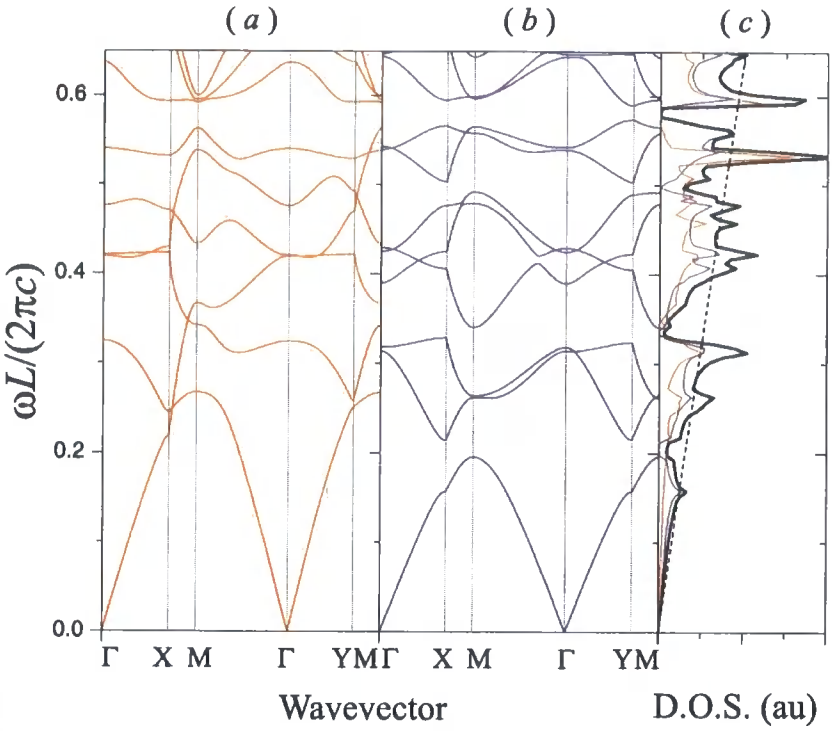

Figure 3.12 Calculated bandstructure for the TE-polarisation (a) and TM-polarisation (b), for the etched Bragg reflector with parameters $\varepsilon_0 = 1.0$ (air), $\varepsilon_1 = 2.25$ (oxidised AlAs) and $\varepsilon_2 = 14.44$ (GaAs), $\Delta = 0.30$ and $\Lambda = 0.35$. (c) The calculated density of states for the same structure. The red line shows the density of TE-polarised states; the blue line the density of TM-polarised states; the black line the total density of states; and the dashed line the density of states for a uniform medium with the same average dielectric constant as the etched Bragg reflector. A complete PBG in two dimensions can be seen centred around $\omega L/(2\pi c) = 0.58$.

Now consider a similar structure, in which the oxidised AlAs is somehow selectively etched away to leave air in its place. Then the complementary etched Bragg reflector structure has $\varepsilon_0 = 9.0$ (AlAs), $\varepsilon_1 = 1.0$ (Air) and $\varepsilon_2 = 14.44$ (GaAs). Band gaps in the TE bandstructure are found in such a structure for a range of values of the parameters Δ and Λ, but no such band gaps are found in the TM-polarised bandstructure. A "gap-map" of the width of the band gap in the TE-bandstructure relative to its centre frequency is shown in figure 3.13. The widest band gap is found in the structure with parameters $\Delta = 0.20$ and $\Lambda = 0.80$, which has a band gap between the first and second TE-polarised photonic bands of relative width $\Delta\omega/\omega_0 = 0.263$.

The widest band gaps for the TE-polarised bandstructure are found for the range of values of the parameters Δ and Λ for which the complementary etched Bragg reflector structure resembles a connected lattice of thin veins of high-ε material in air.

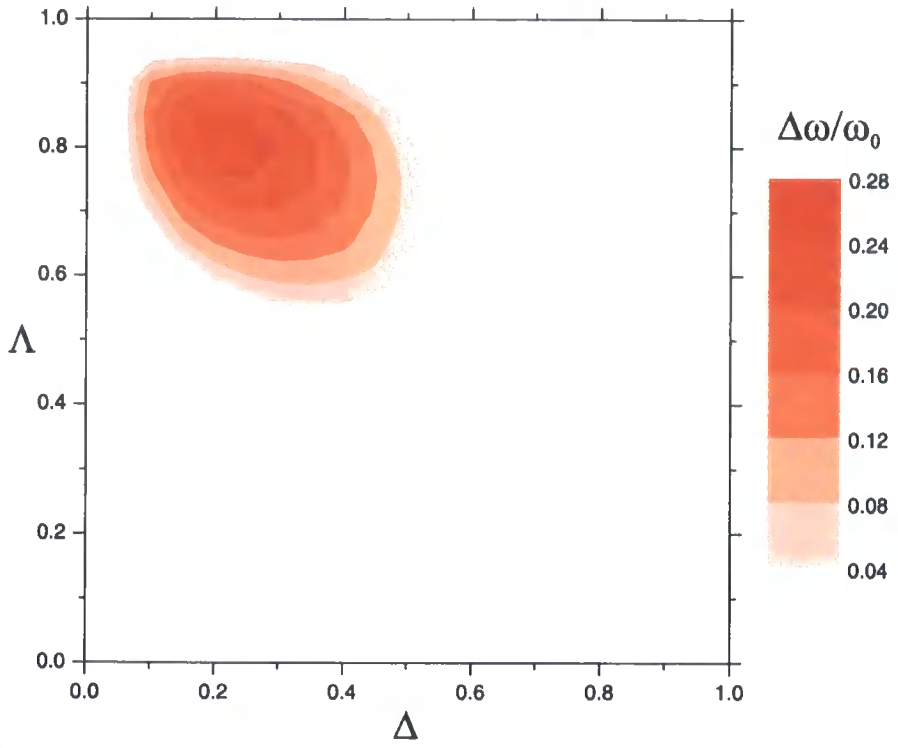

Figure 3.13 A "gap-map" showing the calculated complete 2D photonic band gap between the first and second TE-polarised bands for etched Bragg reflectors with $\varepsilon_0 = 9.0$ (AlAs), $\varepsilon_1 = 1.0$ (air) and $\varepsilon_2 = 14.44$ (GaAs). The size of the photonic band gap is shown as a ratio between the width of the gap and the centre gap frequency. The largest such band gap is $\Delta\omega/\omega_0 = 0.263$ for the parameters $\Delta = 0.20$ and $\Lambda = 0.80$.

3.5 Conclusions

This chapter has presented a Fourier plane wave method and a transfer matrix method for the calculation of the bandstructure, electromagnetic field profiles, density of states and transmission/reflection spectra of 2D photonic crystals. The methods given are widely used in the literature for studies of 2D photonic crystals. Results of calculations of the bandstructure of square and hexagonal lattices of cylindrical air holes in a GaAs background are presented.

This chapter then considered the properties of etched GaAs/oxidised AlAs Bragg reflectors for use as 2D photonic crystals. The bandstructure, density of photonic states and transmission spectra of the crystals have been calculated for a wide range of geometrical parameters describing the structure, from which it is found that band gaps in the TM-polarised bandstructure are obtained for a wide range of these parameters, but no significant band gaps are found for the TE-polarisation. A complementary structure to the etched Bragg reflector has also been considered, in which the reverse was found to be true; TE-polarised band

gaps were found, but no TM-polarised band gaps. Hence it can be concluded that photonic band gaps in the TE-polarised bandstructure or the TM-polarised band-structure are easily achieved, but that finding a structure with a band gap for both polarisations is a more difficult task. However, even with the above caveat, it has been demonstrated that very narrow absolute photonic band gaps can be obtained for certain, restrictive values of the parameters of the etched Bragg reflector.

Perhaps more usefully, it has been shown that structures can be engineered to provide wide "near-gaps", spectral bands where there is a reduction by a factor of about 20 in the total density of photonic states when compared with a uniform dielectric with the same mean relative permittivity. These structures could be of technological use in optoelectronic devices when a suppression of spontaneous emission, rather than a total inhibition, is sufficient.

Chapter 4

Disorder in photonic crystals

Disorder in photonic crystals is of interest for a number of reasons. Many potential applications that result from a photonic crystal's ability to guide, control and manipulate light, and their ability to inhibit or enhance spontaneous emission, rely on the existence of a PBG. However, it is technologically impossible to produce a perfectly periodic photonic crystal, and all real photonic crystals will therefore possess some variation away from the ideal periodic modulation of the relative permittivity. This disorder can damage the photonic band gap, potentially rendering the photonic crystal unsuitable for use in certain applications. Hence, knowing how the presence of disorder in an otherwise periodic dielectric structure affects the properties of photonic crystals is a technologically important question. Also, there is the possibility of light localisation in disordered photonic crystals [9, 113, 114]. This is of fundamental interest, as the lack of interactions between photons make disordered photonic crystals an attractive test bed for theories of the localisation of waves [115]. Further, localised defect states introduced into the PBG by disorder could find technological applications. Defects can form microcavities in the bulk of a photonic crystal, whose resonances can be tuned by engineering the defect's properties.

Many types of disorder can occur adventitiously in particular photonic crystals. For example, inverse opals, 3D photonic crystals constructed by self-assembly methods, will show a dispersion of the radii of the spheres making up the crystal, as well as lattice vacancies and stacking faults [42, 68, 69, 116]. Also, the growth procedure tends to produce islands or domains of ideal material separated by gaps or cracks between these regions (see, for example, [14, 16, 70]). Typical 2D photonic crystals, based on cylinders or rods etched into

dielectric substrates, will show a variation of the radii of these elements, and a random displacement of them away from their intended (ideal) lattice locations. Also, etched elements will display surface roughness. One-dimensional photonic crystals—Bragg reflectors—will show a variation of the thickness of the layers, and the interfaces between them will exhibit a certain amount of roughness. Other types of disorder are also possible—in particular, random variations of the intended dielectric constant could occur.

Disordered photonic crystals have previously been the subject of many studies published in the literature. Previous investigations into disordered 1D photonic crystals [69, 117] have found that the photonic band gap is resilient to a certain level of disorder. Also, it is seen that the introduction of disorder into an otherwise periodic system leads to an increase in the transmission through the photonic crystal at frequencies in the photonic band gap. This could be considered to be a counter-intuitive result—the presence of disorder might be expected to increase the random scattering of light in addition to the attenuation of light provided by the presence of the photonic band gap and so decrease the transmission further. However, if the disorder narrows the photonic band gap by filling all or part of it with disorder-induced states, then the attenuation of light at frequencies in the band gap can be expected to decrease, and the transmission increase.

Disordered 2D photonic crystals have been considered by many groups. 2D square lattices of dielectric cylinders have been studied with models of disorder that include disorder in the position of the cylinders, disorder in the radius of the cylinders, and disorder in the dielectric properties of the cylinders [118–127]. Disorder in the radii of the cylinders has also been studied in hexagonal lattices [123, 128, 129]. These studies have employed both plane wave methods with supercell approximations of the disordered structures, to calculate the effect of disorder on the bandstructure of the photonic crystal, and transfer matrix methods to calculate the effect of disorder on the transmission of the photonic crystals. These studies have established that the PBG in 2D photonic crystals is resilient to a certain level of disorder. Experimental studies of 2D photonic crystals [130, 131] serve to strengthen the conclusions of the theoretical studies.

Theoretical studies of disorder in 3D photonic crystals [68, 132, 133] have usually been very limited. They often rely on supercell approaches, but the level of computer resources and calculation times for 3D systems means that the studies reported in the literature have

small supercells, and the number of different configurations of the disorder considered is small. For example, in ref. [132], the properties of just two random configurations of disordered photonic crystals are calculated for each model of disorder considered. There have also been experimental investigations of disorder in 3D photonic crystals at microwave frequencies [45,47].

This chapter describes the results of studies of disorder in one- and two-dimensional photonic crystals. Section 4.1 is a study of disorder in a Bragg reflector. The eigenfrequencies and lifetimes of the photonic modes in disordered Bragg reflectors are directly calculated using the transfer matrix techniques with outgoing wave boundary conditions described in chapter 2. The statistics of the eigenmodes of 10^4 randomly disordered structures are investigated for various models and levels of disorder, and for various properties and parameters of the Bragg reflectors. Previous studies of disorder effects in 1D photonic crystals have mainly been concerned with the transmission properties, and so the direct calculation of the statistics of the eigenfrequencies and lifetimes of disordered 1D photonic crystals is intended to add to current understanding. A central feature of the work is an investigation of the penetration of the density of states into the photonic band gap when disorder is introduced, and the extent to which the states introduced into the band gap are localised by the disorder. The early work of John [9] suggested that "localisation is possible even for weak randomness". In experimental studies of photonic crystals, the properties of the crystals (including the bandstructure) are usually investigated by measuring the transmission through the photonic crystal. Also, many potential applications of photonic crystals rely on the properties of light transport at frequencies in the PBG that a photonic crystal can provide. Thus in our work the statistics of the eigenmodes are linked to the transmission properties of the disordered 1D photonic crystals by calculating the transmission properties of 10^6 randomly disordered structures for the three related models of disorder and at various levels of disorder.

A notable absence from the literature on disordered photonic crystals is any generally accepted analytical theory of the penetration of the tails of the density of states into the photonic band gap when disorder is present in an otherwise periodic system. This chapter falls short of offering such a theory itself, but the phenomenological relationships between the penetration of the density of states into the photonic band gap, the level of disorder and the width of the photonic band gap found in this study should provide a benchmark for any

analytical theory developed in the future.

The remainder of this chapter is concerned with studies of the effects of disorder on a certain two-dimensional photonic crystal. The ideal photonic crystal consists of an hexagonal lattice of air cylinders of radius $r = 0.4a$ etched into a GaAs substrate ($\varepsilon = 12.96$). Disorder in the position of the cylinders has been considered, and its effects on a complete band gap and an incomplete band gap examined. It will be seen that there are important bandstructure related differences in the two distinct cases. As far as the author is aware this is the first time this kind of disorder has been studied in a 2D photonic crystal with an hexagonal lattice, although the results are expected to be qualitatively similar to the case of the square lattice, which is more widely studied for all types of disorder.

However, the discussion of two-dimensional structures begins with an examination of the effect of lattice vacancies in section 4.2.1. A complete photonic band gap should facilitate the formation of localised states at lattice vacancies, which act as microcavities in the 2D photonic crystal. A defect or vacancy in a photonic crystal with a resonance at a frequency within a complete PBG of the crystal will support a localised defect state, as the electromagnetic fields essentially have nowhere to go—they are attenuated by the bulk of the photonic crystal due to its band gap. Defects in photonic crystals have received much attention in the literature [5, 6, 22, 40, 41, 44, 49, 134–138], including experimental studies conducted at microwave frequencies [87, 92], due to the potential to design defects with electromagnetic properties for many potential applications. For example, individual defects can be coupled together to produce a miniband of defect states [43, 49, 138] in the photonic band gap, which can be used as the basis of optical filters [43, 139] or coupled cavity waveguides [47, 48, 51, 140, 141]. Coupled cavity waveguides are chains of coupled cavities that guide light along the chain by photon tunnelling from one microcavity to the next along the chain. Coupling further microcavities as side chains to the coupled cavity waveguide could also allow for the storage of light [50]. Due to the many potential applications, knowledge of the detailed characteristics of the electromagnetic eigenmodes for defects in photonic crystals is important. Ref. [43] uses the transfer matrix method developed by Pendry and co workers to study the same ideal system as was considered in this study by calculating the transmission spectra of the photonic crystals with vacancies, and found transparency bands, which are attributed to the formation of photonic minibands of allowed states derived from

defect states within the former photonic band gap of the ideal structure. In contrast our calculations concentrate on the bandstructure of the photonic minibands, and the electromagnetic field profiles of the vacancies using a plane wave method based on supercells.

4.1 Disorder in 1D photonic crystals

To study the effects of disorder on 1D photonic crystals, we consider as an ideal structure a Bragg reflector with a unit cell consisting of a pair of layers of refractive indices $n_1 = n_0 + g$ and $n_2 = n_0 - g$ and layer thicknesses d_1 and d_2. In the ideal structures under study, the thicknesses of the layers, d_1 and d_2, are chosen to be equal, such that the period of the Bragg reflector is $D = d_1 + d_2 = 2d_1 = 2d_2$.

Using the transfer matrix method, the dispersion relation for the ideal infinite Bragg reflector can be written in terms of the trace of the transfer matrix across one period of the structure as

$$\cos KD = \frac{1}{2}\left(T_{11}(\omega) + T_{22}(\omega)\right) \tag{4.1}$$

where K is the Bloch wavevector, and D is the period of the Bragg reflector. The optical period of the Bragg reflector is $D_0 = n_1 d_1 + n_2 d_2 = \langle n \rangle D$ where $\langle n \rangle$ is the mean refractive index. For the Bragg reflector under study, where $d_1 = d_2 = D/2$, then $\langle n \rangle = n_0$ and the dispersion relation is of the form

$$\cos KD = \cos\left(\frac{n_1 D\omega}{2c}\right)\cos\left(\frac{n_2 D\omega}{2c}\right) - \frac{1}{2}\left(\frac{n_1}{n_2} + \frac{n_2}{n_1}\right)\sin\left(\frac{n_1 D\omega}{2c}\right)\sin\left(\frac{n_2 D\omega}{2c}\right) \tag{4.2}$$

This can be rewritten as

$$\cos KD = \frac{(n_1 + n_2)^2}{4n_1 n_2}\cos\left(\frac{\omega D}{2c}(n_1 + n_2)\right) - \frac{(n_1 - n_2)^2}{4n_1 n_2}\cos\left(\frac{\omega D}{2c}(n_1 - n_2)\right) \tag{4.3}$$

or, inserting the refractive indices in terms of n_0 and g

$$\cos KD = \frac{n_0^2}{n_0^2 - g^2}\cos\left(\frac{\omega n_0 D}{c}\right) - \frac{g^2}{n_0^2 - g^2}\cos\left(\frac{\omega g D}{c}\right) \tag{4.4}$$

or

$$\cos KD = 1 - \frac{2n_0^2}{n_0^2 - g^2}\sin^2\left(\frac{\omega n_0 D}{2c}\right) + \frac{2g^2}{n_0^2 - g^2}\sin^2\left(\frac{\omega g D}{2c}\right) \tag{4.5}$$

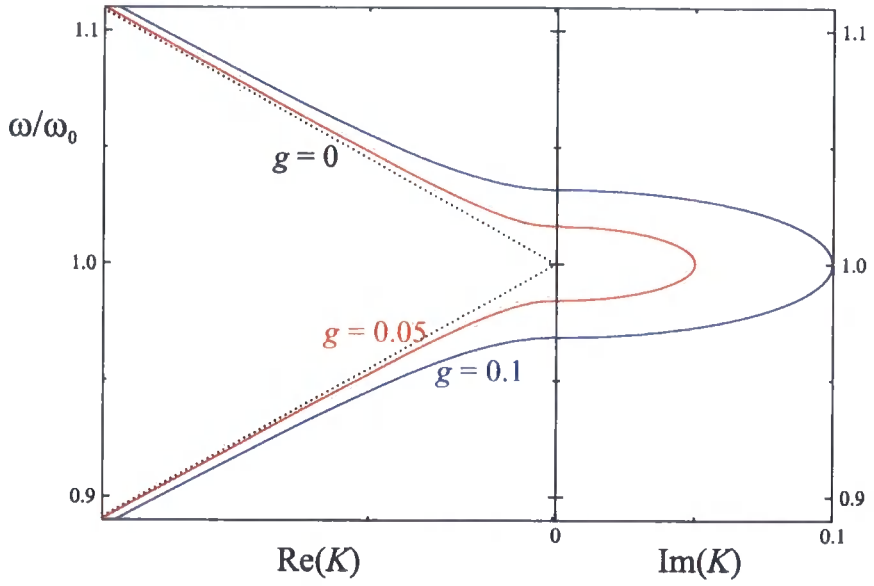

Figure 4.1 Dispersion relations for infinite 1D photonic crystals of mean refractive index $n_0 = 2.0$ and modulation of the refractive index $g = 0$ (dotted line), $g = 0.05$ (red line), and $g = 0.1$ (blue line).

Equation 4.5 can be solved numerically, and the resultant dispersion relation is shown in figure 4.1 for the parameters $n_0 = 2.0$ and $g = 0.05$ and 0.1. Solving equation 4.5, it can be seen that there are photonic band gaps in the mode spectrum of the Bragg reflector one of which is shown in the figure. Furthermore, these PBGs appear for an arbitrarily small modulation g, and only close when $g = 0$. The PBGs occur at the edge of the first Brillouin zone of the crystal, when $K = \pm(2m+1)\pi/D$. Therefore at the edge of the first Brillouin zone, the frequencies of the allowed photonic modes are given by

$$\frac{n_0^2}{n_0^2 - g^2}\sin^2\left(\frac{\omega n_0 D}{2c}\right) - \frac{g^2}{n_0^2 - g^2}\sin^2\left(\frac{\omega g D}{2c}\right) = 1 \tag{4.6}$$

If only small modulations of the refractive index are considered, such that $g \ll n_0$, the second term on the left hand side of equation 4.6 can be neglected. This is equivalent to assuming that all the layers have an almost equal optical thickness, $n_1 d_1 \approx n_2 d_2$. Thus taking the square root of equation 4.6 and rearranging

$$\sin\left(\frac{\omega n_0 D}{2c}\right) \approx \pm\left(\frac{n_0^2 - g^2}{n_0^2}\right)^{1/2} = \pm\left(1 - \frac{g^2}{n_0^2}\right)^{1/2} \approx \pm\left(1 - \frac{g^2}{2n_0^2}\right) \tag{4.7}$$

Therefore, at the edge of the first Brillouin zone, the frequencies of the allowed modes are

$$\omega_1 = \frac{2c}{n_0 D} \arcsin\left(1 - \frac{g^2}{2n_0^2}\right) \tag{4.8}$$

and

$$\omega_2 = \frac{2\pi c}{n_0 D} - \frac{2c}{n_0 D} \arcsin\left(1 - \frac{g^2}{2n_0^2}\right) \tag{4.9}$$

The centre of the PBG is $\omega_0 = (\omega_1 + \omega_2)/2$,

$$\omega_0 = \frac{\pi c}{n_0 D} \tag{4.10}$$

The width of the band gap is given by the difference $\Delta\omega = \omega_2 - \omega_1$:

$$\Delta\omega = \frac{2\pi c}{n_0 D} - \frac{4c}{n_0 D} \arcsin\left(1 - \frac{g^2}{2n_0^2}\right) \tag{4.11}$$

The width of the PBG for a small refractive index modulation g is given by

$$\Delta\omega \approx \frac{4gc}{n_0^2 D} \tag{4.12}$$

and the relative width is

$$\frac{\Delta\omega}{\omega_0} \approx \frac{4g}{\pi n_0} \tag{4.13}$$

Another important quantity to consider is the attenuation of the electromagnetic fields at the centre of the photonic band gap. This is found from the imaginary part of the Bloch wavevector when $\omega = \omega_0$. Let K_0 be the Bloch wavevector when $\omega = \omega_0$. Then, from equation 4.5

$$\cos K_0 D = \frac{e^{iK_0 D} + e^{-iK_0 D}}{2} = \frac{-n_0^2 - g^2}{n_0^2 - g^2} + \frac{4g^2}{n_0^2 - g^2} \sin^2\left(\frac{\pi g}{2n_0}\right) \tag{4.14}$$

When $g \ll n_0$, the second term on the right-hand-side of equation 4.14 can be neglected, and rearranging gives

$$e^{2iK_0 D} + \frac{2\left(n_0^2 + g^2\right)}{n_0^2 - g^2} e^{iK_0 D} + 1 = 0 \tag{4.15}$$

which has solutions

$$e^{iK_0D} = -\left(\frac{n_0 \pm g}{n_0 \mp g}\right) \tag{4.16}$$

Therefore

$$K_0D = (2m+1)\pi - i\ln\frac{n_0 \pm g}{n_0 \mp g} \tag{4.17}$$

and the attenuation of the electromagnetic fields per period of the Bragg reflector at the centre of the band gap is

$$\mathrm{Im}\,(K_0D) = \pm\ln\frac{n_0 \pm g}{n_0 \mp g} \tag{4.18}$$

Now for $x \ll 1$, $\ln(1+x)/(1-x) \approx -2x$, so the attenuation length per period for small g is

$$\mathrm{Im}\,(K_0D) = \frac{D}{2\xi_0} \approx \frac{2g}{n_0} \tag{4.19}$$

where ξ_0 is the attenuation length of the ideal photonic crystal at the centre of the photonic band gap.

When a finite length, L, of the Bragg reflector is considered, the transmission spectrum and mode spectrum of the Bragg reflector can be calculated using the transfer matrix methods for layered dielectric structures outlined in section 2.1. By applying outgoing wave boundary conditions, the frequencies and lifetimes, as well as the electromagnetic field profiles, of the modes can be calculated directly. The ideal structure of finite length has a discrete eigenmode spectrum. The states closest to the edge of the PBG of the infinite structure are referred to as edge-states. As the length of the structure is increased, the edge-states move closer to the edge of the PBG, and coincide with it in the limit $L \to \infty$. Figure 4.2 shows the eigenmode spectrum and lifetimes (a) and the electromagnetic energy density profile U (b) for the first three edgestates above and below the PBG for a Bragg reflector of length $L = 200D$, with average refractive index $n_0 = 2.0$ and modulation of the refractive index $g = 0.025$. Figure 4.2 (c) shows the resultant transmission spectrum. It can be seen that a dip in the transmission occurs for the frequencies in the PBG.

4.1.1 Models of disorder

Three models of disorder have been considered. The first is a random variation of the refractive index of the layers in a period of the finite Bragg reflector, such that the refractive

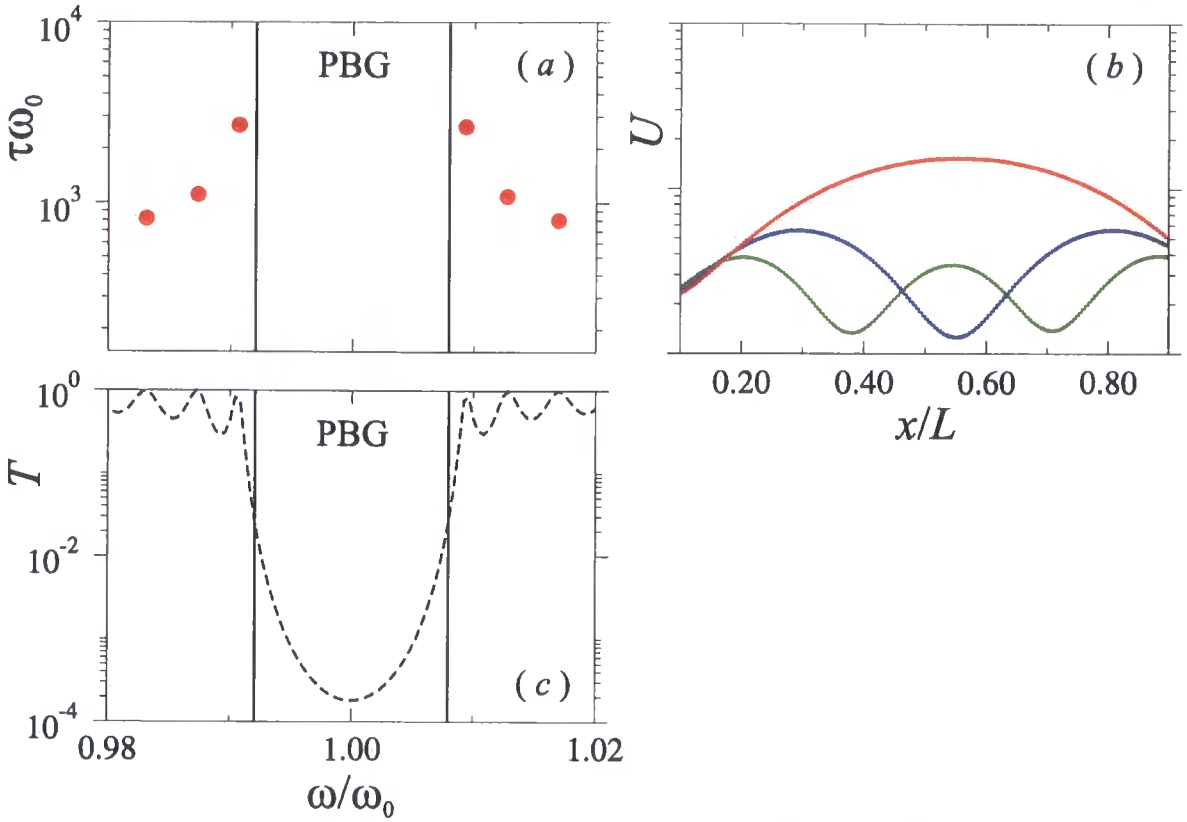

Figure 4.2 (a) Frequencies and lifetimes of the edge-states for an ideal Bragg reflector with the parameters $L = 200D$, $n_0 = 2.0$, and $g = 0.025$. Vertical lines indicate the edge of the PBG for an infinite system. (b) Electromagnetic energy density profile of the states in (a). (c) Transmission spectrum through the structure.

index of the $(2i-1)^{th}$ and $2i^{th}$ layers are

$$n_{2i-1} = n_0 + g + \delta n_0 P_i \tag{4.20}$$

$$n_{2i} = n_0 - g + \delta n_0 P_i \tag{4.21}$$

where P_i is a random number uniformly distributed in the interval $[-1/2, +1/2]$, and δ is a parameter that determines the maximum shift of the refractive index of a layer away from its ideal counterpart. Hence the parameter δ is a measure of the "amount of disorder" present in the structure. The optical thickness of a period in the disordered Bragg reflector is given by

$$D_i = n_{2i-1} d_{2i-1} + n_{2i} d_{2i} = D_0 \left(1 + \delta P_i\right) \tag{4.22}$$

where D_0 is the optical period of the ideal Bragg reflector. Thus the probability distribution of the optical thicknesses of the periods of the disordered Bragg reflector $P\left(D_i\right)$ are

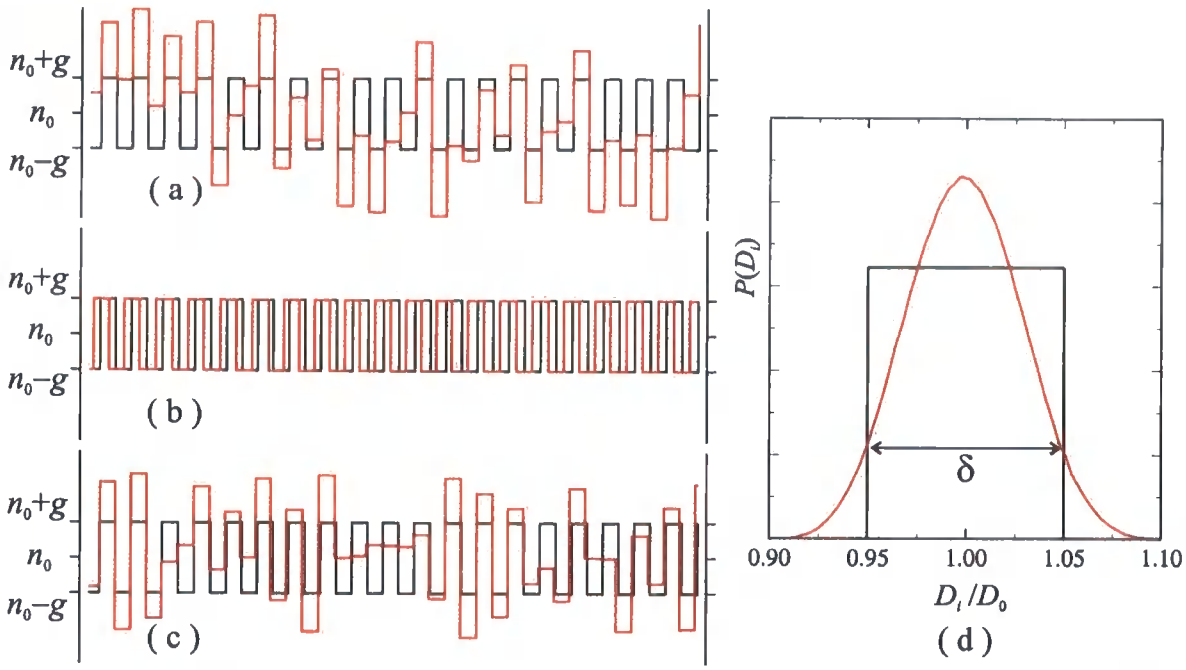

Figure 4.3 An illustration of the resultant refractive index profile of a disordered Bragg reflector (red lines) for the refractive index disorder (a), layer thickness disorder (b) and independent refractive index and layer thickness disorder (c) have been applied. Black lines show the profile for an ideal structure. (d) Probability distributions of the optical thicknesses of the periods in a disordered Bragg reflector. Black line is for the model of disorder in (a) and (b) and red line for (c).

uniformly distributed about D_0 with a width δD_0, as shown in figure 4.3 (d). A typical refractive index profile of a disordered photonic crystal with this refractive index disorder is also shown, in comparison to the ideal refractive index profile, in figure 4.3 (a).

The second type of disorder is a random variation of the layer thickness in a period. The disorder is defined by

$$d_{2i-1} = D\left(1 + \delta P_i\right)/2 \tag{4.23}$$

$$d_{2i} = D\left(1 + \delta P_i\right)/2 \tag{4.24}$$

where P_i is as before. A typical resultant refractive index profile is illustrated in figure 4.3 (b). The probability distribution $P\left(D_i\right)$ is identical to the case of refractive index disorder.

In the third model of disorder the four parameters that determine the optical thickness of a period of the Bragg reflector—n_1, d_1, n_2, and d_2—are allowed to randomly vary indepen-

dently of each other, such that

$$n_{2i-1} = n_0 + g + \delta^{(1)} n_0 P_{2i-1}^{(1)} \tag{4.25}$$

$$n_{2i} = n_0 - g + \delta^{(2)} n_0 P_{2i}^{(1)} \tag{4.26}$$

$$d_{2i-1} = D\left(1 + \delta^{(3)} P_{2i-1}^{(2)}\right)/2 \tag{4.27}$$

$$d_{2i} = D\left(1 + \delta^{(4)} P_{2i}^{(2)}\right)/2 \tag{4.28}$$

where $P_i^{(1,2)}$ are uniformly distributed in the interval $[-1/2, +1/2]$ and $\delta^{(1,2,3,4)}$ are the disorder parameters. In principle, these four disorder parameters could all take different values, but, for simplicity, they have been considered equal in the modelling undertaken. A typical refractive index profile of the resultant Bragg reflector is shown in figure 4.3 (c), and the probability distribution of D_i is shown by the red line in figure 4.3 (d). The probability distribution is very close to a normal distribution, but the maximum deviation of the optical thickness of a period away from D_0 is δD_0. Thus there is a small, but significant, probability for an optical period to have an optical length that is further from the mean than for the other two models of disorder for equivalent values of the disorder parameter δ. It will be shown that this has important consequences when considering the effect of disorder on the system. In the remainder of this chapter, this model of disorder will be referred to as "Gaussian disorder".

4.1.2 Statistics of the eigenmodes of disordered 1D photonic crystals

In order to assess the impact of the disorder on the properties of 1D photonic crystals, the statistics of the disordered photonic crystals were compiled. The eigenfrequencies and lifetimes of 10^4 random structures for the three different models of disorder (see section 4.1.1) and for various combinations of different values of the parameters L, n_0, g and δ. In this way we were able to investigate how the disorder affects photonic crystals with different band gap widths (dependent on g) and to see whether the total length of the structure was significant.

Figure 4.4 shows the frequencies and lifetimes of the eigenmodes of 500 random structures for each kind of disorder. The parameters used in the calculation were $L = 200D$, $n_0 = 2.0$, $g = 0.025$ and $\delta = 0.035$, 0.07, 0.1 and 0.15. Red dots show the frequencies and lifetimes of the ideal ($\delta = 0$) structure, green dots those for the refractive index disorder

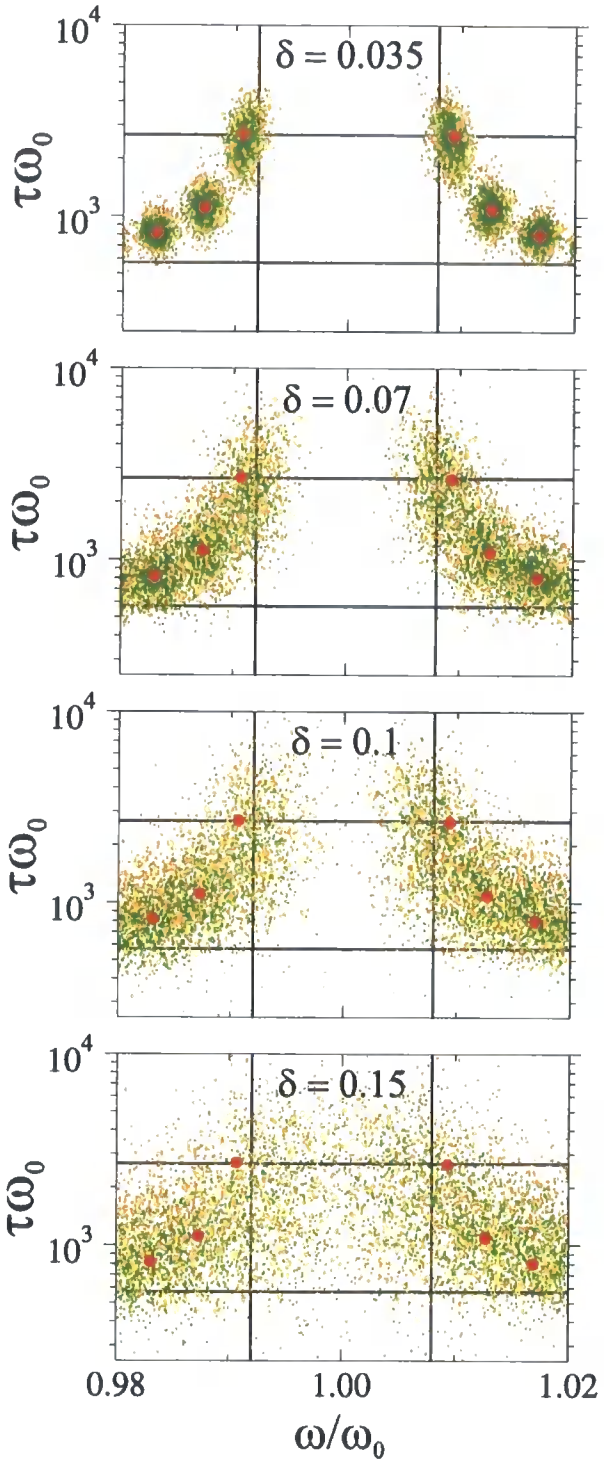

Figure 4.4 Frequencies Re (ω_i) and lifetimes $\tau = 1/\text{Im}\,(\omega_i)$ for the eigenstates of an ideal structure (red dots) and 500 randomly disordered structures using the refractive index (green dots), layer thickness (yellow dots) and Gaussian (orange dots) models of disorder for a Bragg reflector with $L = 200D$, $n_0 = 2.0$, $g = 0.025$, and values of δ as indicated. Vertical lines show the frequencies of the edges of the PBG. The upper horizontal line shows the lifetime of the edge-states in the ideal ($\delta = 0$) structure. The lower horizontal line shows the lifetime of the Fabry-Perot modes in a uniform structure with refractive index n_0 ($g = 0$).

model, yellow dots for layer thickness disorder, and orange dots for Gaussian disorder. Vertical black lines show the position of the edge of the photonic band gap for the ideal, infinite Bragg reflector. The lower horizontal line shows the lifetime of the states of a structure for which $g = 0$. These are the Fabry-Perot modes of a uniform structure of refractive index n_0 and thickness $L = 200D$, surrounded by air ($n_f = 1.0$). Hence the complex eigenfrequencies of these Fabry-Perot modes are

$$\omega = \frac{m\pi c}{n_0 L} - i\frac{c}{n_0 L}\ln\left(\frac{n_0 + n_f}{n_0 - n_f}\right) \tag{4.29}$$

for integer m, and their lifetimes are $\tau\omega_0 = \omega_0/\mathrm{Im}\,(\omega) = 572$. It can be seen that the periodic modulation of refractive index leads to an increase of the lifetime of the eigenmodes, which is more pronounced for states closer to the edge of the photonic band gap. The upper horizontal lines ($\tau\omega_0 = 2650$) show the lifetime of the edge-states closest to the photonic band gap.

When the disorder parameter is small ($\delta = 0.035$), the edge-states of the structure are perturbed in the complex frequency plane, but each state is close its ideal counterpart in both frequency and lifetime and can still be identified with an edge-state in the ideal structure. Some of these shifted edge-states penetrate a little into the PBG of the infinite ideal structure, and the density of states (figure 4.5) has a tail in the band gap.

When δ is increased to 0.07, figure 4.4 and figure 4.5 show that states now penetrate further into the photonic band gap, but that the probability of a state appearing in the centre of the band gap is negligible.

Further increase of the disorder parameter to $\delta = 0.1$ or 0.15 leads to the substantial probability of states appearing throughout the photonic band gap. These states can no longer be associated with a particular edge-state in the ideal structure.

Figure 4.5 shows the density of states for the 10^4 calculated eigenstates for the same structure as the eigenstates in figure 4.4. Strictly speaking, the density of states are histograms, but the bin widths are sufficiently small (much smaller than the separation between modes) that they approximate to density of states curves. Green dots show the density of states for the refractive index model of disorder, yellow dots for the layer thickness model, and orange dots for the Gaussian model.

The density of states for refractive index-type disorder and layer thickness-type disorder are identical for all values of the parameters considered (as expected, due to the identical

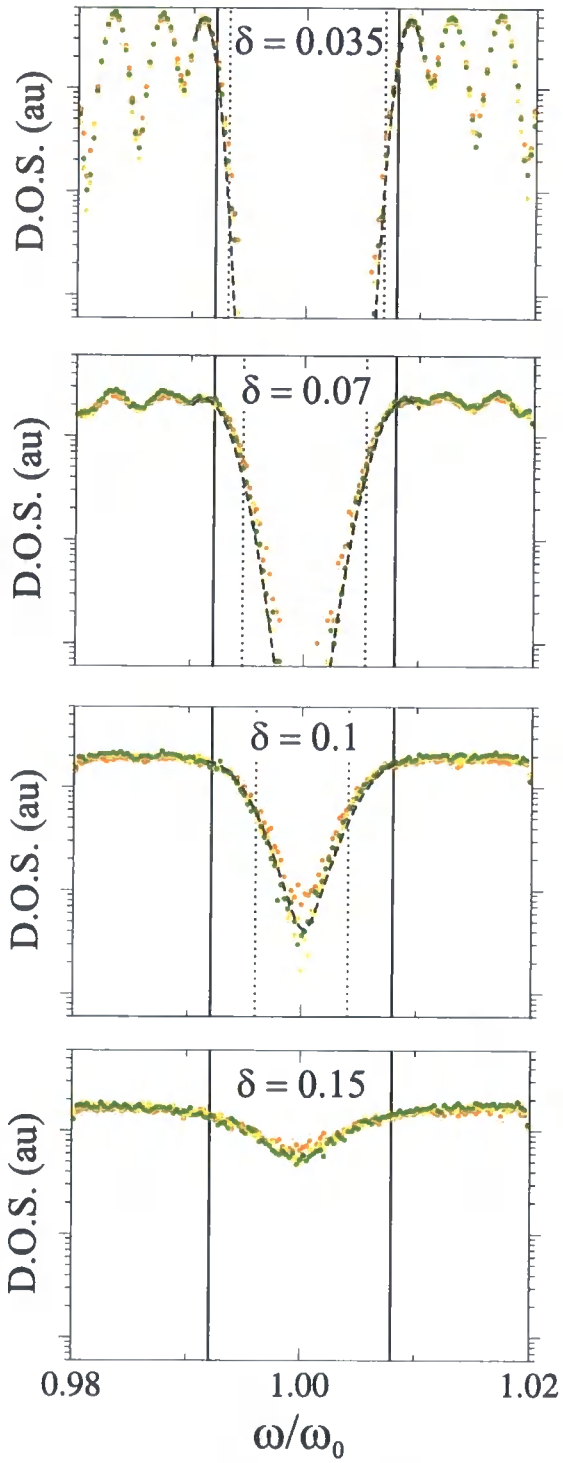

Figure 4.5 Density of states averaged over an ensemble of 10^4 randomly disordered structures using the refractive index (green dots), layer thickness (yellow dots) and Gaussian (orange dots) models of disorder for a Bragg reflector with $L = 200D$, $n_0 = 2.0$, $g = 0.025$, and values of δ as indicated. Vertical solid lines show the edges of the PBG of the infinite 1D photonic crystal. Dashed curves show the fit to the density of states within the PBG using equation 4.30, and the vertical dotted lines indicate the value of Ω used in each case.

probability distribution of the optical period of the disordered Bragg reflectors), and to a very high accuracy can be described by the formula

$$\rho \sim \exp\left(-\frac{(\omega-\omega_e)^2}{\Omega^2}\right) \tag{4.30}$$

where ω_e is the angular frequency of the relevant edge-state and Ω is a constant.

The parameter Ω is found to be proportional to the disorder parameter δ, but does not depend on the length of the structure (as is to be expected, since the density of states is a self-averaging quantity). The dashed curves in figure 4.5 show the fit of the density of the states using equation 4.30, and the vertical dotted lines indicate the value of Ω used.

When $\Omega \ll \Delta\omega/2$, the probability of finding disorder-induced states in the centre of the band gap is negligible. However when $\Omega \sim \Delta\omega/2$, the probability of finding disorder-induced states throughout the band gap becomes substantial.

As can be seen in figure 4.5, the density of states for the Gaussian model of disorder (orange dots) penetrate further into the photonic band gap than those of the other models of disorder. This is due to the differing probability distributions of the optical periods of the disordered Bragg reflectors (see figure 4.3 (d)). The independent layer refractive index and thickness disorder gives a near Gaussian probability distribution for D_i. Thus, the tail of this Gaussian means that there is a significant probability for individual periods in the disordered Bragg reflector to have optical periods outside the interval for which it is possible for the other types of disorder. The periods of the disordered Bragg reflector with these large deviations of the optical thickness can introduce states deeper into the band gap, and hence raise the penetration depth. However, because the Gaussian $P(D_i)$ has a similar width to the square $P(D_i)$ for the refractive index and layer thickness-type disorder, the qualitative changes in the statistics of the eigenmodes and density of states are similar, and are, to a very large degree, also quantitatively similar.

It is interesting to consider whether there is an upper limit for the lifetime of the modes in a disordered photonic crystal. For an isolated defect layer (microcavity) of thickness D (twice the thickness of the other layers) at the centre of the ideal Bragg reflector, the electromagnetic energy density of the associated eigenmode decays exponentially away from the defect, and has a lifetime of $\tau\omega_0 = 4620$ which is approximately double the lifetime

δ	Type of disorder	Proportion of disordered structures with states with lifetimes greater than	
		edge-state	microcavity
0.035	refractive index	64.2% (0.80%)	0.52% (0.07%)
	layer thickness	75.8% (0.87%)	0.43% (0.07%)
	Gaussian	67.4% (0.82%)	2.21% (0.14%)
0.07	refractive index	66.3% (0.81%)	7.94% (0.28%)
	layer thickness	67.0% (0.82%)	8.31% (0.29%)
	Gaussian	63.0% (0.79%)	16.5% (0.41%)
0.1	refractive index	61.3% (0.78%)	13.2% (0.36%)
	layer thickness	61.2% (0.78%)	13.1% (0.36%)
	Gaussian	61.5% (0.78%)	24.0% (0.49%)
0.15	refractive index	56.3% (0.75%)	13.7% (0.37%)
	layer thickness	60.0% (0.77%)	13.0% (0.36%)
	Gaussian	61.4% (0.78%)	28.8% (0.53%)

Table 4.1 Proportion of disordered structures that possess eigenmodes with at least the lifetimes of the edge-states and microcavity modes in the ideal structure. Figures are based on calculation of the complex eigenfrequencies of 10^4 disordered structures with parameters $L = 200D$, $n_0 = 2.0$, $g = 0.025$. Figures in brackets are the standard error.

of the edge-states. Figure 4.4 shows that very few disordered Bragg reflectors have states with lifetimes comparable with the microcavity mode when the disorder parameter is small ($\delta = 0.035$). However, for larger disorder, a greater proportion of disordered structures introduce states into the mode spectrum with lifetimes greater than the microcavity (defect) mode in the ideal structure. Table 4.1 shows the proportion of structures that possess modes of at least the lifetime of the edge-state ($\tau\omega_0 = 2650$) and microcavity ($\tau\omega_0 = 4620$).

As can be seen, the refractive index disorder and layer thickness disorder produce structures that support long-lived eigenmodes at the same rate as each other (to within statistical error). However, the Gaussian disorder model is able to produce structures that support long-lived eigenmodes at a higher rate than the other types of disorder for equivalent values of δ. This can again be attributed to the greater deviation of optical thickness of a small proportion of the periods in the structures with Gaussian disorder. Thus an individual disordered Bragg reflector has a greater probability of having a layer that can act as a "random microcavity" for the Gaussian disorder than for the refractive index or layer thickness disorder.

Figure 4.6 shows calculated electromagnetic energy density profiles for individual eigenstates of particular configurations of refractive index disorder for $n_0 = 2.0$, $L = 200D$, $g = 0.025$ and $\delta = 0.035$, 0.07, 0.1 and 0.15, as indicated. Each figure shows the field pro-

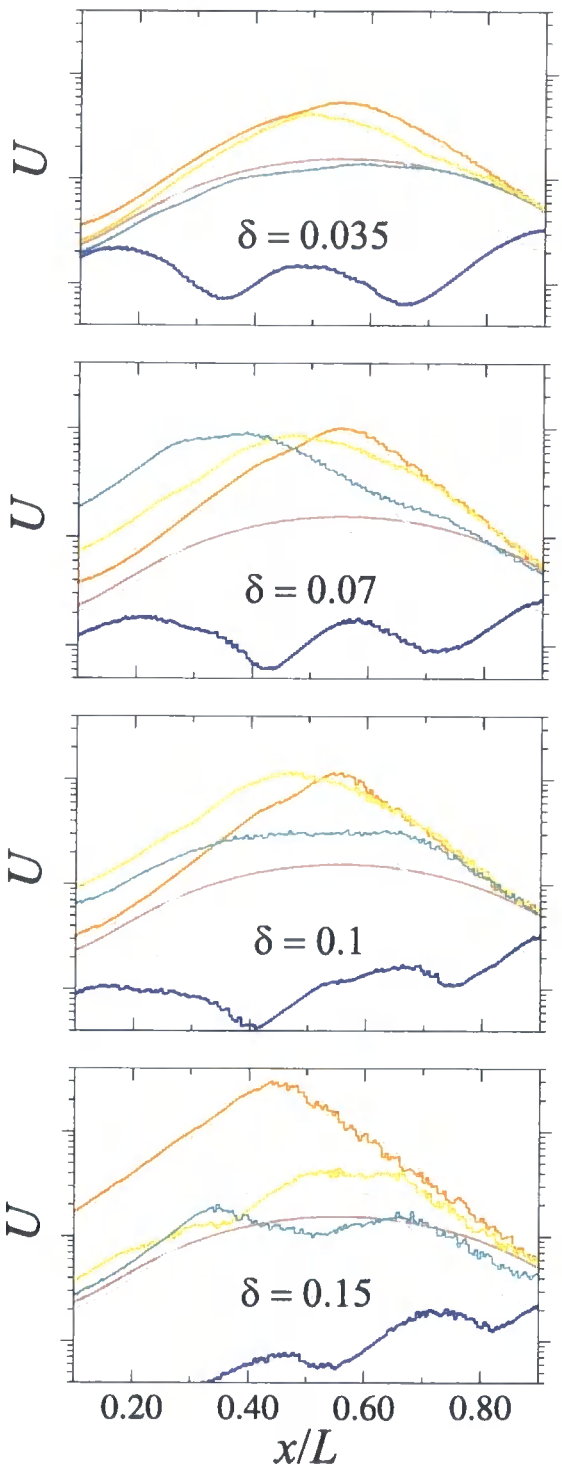

Figure 4.6 Electromagnetic energy density profiles $U(x)$ for eigenstates of individual disordered structures with $L = 200D$, $n_0 = 2.0$, $g = 0.025$ and $\delta = 0.035$, 0.07, 0.1 and 0.15 as indicated. The structures were chosen based on the lifetimes of their eigenstates; the longest-lived (orange), lifetimes similar to the microcavity mode (yellow), lifetimes similar to the edge-states of the ideal structure (green), lifetimes similar to the Fabry-Perot modes of a $g = 0$ structure (blue). Also shown are the profiles of an edge state in the ideal structure (brown) and the microcavity mode (grey).

file of the microcavity mode of an ideal Bragg reflector with an individual half-wave defect layer in the centre of the Bragg reflector (grey curves). The electromagnetic energy density of the microcavity eigenmode decays exponentially with distance away from the defect layer, and can thus be said to be localised upon the defect. Also shown is the field profile of the edge-states in the ideal structure (brown curve). For each value of the disorder parameter δ considered, the orange curve is the field profile of the longest-lived state found in the sample of 10^4 disordered structures, the yellow curve is that of a state with a similar lifetime to the isolated defect (microcavity) mode, the green line is for a state with lifetime similar to the edge-states of the ideal structure (indicated by the higher horizontal line in figure 4.4), and the blue curves are for states with lifetimes similar to the Fabry-Perot modes of a $g = 0$ structure (indicated by the lower horizontal lines in figure 4.4).

For the smallest disorder parameter shown in figure 4.6 ($\delta = 0.035$), the longest-lived state (orange) has approximately the same lifetime as the microcavity mode. The short-lived mode (blue) with lifetime similar to the Fabry-Perot mode of the $g = 0$ structure is similar in profile to the third states away from the edge of the PBG in the ideal structure. These short-lived modes in the disordered structure are thus just perturbed edge-states. Also, the green line shows a perturbed edge-state introduced into the PBG of the ideal structure.

The longer-lived states differ in profile markedly from the edge states of the ideal structure. These states have profiles that decay exponentially away from some localisation site, and are reminiscent of the microcavity mode, and are localised on "random microcavities".

4.1.3 Resilience of the photonic band gap to disorder

By modelling structures with different values of the relative band gap $\Delta\omega/\omega_0$, it was found that the penetration depth parameter, Ω in equation 4.30, is proportional to the square root of the relative band gap width. However, Ω is actually a function of the three independent parameters δ, $\Delta\omega$ and ω_0, and therefore the value of the relative penetration depth Ω/ω_0 should be considered to compare disordered structures of different mean refractive indices (and therefore different ω_0). In figure 4.7, the dimensionless quantity $(\Omega/\delta\omega_0)\sqrt{\omega_0/\Delta\omega}$ is plotted as a function of the average refractive index of the disordered Bragg reflector, which is related to the centre frequency of the band gap by the formula $\omega_0 = \pi c/(n_0 D)$. The plot was made by calculating the ensemble averaged density of states of 10^4 disordered structures

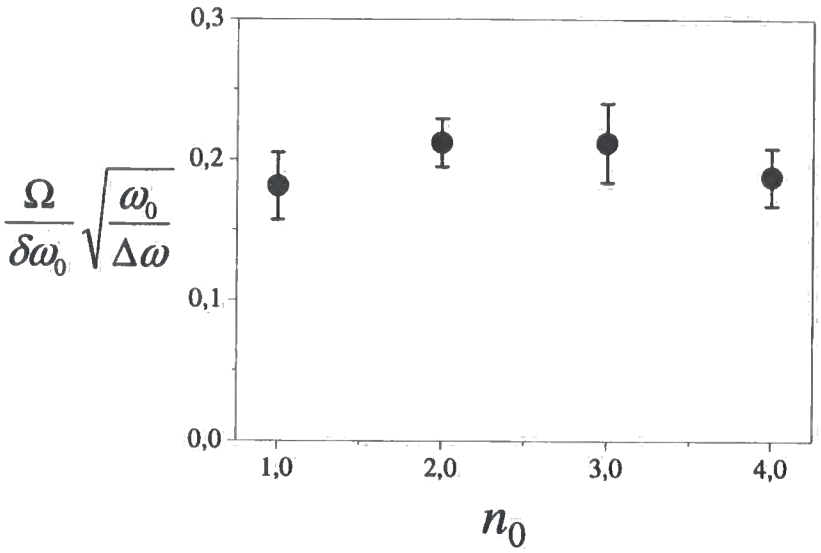

Figure 4.7 The quantity $(\Omega/\delta\omega_0)\sqrt{\omega_0/\Delta\omega}$ for structures of differing mean refractive indices n_0. 10^4 disordered structures were modelled for each set of parameters n_0, g and δ. The vertical bars represent the standard deviation of $(\Omega/\delta\omega_0)\sqrt{\omega_0/\Delta\omega}$ across the sample of structures with different parameters. Structures with g in the range 0.0125 to 0.125 were considered.

of length $L = 400D$ for various combinations of the parameters n_0, g and δ. Structures were modelled with values of $g = 0.0125, 0.025, 0.05, 0.075, 0.1$ and 0.125, which equates to values of the relative width of the PBG, $\Delta\omega/\omega_0$, in the ideal structure in the range $[0.004, 0.16]$. A relative band gap width of 16% corresponds to high refractive index contrast structures of experimental interest. For all values of g, the range of values taken for the disorder parameter δ was chosen to range from structures with small disorder, displaying little penetratrion of the density of states into the PBG, to large disorder with a significant penetration of the density of states. The dots indicate the mean value of $(\Omega/\delta\omega_0)\sqrt{\omega_0/\Delta\omega}$ and the error bars indicate the standard deviation of this quantity across the sample of parameters of the structures considered. The plot of figure 4.7 leads to the conclusion that the relative penetration depth of the density of states is given by the formula

$$\frac{\Omega}{\omega_0} \approx \frac{\delta}{5}\sqrt{\frac{\Delta\omega}{\omega_0}} \tag{4.31}$$

Equation 4.31 provides a way to specify a practical criterion for the resilience of the PBG to the presence of disorder. Given a threshold acceptable level for the suppression of the density of states at the centre of the band gap, S_{th}, where $S_{th} = \rho(\omega_0)/\rho(\omega_e)$ is the ratio of the density of states at the centre and edge of the PBG, the threshold value of the disorder

parameter is given by

$$\delta_{th} = \frac{5}{2\sqrt{-\ln S_{th}}}\sqrt{\frac{\Delta\omega}{\omega_0}} \tag{4.32}$$

For example, the suppression of the density of states by a factor of $S_{th} = 10^{-9}$ (which corresponds to a value of the penetration depth of $\Omega \approx \Delta\omega/9$) gives a threshold disorder parameter of

$$\delta_{th} \approx \sqrt{\frac{1}{3}\frac{\Delta\omega}{\omega_0}} \tag{4.33}$$

Thus a 1D photonic crystal with a level of disorder below this threshold will give the required suppression of the density of states. Note that the function $\sqrt{-\ln S_{th}}$ in equation 4.32 varies very slowly with the chosen value for the threshold suppression factor S_{th}, so the estimate in equation 4.33 can be considered as an approximate threshold value for a wide range of suppression factors.

Figure 4.8 shows how the edge of the PBG varies with the disorder parameter δ for a range of values of the modulation of the refractive index g. Values are based upon the calculation of 10^4 random disordered structures of length $L = 400D$, and the curves are for the values $g = 0.0125$ (green), $g = 0.025$ (purple), $g = 0.05$ (cyan), $g = 0.075$ (blue), $g = 0.1$ (green) and $g = 0.125$ (red). The calculations used a value of $L = 400D$, as the longer length of the structure allows for smaller values of g to be investigated. This is because the attenuation per period is proportional to g, but independent of the length of the structure L, and for a PBG to be established, the electromagnetic fields should be strongly attenuated through the structure. However, the positions of the edges of the band gap do not depend upon the value of L, as the density of states is a self-averaging quantity. This has been checked by calculating similar results for $L = 200D$, which give essentially identical curves (to within statistical error) to those shown in figure 4.8.

For all values of g, the PBG narrows as the disorder parameter δ is increased due to states being introduced further into the photonic band gap. The values in figure 4.8 assume that the edge of the PBG is encountered when some threshold value for the density of states is reached. In practice the density of states was calculated for an ensemble of 10^4 randomly disordered structures for each set of parameters, and the edges of the PBG was taken to be the frequencies at which the averaged density of states dropped to zero.

An approximate value for the threshold disorder parameter δ_{th} is given by the value of

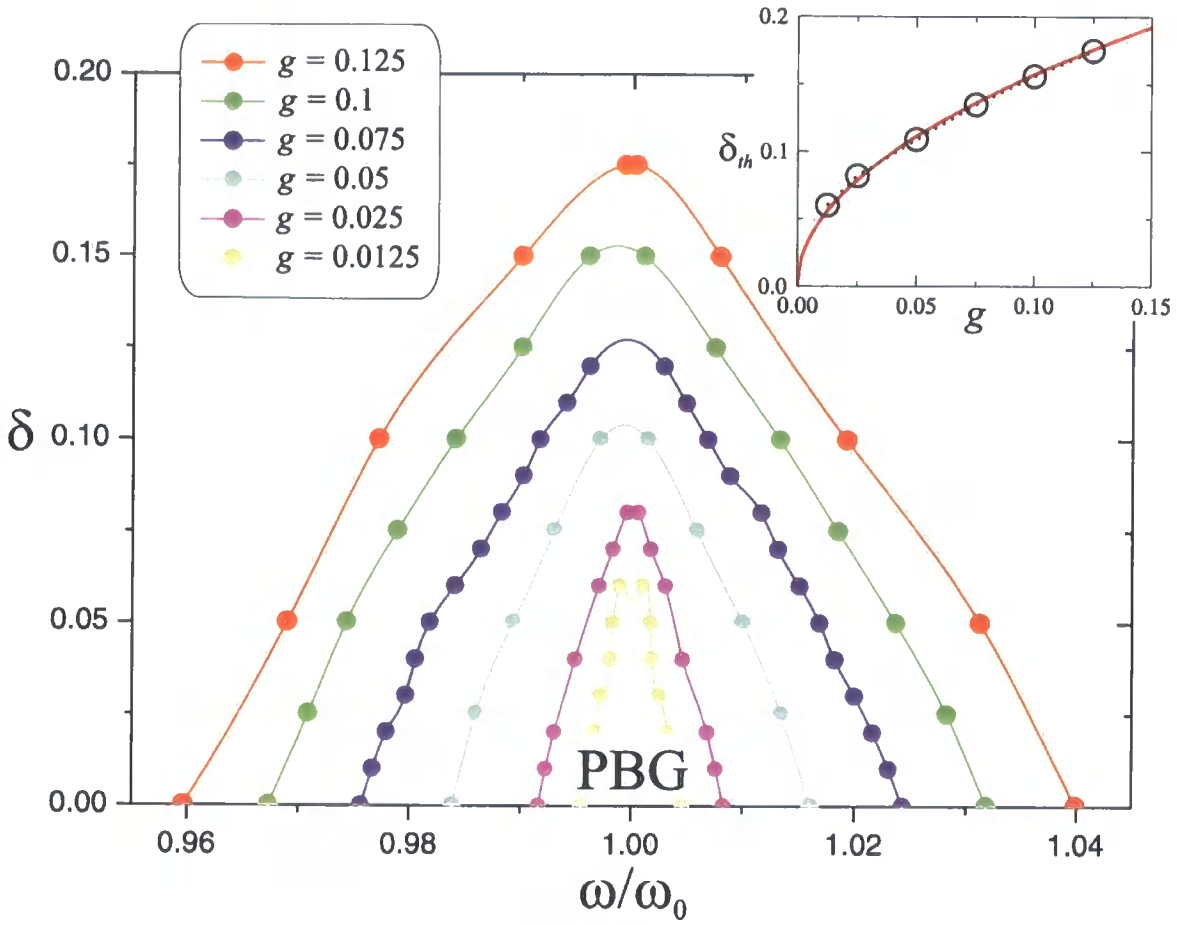

Figure 4.8 Boundary of the PBG as a function of the disorder parameter δ for structures with $n_0 = 2.0$ and different values of the modulation of the refractive index g, as shown. All cases used the "refractive index" model of disorder discussed in the text. (Inset) The threshold value of the disorder parameter as a function of g, as estimated from the tops of the curves of the main figure. The red line shows the fit $\delta_{th} = \sqrt{0.37\Delta\omega/\omega_0}$.

δ at the top of each curve, when the PBG closes completely. The inset to figure 4.8 shows the values of δ_{th}, as estimated from the curves of figure 4.8, plotted against the value of g, which is proportional to the relative width of the PBG. The circles and dotted curve show the calculated values, and the red curve shows the relationship $\delta_{th} = \sqrt{0.37\Delta\omega/\omega_0}$, which is in good agreement with the estimate given in equation 4.33.

4.1.4 Transmission through disordered Bragg reflectors

Thus far, this section has been concerned with the discrete mode spectrum of disordered 1D photonic crystals, and how disorder introduces states into the photonic band gap of the ideal structure. An understanding of this process is important when considering threshold tolerances for disorder in actual photonic crystal devices which rely on the PBG for their op-

eration. However, the properties of photonic crystals are usually investigated experimentally via their transport properties, and so this section looks at the link between the modifications disorder produces in the underlying mode spectrum of the disordered photonic crystals and the modification in the transmission of light through the photonic crystal.

Figure 4.9 shows the transmission spectrum averaged over 10^4 random structures with refractive index disorder (thick red lines). The parameters of the structures are $n_0 = 2.0$, $L = 200D$, $g = 0.025$ and $\delta = 0.035$, 0.07, 0.1 and 0.15, as indicated. For comparison, each figure shows the transmission spectrum of the ideal ($\delta = 0$, dashed curves) structure and for the microcavity mode of the isolated half-wave defect (grey curves). Also shown are the transmission spectra for one random structure, chosen because the structure supports a particularly long-lived "random microcavity" mode (orange lines). The arrows indicate the frequencies of these modes, whose electromagnetic energy density profiles are shown in figure 4.6 by orange curves. The defect (microcavity) mode introduces a Lorentzian spike on the transmission dip of the of the ideal Bragg reflector at the frequency of the defect mode, and a width equal to the reciprocal lifetime of the mode. At the frequency of the mode, the transmission through the structure rises to unity, regardless of the total length of the structure, and despite this frequency being at the centre of the band gap. It can be seen that states shifted or induced into the band gap by the disorder introduce similar spikes on the transmission dip of the ideal Bragg reflector. These spikes raise the ensemble averaged transmission in the parts of the band gap where they occur.

For small values of the disorder parameter δ, the penetration depth of the density of states is small compared to the band gap width, and states only appear at the edge of the band gap. Thus the ensemble-averaged transmission coefficient is similar to the transmission for the ideal structure, apart from the narrowing of the PBG. Although states only appear in the edge of the band gap, the averaged transmission at the centre of the band gap is raised above the level of the ideal structure. This effect is small, as only the tails of the Lorentzian spikes that states in the edge of the band gap introduce onto the transmission dip can effect the transmission at the centre of the band gap. When δ is increased to 0.07, the PBG is narrowed further, as states are introduced deeper into the PBG.

Figure 4.10 shows the ensemble-averaged transmission (solid lines) and the standard deviation of the transmission (dashed lines) at the centre of the PBG for 10^6 disordered

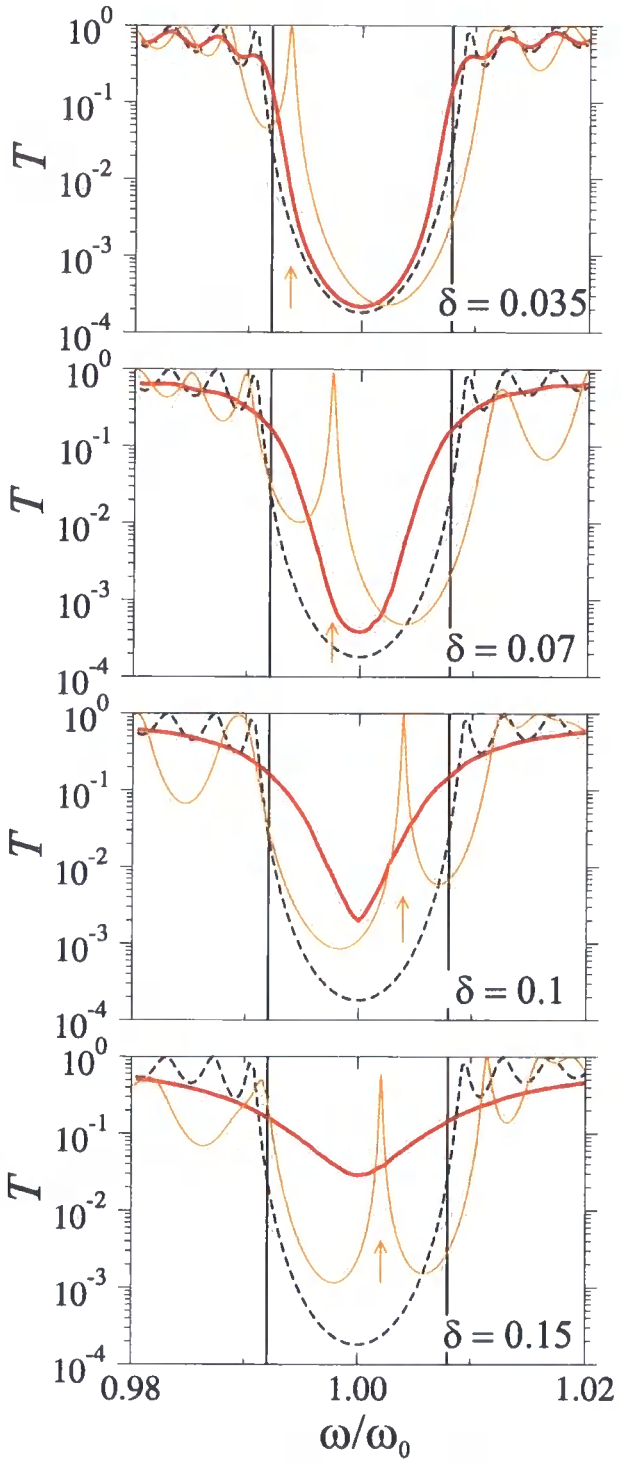

Figure 4.9 Transmission spectra for a single structure (orange curves) and an ensemble of 10^4 randomly disordered structures (thick red curves) with parameters $n_0 = 2.0$, $L = 200D$, $g = 0.025$ and $\delta = 0.035$, 0.07, 0.1 and 0.15. Vertical lines indicate the edges of the PBG for $\delta = 0$. Arrows indicate the frequencies for which the profiles of the electromagnetic energy density are plotted in figure 4.6.

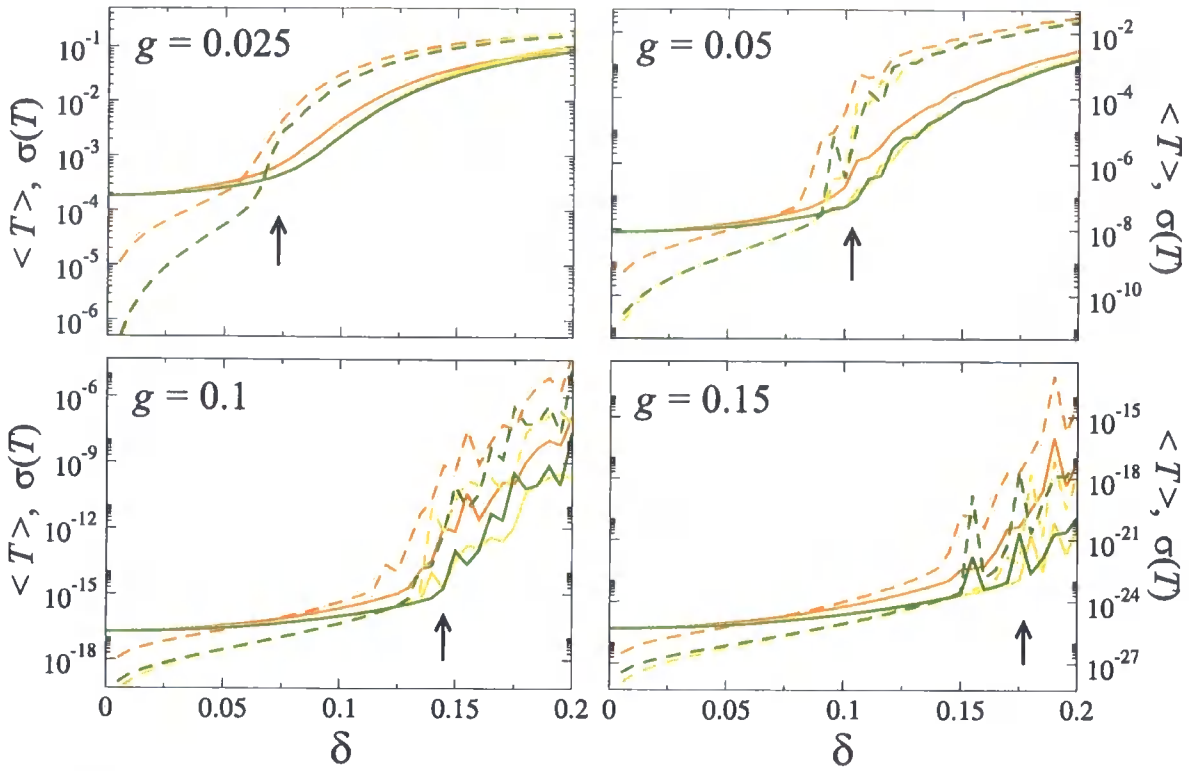

Figure 4.10 Mean (solid lines) and standard deviation (dashed lines) of the transmission coefficient of 10^6 randomly disordered structures at the centre of the band gap as a function of δ for modulations of the refractive index $g = 0.025$, 0.05, 0.1 and 0.15, as indicated. Green curves are for refractive index disorder, yellow curves for layer thickness disorder, and orange curves are for Gaussian disorder. Arrows indicate threshold values of the disorder parameter as estimated from equation 4.33.

structures, for the three models of disorder considered, as a function of the disorder parameter δ. Green lines show the case of refractive index disorder, yellow lines show layer thickness disorder, and orange lines show Gaussian disorder. The parameters of the structures where $L = 200D$, $n_0 = 2.0$ and $g = 0.025$, 0.05, 0.1, and 0.15 as indicated, and calculations used a sample of 10^6 disordered structures. The arrows indicate the threshold values of the disorder parameter as estimated from equation 4.33. For all the cases considered, the dependences of $\langle T \rangle$ on the disorder parameter δ are characterised by a threshold; when $\delta < \delta_{th}$, the ensemble-averaged transmission at the centre of the band gap grows very slowly with increasing δ. However, when δ reaches δ_{th}, a threshold occurs in the dependence of $\langle T \rangle$ on δ, such that for $\delta > \delta_{th}$, $\langle T \rangle$ grows much faster with increasing δ. Such behaviour is readily explained. The increase of the mean transmission is caused by the transmission resonances of the eigenstates introduced into the PBG by the disorder. When the disorder parameter δ is small, the penetration depth parameter, Ω, of the density of states into the

PBG is small compared to the width of the band gap, and edge-states are only likely to be introduced into the edge of the band gap. Thus the transmission at the centre of the band gap is only affected by the tails of these Lorentzian spikes in the transmission spectrum, and so rises little for small δ. However, the penetration depth parameter Ω is proportional to δ, so as δ is increased, states are introduced deeper into the band gap, until the disorder parameter reaches the threshold value δ_{th}, there is a significant probability of finding states throughout the band gap (not only shifted edge-states, but random microcavity states also). Thus the mean transmission at the band gap centre rises much more rapidly with increasing δ, as the probability of having a transmission resonance at (or near) the centre of the band gap is increased. Note that for any individual structure in the ensemble, when $\delta > \delta_{th}$ the transmission at a certain frequency can be any value from zero to one.

It is also interesting to consider the standard deviation of the transmission coefficient at the centre of the band gap, $\sigma(T)$. When $\sigma(T) \ll \langle T \rangle$ for a particular frequency, the transmission through the disordered photonic crystal is well defined at that frequency, and will not vary much from one random configuration of disorder to the next. However, if $\sigma(T) \sim \langle T \rangle$ the transmission through any particular disordered structure becomes impossible to predict, as it will vary widely from one configuration of disorder to the next. From figure 4.10 it can be seen that $\sigma(T)$ displays a similar threshold behaviour in its dependence on δ to $\langle T \rangle$ at the centre of the band gap. For $\delta < \delta_{th}$, $\sigma(T)$ grows more slowly for increasing δ than for $\delta > \delta_{th}$. Furthermore, for values of δ below the threshold value, $\sigma(T) \ll \langle T \rangle$, but above the threshold value $\sigma(T) \gg \langle T \rangle$. (For very large values of δ, the rate of increase of $\sigma(T)$ with δ slows again, as can be seen for the cases of $g = 0.025$ and $g = 0.05$.) Thus figure 4.10 shows that the estimated values of threshold disorder parameter from equation 4.33 has a physical significance; for $\delta < \delta_{th}$, the transmission through the disordered Bragg reflector is well defined and predictable, and is not likely to significantly differ from the value of the ideal structure, but for $\delta > \delta_{th}$ this is no longer the case. This physical relevance of the threshold disorder parameter also justifies the chosen value of the threshold suppression factor $S_{th} = 10^{-9}$ used to obtain the estimate in equation 4.33.

The dependence of the transmission coefficient averaged over an ensemble of randomly disordered structures on the sample thickness L is shown in figure 4.11. Within the photonic band gap, the ensemble-averaged transmission coefficient $\langle T \rangle$ decays exponentially with

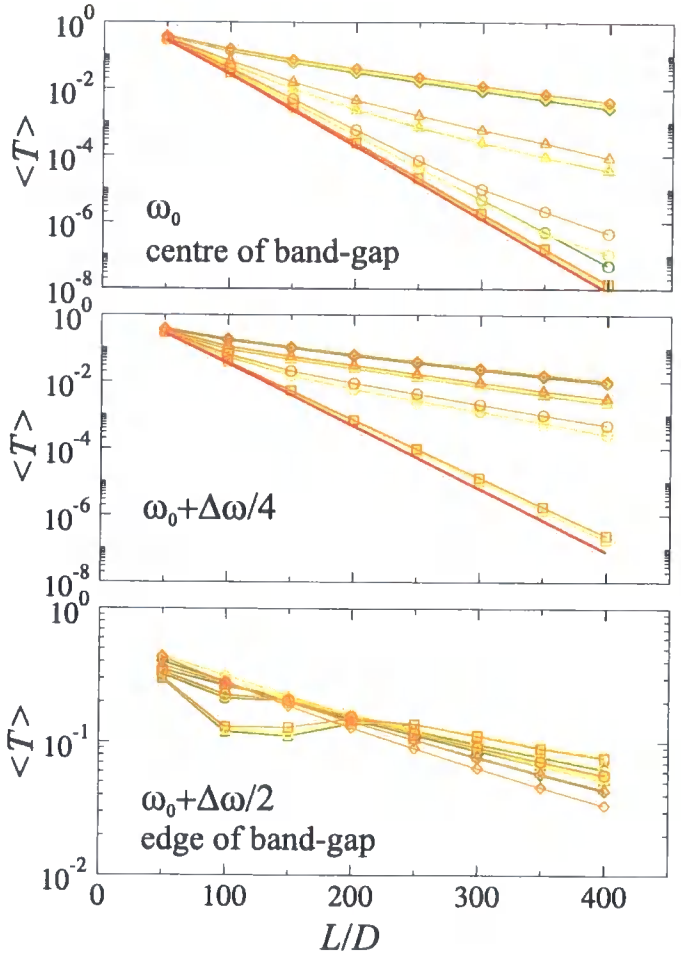

Figure 4.11 The dependence of the transmission coefficient averaged over an ensemble of 10^6 randomly disordered Bragg reflectors as a function of the total length of the structure for three different frequencies as indicated. Four values of the disorder parameter are considered—$\delta = 0.035$ (squares), 0.07 (circles), 0.1 (triangles) and 0.15 (diamonds). The three models of disorder are considered as described in the text—refractive index (green), layer thickness (yellow) and Gaussian (orange) disorder. Red lines are for an ideal structure, and all structures considered have $g = 0.025$ and $n_0 = 2.0$.

increasing sample thickness L. An attenuation length ξ can thus be defined as

$$\langle T \rangle = \exp\left(-L/\xi\right) \tag{4.34}$$

The attenuation length ξ increases with increasing δ at the gap centre. However, at the edge of the photonic band gap, $\langle T \rangle$ demonstrates more complicated behaviour when δ is small; in this case $\langle T \rangle$ is determined by the frequency of an edge state. Nevertheless, when δ is large enough, $\langle T \rangle$ decays exponentially with sample thickness at the edge of the band gap.

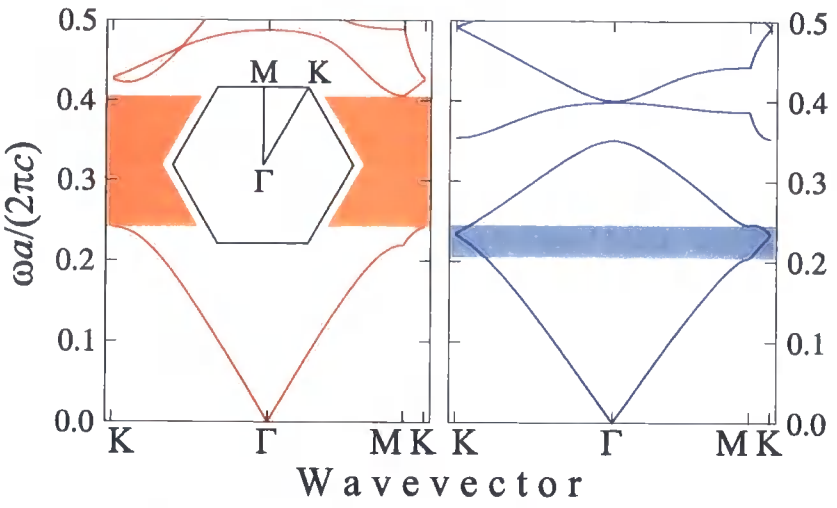

Figure 4.12 TE-polarised (left) and TM-polarised (right) bandstructures for the hexagonal lattice of cylindrical air holes of radius $r = 0.4a$ etched into a GaAs background. The red shaded region indicates the spectral region of a complete 2D photonic band gap for the TE-polarisation, whereas the blue shaded region indicates the spectral region of an incomplete band gap for the TM-polarisation in the Γ-M direction of the crystal's first Brillouin zone. (Inset) The first Brillouin zone of the photonic crystal.

4.2 Disorder in 2D photonic crystals

In this section, disorder in a type of 2D photonic crystal is considered. The ideal photonic crystal consists of a honeycomb-like array of air cylinders etched into a dielectric substrate and arranged on an hexagonal lattice. The dielectric is taken to be the semiconductor GaAs, and to have a relative permittivity of $\varepsilon = 12.96$. The air cylinders are taken to have a radius of $r = 0.4a$, where a is the lattice constant. The calculated bandstructure of the ideal photonic crystal is shown in figure 4.12. The ideal photonic crystal possesses a wide, complete photonic band gap for the TE-polarisation which is centred on $\omega a/(2\pi c) \approx 0.323$ and of width 50% relative to its centre frequency. For the TM polarisation, a PBG exists for the Γ-M direction in reciprocal space centred on $\omega a/(2\pi c) \approx 0.223$ and of width 18% relative to its centre frequency. However, this PBG narrows and eventually closes when the propagation direction is shifted toward the Γ-K direction in reciprocal space. Thus, TE-polarised light in this structure can be used to study the effect of disorder in a photonic crystal with a complete PBG, while TM-polarised light can be used to study the effect of disorder when there is an incomplete band gap.

4.2.1 Microcavities and vacancies in 2D photonic crystals

In this section, the properties of microcavities and defects caused by vacancies in 2D photonic crystals are examined. A microcavity in a 2D photonic crystal can be formed by altering the properties of one cylinder in the lattice of air holes or dielectric rods. Usually the radius of the rod is changed, but the relative permittivity of the rod could also be altered [2]. The modified rod then forms a defect in an otherwise periodic photonic crystal. If the defect has appropriate properties, localised modes with frequencies in the PBG can form at the defect. The frequencies of the modes can be tuned by adjusting the properties of the defect. A vacancy—a missing rod—is a special case of a defect, where the radius of the defect rod is reduced to zero.

Microcavities and vacancies can be studied by the plane wave method presented in section 3.2. However, due to the periodic boundary conditions used in this method, a "supercell" approach must be adopted. A supercell consisting of many rods is chosen as the unit cell of a "superlattice", and one rod is removed from each supercell to form the vacancy. The resultant structure is a superlattice of vacancies with the periodicity of the supercell. In order to study the properties of a single vacancy, the supercell must be made large enough, so that the interactions between neighbouring vacancies in the superlattice can be neglected. The large unit cells used for this kind of supercell approach means that in order to achieve convergence of the eigenfrequencies to a reasonable accuracy, many more plane waves must be used in the calculations.

This section studies the properties of a vacancy in the hexagonal lattice of cylindrical air holes of radius $r = 0.4a$ in a GaAs background. Similar microcavities have been considered previously [2,3,134]. An hexagonal supercell of 35 air holes and 1 vacancy is used, such that the distance between neighbouring vacancies in the superlattice is $L = 6a$. The superlattice has the primitive lattice vectors

$$\mathbf{a}_1 = \frac{L}{2}\hat{\mathbf{j}} + \frac{L\sqrt{3}}{2}\hat{\mathbf{k}}, \quad \mathbf{a}_2 = \frac{L}{2}\hat{\mathbf{j}} - \frac{L\sqrt{3}}{2}\hat{\mathbf{k}} \tag{4.35}$$

and the primitive reciprocal lattice vectors

$$\mathbf{g}_1 = \frac{2\pi}{L}\hat{\mathbf{j}} + \frac{2\pi}{L\sqrt{3}}\hat{\mathbf{k}}, \quad \mathbf{g}_2 = \frac{2\pi}{L}\hat{\mathbf{j}} - \frac{2\pi}{L\sqrt{3}}\hat{\mathbf{k}} \tag{4.36}$$

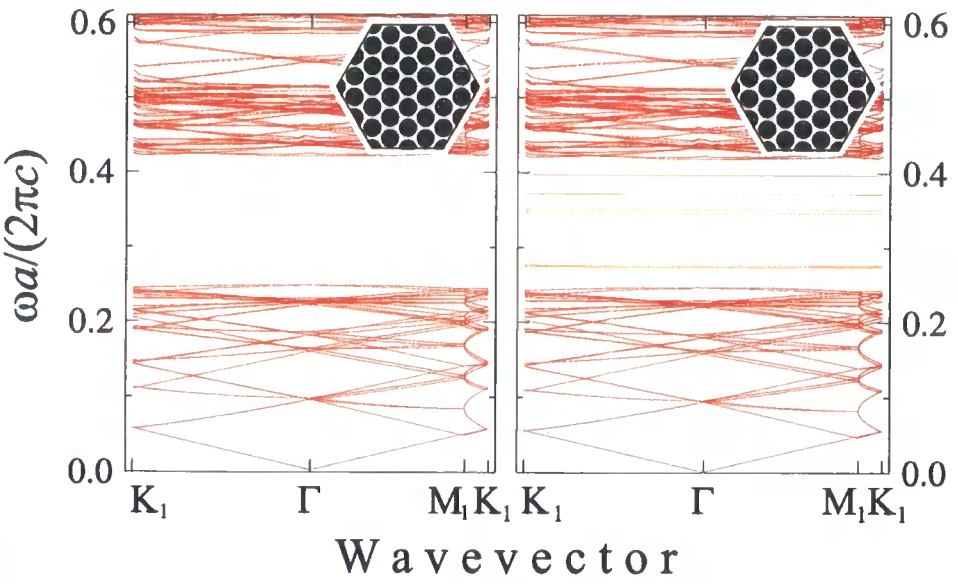

Figure 4.13 TE-polarised bandstructures for photonic superlattices for an ideal hexagonal lattice (left) and an hexagonal lattice containing a vacancy (right). The insets are illustrations of the supercell used for the calculation.

In the plane wave method used, the dielectric structure is described by a Fourier expansion of the supercell based on the reciprocal lattice vectors. The first Brillouin zone of the superlattice is six times smaller than that of the photonic crystal. The bandstructure of the superlattice of vacancies can be calculated (see section 3.2), and this is shown in figure 4.13 for the TE-polarisation. Also shown for comparison is the bandstructure of the ideal photonic crystal calculated using a similar supercell approach.

It can be seen that the introduction of a vacancy into the photonic crystal causes six defect states in the photonic band gap of the ideal photonic crystal. As there is a superlattice of vacancies, neighbouring vacancies can interact, creating photonic minibands of defect states in the photonic band gap. The width of the minibands depend on the spatial overlap between the localised states, and therefore on the separation of the vacancies. Here the minibands are very thin, and to good approximation can be said to be dispersionless. Hence the frequencies of the minibands correspond closely to the frequencies of the eigenmodes of an isolated vacancy. The frequencies and the widths of the minibands of the six defect states are given in table 4.2.

The electromagnetic field profiles of the defect eigenmodes can also be calculated. Figure 4.14 shows the magnetic field profiles at the Γ-point of the superlattice's first Brillouin zone of the six defect states localised on the vacancies in the photonic crystal. As the fre-

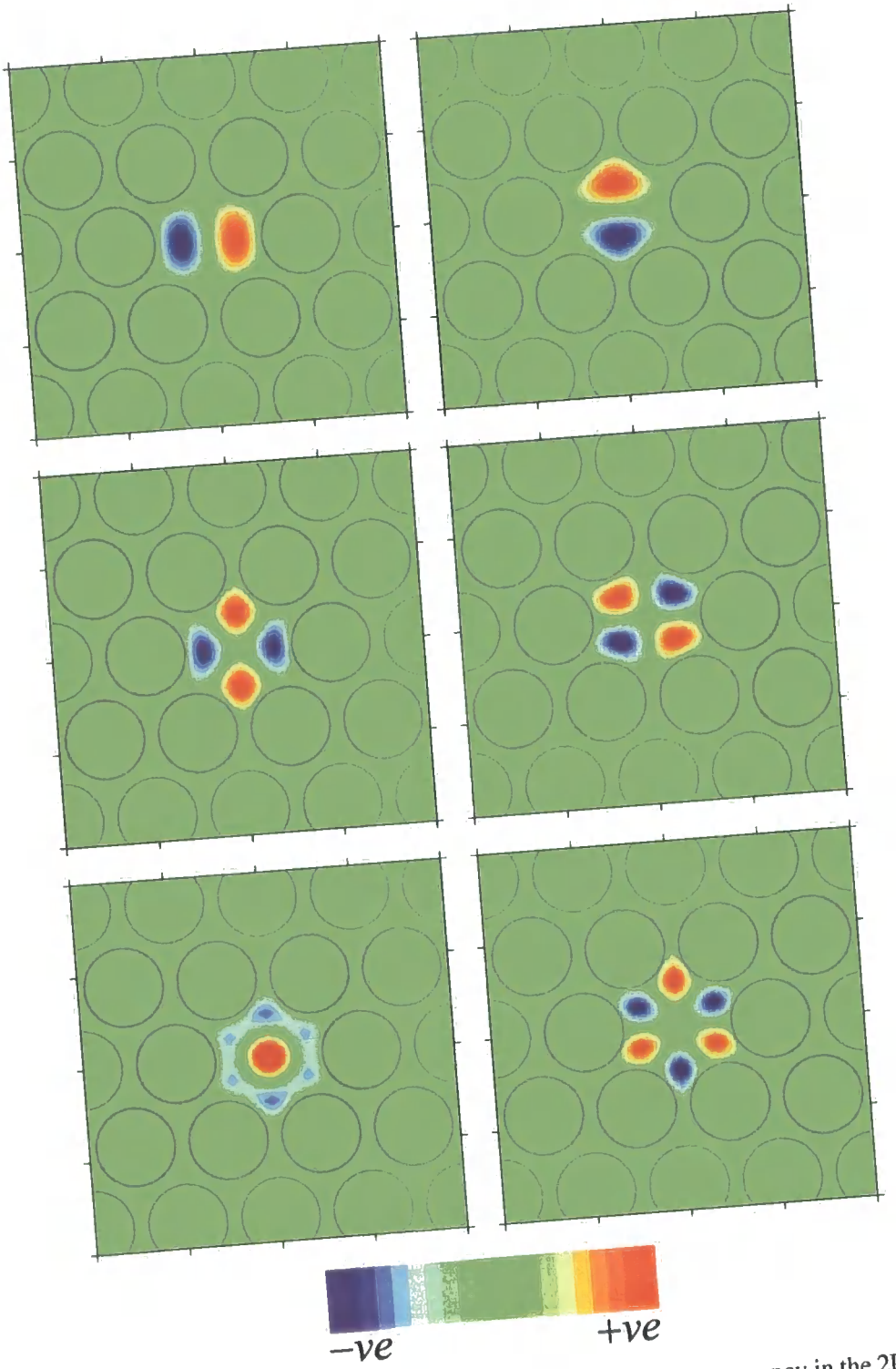

Figure 4.14 Magnetic field profiles of eigenmodes localised upon a vacancy in the 2D hexagonal lattice of air holes with circular cross section and radii $r = 0.4a$ in a GaAs background.

$\omega_0 a/(2\pi c)$	$\Delta\omega/\omega_0$	Symmetry
0.274	1.9×10^{-4}	dipole
0.276	3.2×10^{-4}	dipole
0.346	1.0×10^{-4}	quadrapole
0.350	0.7×10^{-4}	quadrapole
0.371	1.9×10^{-4}	monopole
0.396	1.2×10^{-4}	hexapole

Table 4.2 Frequencies ($\omega_0 a/(2\pi c)$), width to centre frequency ratio ($\Delta\omega/\omega_0$), and symmetries of eigenstates for the six localised defect modes, as described in the text. The naming convention for the symmetries of the modes follows ref. [2].

quency of the defect modes increases, the field patterns become more complex. The four states with lowest frequencies form two pairs of doublets. These states are almost at the same frequency, but are split by being aligned differently with respect to the hexagonal lattice. Following the naming convention of ref. [2] the first doublet is made up of dipole modes, the second doublet comprises quadrapole modes, the fifth state is a monopole mode and the sixth is a hexapole mode. In general, the localised modes with higher frequencies have a more complex field profile which contain more nodes and anti-nodes than those of lower frequency. (The states in figure 4.14 are comparable to those published in ref. [2] (page 100), although these vacancy states were calculated for a photonic crystal with rod radii $r = 0.45a$, and the authors did not resolve the frequency differences between the doublet states.)

All the modes of figure 4.14 can be characterised by their symmetries, which they share in common with the hexagonal Bravais lattice. Group theory can be applied to give the modes a rigorous classification [3, 142], but here we will only discuss the simple symmetries that are apparent from an examination of figure 4.14.

The dipole modes are symmetric under mirror reflections about one plane, and antisymmetric about the plane perpendicular to this. They are also antisymmetric under rotations of π. The lower frequency quadrapole mode is symmetric about two perpendicular planes and rotations of π, whereas the higher frequency quadrapole mode is antisymmetric under the same transformations. The monopole mode is symmetric under all the transformations of that leave the hexagonal Bravais lattice unchanged. The highest frequency hexapole mode is symmetric about mirror reflections in the planes that join two Bravais lattice points and pass through the centre of the vacancy and antisymmetric in the planes rotated 30° with respect to these. The hexapole mode is also antisymmetric under rotations of $\pi/3$. Table 4.2

summarises the symmetries of the microcavity modes.

4.2.2 Positional disorder for a complete band gap

This section describes an examination of the effect of a certain type of disorder on the transmission and reflection spectra of a particular 2D photonic crystal with a complete PBG. The (ideal) photonic crystal is made up of air cylinders of radius $0.4a$ etched in a GaAs substrate ($\varepsilon = 12.96$), and arranged in a hexagonal lattice. It possesses a wide, complete 2D PBG for the TE-polarisation, and as such is well suited for this study. The transmission and reflection spectra can be directly measured by experiment. However, a deeper understanding of how disorder modifies the properties of the photonic crystal can be gained from examining the effects of disorder on the eigenmode spectrum of the photonic crystal. With this in mind, this section is split into a discussion of the calculated transmission and reflection spectra, and a study of the disorder induced states in the photonic band gap.

The bandstructure of the ideal crystal for this polarisation, calculated using a plane wave method (see section 3.2), is shown in figure 4.12. The disorder is of the form of a random shift of the individual cylinders away from their ideal lattice positions; the centre of each air cylinder in the disordered structure is located at a random position within a circle of radius $a\delta$ that is centred on the ideal lattice point. Thus, if the i^{th} (ideal) lattice point is at (y_{0i}, z_{0i}), the air cylinder is centred on a point $(y_{0i} + \delta P_i a \cos\alpha_i, z_{0i} + \delta P_i a \sin\alpha_i)$, where P_i is a random number uniformly distributed in the interval $[0, 1]$ and α_i is a uniformly distributed random angle. Hence $a\delta$ is the maximum shift of a cylinder away from its ideal lattice location, and the parameter δ is a measure of the "amount of disorder".

This study is a continuation of previous work which looked at disorder in the same ideal structure [128, 129]. However, in ref. [128] and [129] the disorder was of the form of a random change of the individual cylinder radii. Those studies found a threshold-like behaviour for the modification of the transmission spectra as a function of the "amount of disorder"; for small disorder the modification of the transmission spectra is small, but above the threshold, the modification becomes large.

Calculations of the transmission and reflection spectra have been conducted using a combination of transfer matrix and multiple scattering methods, with a modified version of the publicly available code developed by Pendry *et al.* (see section section 3.3). A disordered

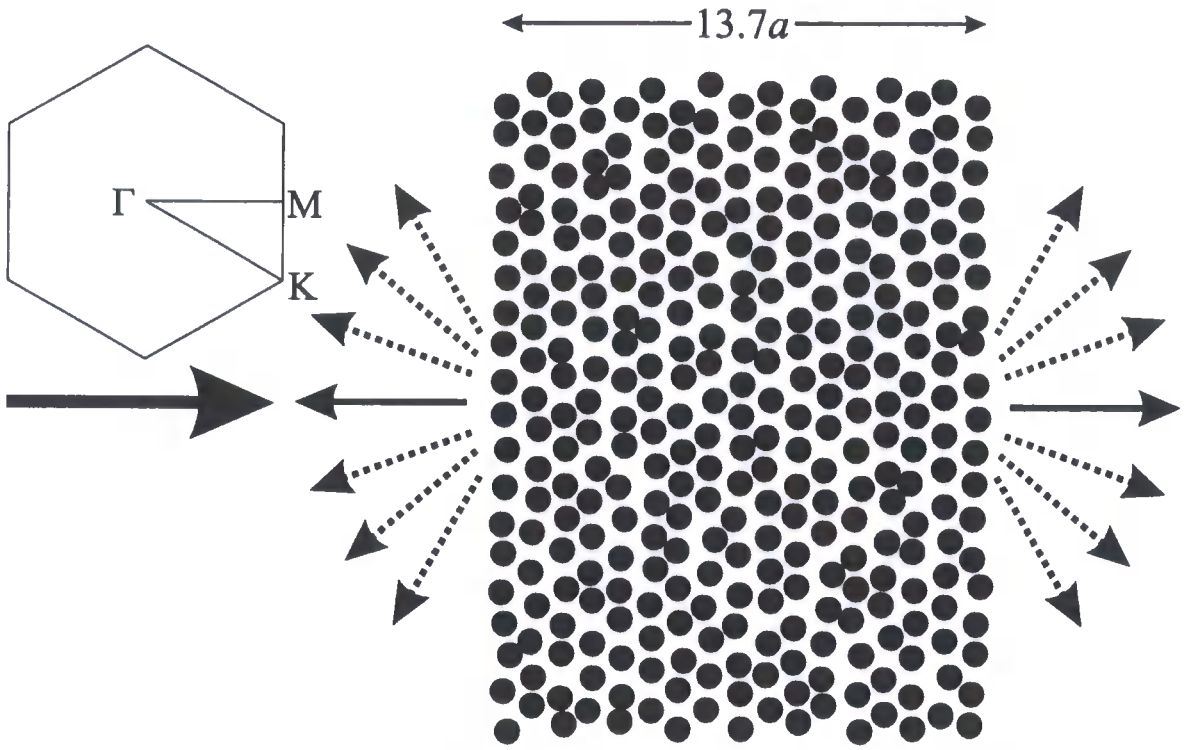

Figure 4.15 A schematic representation of the calculations of transmission and reflection undertaken. A disordered supercell is shown. The large arrow indicates the direction of incident light. The small solid arrows show the direction of ballistic transmission (right) and specular reflection (left). The dotted arrows indicate scattered transmission and reflection. Also shown is the first Brillouin zone of the ideal photonic crystal, which indicates the directions in reciprocal space.

supercell consisting of 17 rows of 19 cylinders is used in the calculations (shown in figure 4.15), and each cylinder was described by a 7 by 6 mesh. Periodic boundary conditions were imposed at the top and bottom sides of the structure in figure 4.15, and the sample thickness used in the modelling was $13.7a$.

In order to model the spectra of real disordered photonic crystals (which usually display smooth transmission dips in the spectral regions of PBGs), the calculations where averaged over several random configurations of disorder. The values of the disorder parameter used in the modelling were $\delta = 0.01, 0.02, 0.05, 0.1, 0.15$ and 0.2, and for each case the spectra were calculated for ten random configurations of the disordered crystal. Experimentally, the transmission spectrum of photonic crystals is usually studied in one of two ways, as illustrated in figure 4.15. The ballistic transmission can be measured, where the transmitted light is parallel to the incident light; or the total transmission is measured, where all the light emerging from the rear of the sample is collected, and comprises the ballistic and scattered

contributions. Hence, in the modelling undertaken, the ballistic and scattered contributions to the transmitted light are considered separately. Likewise for the reflection spectra, the total reflection is separated into contributions from the specular reflection (anti-parallel to the incident light) and scattered reflection. In the modelling, light is taken as incident along the Γ-M direction of the ideal crystal's Brillouin zone in reciprocal space, as indicated in figure 4.15.

Figure 4.16 shows the calculated transmission and reflection spectra. The thin lines are the spectra for one individual configuration of disorder, shown as an example, and the thick lines are the mean spectra, averaged over all ten random configurations and additionally smoothed to remove the remaining traces of the spikes. The ballistic transmission of the ideal crystal is also shown (as a dotted black line) for comparison. The ideal crystal does not display any scattering of light, as the band gap under study is below the diffraction cut-off of the crystal.

It can be seen from figure 4.16 that for small amounts of disorder ($\delta \leq 0.05$) there is very little modification of the ballistic transmission relative to that for the ideal structure. For larger amounts of disorder, the modifications of the transmission spectra become rapidly more pronounced. For individual configurations of disorder, sharp spikes are present in the spectra, which correspond to localised states introduced into the PBG by the disorder. These sharp spikes then lead to an increase of the transmission on average in the region of the PBG where they occur. Also the width of the ballistic transmission dip decreases with increasing disorder. This is due to the fact that small amounts of disorder can only introduce states into the PBG near its upper and lower edges (perturbed edge-states) and thus act to narrow the band gap of the photonic crystal. Only when the disorder becomes large can it introduce states into the centre of the PBG, and influence the transmission there. The transmission spectra of figure 4.16 also show the calculated scattered transmission through the disordered supercells. For a relatively small amount of disorder ($\delta = 0.01$), the scattered transmission in the transmission dip of the ideal photonic crystal is $\sim$3 orders of magnitude smaller than the ballistic transmission. Figure 4.17 (a) shows the averaged transmission at the minimum as a function of the deviation δ for both ballistic and scattered transmission. The different behaviour of the minimum transmission depending on the ballistic or scattered nature of the light is clear here. The ballistic transmission is resistant to disorder up to some

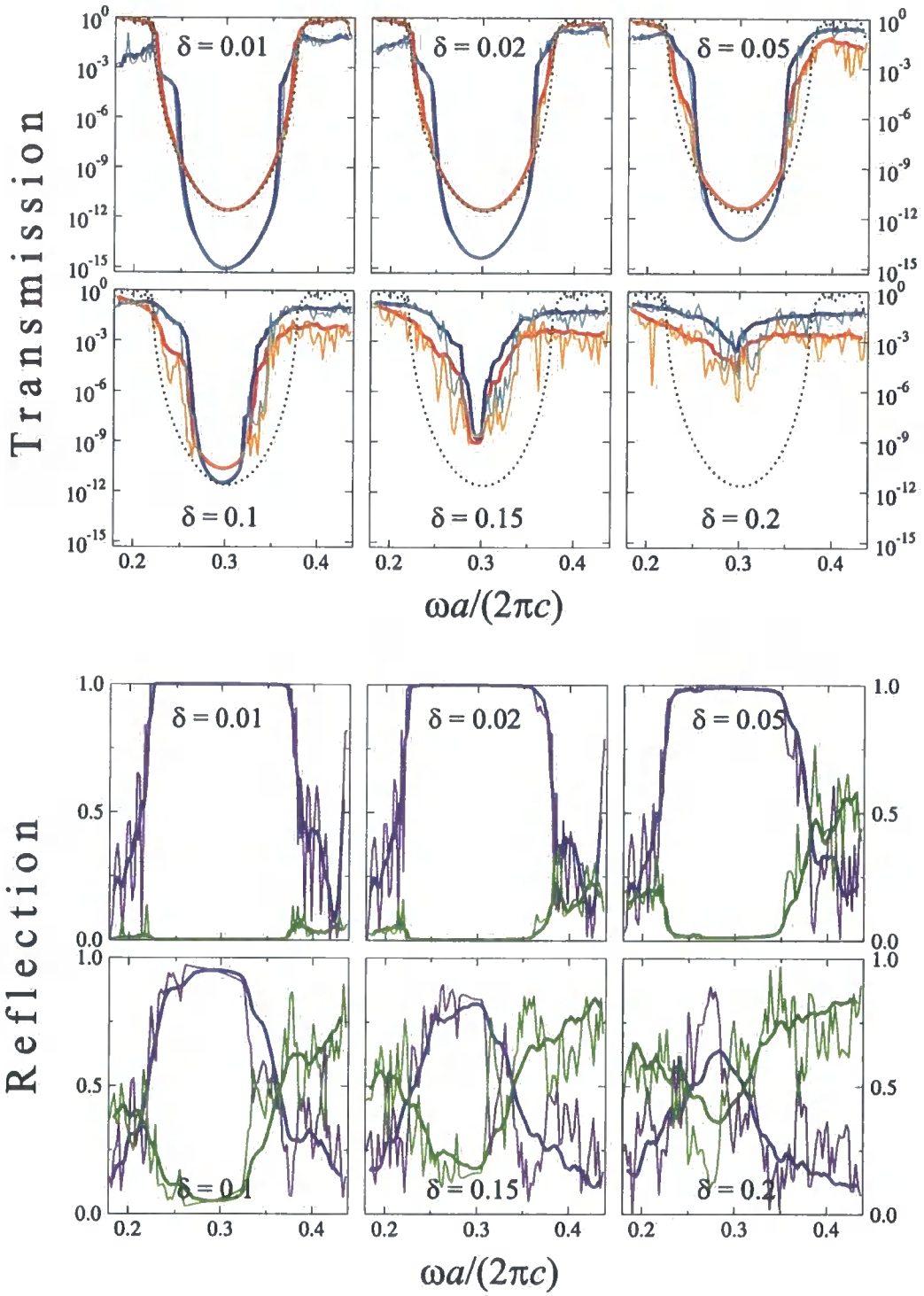

Figure 4.16 Top—calculated transmission spectra for disordered photonic crystals with δ = 0.01, 0.02, 0.05, 0.1, 0.15 and 0.2. Red lines are the ballistic transmission, blue lines are the scattered transmission—the thin lines for an individual configuration of disorder, and the heavy lines for the mean averaged over 10 random configurations of disorder. The ballistic transmission spectrum of the ideal photonic crystal is also shown (black dotted line) for comparison. Bottom—calculated reflection spectra for the same structures. Indigo lines are the specular reflection, and green lines are the scattered reflection.

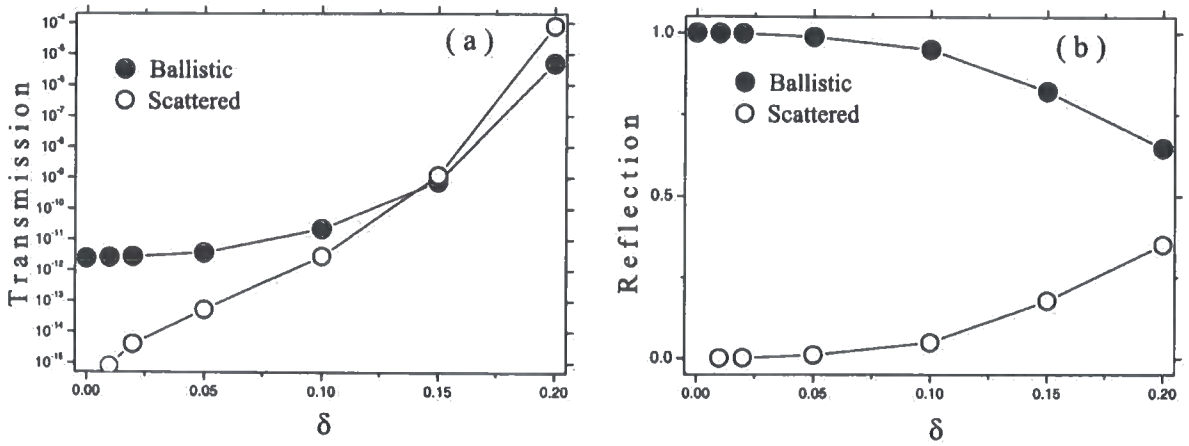

Figure 4.17 (a) The transmission coefficient at the minimum of the spectral dip for the averaged ballistic transmission (closed circles) and averaged scattered transmission (open circles) as a function of the disorder parameter δ. (b) The reflection coefficient at the spectral maximum for the averaged ballistic reflection (closed circles), and at the spectral minimum for the averaged scattered reflection (open circles) as a function of δ.

threshold value of δ, after which it increases rapidly. The threshold-like behaviour of the ballistic transmission has been seen in other studies [69, 124, 126, 128, 129]. The scattered transmission increases rapidly with δ even for small values of δ. Moreover, the scattered transmission increases with δ at a faster rate than the ballistic transmission does, so that for large value of the disorder parameter, scattered light is dominant in the transmission spectrum.

Also present in the transmission spectra is an effect attributed to Rayleigh scattering. The ballistic transmission on the upper frequency edge of the transmission dip is smaller than that on the lower edge when disorder is present. This is because the Rayleigh scattering due to disorder, which removes light from the ballistic transmission, is stronger at the higher frequencies.

The bottom of figure 4.16 shows the reflection spectra calculated for $\delta = 0.01$, 0.02, 0.05, 0.1, 0.15 and 0.2. Again it can be seen that for small disorder, the scattered reflection remains very small, and in the region of the ideal crystal's photonic band gap the ballistic reflection is close to unity. Upon increasing the amount of disorder, the averaged scattered reflection begins to grow. For $\delta \geq 0.1$ this growth increases in rate (see figure 4.17 (b)). The decline of the averaged ballistic reflection with increasing δ mirrors the rise of the scattered reflection. Also, once again, the effect of Rayleigh scattering can be seen, as the averaged scattered reflection near the upper frequency edge of the PBG is greater than that near the

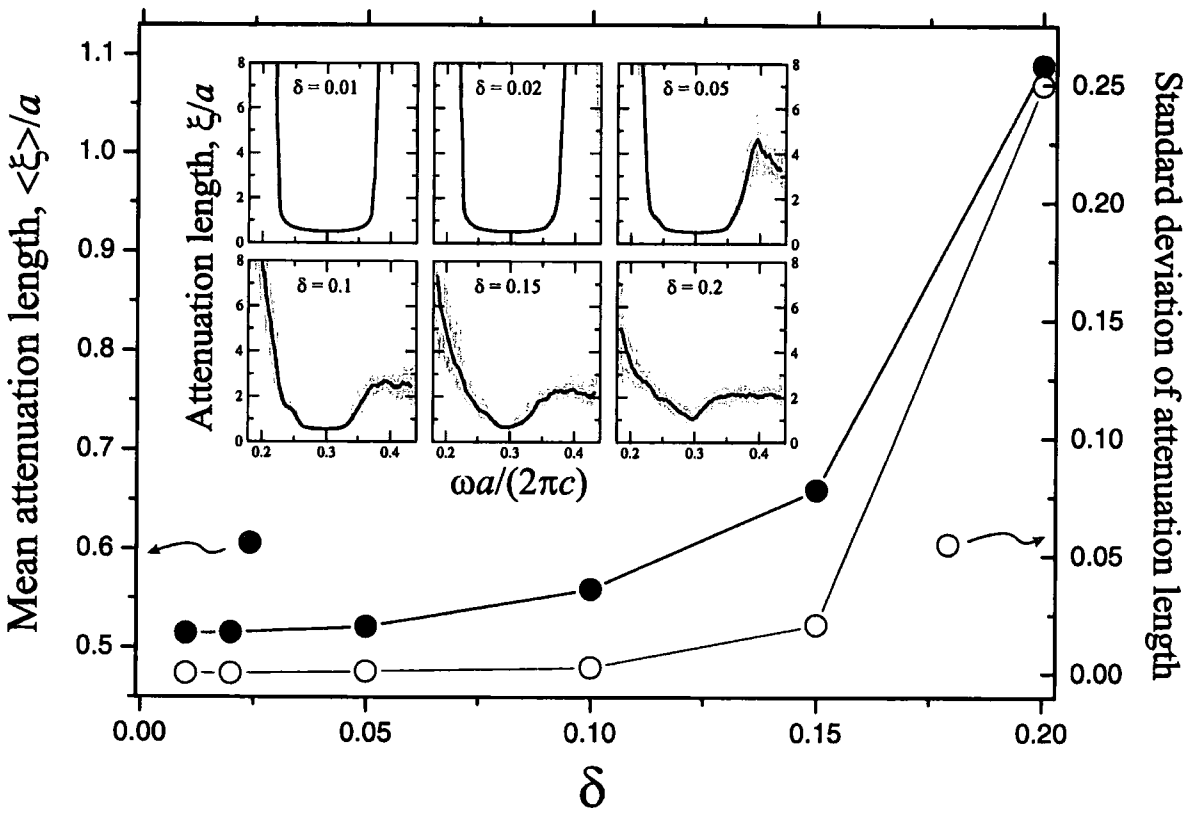

Figure 4.18 The mean attenuation length (closed circles, left axis) and its standard deviation (open circles, right axis) at the centre of the ideal crystal's photonic band gap as a function of δ. Inset—the spectra of the attenuation lengths for δ = 0.01, 0.02, 0.05, 0.1, 0.15 and 0.2. Black lines are the mean over the ten random configurations, and grey lines are the ten individual configurations.

lower frequency edge, and the onset of significant amounts of scattered reflection occurs at a lower value of δ for the upper frequency edge.

When light is incident upon a finite photonic crystal, attenuation of the light occurs in the spectral region of the infinite crystal's PBG, and a transmission dip (such as is shown by the transmission spectra of figure 4.16) is observed. In the photonic crystal under consideration, the transmission coefficient decays exponentially with an increase of path length through the crystal for both ballistic and scattered light [129]. An attenuation length, ξ, can be defined by writing the ballistic transmission coefficient through the structure, T_B, as

$$T_B = e^{-L/\xi} \tag{4.37}$$

where L is the thickness of the sample, which in the modelling undertaken is $L = 13.7a$. Figure 4.18 shows the mean and standard deviation of the attention length at the centre of the

PBG as a function of the deviation δ, and the insets show the attenuation lengths as a function of frequency for different values of δ. As the disorder in the photonic crystals increases, the mean attenuation length rises. For the ideal crystal, at a frequency corresponding to the centre of the photonic band gap, the attenuation length is $0.51a$. Small amounts of disorder ($\delta \leq 0.1$) have very little effect on the attenuation length at the centre of the PBG. When $\delta = 0.1$, the attenuation length has reached $0.56a$, which is only a 10% increase on the ideal value. However for larger amounts of disorder ($\delta \geq 0.15$), the rate of increase of the attenuation length increases, and for $\delta = 0.2$ the attenuation length at the centre of the PBG is $1.1a$, a 110% increase on the ideal value. Also for small disorder ($\delta \leq 0.1$), the standard deviation of the attenuation length at the centre of the PBG ($\sim 10^{-4}$) is approximately three orders of magnitude smaller than the mean, implying that it is very unlikely that any disorder-induced localised states will penetrate to the centre of the band gap and affect the attenuation length there. As the value of δ increases, the standard deviation of the attenuation length at the centre of the PBG begins to rise rapidly, suggesting that it is more probable for a disorder-induced localised state to be present at the centre of the PBG. The behaviour described is of course very similar to that found for disorder in 1D photonic crystals.

The plane wave method can be used to study the eigenmodes of the electromagnetic field in disordered 2D photonic crystals. In the calculations undertaken, a rectangular supercell of 93 cylinders was chosen. A rectangular supercell was chosen, as this shape allows for the imposition of periodic boundary conditions without breaking the local order of the ideal photonic crystal at the edge of the supercell. The dimensions of the rectangular supercell are $L_y = 8a$ and $L_z = 5a\sqrt{3}$, where a is the lattice constant of the photonic crystal. The rectangular superlattice has the primitive lattice vectors

$$\mathbf{a}_1 = L_y\hat{\mathbf{j}} \qquad \mathbf{a}_2 = L_z\hat{\mathbf{k}} \tag{4.38}$$

and primitive reciprocal lattice vectors

$$\mathbf{g}_1 = \frac{2\pi}{L_y}\hat{\mathbf{j}} \qquad \mathbf{g}_2 = \frac{2\pi}{L_z}\hat{\mathbf{k}} \tag{4.39}$$

The photonic bands at frequencies close to the photonic band gap are almost dispersionless, and so the eigenfrequencies of the disordered photonic crystal are calculated at the

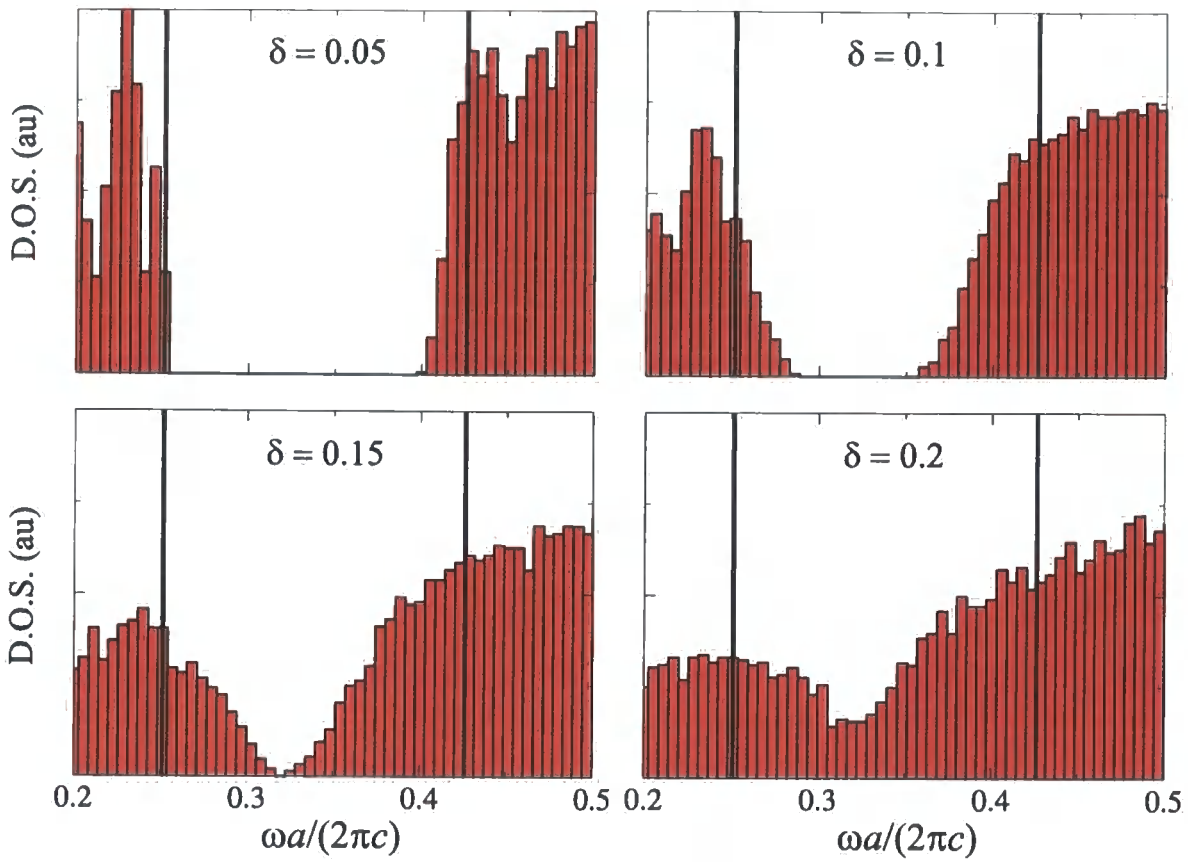

Figure 4.19 TE-polarised density of states (DOS) averaged over twenty random configurations of disorder for the values $\delta = 0.05$, 0.1, 0.15 and 0.2. The vertical black lines show the upper and lower edges of the PBG of the ideal photonic crystal.

Γ-point in the first Brillouin zone of the superlattice. By using the histogram method, and counting the eigenfrequencies into frequency bins, the density of states can also be found. Figure 4.19 shows the density of states (DOS) calculated in this way, averaged over twenty random configurations of disorder for each of the values $\delta = 0.05, 0.1, 0.15$ and 0.2. A basis set of 10201 plane waves was used for the calculation. When performed with no disorder, the calculation gives the band gap to be between $\omega a/(2\pi c) = 0.252$ and 0.426, which indicates convergence to approximately 5% at frequencies corresponding to the PBG of the ideal crystal. From figure 4.19, it can be seen how states are introduced into the PBG for small amounts of disorder ($\delta = 0.05$ and 0.1), but these states are confined to a spectral region near the edge of the PBG and there is a vanishing probability for a localised state to be introduced into the centre of the PBG. It is these states which cause the narrowing of the PBG, which is manifested in the spectra of figure 4.16. Also note how states are introduced into the upper portion of the PBG much more readily than the lower, so that for small disorder the states

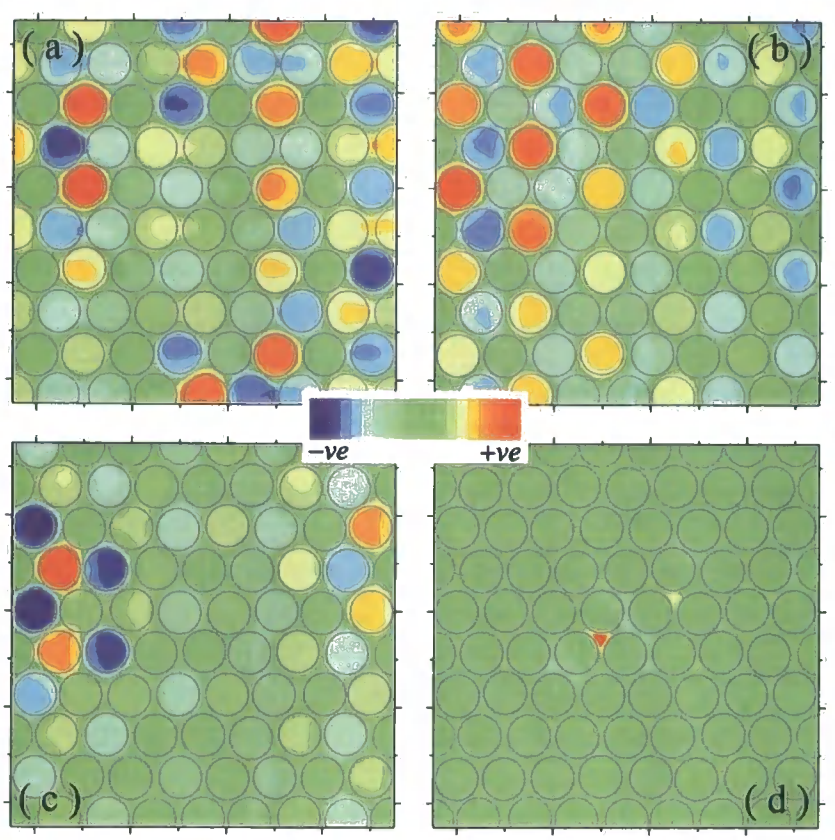

Figure 4.20 Magnetic field profiles of localised states introduced into the PBG by disorder when $\delta = 0.05$, calculated using a plane wave method. The field profiles shown are for different configurations of disorder, and represent the four deepest lying disorder-induced state within the photonic band gap ((a) and (b) are from states in the lower frequency portion of the band gap, whereas (c) and (d) are from states in the upper portion).

from the upper band penetrate the gap more deeply than those from the lower band. At the threshold amount of disorder, the probability of disorder-induced localised states being introduced into the centre of the former PBG becomes non-zero. It is these localised states that produce the sharp spikes in the transmission dip of the disordered photonic crystals, and which lead to the raising of the level of configuration-averaged transmission.

Figures 4.20 to 4.23 show the magnetic field profiles for the four deepest lying disorder-induced states in the former PBG of the TE-polarised bandstructure for disordered photonic crystals with $\delta = 0.05$, 0.1, 0.15 and 0.2 respectively. The field profiles of the eigenstates where calculated at the Γ point of the Brillouin zone. The magnetic field profiles are shown, as for the TE polarisation it is perpendicular to the plane of refractive index variation, and so is easier to visualise than the electric field, which lies in the plane and varies in direction as well as magnitude. The four states in each figure are the four deepest lying disorder-induced states within the PBG of the ideal crystal, calculated with different configurations of the ran-

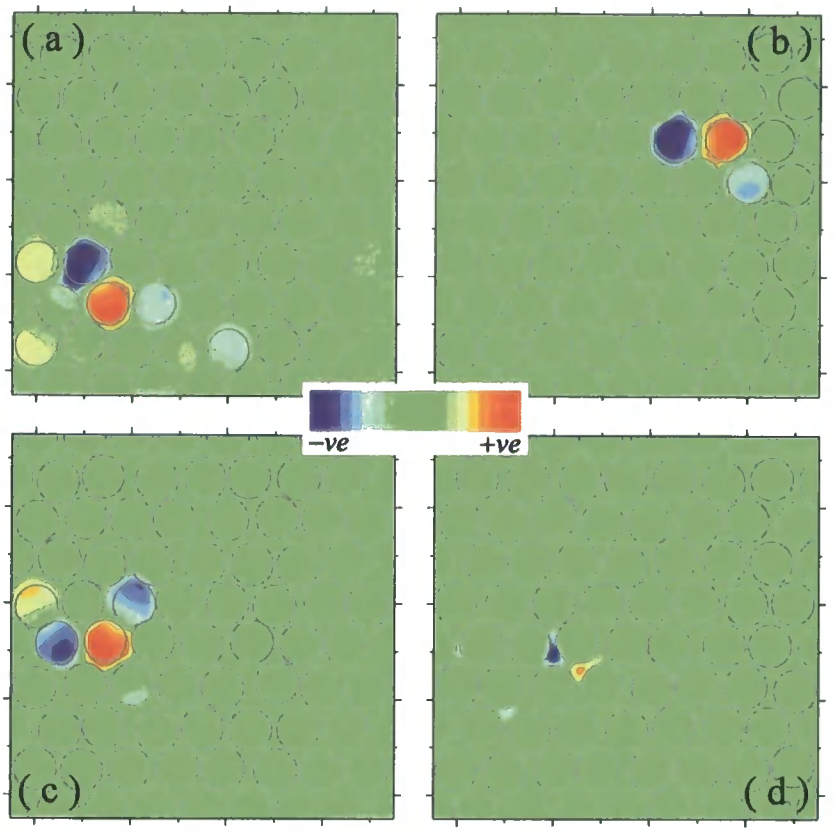

Figure 4.21 Magnetic field profiles of localised states introduced into the PBG by disorder when $\delta = 0.1$, calculated using a plane wave method. The field profiles shown are for different configurations of disorder, and represent the four deepest lying disorder-induced state within the photonic band gap ((a) and (b) are from states in the lower frequency portion of the band gap, whereas (c) and (d) are from states in the upper portion).

dom positional disorder of the air cylinders in the crystal. (a) and (b) show the profiles of the states introduced into the lower part of the photonic band gap, and (c) and (d) are the states introduced into the upper part. Thus, using the nomenclature of ref. [2], the states in (a) and (b) represent "air defect" (removal of dielectric) or acceptor type modes, and (c) and (d) are "dielectric defect" (addition of dielectric) or donor-type modes. When the disorder parameter is small ($\delta = 0.05$), an inspection of figure 4.20 shows that the states are delocalised, with the magnetic field intensity quite well distributed throughout the photonic crystal (the exception being (d)). These states are very close to the edge of the PBG of the ideal crystal. For example, the states of figure 4.20 (a) and (b) have frequencies of $\omega a/(2\pi c) = 0.252$ and 0.253 respectively, less than 1% of the band gap's width from the band edge.

When the disorder parameter is increased to $\delta = 0.1$, the disorder is able to induce eigenmodes at frequencies deeper within the PBG of the ideal crystal (see figure 4.19). Thus the magnetic field profiles of the deepest lying disorder-induced states (figure 4.21) are at

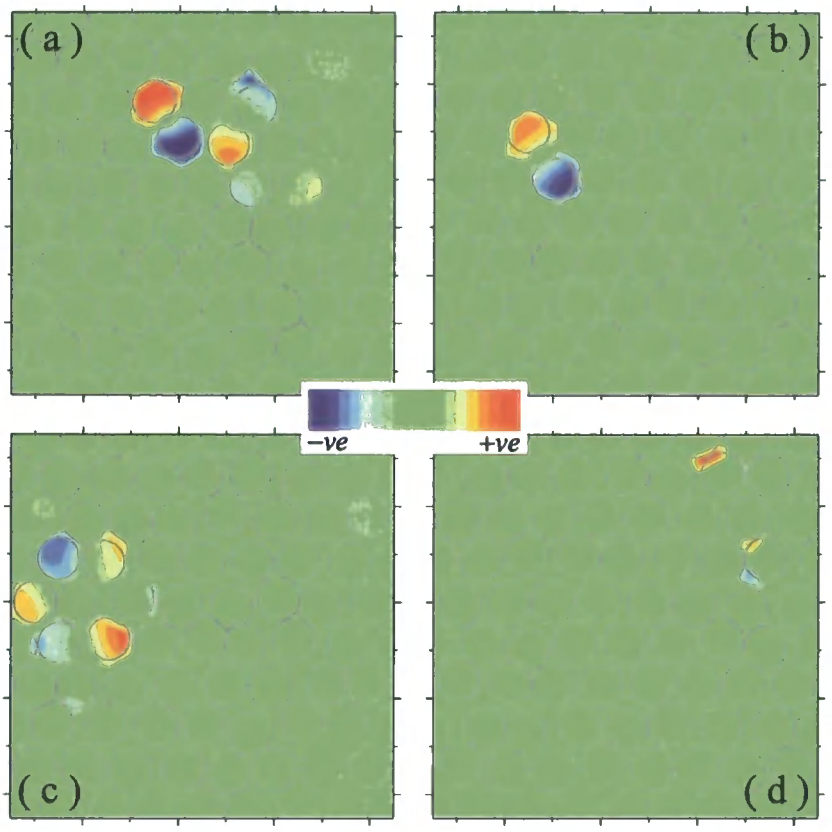

Figure 4.22 Magnetic field profiles of localised states introduced into the PBG by disorder when $\delta = 0.15$, calculated using a plane wave method. The field profiles shown are for different configurations of disorder, and represent the four deepest lying disorder-induced state within the photonic band gap ((a) and (b) are from states in the lower frequency portion of the band gap, whereas (c) and (d) are from states in the upper portion).

localised sites within the disordered photonic crystal. The profiles of the eigenmodes are reminiscent of "random microcavity" modes; they can be compared to the magnetic field profiles of the microcavities created by vacancies within the photonic crystal in figure 4.14.

As the disorder parameter is further increased to $\delta = 0.15$, states have a significant probability of being found at the centre of the former PBG, and the states found there are again localised on random microcavities (figure 4.22). When $\delta = 0.2$, the features associated with the periodic modulation of the dielectric constant are largely absent. However, the modes at the centre of the former photonic band gap, whose magnetic field profiles are shown in figure 4.23, are still localised on random microcavities by the disorder.

Strictly speaking, the plane wave calculations give the eigenfrequencies of an artificial rectangular lattice of identically disordered supercells and the calculation actually produces minibands of disorder-induced localised states within the ideal photonic crystal's PBG. Thus, when the supercell is large enough to ignore the super-crystalline nature of the structure, the

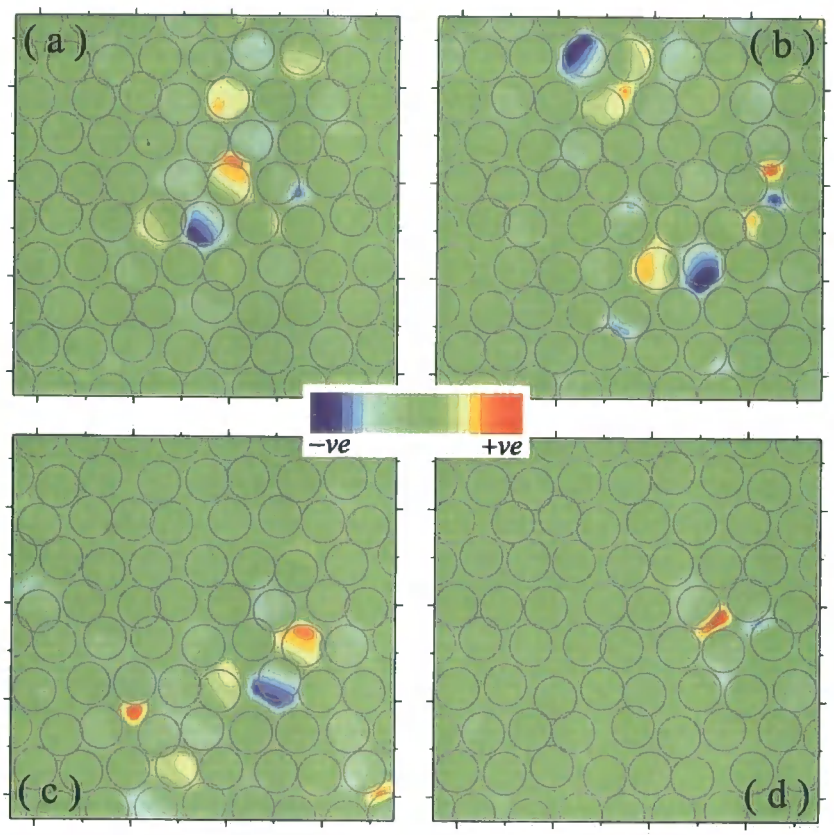

Figure 4.23 Magnetic field profiles of localised states introduced into the PBG by disorder when $\delta = 0.2$, calculated using a plane wave method. The field profiles shown are for different configurations of disorder, and represent the four deepest lying disorder-induced state within the photonic band gap ((a) and (b) are from states in the lower frequency portion of the band gap, whereas (c) and (d) are from states in the upper portion).

width of each miniband gives a rough estimate of the reciprocal lifetime of the localised state. Dispersion curves of the localised states shown in figures 4.20 to 4.23 have been calculated, and indeed minibands are seen. However, the minibands are very narrow, and show very little dispersion. For a typical disordered structure, the miniband of the states introduced the deepest into the lower frequency half of the band gap have frequencies and relative widths given in table 4.3. This confirms what has already been seen from an inspection of the field profiles of figures 4.20 to 4.23; that the states close to the band edge when $\delta = 0.05$ are delocalised, whereas the other deeper lying states are essentially localised.

4.2.3 Positional disorder for an incomplete band gap

This section reports a study of the effect of disorder on a two-dimensional photonic crystal with an incomplete band gap. The ideal system and the model of disorder considered

δ	$\omega_0 a/(2\pi c)$	$\Delta\omega/\omega_0$
0.05	0.26	0.5%
0.1	0.29	0.02%
0.15	0.32	0.03%
0.2	0.34	0.06%

Table 4.3 Frequencies ($\omega_0 a/(2\pi c)$) and width to centre frequency ratio ($\Delta\omega/\omega_0$) for mini-bands of the deepest lying disorder-induced states introduced into the photonic band gap by disorder.

is identical to those considered in section 4.2.2, and the transmission and reflection spectra have been modelled in a similar way, as illustrated in figure 4.15. However, in order to examine the differences caused by the band gap closing for certain directions in the first Brillouin zone, the TM polarisation has been modelled.

Figure 4.24 shows the calculated transmission and reflection spectra for the disorder parameters $\delta = 0.01, 0.02, 0.05, 0.1, 0.15$ and 0.2. The thin lines are for the spectra of one individual configuration of the disorder, and the heavy lines are the mean spectra, averaged over ten random configurations of disorder and additionally smoothed to remove remaining traces of the spikes. The ballistic transmission of the ideal crystal is also shown (as a dotted black line) for comparison.

As can be seen from the transmission spectra of figure 4.24, light incident on the ideal photonic crystal in the Γ-M direction in the spectral region of the incomplete PBG undergoes attenuation, and a transmission dip is observed in the ballistic transmission which is symmetrical about the centre of the PBG. When disorder is introduced into the photonic crystal, light can undergo scattering. For the smallest amount of disorder considered ($\delta = 0.01$), the scattered transmission is comparable to the ballistic transmission, but for larger disorder parameters the scattered light dominates the transmission spectra.

The transmission spectra of figure 4.24 display many similar features to the case of disorder in a photonic crystal with a complete PBG in section 4.2.2. Figure 4.25 shows the transmission coefficient at the minimum (T_{min}) of the spectral dip in the region of the incomplete PBG as a function of the disorder parameter δ. The threshold-like behaviour of the ballistic transmission, and the different behaviour of the scattered transmission, can be seen. Interestingly, it is seen that for small values of δ, T_{min} can be smaller than for its ideal crystal counterpart, despite the fact that one might expect disorder to decrease the attenuation within the crystal, and therefore lead to more transmission. However, for the narrow PBG

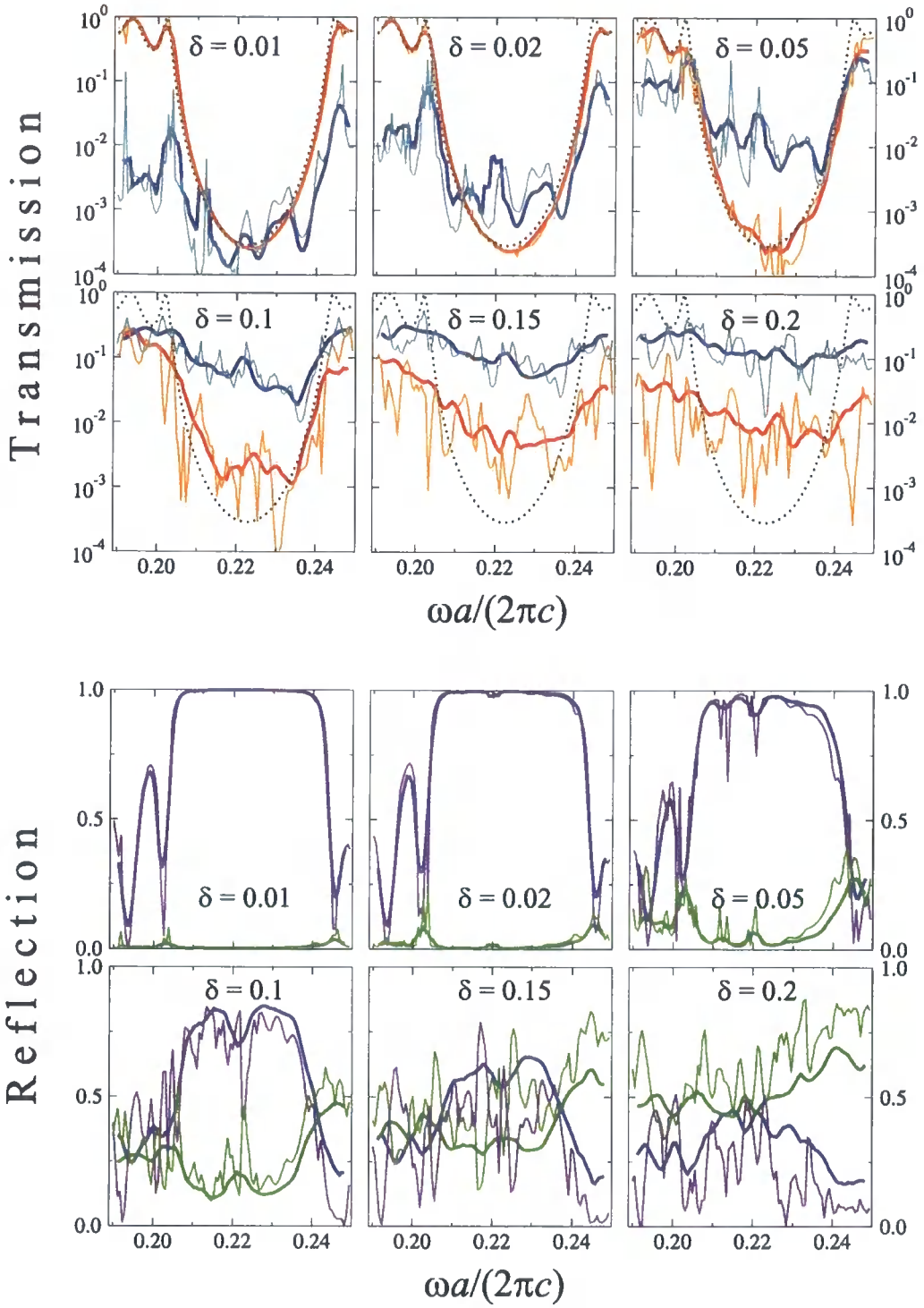

Figure 4.24 Top—calculated transmission spectra for disordered photonic crystals with $\delta =$ 0.01, 0.02, 0.05, 0.1, 0.15 and 0.2. Red lines are the ballistic transmission, blue lines are the scattered transmission—the thin lines for an individual configuration of disorder, and the heavy lines for the mean averaged over 10 random configurations of disorder. The ballistic transmission spectrum of the ideal photonic crystal is also shown (black dotted line) for comparison. Bottom—calculated reflection spectra for the same structures. Indigo lines are the specular reflection, and green lines are the scattered reflection.

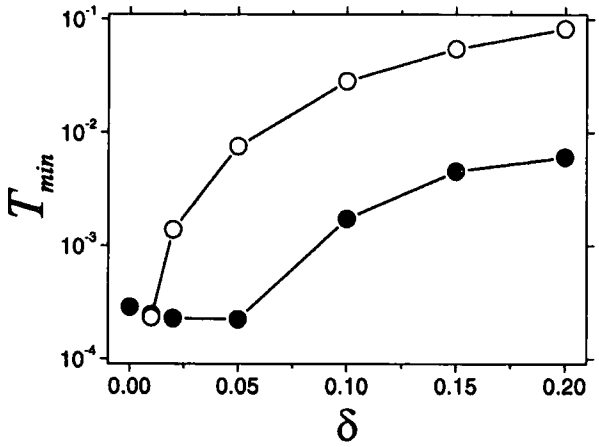

Figure 4.25 The transmission coefficient at the minimum (T_{min})) in the region of the incomplete TM-polarised band gap for ballistic light (closed circles) and scattered light (open circles) as a function of the disorder parameter δ.

under study, where the total attenuation of light through the crystal is small, the effect of Rayleigh scattering in the disordered crystal (which serves to remove light from the ballistic transmission) can be large enough to cause the minimum transmission to be reduced when disorder is introduced.

The transmission spectra of figure 4.24 also display many features in contrast to the case of disorder in a photonic crystal with a complete PBG. The averaged scattered transmission spectra in figure 4.24 display an asymmetric, triangular shape. The reasons for this asymmetry can be understood in terms of the following simple physical arguments based on the bandstructure in figure 4.12. Suppose light is incident on the disordered crystal in the Γ-M direction at a frequency corresponding to the incomplete PBG. In this case, an evanescent wave will be excited in the crystal, characterised by some attenuation length. Due to the disorder, the wave can be scattered into a propagating state in a direction closer to Γ-K. The wave can then proceed to the rear of the sample without further attenuation, and be transmitted. Also possible is the scattering of the incident wave into another evanescent state (as opposed to propagating state) that is closer to the Γ-K direction, and thus characterised by a smaller attenuation length (since the PBG is smaller for directions away from Γ-M, see figure 4.12). The direction of the shape modification depends on the details of the curvature of the bandstructure between the Γ-M and Γ-K directions for the photonic crystal. For the present case, the change in wavevector needed to scatter to a propagating state is larger for higher frequencies (in the second photonic band) then for the lower frequencies (in the first photonic band), and so the shift of the minimum transmission is to higher frequencies.

To a lesser degree, the averaged ballistic transmission also displays a shape asymmetry, which can be explained by similar reasoning. Once the incident wave has been scattered by the disorder, it can then be scattered a second time, occasionally back into the Γ-M direction where it will contribute to the ballistic transmission. This second-order effect leads to the shift of the minimum in the transmission away from the centre of the PBG.

Usually, experimental studies assign the centre of the PBG of real photonic crystals to the minimum of the transmission spectrum. However, when scattered light is dominant in the total transmission, the shape asymmetry discussed above means that the minimum of the total transmission will depend on the details of the bandstructure of the photonic crystal, and does not correspond to the centre of the PBG. Simply assigning the centre of the PBG to the minimum of the transmission through the crystal can thus lead to significant error in (disordered) photonic crystals with an incomplete PBG.

When light is scattered into propagating modes away from the incident Γ-M direction, it is free to propagate through the photonic crystal without attenuation. Thus the light will experience multiple reflections in the crystal, and this leads to Fabry-Perot oscillations in the transmission spectra for scattered light in the spectral region of the incomplete PBG, which can be seen in figure 4.24. From the scattered transmission spectra for individual configurations of disorder, it can be seen that these Fabry-Perot oscillations have a similar period to the Fabry-Perot oscillations outside the PBG for the ballistic transmission. In fact, the spectral period of the Fabry-Perot oscillations is inversely proportional to the path length of the light through the structure, and thus is proportional to a factor of $\cos\alpha$, where α is the angle of propagation relative to the surface normal. The Fabry-Perot oscillations in the scattered transmission within the PBG are due to light scattering from evanescent waves in the incident Γ-M direction into propagating waves closer to the Γ-K direction. Thus $\alpha \leq 30°$, and the difference between the period of the Fabry-Perot oscillations in the ballistic transmission outside the PBG and the width of the Fabry-Perot oscillations in the scattered transmission within the PBG is only around 10%.

These Fabry-Perot oscillations can be differentiated from the spikes caused by the localised modes. The spikes in the transmission dip are due to states being introduced into the former PBG by the disorder, and as such their spectral position and width are random in nature. However, the oscillations observed in the scattered transmission have a more systematic

nature—they are seen throughout the former PBG and differing configurations of disorder give rise to similar oscillations, so they are also seen in the ensemble-averaged scattered transmission.

The observation of Fabry-Perot modes in the scattered transmission within the former PBG is a bandstructure related effect. It relies on the PBG closing for some direction of propagation, such that evanescent modes excited in the crystal by the incident wave can be scattered into propagating modes in directions where the modes lie outside the PBG. Thus the observation should be unique to cases where the PBG is incomplete.

Figure 4.24 also shows the calculated reflection spectra for $\delta = 0.01, 0.02, 0.05, 0.1, 0.15$ and 0.2. For small disorder parameters ($\delta \leq 0.02$) the reflection spectra are very similar to that of the ideal crystal, i.e. very little scattering appears and there is a distinct stop-band in the spectral region of the incomplete PBG. For $\delta = 0.05$, the scattered reflection has begun to grow, and for individual configurations of the disorder, spikes interrupt the stop-band in the ballistic reflection spectra. These spikes lead to an overall lowering of the averaged reflection spectrum. For larger disorder parameters ($\delta \leq 0.1$), the stop-band of the averaged ballistic transmission begins to flatten out, and by $\delta = 0.2$, scattered light dominates the reflection, as well as the transmission, spectrum.

4.3 Conclusions

In this chapter, disordered 1D and two-dimensional photonic crystals have been considered. Three models of disorder in 1D photonic crystals were investigated, and the penetration of the density of states into the photonic band gap was quantitatively investigated. It was found that the tail of the density of states in the band gap has a Gaussian form, characterised by a penetration depth. A relationship between the relative penetration depth of the density of states in the PBG, relative gap-width and disorder parameter has been found for small relative gap widths—the penetration depth is proportional to the disorder parameter, but proportional to the reciprocal square-root of the relative gap-width. This phenomenological analysis will be of use in the formulation of an analytical model of disordered photonic crystals, as results presented here should form the one-dimensional limit of any such theory.

Also, the transmission properties of disordered 1D photonic crystals were considered. It

was found that there is a threshold disorder parameter, below which the transmission through the photonic crystals increases slowly with increasing disorder. An estimate for the threshold level is given, based on the statistics of the eigenmodes of disordered photonic crystals. Below the threshold level of disorder, the penetration depth of the density of states into the band gap is small compared to the gap width, and only perturbed edge-states penetrate the edges of the band gap; only the tails of the Lorentzian transmission resonances affect the transmission in the centre of the band gap, and changes in transmission are small. Above the threshold level of disorder, the penetration is comparable to the gap-width, and states penetrate further into the band gap, and the transmission is increased throughout the band gap. Disorder-induced states are seen to be localised random microcavity modes, as well as perturbed edge states.

The effect of disorder on the spectra of two-dimensional photonic crystals composed of air cylinders in a GaAs substrate has been investigated. The disorder was of the form of a random shift of the air cylinders away from their ideal lattice locations. Two distinct cases were considered—a photonic crystal with a complete photonic band gap and a photonic crystal with an incomplete photonic band gap. In both cases, a threshold behaviour in the ballistic transmission on the disorder parameter is found. For the complete PBG, it was found that for small levels of disorder there is a vanishing probability of disorder-induced localised states appearing in the centre of the former photonic band gap, but that the PBG is narrowed by perturbed states introduced at its edges. A threshold amount of disorder was found to exist, where the probability of finding disorder-induced localised states throughout the former PBG becomes significant. These disorder induced states are shown to include states localised on random microcavities, as well as perturbed edge states.

For the incomplete PBG, scattered light dominates the spectra, even for small disorder parameters. The transmission spectrum has dips in the PBG, which become asymmetric for disordered photonic crystals, such that the minimum transmission does not coincide with the centre of the PBG in disordered photonic crystals with incomplete band gaps. Fabry-Perot type oscillations appear within the band gap for scattered transmitted light. These are bandstructure-related effects, and depend upon the PBG closing for certain directions in the crystal, so that light is scattered by the disorder from attenuated evanescent states to propagating states.

Chapter 5

Two-dimensional photonic crystals with quasicrystalline unit cells

Crystals are periodic, and possess both translational and rotational symmetries. For a crystal to possess an n-fold rotational symmetry, a rotation of the crystal through an angle $2\pi/n$ centred on any lattice point of the Bravais lattice must recreate the lattice identically. Due to the periodicity of a crystal, possible values of n are $n = 2$, 3, 4, or 6; degrees of rotational symmetry above 6 are not possible.

Two dimensional photonic crystals are usually built from dielectric rods in air or air cylinders in a dielectric substrate, with the cylinders/rods placed on the lattice points of a 2D crystal lattice. Such structures can give rise to large photonic band gaps, but the band gaps tend to be highly anisotropic in both spectral position and width, and a complete photonic band gap will only result if the the band gaps for different directions are wide enough to overlap for some band of frequencies. That requires a large dielectric contrast between the dielectric materials used for the construction of the photonic crystals.

Often it is desirable to have a photonic band gap material with a band gap which is as isotropic as possible. A near isotropic band gap facilitates the spectral overlap of band gaps for different directions in the material without the need for particularly large band gaps. Thus a smaller refractive index contrast would be needed for the onset of a complete photonic band gap in the material. A lower refractive index contrast in a photonic crystal could be advantageous because it would reduce losses from Fresnel reflection when light is coupled into and out of the structure.

Quasicrystals [143–145] are not periodic but do possess long-range order and can display eight-fold (octagonal), ten-fold (decagonal), twelve-fold (dodecagonal), or even higher degrees of rotational symmetry. 2D quasicrystal structures can be generated by projecting points onto a 2D-plane from a regular array in a higher-dimensional space or by the positioning of tiles according to detailed matching rules [143, 145, 146]. 2D photonic quasicrystals are structures possessing an aperiodic modulation of the relative permittivity with long range order based upon quasicrystalline tilings, and they can be constructed by decorating the quasiperiodic tiling with the usual dielectric rods or cylinders. Due to the increased degree of rotational symmetry that a photonic quasicrystal can possess compared to its periodic counterpart, it has been suggested that photonic band gap materials based on quasiperiodic tilings would possess more isotropic band gaps. Several experimental and theoretical studies have shown evidence of 2D PBGs, accompanied by dips in the transmission spectrum, in different photonic structures based on quasicrystalline geometries [76, 77, 147–156]. Further, these studies have found that the band gap formed from photonic quasicrystals is due to the short range quasicrystalline structure and not due to the periodicity enforced by the boundary conditions of calculations based on a supercell approach [148]. This would seem to be supported by studies that look at the transmission through a finite thickness of the photonic quasicrystalline structures [151], which do not rely on periodic boundary conditions (at least in the direction of the incident and transmitted light). These studies show distinct dips in the transmission spectrum which maintain their frequency and deepen exponentially with an increase in the thickness of the photonic quasicrystalline sample. Also, band gaps in 1D structures based on the Fibonacci sequence have previously been demonstrated [66, 157], but there is evidence that a minimum system size is required for the formation of a true PBG where light decays exponentially with increase of system size [158]. To the author's knowledge, no theoretical study on the properties of 3D photonic quasicrystals have been conducted, probably due to the computational resources that such calculations would require. However, recently Man *et al.* have circumvented this computational problem by performing an experiment on a 3D photonic quasicrystal with icosahedral symmetry at microwave frequencies [159].

The first half of this chapter reports studies of the bandstructures of 2D photonic crystals with square unit cells based on an octagonal quasicrystal with the aim of maximising the PBG width and isotropy. The chosen quasicrystalline structure is the Ammann-Beenker

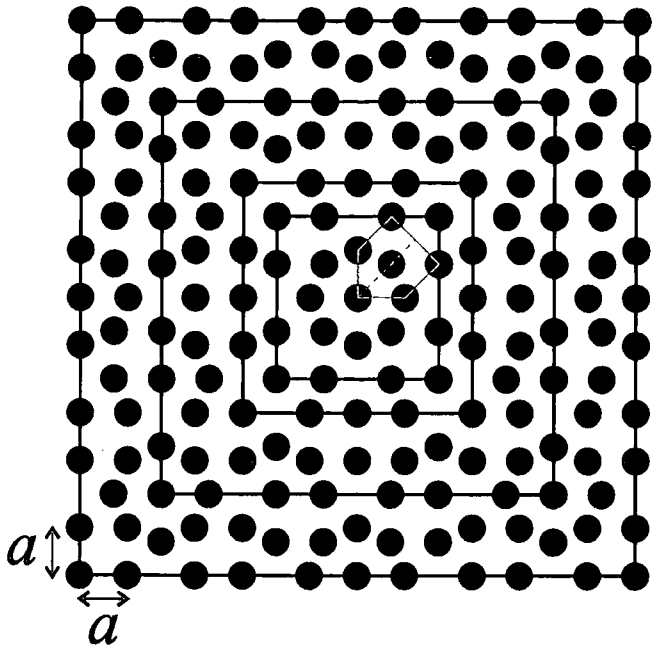

Figure 5.1 Schematic diagram showing the square unit cells of the 2D photonic crystal that are based upon an octagonal Ammann-Beenker tiled quasicrystal. The black circles represent the air cylinders. The quasicrystal is made up of two basic tiles, a square and a rhomb, and a is the length of the sides of these tiles. The squares indicate the four different unit cells used to build the photonic crystal, of side lengths $L = 3.41424a$, $L = 4.82848a$, $L = 8.24212a$, $L = 11.6568a$. The green lines indicate the quasicrystalline feature associated with the most prominent diffraction peaks, as discussed in section 5.1.1.

tiling, which displays octagonal 8-fold rotational symmetry [145]. The Ammann-Beenker tiling consists of two types of tiles—a square tile and a rhomb whose internal acute angles are 45°. Both types of tile have the same side lengths which we denote by a. A 2D photonic structure is constructed by decorating the Ammann-Beenker tiling with cylindrical air holes at the vertices of the tiles. The air holes are embedded in a background dielectric taken to have a relative permittivity of $\varepsilon = 9.0$. The positions of the cylinders in this scheme are shown in figure 5.1. Several different sizes of square unit cell can be chosen which do not result in broken cylinders on building up the crystal. The four sizes considered in this chapter are shown by the squares in figure 5.1, and contain 14 cylinders (side length $L = 3.41424a$), 28 cylinders ($L = 4.82848a$), 82 cylinders ($L = 8.24212a$) and 164 cylinders ($L = 11.6568a$). Finally the radii r of the air cylinders (or, equivalently, the filling fraction f of the air cylinders in the unit cell) can also be varied, and the dependence of the bandstructure on the radii of the cylinders is investigated for the range $0.12a \leq r \leq 0.38a$. For $r > 0.38a$ the air cylinders begin to overlap.

It should be noted that the structure described above is periodic, with local quasicrys-

talline order within the unit cell. The properties of such crystals are interesting, as the larger unit cells will be shown to facilitate more isotropic band gaps due to the increase in range of the quasicrystalline order. However, the computational scheme employed is identical to the one of considering a photonic quasicrystal within a supercell approximation. The four sizes of unit cell or supercell investigated will allow for an examination of the supercell approximation when applied to the case of photonic quasicrystals, specifically on how the size of the chosen supercell affects the calculation. As both these cases are of interest, both will be discussed in the context of the results presented. The two cases will be distinguished by referring either to unit cells of the photonic crystal or to supercells of the photonic quasicrystal.

The structures studied in this chapter (air cylinders in a dielectric background on an octagonal quasicrystalline unit cell) are complementary to those studied in ref. [147]. Ref. [147] studied the same octagonal quasicrystalline supercell but with cylindrical dielectric rods in air, and found photonic band gaps in the TM-polarised bandstructure. It will be shown that the structures studied in this chapter have photonic band gaps in the TE-polarised bandstructure, but not in the TM-polarised bandstructure.

The second half of this chapter describes an examination of microcavities in the octagonal photonic quasicrystal, formed by cylinder vacancies in the decorated Ammann-Beenker tiling. The lack of translational order in the the photonic quasicrystal means that there are many inequivalent sites for the vacancies, and four microcavities based on different vacancies will be studied. It will be shown that localised modes with eigenfrequencies in the band gap can form at the microcavities, and the field profiles and properties of some of these modes are examined. The properties of the microcavities are calculated using the plane wave method with a supercell approximation.

Some of the work presented in section 5.1 was performed by David Roper [160] as part of an MSci project at the University of Durham that the author helped to co-supervise. Any results taken from this project and not calculated by the author are explicitly acknowledged.

5.1 Octagonal photonic quasicrystals

This section describes an examination of a 2D photonic crystal composed of square unit cells with local octagonal quasicrystalline order. As discussed above, the computational scheme is the same as when looking at 2D octagonal photonic quasicrystals in a supercell approximation, and this will be discussed as appropriate. The calculated diffraction pattern of the photonic quasicrystal is presented in section 5.1.1, before the bandstructure of the photonic crystal for four different quasicrystalline unit cells is presented, both as a function of the unit cell size and the filling fraction of the unit cell. The calculated transmission and reflection spectra are presented, before finally an estimate on the position of the band gaps (based on treating the crystal as an effective medium) is given.

5.1.1 Diffraction pattern

The diffraction patterns from quasicrystalline structures display sharp diffraction images of non-crystallographic symmetry. As already mentioned, the long range order but lack of translational periodicity can lead to degrees of rotational symmetry not allowed in crystals, and this is reflected in the x-ray diffraction images of quasicrystals [143, 145], and the optical diffraction images of the dielectric contrast in photonic quasicrystals [151, 155].

Figure 5.2 shows the Fourier representation of the dielectric contrast of the structure shown in figure 5.1. The diffraction pattern displays eight-fold rotational symmetry. Four series of intense peaks dominate the diffraction pattern, which can be indexed by choosing a set of reciprocal lattice vectors corresponding to the innermost series. These reciprocal lattice vectors are denoted $\pm\mathbf{F}_i$ ($i = 1, 2, 3, 4$), where

$$\begin{aligned} \mathbf{F}_1 &= (\cos(0), \sin(0)) = (1000) \\ \mathbf{F}_2 &= (\cos(\pi/4), \sin(\pi/4)) = (0100) \\ \mathbf{F}_3 &= (\cos(2\pi/4), \sin(2\pi/4)) = (0010) \\ \mathbf{F}_4 &= (\cos(3\pi/4), \sin(3\pi/4)) = (0001) \end{aligned} \tag{5.1}$$

where the unit of reciprocal length used in reciprocal space is related to the length a of the

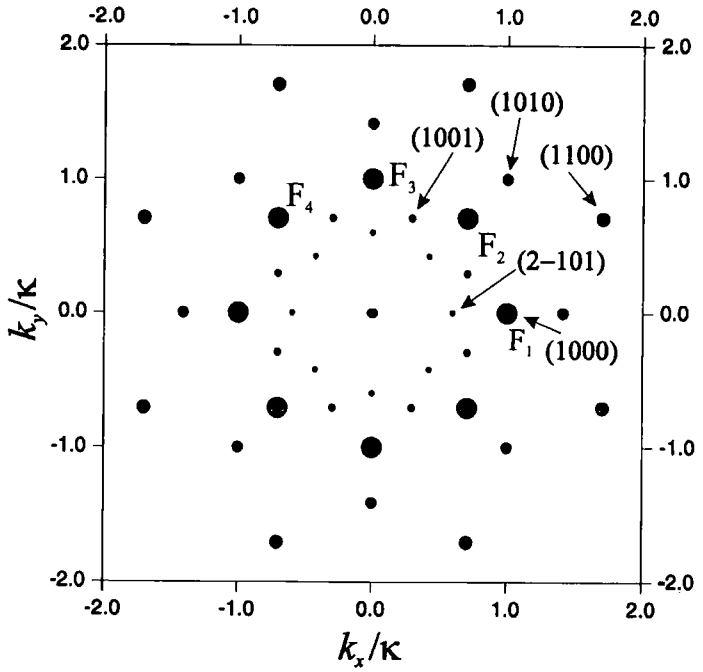

Figure 5.2 The Fourier representation of the dielectric contrast of the largest unit cell shown in figure 5.1. The radius of the spot is proportional to the squared magnitude of the Fourier coefficient. The diffraction pattern displays eight-fold rotational symmetry. The most prominent series of peaks can be used as basic reciprocal lattice vectors $\mathbf{F}_i$ $(i = 1, 2, 3, 4)$ to index the rest of the diffraction peaks, as shown. Diffraction pattern calculated by D. T. Roper [160].

sides of the tiles that make up the octagonal quasi-periodic tiling by

$$\kappa = |\mathbf{F}_i| = \frac{2\pi}{a}\frac{2}{1+\sin(\pi/4)} \approx 1.171573\frac{2\pi}{a} \tag{5.2}$$

The vectors are expressed in both Cartesian coordinates and a symbolic four-dimensional vector notation. Using this symbolic four-dimensional notation, the four major series of diffraction peaks can be defined by symmetrical sets of vectors based on (1000), (1010), (1100) and (1001). The calculated intensities of the most prominent series of diffraction peaks, their indexes and the related elements of the tiles that make up the octagonal quasicrystal are given in table 5.1. The (1000) series of peaks are the most prominent, and are associated with the element consisting of a tile side and half the square tile's diagonal, as indicted by the dotted line in figure 5.1.

reciprocal lattice vector (RV)	Magnitude RV/$\lvert F_i \rvert$	$\frac{Ga}{2\pi}$	Magnitude of Fourier coefficient $\varepsilon/(1/\varepsilon)$	element of tile associated with RV
(0000)	0	0.0	8.12/0.209	
(2-101)	$2-\sqrt{2}$	0.68...	0.13/0.015	$\frac{1+\sqrt{2}}{4(\sqrt{2}-1)}a \approx 1.457106a$
(1001)	$\sqrt{2-\sqrt{2}}$	0.89...	0.18/0.021	$\frac{\sqrt{2}+1}{2\sqrt{2}\sqrt{2-\sqrt{2}}}a \approx 1.115221a$
(1000)	1	1.17...	0.50/0.056	$\frac{2+\sqrt{2}}{4}a \approx 0.85355a$ Half of the sum of a tile side and a half a diagonal of a square
(1010)	$\sqrt{2}$	1.65...	0.27/0.031	$\frac{2+\sqrt{2}}{4\sqrt{2}}a \approx 0.60355a$ Half of the sum of a tile side and a diagonal of a square
(1100)		2.16...	0.32/0.036	$0.4617a$

Table 5.1 Magnitudes of different Fourier coefficients of the photonic quasicrystal for a cylinder radius of $r = 0.17a$.

5.1.2 Bandstructure

The bandstructures of the photonic structures under consideration are calculated by the plane wave method (see section 3.2). The square unit cells of octagonal quasicrystalline order shown in figure 5.1 are arranged on a periodic square lattice. Figure 5.3 shows the convergence of the eigenfrequencies of the edge states immediately above and below the photonic band gap for the unit cell containing 164 cylinders (a), 82 cylinders (b), 28 cylinders (c) and 14 cylinders (d) of radius $r = 0.17a$ in the octagonal quasicrystalline geometry as the number of plane waves used in the truncated basis set is increased. The horizontal dashed lines indicate the eigenfrequencies calculated for the lower eigenfrequency with 8281 plane waves. Note that the frequency axis in figure 5.3 has been shifted to allow the four cases (a) to (d) to be displayed on the same graph with clarity. It can be seen that the calculated eigenfrequencies converge more rapidly for the smaller unit cells than for the larger unit cells. This is to be expected, as the plane waves used in the calculation have wavelengths related to the side length L of the unit cell, whereas the dielectric function within the unit cell vaires on a length scale of a. Thus when the ratio L/a is increased, more plane waves are needed of shorter wavelength to be able to represent accurately the finer details of the dielectric variation. Hence more plane waves should be used for the largest unit cells to ensure convergence of the eigenfrequencies to a reasonable accuracy. Figure 5.4

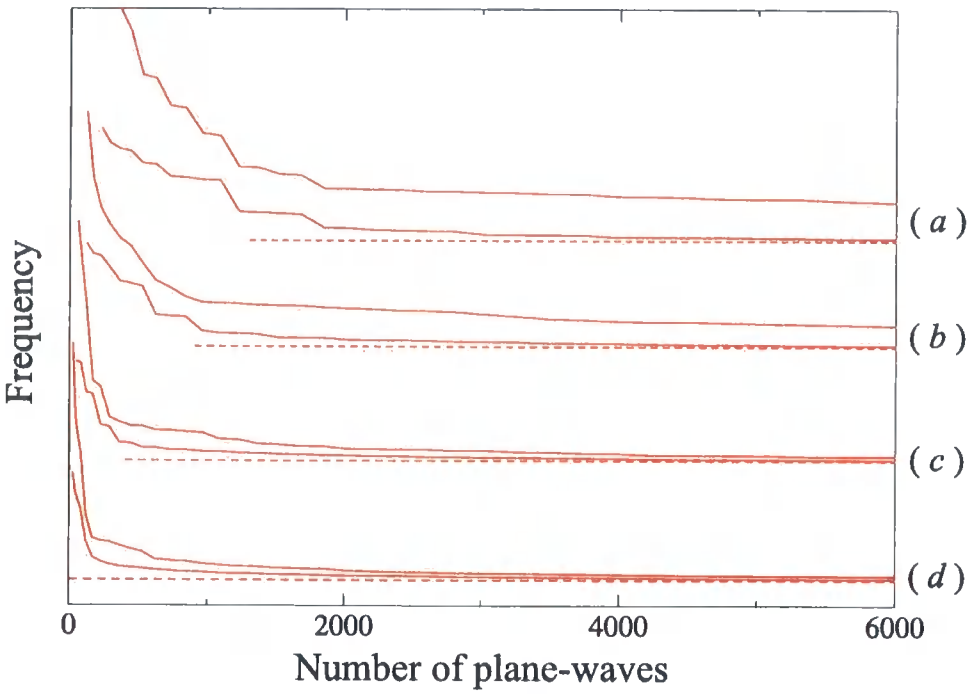

Figure 5.3 Graph showing the convergence of the eigenfrequencies calculated with a plane wave method for the four different sized unit cells of quasicrystalline order discussed in the text. The eigenfrequencies are of states immediately above and below the band gap for cylinders with radius $r = 0.17a$ with unit cells containing (a) 164, (b) 82, (c) 28 and (d) 14 cylinders. Note the frequency axis is shifted for clarity of display. The horizontal dashed lines indicate the eigenfrequencies calculated using 8281 plane waves. Convergence data courtesy of D. T. Roper [160].

shows the bandstructures for the TE polarisation of the photonic crystals based on different sizes of unit cell and when the air cylinders have radii $r = 0.17a$, $r = 0.24a$ and $r = 0.34a$ respectively. These values of the radius give filling fractions of the air cylinders as 11%, 22% and 44% respectively. The bandstructures and density of states were calculated with basis sets appropriate for a square lattice of 10201, 3721, 2601 and 1681 plane waves for the unit cells containing 164, 82, 28 and 14 cylinders respectively. The values for the number of plane waves used where chosen using convergence calculations such as the one illustrated by figure 5.3 to ensure convergence of the eigenfrequencies to better than 1% in all cases at the frequency range of interest. Significant band gaps only occur in the bandstructure for the TE polarisation and therefore results for the TM polarisation are not given here.

Figure 5.5 shows the positions of the band gap edges as a function of the size of the unit cell for the TE polarisation. For a small filling fraction ($r = 0.17a$, filling fraction 11%), it can be seen that there is a minimum size of the quasicrystalline unit cell before any significant band gap opens up in the bandstructure. For the two smaller unit cells, the band gap around

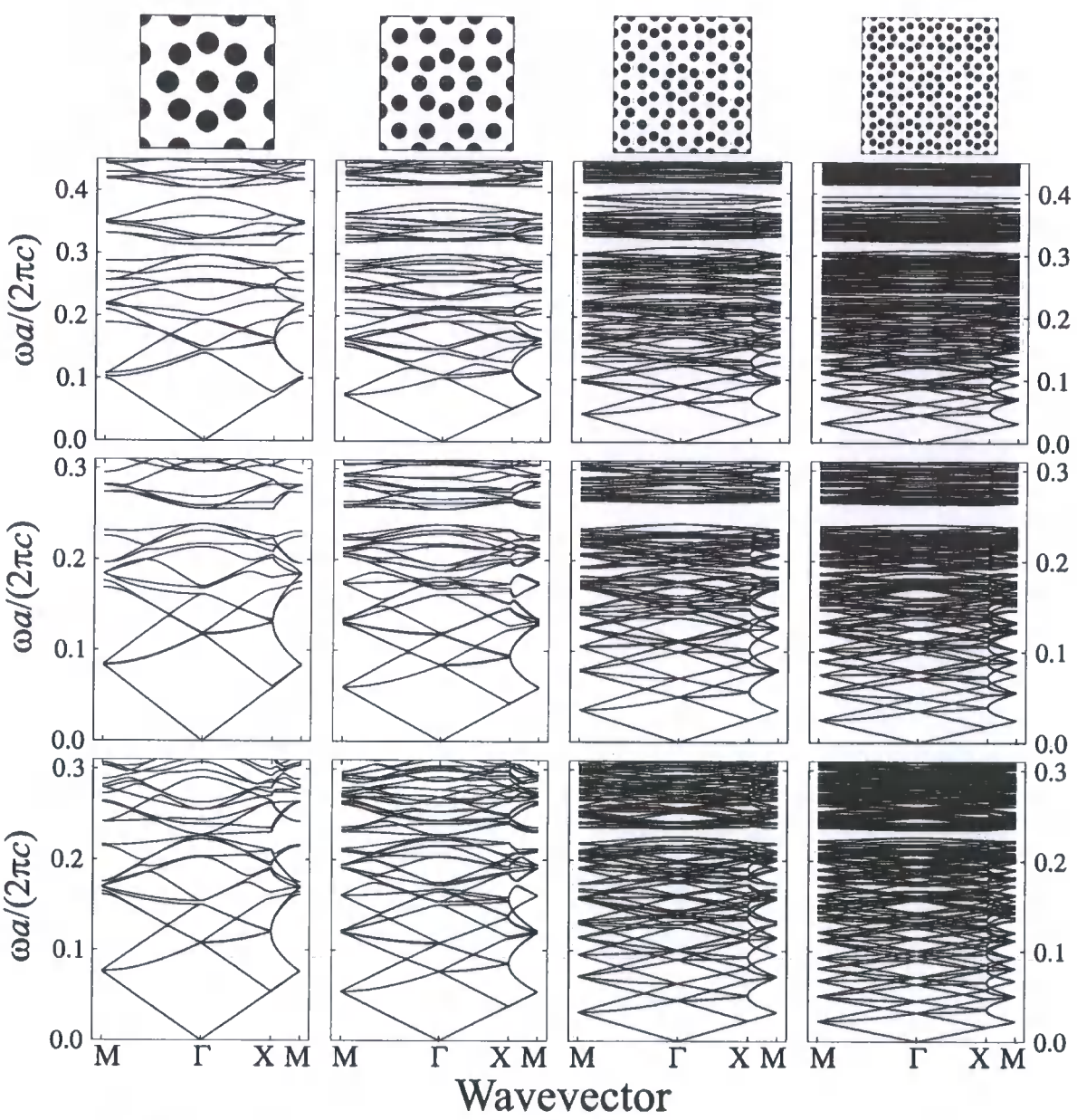

Figure 5.4 Calculated TE bandstructures for the four different sizes of unit cell with air cylinders of radius $r = 0.17a$ (bottom), $r = 0.24a$ (middle), and $r = 0.34a$ (top). The points of high symmetry in the Brillouin zone are Γ: $\mathbf{K} = (0, 0)$; X: $K = (\pi/L, 0)$; and M: $K = (\pi/L, \pi/L)$. The results for the unit cell with 14 cylinders are far left, 28 cylinders centre left, 82 cylinders centre right, and 164 cylinders far right, as indicated by the (scaled) illustrations of the unit cell used.

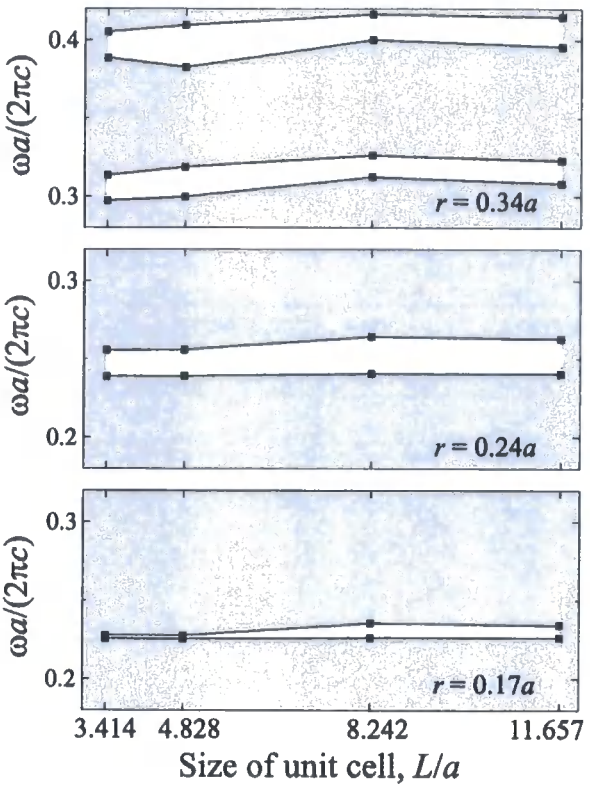

Figure 5.5 Diagrams of allowed bands in the TE bandstructure as a function of the size of the square quasicrystalline unit cell used to form the 2D photonic crystal, for air cylinders with radius $r = 0.17a$ (bottom), $r = 0.24a$ (middle), and $r = 0.34a$ (top). The grey regions represent allowed bands, and the white regions are the PBGs.

$\omega a/(2\pi c) = 0.23$ has a width, $\Delta\omega$, that is less than 1% of the centre frequency, ω_0. However, when the unit cell size is increased to include 82 cylinders, the gap opens up to the relative size of $\Delta\omega/\omega_0 = 4.0\%$, before reducing to $\Delta\omega/\omega_0 = 3.5\%$ for the larger unit cell including 164 cylinders. Only the two larger unit cells repeat the central octagonal feature consisting of 17 cylinders of the tile feature of a tile side plus half the diagonal of a square (the tile feature associated with the most pominent diffraction peaks, illustrated by the green lines in figure 5.1), suggesting that Fourier components related to this feature are important for the formation of a sizeable PBG in this structure. Thus for small filling fractions, a minimum range of the quasicrystalline order must be present before the formation of significant band gaps, which is in agreement with the results of ref. [156], which showed similar behaviour in a photonic quasicrystal with 10-fold rotational symmetry.

For an intermediate filling fraction ($r = 0.24a$, filling fraction 22%), it can be seen that there is a sizeable PBG in the TE polarisation for all the unit cells considered. Again the largest band gap is found for the unit cell based on 82 cylinders of the quasicrystal,

and has a relative width of $\Delta\omega/\omega_0 = 9.4\%$. For a large filling fraction of the air cylinders ($r = 0.34a$, filling fraction 44%), two band gaps occur in the TE bandstructure for all sizes of unit cell considered. The first of the band gaps is centred around $\omega a/(2\pi c) = 0.31$ and the second around $\omega a/(2\pi c) = 0.40$. The maximum width of both band gaps occurs for the unit cell based on 28 cylinders, and the gaps have relative widths of $\Delta\omega/\omega_0 = 6.2\%$ and 6.8% respectively. A small band gap also occurs in the TM bandstructure of this photonic crystal, at around $\omega a/(2\pi c) = 0.42$, but is not shown in this thesis.

It is also apparent from the TE bandstructures of figure 5.4 that the band gap edges become "flatter" with increasing size of the unit cell used to construct the photonic crystal, reflecting less anisotropy in the spectral position and relative width of the PBG. Defining $(\Delta\omega)_{min}$ and $(\Delta\omega)_{max}$ as the minimum and maximum width of the photonic band gap for any particular direction in the photonic quasicrystal, a measure of the anisotropy of the band gap width can be taken as

$$\eta = \frac{(\Delta\omega)_{max} - (\Delta\omega)_{min}}{\omega_0} \tag{5.3}$$

where ω_0 is the centre frequency of the band gap. The anisotropy value η has been calculated from the bandstructures in figure 5.4 for the four sizes of unit cell for air cylinders of radius $r = 0.17a$, $0.24a$, and $0.34a$ and the results are shown in table 5.2. It can be seen that increasing the size of the unit cell, and therefore increasing the range of local quasicrystalline order, decreases the anisotropy displayed in the width of the photonic band gap. This reduction in the anisotropy of the PBG can be attributed to the increase in the range of the quasicrystalline order in the crystal.

Figure 5.6 shows the calculated reflection and transmission coefficients for the photonic crystal with a quasicrystalline unit cell of 164 cylinders and with a cylinder radius of $r = 0.17a$. The TE-polarised spectra are shown in red, and the TM-polarised spectra in blue, and they were calculated by the combination of transfer matrix and multiple scattering methods described in section 3.3. The sample modelled was one unit cell thick and periodic boundary conditions were applied at the top and bottom edges of the unit cell. Significant transmission dips occur for both polarisations for the frequency range $\omega a/(2\pi c) = [0.20, 0.23]$, with the TE polarisation displaying a minimum transmission of 0.10, and the TM polarisation of 0.45. The TE bandstructure of the corresponding photonic crystal (figure 5.4, bottom right) displays a PBG in the same frequency range, and this transmission dip can be seen to be a

r/a	L/a	$\omega_0 a/(2\pi c)$	$\Delta\omega/\omega_0$	$(\Delta\omega)_{min}$	$(\Delta\omega)_{max}$	η
0.17	3.41424	0.227	0.9%	0.00202	0.0258	10.5%
	4.82848	0.227	1.0%	0.00223	0.0185	7.2%
	8.24212	0.231	4.0%	0.00936	0.0172	3.4%
	11.6568	0.230	3.5%	0.00813	0.0141	2.6%
0.24	3.41424	0.247	6.8%	0.0170	0.0425	10.3%
	4.82848	0.248	6.9%	0.0170	0.0307	5.5%
	8.24212	0.253	9.4%	0.0238	0.0307	2.7%
	11.6568	0.252	8.9%	0.0227	0.0261	1.3%
0.34	3.41424	0.305	5.4%	0.0168	0.0442	9.0%
	4.82848	0.309	6.2%	0.0223	0.0293	2.3%
	8.24212	0.319	4.4%	0.0140	0.0281	4.4%
	11.6568	0.316	4.6%	0.0147	0.0200	1.7%

Table 5.2 Frequencies, widths and anisotropies of the lowest photonic band gap for photonic crystals with octagonal quasicrystalline unit cells.

consequence of the photonic band gap in the bandstructure. Since only the finite structure is considered in the direction of incident and transmitted light, the stop bands in the spectra for the TE-polarisation are a result of the quasicrystalline order, and not due to periodicity. The coincidence of the stop bands in the reflection spectra and the band gaps in the bandstructure for the TE-polarisation would seem to suggest that the band gaps are due to the short-range quasicrystalline order, and not the longer range periodicity of the crystal. This agrees with the conclusions of past studies [148].

The behaviour of the PBG as a function of the filling fraction has also been investigated for photonic crystals with a quasicrystalline unit cell containing 164 cylinders. The TE band-structures have been calculated for unit cells with cylinder radii $r = 0.12, 0.13, \ldots, 0.37, 0.38$, with each of the twenty-eight calculations performed using a basis set of 10201 plane waves. Figure 5.7 shows the bands as a function of filling fraction, where the grey shaded regions represent allowed photonic bands and the intervening regions are the PBGs.

The main band gap begins to open at a filling fraction of the air cylinders of just 7%. This gap is at a maximum relative width of 10.4% which is acheived for filling fractions of around 30%. For filling fractions of above 20%, other band gaps open up in the bandstructure at lower and higher frequencies to the main band gap. The band gaps tend to shift to higher frequencies with increasing filling fractions of the air cylinders. This is because as the filling fraction of air increases, the average dielectric constant of the unit cell decreases, and the free photon dispersion gradient increases. Thus the photonic bands tend to stretch out along

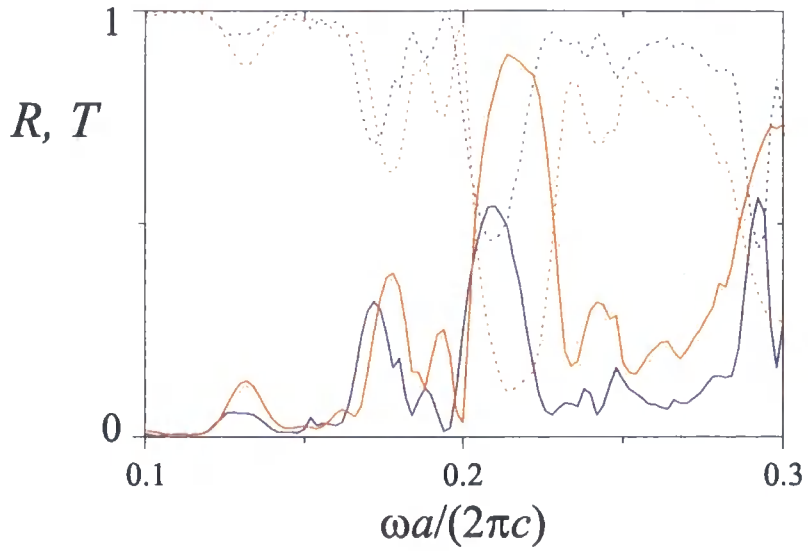

Figure 5.6 Reflection (solid lines) and transmission (dotted lines) spectra for a photonic crystal with a quasicrystalline unit cell and cylinder radii $r = 0.17a$ for the TE polarisation (red) and TM polarisation (blue).

this increased gradient, shifting the band gaps to higher frequencies.

5.1.3 Effective medium estimates

By characterising a photonic crystal with its average refractive index, an estimate can be obtained as to the frequency one would expect to find any band gaps due to Bragg-like scattering. If a light wave propagates in a structure for which the spatially varying relative permittivity has substantial distinct Fourier components related to some reciprocal lattice vector $\mathbf{G}$, the wave can be reflected back anti-parallel to the incident wave if the magnitude of its wavevector $|\mathbf{K}|$ ($\approx \langle n \rangle \omega/c$, where $\langle n \rangle$ is the mean refractive index) is equal to $|\mathbf{G}|/2$.

The octagonal quasicrystalline structure under study has four series of distinct Fourier components. Using the symbolic four-dimensional notation, these four series are related to the reciprocal lattice vectors (1000), (1001), (1010) and (1100). The magnitudes of the vectors are given in table 5.1. Thus the centre of the band gaps ω_0 due to scattering from these reciprocal lattice vectors is estimated as

$$\frac{\omega_0 a}{2\pi c} = \frac{1.171573}{2\langle n \rangle}\frac{G}{F} \tag{5.4}$$

The dotted black lines in figure 5.7 show the estimated values of the centre frequencies of the band gaps due to Bragg-like scattering from the indicated series of reciprocal lattice vectors.

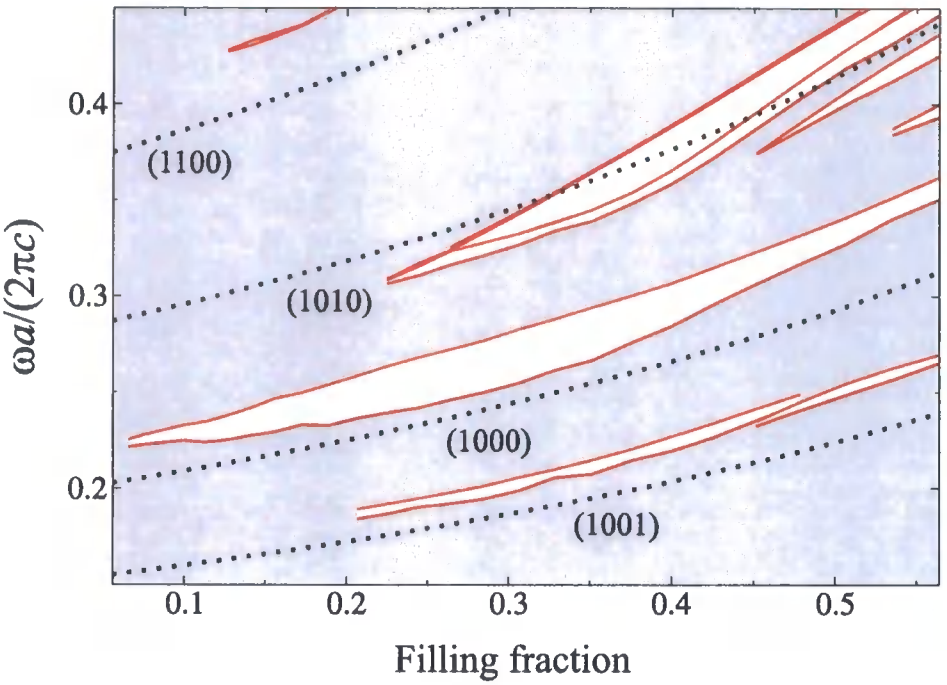

Figure 5.7 Diagram of allowed bands in the TE bandstructure as a function of the filling fraction of air cylinders in the photonic crystal with a unit cell based on 164 cylinders of the quasicrystal. Grey regions indicate allowed photonic bands, and white regions indicate the photonic band gaps. Red lines are the spectral positions of the band gap edges. Dotted lines indicate the centre of photonic band gaps as estimated from Bragg-like diffraction from certain indicated directions in the quasicrystalline unit cell.

The most prominent series of peaks in the diffraction pattern are those related to the (1000) vector, and it can be seen that the values that this simple estimate gives for the position of the main band gap is accurate to within 12% of the "full" plane wave calculations presented earlier. Thus it can be concluded that this main band gap is associated with Bragg-like scattering from planes within the quasicrystalline structure that have a period of half the sum of a tile side and half the diagonal of a square tile, which is the tile element associated with the (1000) series of diffraction peaks.

5.1.4 Electromagnetic field profiles

The plane wave method used for the calculation of the eigenfrequencies (bandstructure) of the 2D photonic crystal with an octagonal quasicrystalline unit cell can also be used to calculate the eigenvectors or electromagnetic field profiles of the eigenmodes. This has been done for six eigenmodes of the structure when $r = 0.17a$ (figure 5.8), $r = 0.24a$ (figure 5.9) and $r = 0.34a$ (figure 5.10). In these figures, (a), (b) and (c) show eigenmodes in the

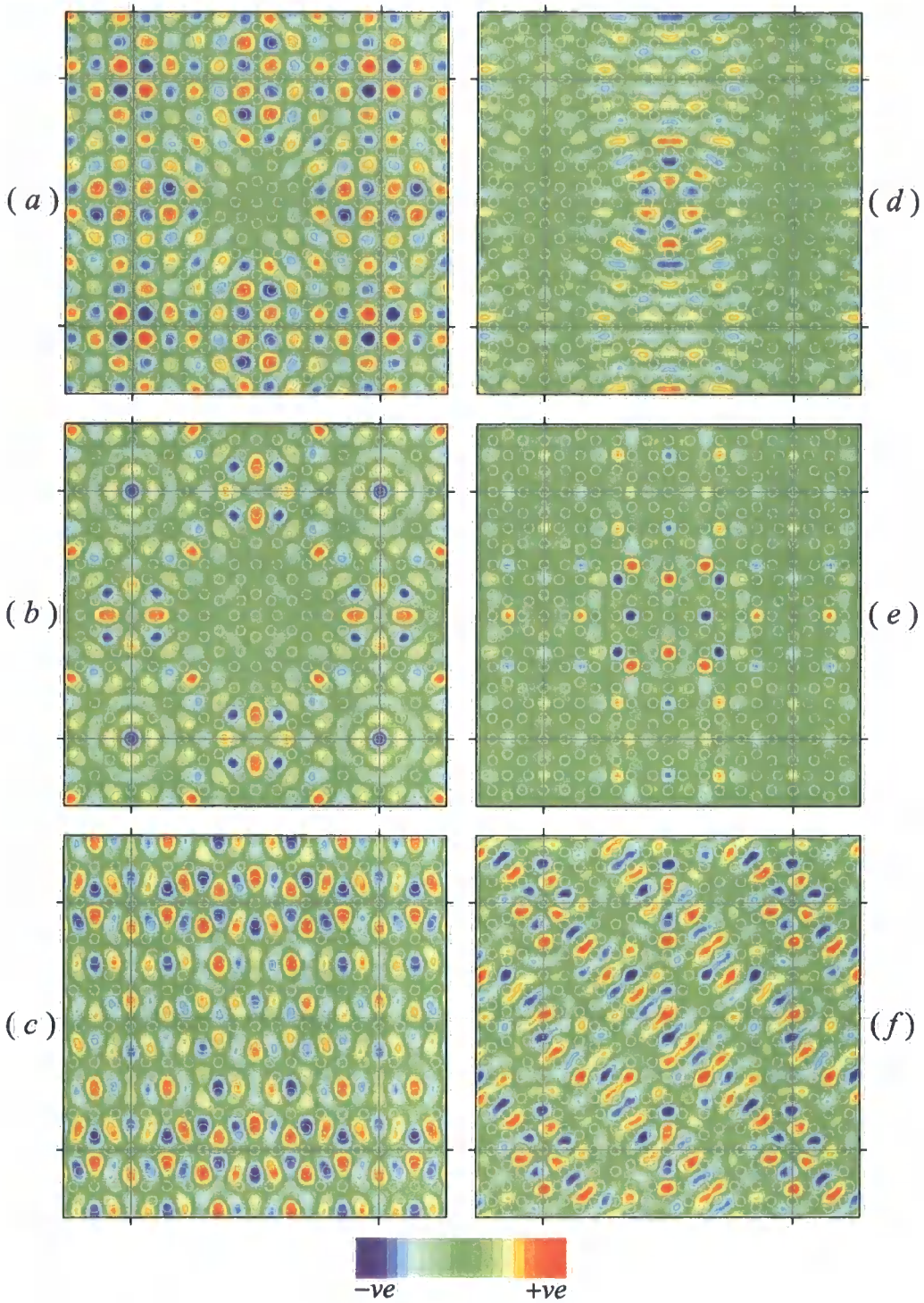

Figure 5.8 Magnetic field profiles of selected eigenmodes at the Γ point of the 2D photonic crystal with a unit cell of 164 air cylinders of radius $r = 0.17a$ based on the octagonal quasicrystalline geometry shown in figure 5.1. (a), (b) and (c) are states in the dielectric band, and (d), (e) and (f) are in the air band. The eigenfrequencies of the states are $\omega a/(2\pi c) = 0.2122$ (a), 0.2172 (b), 0.2262 (c), 0.2343 (d), 0.2389 (e), and 0.2420 (f).

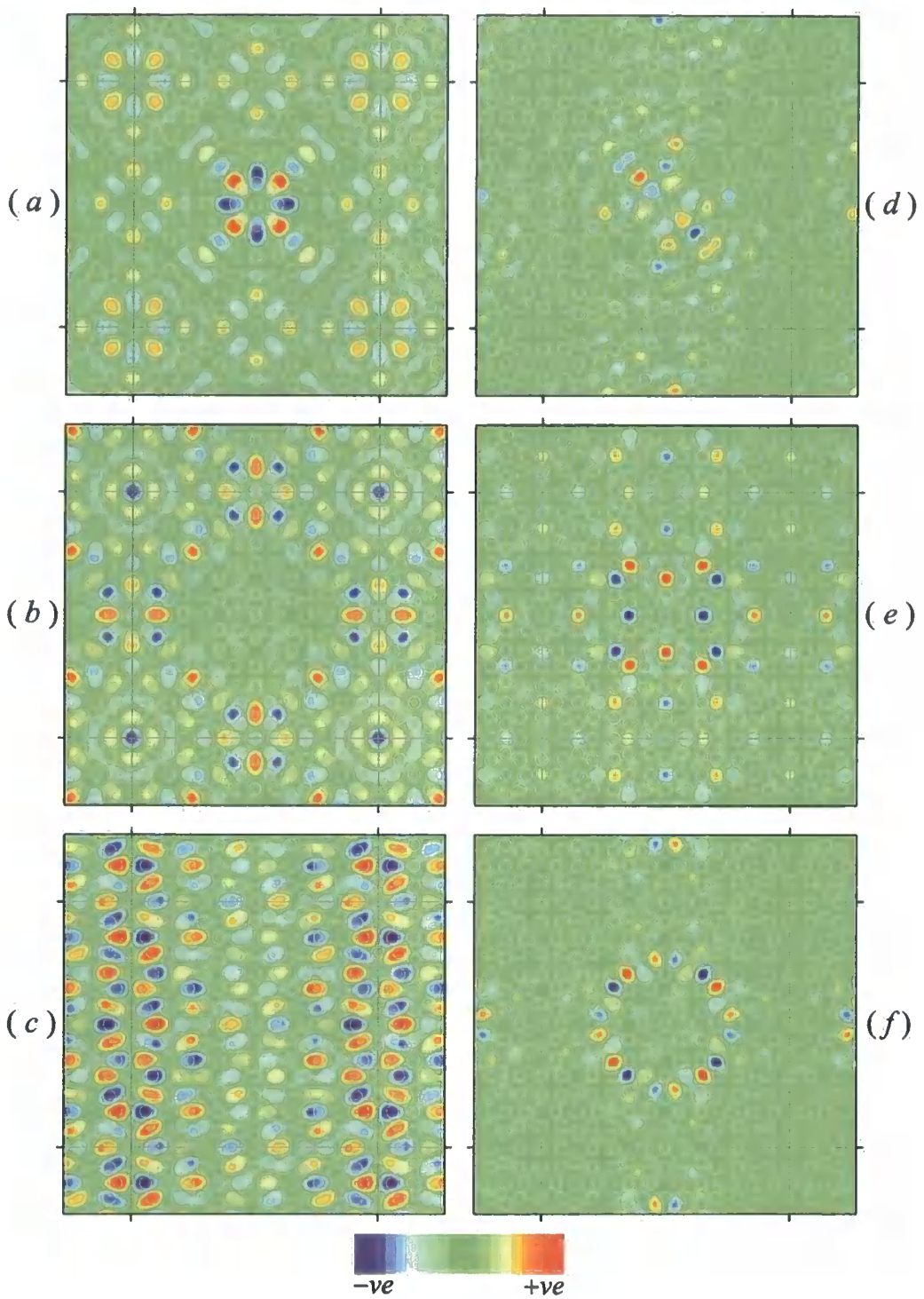

Figure 5.9 Magnetic field profiles of selected eigenmodes at the Γ point of the 2D photonic crystal with a unit cell of 164 air cylinders of radius $r = 0.24a$ based on the octagonal quasicrystalline geometry shown in figure 5.1. (a), (b) and (c) are states in the dielectric band, and (d), (e) and (f) are in the air band. The eigenfrequencies of the states are $\omega a/(2\pi c) = 0.2273$ (a), 0.2312 (b), 0.2405 (c), 0.2633 (d), 0.2656 (e), and 0.2702 (f).

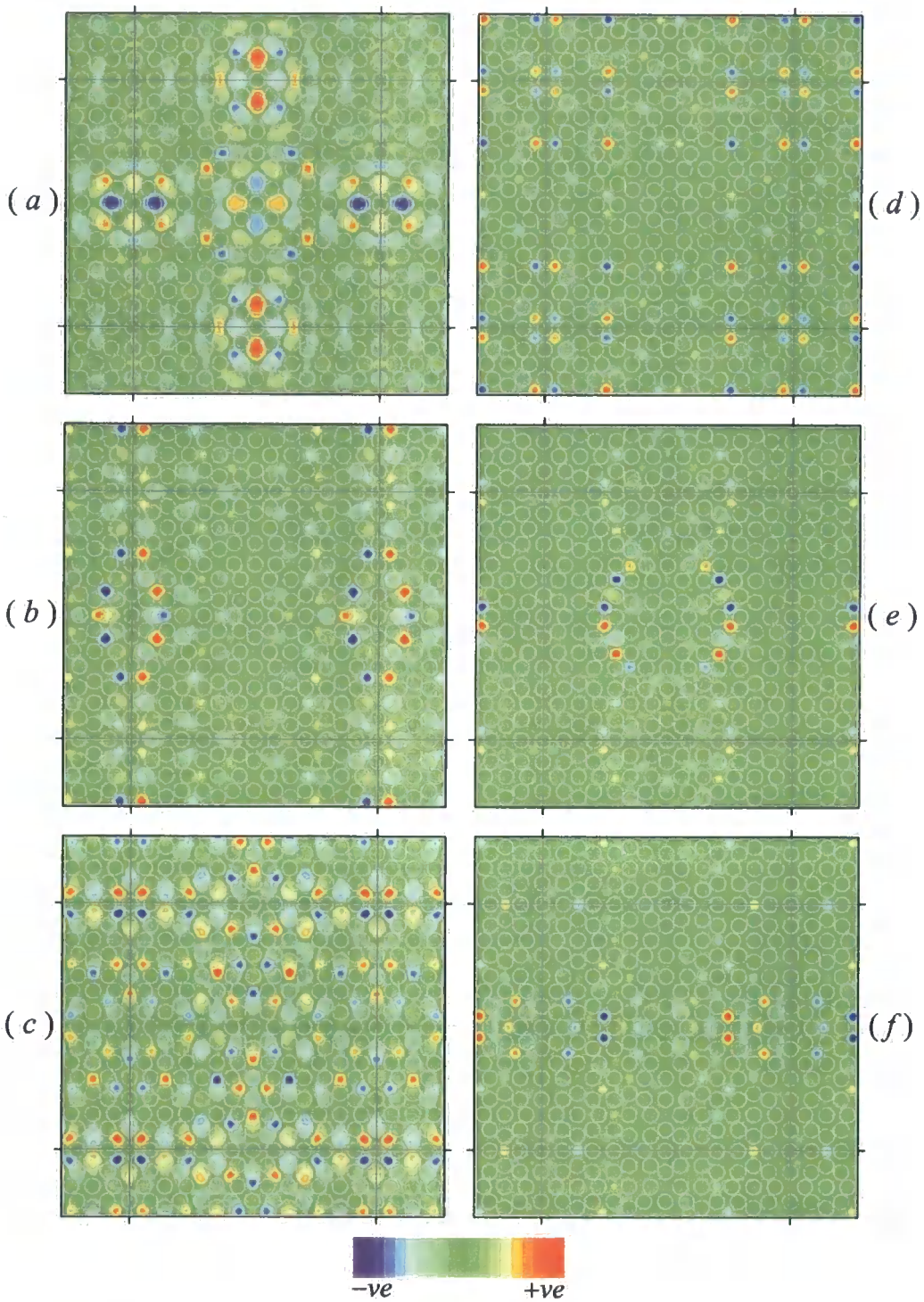

Figure 5.10 Magnetic field profiles of selected eigenmodes at the Γ point of the 2D photonic crystal with a unit cell of 164 air cylinders of radius $r = 0.34a$ based on the octagonal quasicrystalline geometry shown in figure 5.1. (a), (b) and (c) are states in the dielectric band, and (d), (e) and (f) are in the air band. The eigenfrequencies of the states are $\omega a/(2\pi c) = 0.2890$ (a), 0.2945 (b), 0.3083 (c), 0.3230 (d), 0.3324 (e), and 0.3361 (f).

dielectric (or photonic valence) band and (d), (e) and (f) show eigenmodes in the air (or photonic conduction) band. The states shown in (c) and (d) are the states at the edge of the PBG, and the frequencies of the eigenstates are given in all cases in the figure captions. The electromagnetic field profiles display the strict four-fold rotational symmetry of the square lattice used. Also many of the states shown have a concentration of the electromagnetic energy density at the edges and corners of the unit cell, for example figure 5.8 (a) or (b) or figure 5.9 (a) or (b). The edges of the unit cell are where the quasicrystalline order is broken, and hence they can be considered as defect points (corners) or planes (edges) of a quasicrystal. As such, the electromagnetic field can be localised on these defects.

5.2 Microcavities in photonic quasicrystals

Calculations in section 5.1 have demonstrated that photonic crystals made up of octagonal quasicrystalline unit cells based on Ammann-Beenker tiling decorated with air cylinders in a dielectric background can support a complete 2D photonic band gap in the TE-polarised band structure. This section describes studies of the optical properties of vacancies in such structures. We show that the vacancies form microcavities in the photonic quasicrystal, and if the eigenfrequencies of the cavity modes are within the photonic band gap of the structure, localised modes to can occur in the cavity region. The lack of translational symmetry in photonic quasicrystals means that there are many inequivalent points at which to site the vacancies in order to form a microcavity. This range of inequivalent vacancy sites means that there are many possibilities when designing microcavities with localised states of desirable properties in photonic quasicrystals. Refs. [147] and [148] have studied the properties of vacancies in complementary photonic structures to the one studied here—one consisting of dielectric rods decorating the Ammann-Beenker tiling in air.

This section describes the properties of four different cavities in the octagonal quasicrystalline structure, labelled cavity A, cavity B, cavity C and cavity D. The method of calculation is similar to that used in section 5.1—a square supercell of local octagonal quasicrystalline order is constructed, from which a cylinder or cylinders are removed to form the microcavity. The chosen supercell is a square of side length $L = 11.6568a$ (see figure 5.1). Cavity A consisting of a single vacancy at the centre of the supercell, as shown by the inset of figure 5.11,

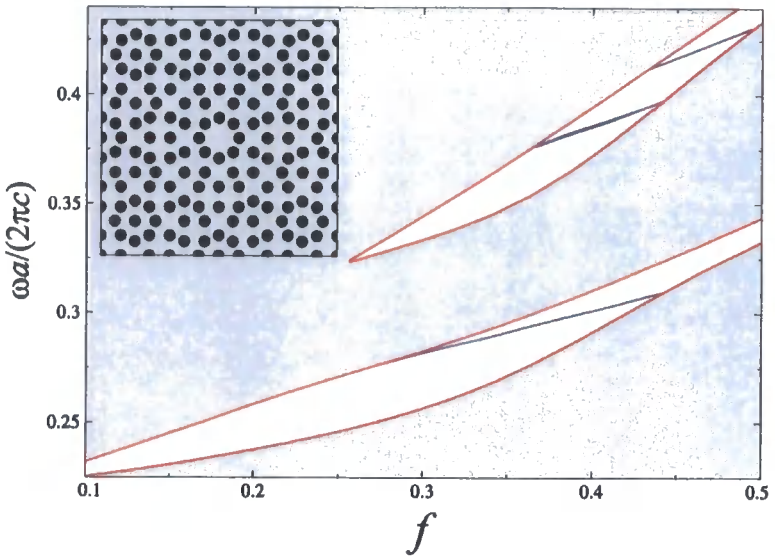

Figure 5.11 Calculated eigenfrequencies (blue lines) of the localised modes of the microcavity structure illustrated (inset) as a function of the filling fraction f of the air cylinders. Grey regions indicate the allowed photonic bands, and red lines are the eigenfrequencies of the edge states of the PBG, shown by the intervening white regions. (Inset) An illustration of the microcavity structure labelled "cavity A" in the text.

will be discussed in section 5.2.1. A larger cavity, cavity B, created by removing the central 9 cylinders in the quasicrystal is studied in section 5.2.2. Section 5.2.3 studies the properties of cavities C and D, created by removing a cylinder from two inequivalent points in the quasicrystalline lattice. The eigenfrequencies of the cavity modes have been calculated for cylinder radii of $r = 0.12a$, $0.13a$, ..., $0.37a$, and $0.38a$. Each of the 27 calculations for each cavity used a plane wave basis set of 10201 plane waves, which ensures convergence of the eigenvalues, even for the large supercell under consideration (see figure 5.3).

5.2.1 Cavity A

Cavity A is created by removing the central cylinder from the octagonal quasicrystal, as shown by the inset of figure 5.11. The eigenfrequencies of the resulting localised states are shown as a function of the filling fraction f of the air cylinders in the supercell by the blue lines of figure 5.11. Figure 5.11 shows the allowed photonic bands of the photonic quasicrystal as grey regions, and the intervening white regions are the photonic band gaps. The red lines represent the frequencies of the band gap edge states. It can be seen that there are no localised states for small filling fractions below 27%. For intermediate filling fractions between 27% and 44%, there is one localised state in the first band gap of the

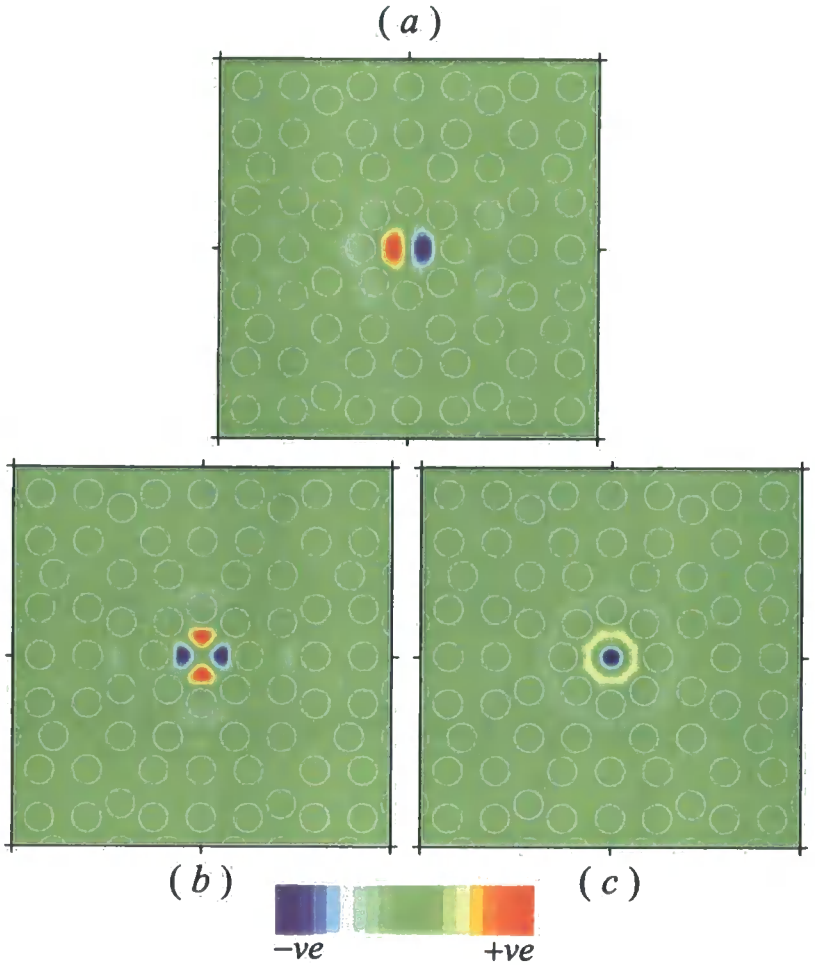

Figure 5.12 Profiles of the amplitude of the magnetic field for the localised eigenmodes of the microcavity structure labelled "cavity A" in the text for a cylinder radius (filling fraction) of $r = 0.34a$ ($f = 0.44$). Grey circles indicate the positions of the air cylinders in the structure.

photonic quasicrystal. The magnetic field profile of this mode is shown in figure 5.12 (a) for a structure with cylinder radii of $0.34a$ (filling fraction $f = 0.44$). It can be seen that the state is indeed localised on the vacancy site, and (following the same naming convention as in section 4.2.1) the mode can be characterised as a dipole mode. For intermediate and larger filling fractions, modes with frequencies in the second band gap are supported by the vacancy. For the structure with cylinder radius $r = 0.34a$ ($f = 0.44$), all three of these localised modes exist in the same structure, and are shown in figure 5.12; the modes with eigenfrequencies in the second band gap are in (b) and (c), and are quadrapole and monopole modes respectively.

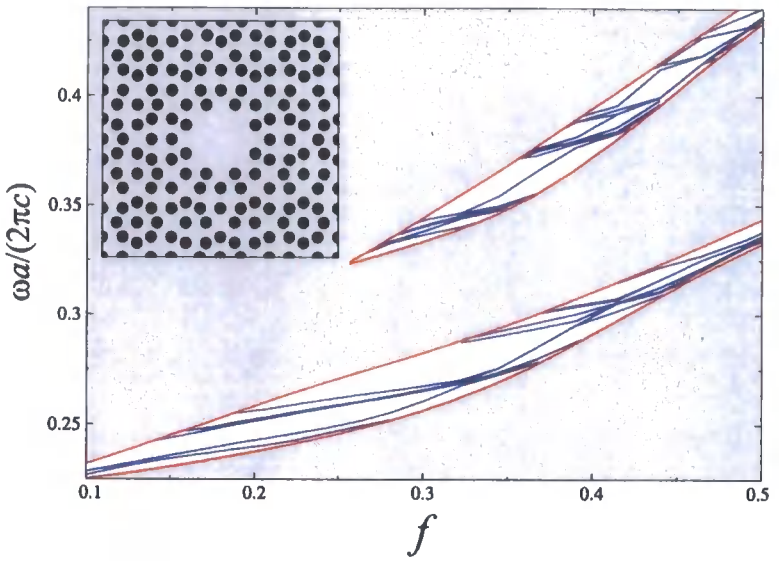

Figure 5.13 Calculated eigenfrequencies (blue lines) of the localised modes of the microcavity structure illustrated (inset) as a function of the filling fraction f of the air cylinders in the structure illustrated. Grey regions indicate the allowed photonic bands, and red lines are the eigenfrequencies of the edge states of the PBG, shown by the intervening white regions. (Inset) An illustration of the microcavity structure labelled "cavity B" in the text.

5.2.2 Cavity B

Cavity B is created by removing the central 9 cylinders from the photonic quasicrystal—the resulting cavity is approximately three times larger in "radius" than cavity A considered in section 5.2.1 and is illustrated in the inset to figure 5.13. It was seen that cavity A supported only three distinct localised modes for the two lowest frequency band gaps, because the band gaps are at low frequencies. For a cavity to support a localised mode at a frequency in a band gap of the photonic crystal, the optical size of the cavity must be a least half the wavelength of the frequency of the band gap. The larger optical size of cavity B should enable the cavity to support more localised modes, of lower frequencies, than cavity A. Indeed, figure 5.13 shows the frequencies of modes localised on cavity B, and shows that many more localised modes are supported for the whole range of filling fractions considered.

For small filling fractions ($f < 0.15$) two localised modes are supported in the lowest band gap. These modes are shown in figure 5.14 for the structure with a cylinder radius of $r = 0.17a$. For intermediate and large filling fractions, many more modes are supported by the cavity. For example, five localised modes exist when $r = 0.24a$ ($f = 0.22$) and the magnetic field profiles of these modes are shown in figure 5.15. The lowest two frequency modes are both dipole modes and are shown in (a) and (b). (c) and (d) show higher frequency

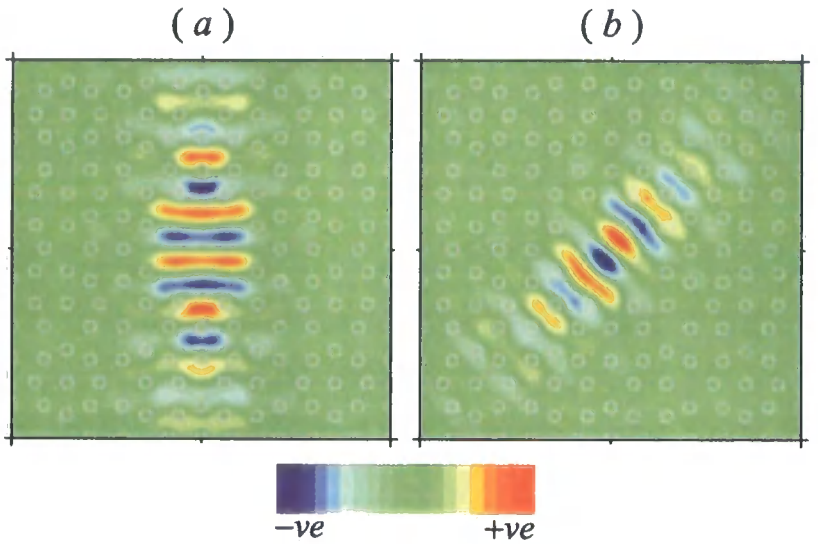

Figure 5.14 Profiles of the amplitude of the magnetic field for the localised eigenmodes of the microcavity structure labelled "cavity B" in the text for a cylinder radius (filling fraction) of $r = 0.17a$ ($f = 0.11$). Grey circles indicate the positions of the air cylinders in the structure.

modes characterised as quadrapole modes. (d) shows the highest frequency mode, which is an octapole mode which is antisymmetric under rotations of $\pi/4$.

If the crystalline nature of the supercell approximation is taken into account, then the interaction of the localised modes of microcavities in neighbouring unit cells actually causes the formation of photonic minibands. Figure 5.16 shows the calculated dispersion of the minibands for the localised modes whose field profiles are shown in figure 5.14 and 5.15. In fact, the localised cavity eigenmodes presented in figure 5.14 and 5.15 are actually the field profiles of the crystal eigenmodes at the Γ-point in the first Brillouin zone in reciprocal space when a square unit cell of quasicrystalline order containing the microcavities is considered. The equivalent bandstructure of the photonic crystal with a quasicrystalline unit cell (i.e. no microcavities) are also shown in figure 5.16 for comparison.

When the air cylinders have a radius $r = 0.17a$, then cavity B is seen to result in four photonic minibands. These minibands form two pairs of doubly degenerate states at the highly symmetric Γ and M points in the first Brillouin zone of the square superlattice. They are able to do this as the eigenmode field profiles possess some of the same symmetries as as the crystal. For example, the mode shown by figure 5.14 (a) is physically identical if it is allowed to be rotated through an angle of $\pi/2$, and as long as suitable combinations of degenerate eigenmodes are chosen so as to ensure orthogonality, this is exactly what one

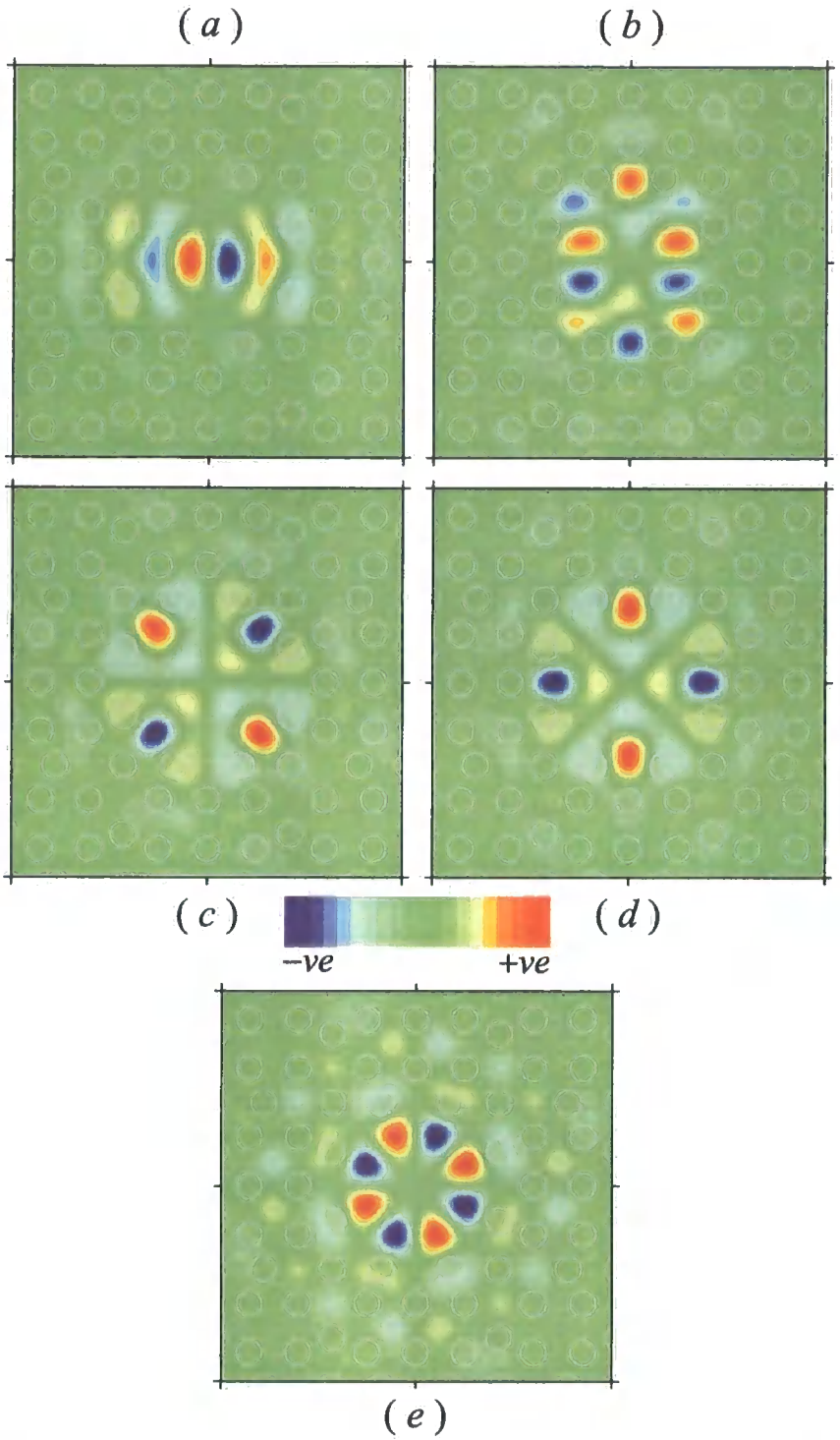

Figure 5.15 Profiles of the amplitude of the magnetic field for the localised eigenmodes of the microcavity structure labelled "cavity B" in the text for a cylinder radius (filling fraction) of $r = 0.24a$ ($f = 0.22$). Grey circles indicate the positions of the air cylinders in the structure.

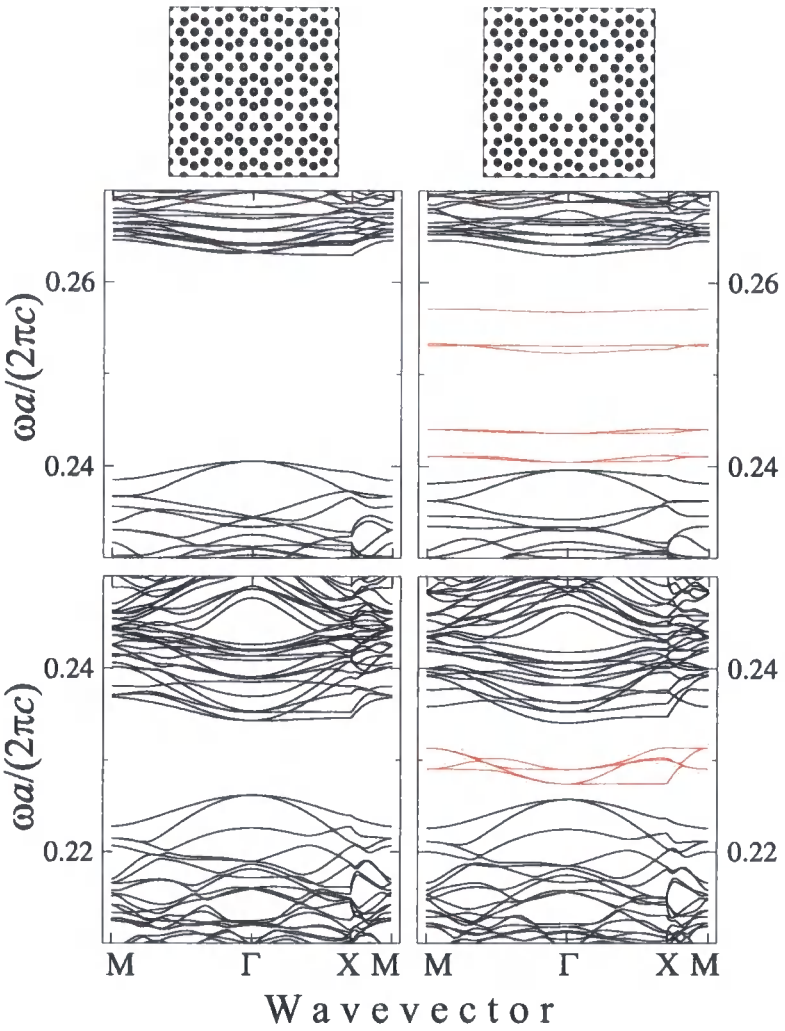

Figure 5.16 Bandstructure of the crystal with the illustrated unit cell for air cylinders of radius $r = 0.17a$ (bottom) and $r = 0.24a$ (top). Photonic minibands of cavity modes are highlighted in red.

sees—the second degenerate mode has a field profile identical to figure 5.14 (a) but rotated through $\pi/2$. Away from the highly symmetric Γ and M points, the degeneracy of these two modes is lifted, and four distinct minibands of photonic states are seen. By inspection of the magnetic field profiles of figure 5.14, it can be seen that there is a large overlap of the localised modes in adjacent unit cells of the crystal. This is reflected in the band structure of figure 5.16 by the relatively large width of the associated minibands. In fact, the width of the minibands is larger than the frequency separation between them, such that the minibands overlap to form one continuous band of allowed states in the photonic band gap. The large width of the associated minibands means that the eigenfrequencies of the two modes of the vacancy in the photonic quasicrystal cannot accurately be calculated. Such a calculation would require a larger supercell to be employed, such that the vacancies in neighbouring

Eigenfrequency $\omega a/(2\pi c)$	Symmetries	Figure 5.15
0.241	dipole	(a)
0.244	dipole	(b)
0.253	quadrapole	(c) and (d)
0.257	octapole	(e)

Table 5.3 Eigenfrequencies and properties of eigenmodes for "cavity B" (described in text) in photonic quasicrystal with air cylinders of radii $r = 0.24a$.

supercells do not interact, and the width of the minibands is reduced.

The bandstructure of the photonic quasicrystal when $r = 0.24a$ shows many interesting features. The dipole modes of figure 5.15 (a) and (b) form two pairs of doubly degenerate eigenmodes at the Γ and M points of the first Brillouin zone of the super-lattice. However, the quadrapole modes of figure 5.15 (c) and (d) are split in frequency at the Γ point in the first Brillouin zone. For an isolated defect in an otherwise perfect quasicrystalline structure, the symmetry of the quasicrystal would mean that the two modes shown by figure 5.15 (c) and (d) are identical and have the same frequency. This is because they share some of the symmetries of the octagonal photonic quasicrystal, in that rotation of figure 5.15 (c) by an angle of $\pi/4$ results in the field pattern shown by figure 5.15 (d). However, rotations through an angle of $\pi/4$ is not a symmetry of the crystal, and so the imposition of periodic boundary means that the field profiles of the eigenmodes are aligned differently within the square supercell to each other. The octapole mode, whose magnetic field profile is shown by figure 5.15 (e) displays the symmetry of the octagonal quasicrystal, and so this mode is not degenerate with any other.

The small overlap of field profiles from the mode localised on neighbouring microcavities for the structure with $r = 0.24a$ results in a narrow width of the associated photonic minibands in the bandstructure of the superlattice. Thus the eigenfrequencies of the cavity modes can be found with reasonable accuracy from the frequencies of the minibands, and these are shown in table 5.3, along with the properties of the eigenmodes.

5.2.3 Cavities C and D

The microcavities studied in section 5.2.1 and section 5.2.2 maintain the octagonal symmetry of the photonic quasicrystal in which they are embedded. However, the lack of trans-

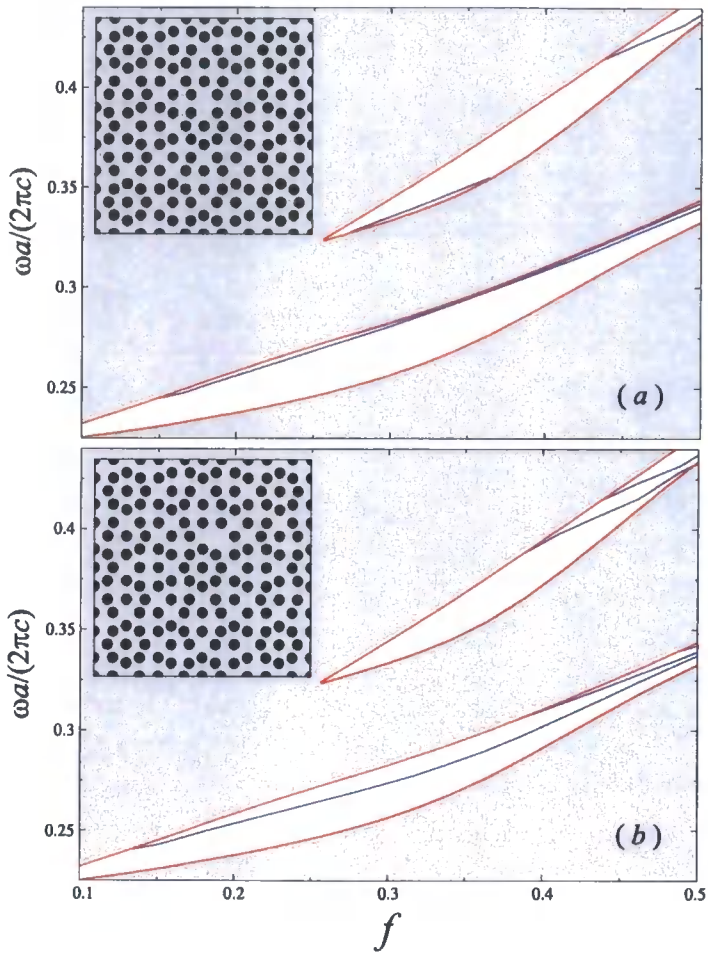

Figure 5.17 Calculated eigenfrequencies (blue lines) of the localised modes of the microcavity structure illustrated (inset) as a function of the filling fraction f of the air cylinders. Grey regions indicate the allowed photonic bands, and red lines are the eigenfrequencies of the edge states of the PBG, shown by the intervening white regions. (Inset) An illustration of the microcavity structure labelled "cavity C" (a) and "cavity D" (b) in the text.

lational symmetry of the photonic quasicrystal means that there are many inequivalent points at which vacancies could be sited in order to form a microcavity in the structure, and these vacancies will not maintain the rotational symmetry of the system. This section considers cavities formed by vacancies at two such inequivalent points—"cavity C" is a single vacancy in the central octagonal ring of 8 cylinders, as illustrated by the inset of figure 5.17 (a); and "cavity D" is a single vacancy as illustrated in figure 5.17 (b). It should be noted that these vacancies are chosen as examples, and many more inequivalent points exist in the structure to form cavities with their own unique properties.

Figure 5.17 shows the eigenfrequencies of modes localised on cavity C (a) and cavity D (b) as a function of the filling fraction f of the air cylinders in the crystal. In figure 5.17 the grey regions indicate the allowed photonic bands of the crystal, and the intervening white

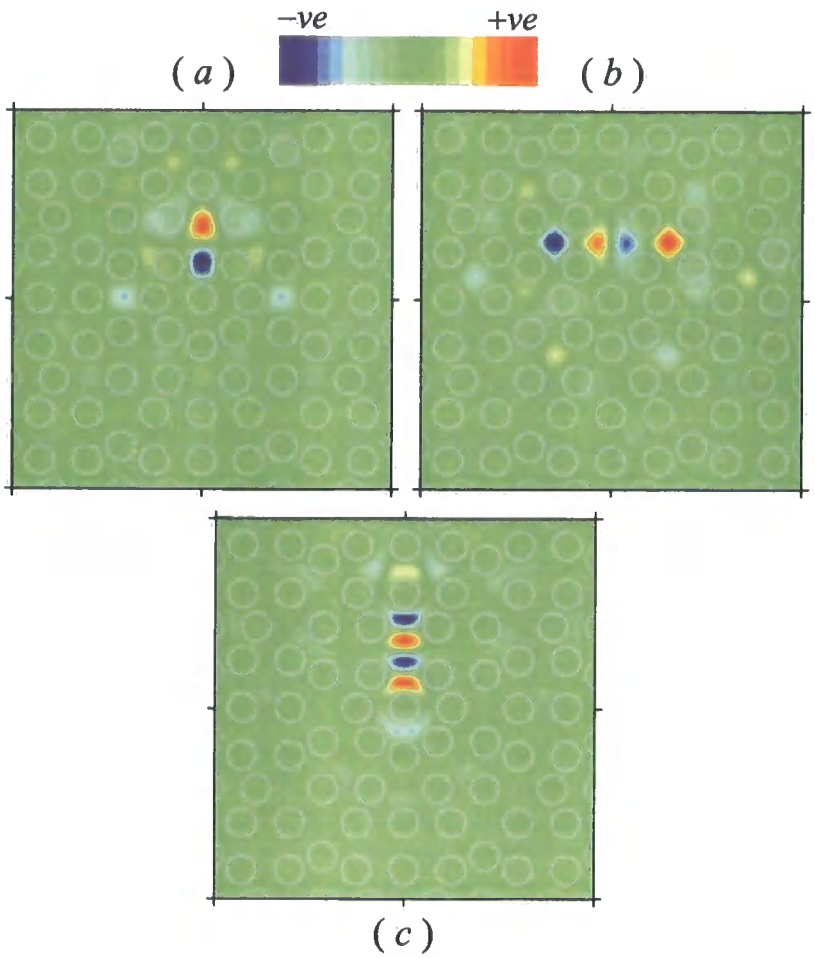

Figure 5.18 Profiles of the amplitude of the magnetic field for the localised eigenmodes of the microcavity structure labelled "cavity C" in the text for a cylinder radius (filling fraction) of $r = 0.34a$ ($f = 0.44$). Grey circles indicate the positions of the air cylinders in the structure.

regions are the photonic band gaps. In both cases, there is a single localised cavity mode for small filling fractions of $f > 0.15$, and for larger filling fractions more localised modes are supported. When the cylinder radius (filling fraction) reaches $r = 0.34a$ ($f = 0.44$), cavity C supports three localised modes, shown in figure 5.18, and cavity D supports four localised modes, shown in figure 5.19. Although there is no rotational symmetry in the system, the modes can be characterised by considering the symmetry of the modes with respect to the cavity itself. For example, the three modes of cavity C shown in figure 5.18 possess symmetry about lines drawn horizontally and vertically through the centre of the microcavity. Also, in general, the higher frequency modes have more complicated field profiles, which possess more nodes and anti-nodes than those of lower frequency.

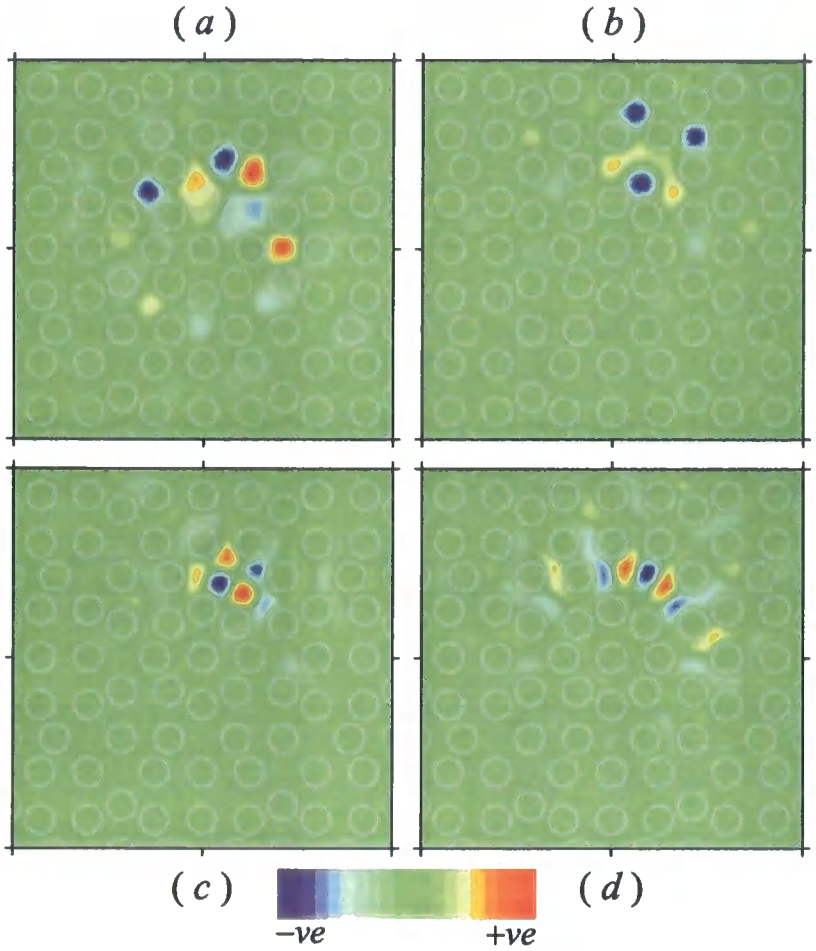

Figure 5.19 Profiles of the amplitude of the magnetic field for the localised eigenmodes of the microcavity structure labelled "cavity D" in the text for a cylinder radius (filling fraction) of $r = 0.34a$ ($f = 0.44$). Grey circles indicate the positions of the air cylinders in the structure.

5.3 Conclusions

This chapter has been concerned with the bandstructure of a 2D photonic crystal with a square unit cell based on an octagonal quasicrystalline tiling. The presence of a photonic band gap for the TE-polarised bandstructure is demonstrated for a wide range of parameters of the structure. The bandstructure was investigated as a function of the size of the quasicrystalline unit cell, and it is found that the larger unit cells possess more isotropic band gaps due to the increase of the range of the quasicrystalline order, although in all the cases studied, the widest band gaps were found for intermediate sized unit cells. It is shown that for small filling fractions the repetition of certain features in the quasicrystalline unit cell as it is made larger is coincident with the opening up of a substantial photonic band gap in the TE-polarised bandstructure. These same features of the quasicrystalline unit cell are

also associated with the main peaks in the calculated diffraction pattern, and estimates of the position of the band gap from an effective medium approximation suggest that the band gaps are due to Bragg-like diffraction from planes associated with these features.

By considering the largest quasicrystalline unit cell as a photonic quasicrystal in a supercell approximation, it is seen that octagonal photonic quasicrystal possess photonic band gaps. The calculated reflection and transmission spectra through a single unit cell for small filling fractions display stop bands in the same spectral range as the calculated photonic band gaps, suggesting that the band gap formation is due to the local octagonal quasicrystalline order of the unit cell, and not due to the periodicity of the supercell approximation. However, it was also shown that the electromagnetic field profiles of the eigenmodes display the strict four-fold rotational symmetry of the square supercell, and that states can be localised on "defects" caused by the breaking of the aperiodic quasicrystalline order in the crystal.

The properties of modes with frequencies in the photonic band gap and localised on microcavities in the photonic quasicrystal were also examined, and the profile of the amplitude of the magnetic field have been calculated for the modes of several structures. Localised microcavity modes in the photonic quasicrystal with the symmetry of the supercell are shown to be split in frequency by the periodic boundary conditions of the supercell approximation.

Chapter 6

Excitonic interactions of light in photonic structures

Quantum wells [161, 162] are planar heterostructures engineered to produce a potential profile that confines electrons and holes to a plane. This confinement discretises the allowed energies of the electron and holes into sub-bands (the electrons/holes are still free within the plane of the quantum well), as long as the size of the quantum well is less than the mean free path of the electrons and holes. The confining potential can be produced in many ways, but perhaps the most conceptually simple is the so-called type I quantum well, which consists of a thin layer of semiconductor embedded in another semiconductor of a larger band gap between the electron valence and conduction bands. This difference in band gaps leads to a finite square well potential, which can confine electrons in the conduction band and holes in the valence band.

Excitons are electron-hole pairs, bound together by the Coulomb attraction between them. When an exciton is created in a quantum well, it is confined close to the 2D plane of the quantum well, and is referred to as a quantum well exciton. The energy of the exciton depends on the structural details of the quantum well, as it is dependent on the nature of the electron and hole sub-bands and the form of the Coulomb interaction between the electron and hole will depend on the dielectric properties of the heterostructure and the carrier's confinement. Excitons can be formed from the carriers created by incident light promoting an electron from the valence band of the quantum well to the conduction band. The frequency of the light required to do this must be greater than the band gap plus the confinement ener-

gies of the lowest electron and hole sub-bands in the quantum well. Pairs of electrons and holes can then relax into bound exciton states, before radiatively recombining, which results in a chain of resonant light-exciton interactions.

Quantum well excitons possess a dipole moment which contributes to the dielectric polarisation of the quantum well near the exciton resonance. This interaction between excitons and the incident light results in a polariton effect, consisting of a coherent chain of light absorption-emission processes by an exciton. Thus the quantum well exciton can reflect the incident light. Exciton-polaritons are part-matter part-light quasi-particles formed by this interaction between the exciton's dipole moment and light in the quantum well. Exciton-polaritons combine the properties of electromagnetic modes (high group velocities, large coherence lengths) and excitons (finite-effective masses, dipole moments, coupling by exchange interaction). The main thrust of interest in the study of polaritons is as a result of the realisation that exciton-polaritons, being bosons, should be able to coherently scatter into the ground state to form a Bose condensate, which could result in the emission of coherent, monochromatic light, which is currently referred to as the polariton laser effect [163, 164]. Theoretically such a process could form the basis of a threshold-less laser, as no population inversion is required for the lasing effect to occur.

Usually quantum well exciton-polaritons are studied in the context of microcavities—so called cavity polaritons [96, 165, 166]. A quantum well (or multiple quantum wells) is embedded in the cavity layer of a microcavity enclosed by two Bragg reflectors. The optical confinement provided by the microcavity greatly enhances the strength of the exciton-light coupling, allowing the strong coupling regime to be realised. The strong-coupling regime is realised when the splitting between the exciton-polariton modes (often referred to as the Rabi splitting) exceeds the width of the modes, allowing the splitting to be resolved in the reflection spectrum of the cavity-polaritons and is characterised by an anti-crossing of the exciton-polariton modes [94]. (The weak-coupling regime is realised when there is no splitting between the exciton-polariton modes, and occurs in devices such as vertical-cavity surface-emitting lasers (VCSELs).)

Strongly-coupled polaritons have been theoretically studied in a number of papers, see for example [94, 167–172]. Three optically active exciton-polariton modes are found, distinguished by their polarisation. Transverse (T) modes have TE-polarisation, and longitudinal

(L) and Z modes have TM-polarisation.

Another way of producing optical confinement is to embed the quantum well in a planar dielectric waveguide, where guided light modes are confined to the waveguide by total internal reflection. Such guided modes have an infinite theoretical lifetime in an ideal waveguide, and require the in-plane wavevector to exceed the magnitude of the waveguide in the cladding of the waveguide. Cavity polaritons with smaller in-plane wavevectors have a short lifetime of just a few picoseconds [96], which renders manipulation with them difficult. On the other hand, waveguide polaritons possessing large in-plane wavevectors propagate in the wave-guiding regime of light, and can have much longer lifetimes. The longer lifetimes derive from the lifetime of the waveguide mode—the light is confined to the waveguide and so the lifetime of the polariton is determined only by properties of the exciton. These long-lived polaritons could be more suitable for device applications. However, total internal reflection necessarily requires large angles of propagation of light in the waveguide (greater than the critical angle for total internal reflection) and the eigenstates of the waveguide polaritons thus cannot be observed by direct optical experiments, such as in transmission or reflection spectra. Thus it is important to correctly model the propagation of waveguide polariton modes and to calculate the electromagnetic field profiles induced in the waveguide structure by the waveguide polaritons.

This chapter first discusses the interaction of light with a quantum well exciton, and derives the reflection and transmission coefficients for evanescent plane waves incident upon the quantum well in the context of non-local dielectric response theory. The reflection of a quantum well placed behind a dielectric interface at which total internal reflection can take place is discussed, and it is shown that the excitonic response is greatly enhanced when angles of incidence close to the critical angle of total internal reflection are considered. A generalised transfer matrix approach is then used to calculate the dispersion relation of waveguide polaritons for two distinct cases—a quantum well in the guiding layer of the waveguide, and a quantum well in the cladding layer of the waveguide. In both cases, the T-polariton mode dispersion curves are seen to display anti-crossing behaviour indicative of the strong coupling regime of the exciton interacting with light.

6.1 Total internal reflection at a dielectric interface

Consider an interface normal to the z-direction between two dielectric media (labelled 1 and 2) having refractive indices n_1 and n_2, respectively, where $n_1 > n_2$. Let a plane light wave of angular frequency ω be incident on medium 2 from medium 1 at an angle of incidence θ in the xz-plane. When θ exceeds the critical value θ_c defined by the equation

$$\sin\theta_c = \frac{n_2}{n_1} \tag{6.1}$$

total internal reflection takes place and the reflection coefficient becomes equal to unity. Above this critical angle of incidence, the component of the wavevector $\mathbf{k}$ perpendicular to the interface becomes imaginary in medium 2, resulting in the amplitude of the electromagnetic wave decaying exponentially. The spatial variation of the electric field E is described by

$$E \sim e^{-\chi z} e^{ik_x x} \tag{6.2}$$

where

$$k_z = i\chi, \qquad k_x^2 - \chi^2 = k^2, \qquad k = n_2\omega/c \tag{6.3}$$

and c is the velocity of light in vacuum. The structure and electric field profile of the dielectric interface in total internal reflection is illustrated in figure 6.1.

Formally, the electromagnetic field can be considered as a plane wave propagating in the direction defined by the complex angle [57, 173]

$$\theta_2 = -i \ln\left(ib + \sqrt{1 - b^2}\right) \tag{6.4}$$

where $b = (n_1/n_2)\sin\theta_1$.

Equation 6.4 is a generalised form of Snell's law and gives a proper mathematical description of the electromagnetic field in the case of total internal reflection. Bearing in mind equation 6.4, one can write

$$k_z = i\chi = k\cos\theta_2 \tag{6.5}$$

where the cosine of the angle of refraction is seen to be purely imaginary.

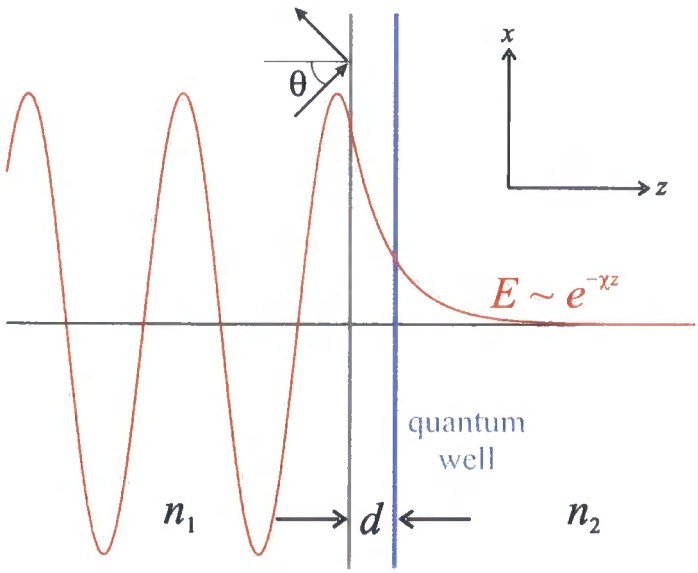

Figure 6.1 The electric field in the case of total internal reflection of light incident upon the interface of dielectric media having refractive indices n_1 and n_2. A quantum well is placed a distance d behind the interface.

The reflection coefficient of a dielectric interface is given by the Fresnel formula as

$$r = \frac{p_1 - p_2}{p_1 + p_2} \tag{6.6}$$

where $p_{1,2} = n_{1,2} \cos\theta_{1,2}$ for TE-polarised waves and $p_{1,2} = \cos\theta_{1,2}/n_{1,2}$ for TM-polarised waves. For angles of incidence exceeding the critical angle for total internal reflection, $\cos\theta_2$ is purely imaginary, and we write

$$p_2 = i\zeta_2 \tag{6.7}$$

Then

$$r = \frac{p_1 - i\zeta_2}{p_1 + i\zeta_2} = \frac{p_1^2 - \zeta_2^2 - 2ip_1\zeta_2}{p_1^2 + \zeta_2^2} \tag{6.8}$$

and the reflectivity is

$$R = |r|^2 = 1 \tag{6.9}$$

as expected in total internal reflection. Writing the reflection coefficient as $r = |r| \exp(i\varphi)$, the phase φ is given by

$$\tan\varphi = -\frac{2p_1\zeta_2}{p_1^2 - \zeta_2^2} \tag{6.10}$$

As the angle of incidence approaches the critical angle θ_c, then $\zeta_2 \to 0$ and $r \to 1$.

6.2 Reflection and transmission through quantum well containing exciton

This section presents a derivation of the reflection and transmission coefficients for light incident on a quantum well exciton. The exciton contributes to the dielectric polarisation of the quantum well at all points within the exciton's wavefunction, and this can be accounted for by the theory of non-local dielectric response [96, 174–178]. First we describe the solution of the inhomogeneous wave equation in terms of Green functions. Then, the usual case of a quantum well exciton interacting with a propagating electromagnetic plane wave is briefly derived. The final part of this section derives the generalised formulae for use when the quantum well exciton interacts with an evanescent electromagnetic plane wave.

6.2.1 Solution of the inhomogeneous wave equation

In the vicinity of a quantum well, the quantum well exciton makes a significant contribution to the displacement field when the frequency of light is close to the excitonic resonance frequency ω_0:

$$\mathbf{D} = \varepsilon_b \mathbf{E} + 4\pi \mathbf{P}_{exc} \tag{6.11}$$

Thus the electromagnetic field in the vicinity of the quantum well is described by the wave equation

$$\nabla \times \nabla \times \mathbf{E} - k^2 \mathbf{E} = 4\pi k_0^2 \mathbf{P}_{exc} \tag{6.12}$$

where the right-hand term accounts for the excitonic contribution to the dielectric polarisation $\mathbf{P}_{exc}$ and $k = k_0\sqrt{\varepsilon_b} = (\omega_0/c)\sqrt{\varepsilon_b}$ is the wavevector of the light, and ε_b is the background relative permittivity in the quantum well and surrounding barrier material (assumed to be equal for simplicity). According to the theory of non-local dielectric response, the polarisation can be written as

$$\mathbf{P}_{exc}(z) = \frac{1}{4\pi} \int \tilde{T}(\omega, z, z') E(z') \, dz' \tag{6.13}$$

where the non-local dielectric susceptibility is given by $\tilde{T}(\omega, z, z') = T(\omega) \Phi(z) \Phi(z')$. The function $\Phi(\mathbf{r})$ is proportional to the envelope of the exciton wavefunction $\Psi(\mathbf{r}, \mathbf{r}')$ taken

with equal electron and hole coordinates. Hence $\Phi(\mathbf{r}) = \Psi(\mathbf{r},\mathbf{r})/\sqrt{S}$, where S is the area of the quantum well and

$$T(\omega) = \frac{\varepsilon_b \omega_{LT} \pi a_B^3}{\omega_0 - \omega - i\Gamma} \tag{6.14}$$

In equation 6.14, ω_{LT} and a_B are respectively the longitudinal-transverse splitting and the Bohr radius of the exciton in the bulk material, and Γ is the non-radiative exciton damping. $T(\omega)$ describes the frequency dependence of the optical susceptibility (see, for example, ref. [179] page 3).

The wave equation 6.12 can be solved by a Green function method. The electric field $\mathbf{E}(\mathbf{r})$ can be represented in the form

$$\mathbf{E}(\mathbf{r}) = \mathbf{E}_0 + \tilde{\mathbf{E}} \tag{6.15}$$

where $\mathbf{E}_0$ is the solution to the homogeneous counterpart of equation 6.12 and $\tilde{\mathbf{E}}$ can be expressed in terms of the Green function $G_{\alpha\beta}$ as

$$\tilde{E}_\alpha = k_0^2 T \Lambda_\beta \int G_{\alpha\beta}(x, z - z')\, \Phi(z')\, dz' \tag{6.16}$$

where $\alpha, \beta = x, y, z$,

$$\Lambda_\beta = \int \Phi(z)\, E_\beta(z)\, dz \tag{6.17}$$

and

$$G_{\alpha\beta}(\mathbf{r}) = \left(\delta_{\alpha\beta} + \frac{1}{k^2}\frac{\partial^2}{\partial\alpha\partial\beta}\right) \bar{G}(x, z - z') \tag{6.18}$$

where $\bar{G}$ will be given in section 6.2.2 for propagating plane wave solutions and in section 6.2.3 for evanescent ones.

The TE-polarisation has only one non-zero component of the electric field vector, such that $\mathbf{E} = (0, E_y, 0)$, and this is given by $E_y = E_{0,y} + \tilde{E}_y$, where, from equation 6.16

$$\tilde{E}_y(x, z) = k_0^2 T \Lambda_y \int \Phi(z')\, G_{yy}(x, z - z')\, dz' \tag{6.19}$$

The TM-polarisation of light has two non-zero components of the electric field vector, such

that $\mathbf{E} = (E_x, 0, E_z)$. The components of the electric field are given by equation 6.16 as

$$\tilde{E}_x(x,z) = k_0^2 T \Lambda_x \int \Phi(z') G_{xx}(x, z-z')\, dz' + k_0^2 T \Lambda_z \int \Phi(z') G_{xz}(x, z-z')\, dz' \tag{6.20}$$

$$\tilde{E}_z(x,z) = k_0^2 T \Lambda_x \int \Phi(z') G_{xz}(x, z-z')\, dz' + k_0^2 T \Lambda_z \int \Phi(z') G_{zz}(x, z-z')\, dz' \tag{6.21}$$

Inserting the forms of $G_{\alpha\beta}$ from equation 6.18 give the projections of the electric field vector as

$$\tilde{E}_y(x,z) = k_0^2 T \Lambda_y \int \Phi(z') \bar{G}(x, z-z')\, dz' \tag{6.22}$$

for the TE-polarised electric field and

$$\begin{aligned}\tilde{E}_x(x,z) = k_0^2 T \Lambda_x \int \Phi(z') \bar{G}(x, z-z')\, dz' + \frac{k_0^2 T \Lambda_x}{k^2} \int \Phi(z') \frac{\partial^2}{\partial x^2} \bar{G}(x, z-z')\, dz' \\ + \frac{k_0^2 T \Lambda_z}{k^2} \int \Phi(z') \frac{\partial^2}{\partial x \partial z} \bar{G}(x, z-z')\, dz'\end{aligned} \tag{6.23}$$

$$\begin{aligned}\tilde{E}_z(x,z) = \frac{k_0^2 T \Lambda_x}{k^2} \int \Phi(z') \frac{\partial^2}{\partial x \partial z} \bar{G}(x, z-z')\, dz' + k_0^2 T \Lambda_z \int \Phi(z') \bar{G}(x, z-z')\, dz' \\ + \frac{k_0^2 T \Lambda_z}{k^2} \int \Phi(z') \frac{\partial^2}{\partial^2 z} \bar{G}(x, z-z')\, dz'\end{aligned} \tag{6.24}$$

for the TM-polarised electric field.

6.2.2 Propagating wave solutions

Normally we are interested in the interaction of propagating waves with the quantum well. For a propagating wave, the homogeneous solution $\mathbf{E}_0$ is a plane wave having the form $E_{0,\alpha} e^{ik_z|z|} e^{ik_x x}$, and the Green's function is given by

$$\bar{G}(x, z-z') = \frac{i}{2k_z} e^{ik_z|z-z'|} e^{ik_x x} \tag{6.25}$$

The electric field components are given by equation 6.22 for the TE-polarisation and equation 6.23 and 6.24 for the TM-polarisation. Performing the necessary differentiation and cancelling the factor $e^{ik_x x}$ gives

$$E_y(z) = E_{0,y} e^{ik_z z} + k_0^2 T \Lambda_y \int \Phi(z') \bar{G}(z-z')\, dz' \tag{6.26}$$

$$E_x(x) = E_{0,x}e^{ik_z z} + k_0^2 T\Lambda_x \frac{k_z^2}{k^2}\int \Phi(z')\,\bar{G}(z-z')\,dz' + i\frac{k_x}{k^2}k_0^2 T\Lambda_z \int \Phi(z')\,\frac{d}{dz}\bar{G}(z-z')\,dz' \tag{6.27}$$

$$E_z(z) = E_{0,z}e^{ik_z z} i\frac{k_x}{k^2}k_0^2 T\Lambda_x \int \Phi(z')\,\frac{d}{dz}\bar{G}(z-z')\,dz' + \frac{k_x^2}{k^2}k_0^2 T\Lambda_z \int \Phi(z')\,\bar{G}(z-z')\,dz' - \frac{1}{k^2}k_0^2 T\Lambda_z \Phi(z) \tag{6.28}$$

The quantities $\Lambda_\alpha = \int \Phi(z)\,E_\alpha(z)\,dz$ can be found by multiplying the left and right hand sides of equation 6.26 to 6.28 by $\Phi(z)$ and integrating over all z. The resulting equations can then be rearranged to give

$$\Lambda_y = \frac{E_{0,y}\int \Phi(z)\,e^{ik_z z}dz}{1 - k_0^2 TL} \tag{6.29}$$

$$\Lambda_x = \frac{E_{0,x}\int \Phi(z)\,e^{ik_z z}dz}{1 - k_0^2 TL\,(k_z^2/k^2)} \tag{6.30}$$

$$\Lambda_z = \frac{E_{0,z}\int \Phi(z)\,e^{ik_z z}dz}{1 - k_0^2 TL\,(k_x^2/k^2) + k_0^2 T\int (\Phi(z))^2\,dz/k^2} \tag{6.31}$$

where L is defined as

$$L = \iint \Phi(z)\,\Phi(z')\,\bar{G}(z-z')\,dz\,dz' \tag{6.32}$$

Equations 6.29, 6.30 and 6.31 can then be substituted back into the equations for the electric field to give the form of the electric field everywhere. The quantity L can be found by performing the integration directly

$$L = \frac{i}{2k_z}\left(\int \Phi(z)\cos(k_z z)dz\right)^2 + \frac{i}{2k_z}\left(\int \Phi(z)\sin(k_z z)dz\right)^2 - \frac{1}{2k_z}\iint \Phi(z)\,\Phi(z')\sin(k_z|z-z'|)dz\,dz' \tag{6.33}$$

The reflection coefficient, r, is given by the ratio of the complex amplitude of the left (reflected wave, coefficient of $e^{ik_z z}$) and right travelling (incident wave, coefficient of $e^{-ik_z z}$) waves far to the left of the quantum well (as $z \to -\infty$). The transmission coefficient, t, is the ratio of the complex amplitudes of the right-travelling waves (coefficients of $e^{ik_z z}$) far to the right (transmitted wave) and left (incident wave) of the quantum well. Assuming the

exciton is in the ground state

$$r_{qw} = \frac{i\tilde{\Gamma}_0}{\tilde{\omega}_0 - \omega - i\left(\Gamma + \tilde{\Gamma}_0\right)} \tag{6.34}$$

$$t_{qw} = 1 + \frac{i\tilde{\Gamma}_0}{\tilde{\omega}_0 - \omega - i\left(\Gamma + \tilde{\Gamma}_0\right)} = 1 + r_{qw} \tag{6.35}$$

for the TE-polarisation, where

$$\tilde{\Gamma}_0 = \frac{\Gamma_0}{\cos\theta} \tag{6.36}$$

is the exciton radiative broadening for an incident angle of θ, and

$$\Gamma_0 = \frac{k}{2}\omega_{LT}\pi a_B^3 \left(\int \Phi(z)\cos(k_z z)dz\right)^2 \tag{6.37}$$

is the exciton radiative broadening for normal incidence and

$$\tilde{\omega}_0 = \omega_0 - \frac{k^2\omega_{LT}\pi a_B^3}{2k_z}\iint \Phi(z)\,\Phi(z')\sin(k_z|z-z'|)dz\,dz' \tag{6.38}$$

is the renormalisation of the resonance frequency due to the polariton effect.

Similar expressions can be found for the reflection and transmission coefficients in the TM polarisation:

$$r_{qw} = \frac{i\tilde{\Gamma}_0'}{\tilde{\omega}_0' - \omega - i\left(\Gamma + \tilde{\Gamma}_0'\right)} - \frac{i\tilde{\Gamma}_0''}{\tilde{\omega}_0'' - \omega - i\left(\Gamma + \tilde{\Gamma}_0''\right)} \tag{6.39}$$

$$t_{qw} = 1 + \frac{i\tilde{\Gamma}_0'}{\tilde{\omega}_0' - \omega - i\left(\Gamma + \tilde{\Gamma}_0'\right)} + \frac{i\tilde{\Gamma}_0''}{\tilde{\omega}_0'' - \omega - i\left(\Gamma + \tilde{\Gamma}_0''\right)} \tag{6.40}$$

where

$$\tilde{\Gamma}_0' = \Gamma_0\cos\theta \tag{6.41}$$

$$\tilde{\omega}_0' = \omega_0 + \frac{k_z}{2}\omega_{LT}\pi a_B^3 \iint \Phi(z)\,\Phi(z')\sin(k_z|z-z'|)\,dz\,dz' \tag{6.42}$$

$$\tilde{\Gamma}_0'' = \frac{\Gamma_0\sin^2\theta}{\cos\theta} \tag{6.43}$$

$$\tilde{\omega}_0'' = \omega_0 + \frac{k_x^2}{2k_z}\omega_{LT}\pi a_B^3 \iint \Phi(z)\,\Phi(z')\sin(k_z|z-z'|)\,dz\,dz' + \omega_{LT}\pi a_B^3 \int [\Phi(z)]^2\,dz \tag{6.44}$$

The exciton polariton's eigenfrequencies are given by the poles of r_{qw} (equation 6.34 and equation 6.39).

6.2.3 Evanescent wave solutions

In the case of a quantum well placed behind a dielectric interface at which total internal reflection occurs, it is possible for an evanescent wave to interact with a quantum well exciton. Although now there are only evanescent fields, it is still convenient to define reflection and transmission coefficients in a formal mathematical fashion. For the purpose of developing the theory, we consider the somewhat artificial case where an "incident" evanescent wave field exists in the absence of a dielectric interface. The reflection coefficient is then introduced as the ratio of the amplitude of the wave decaying to $z = +\infty$ (incident field) to the amplitude of the wave decaying to $z = -\infty$ (reflected field) far to the left from the quantum well. The transmission coefficient is introduced as the ratio of the amplitude of the wave decaying to $z = +\infty$ far to the right (transmitted field) and far to the left (incident field) of the quantum well.

The basic equations used for solving the wave equation 6.12 are similar to before, but the Green function is now

$$\bar{G}(x, z-z') = \frac{1}{2\chi}e^{-\chi|z-z'|}e^{ik_x x} \tag{6.45}$$

The solution to the homogeneous wave equation is an evanescent plane wave having the form $E_{0,\alpha}e^{-\chi z}e^{ik_x x}$.

For the TE-polarisation case, the electric field obeys the equation

$$E_y(z) = E_{0,y}e^{-\chi z} + k_0^2 T\Lambda_y \int \Phi(z')\,\bar{G}(z-z')\,dz' \tag{6.46}$$

and for the TM-polarisation case, the non-zero components of electric field satisfy the equations

$$\begin{aligned} E_x(z) = E_{0,x}e^{-\chi z} &- k_0^2 T\Lambda_x \frac{\chi^2}{k^2}\int \Phi(z')\,\bar{G}(z-z')\,dz' \\ &+ i\frac{k_x}{k^2}k_0^2 T\Lambda_z \int \Phi(z')\,\frac{\partial}{\partial z}\bar{G}(z-z')\,dz' \end{aligned} \tag{6.47}$$

$$E_z(z) = E_{0,z}e^{-\chi z} + i\frac{k_x}{k^2}k_0^2 T\Lambda_x \int \Phi(z')\frac{\partial}{\partial z}\bar{G}(z-z')\,dz' + \frac{k_x^2}{k^2}k_0^2 T\Lambda_z \int \Phi(z')\bar{G}(z-z')\,dz' - \frac{1}{k^2}k_0^2 T\Lambda_z \Phi(z) \tag{6.48}$$

Then the quantities $\Lambda_\alpha = \int \Phi(z) E_\alpha(z)\,dz$ are explicitly found by multiplying the electric field projections by the function $\Phi(z)$ and integrating over z. Carrying out this procedure yields

$$\Lambda_y = E_{0,y}\int \Phi(z')e^{-\chi z}dz + k_0^2 T\Lambda_y \iint \Phi(z)\Phi(z')\bar{G}(z-z')\,dz\,dz' \tag{6.49}$$

$$\Lambda_x = E_{0,x}\int \Phi(z')e^{-\chi z}dz + k_0^2 T\Lambda_x\frac{\chi^2}{k^2}\iint \Phi(z)\Phi(z')\bar{G}(z-z')\,dz\,dz' + ik_0^2 T\Lambda_x\frac{k_x}{k^2}\iint \Phi(z)\Phi(z')\frac{d}{dz}\bar{G}(z-z')\,dz\,dz' \tag{6.50}$$

$$\Lambda_z = E_{0,z}\int \Phi(z')e^{-\chi z}dz + ik_0^2 T\Lambda_x\frac{k_x}{k^2}\iint \Phi(z)\Phi(z')\frac{d}{dz}\bar{G}(z-z')\,dz\,dz' + k_0^2 T\Lambda_z\frac{k_x^2}{k^2}\iint \Phi(z)\Phi(z')\bar{G}(z-z')\,dz\,dz' - k_0^2 T\Lambda_z\frac{1}{k^2}\int [\Phi(z)]^2\,dz \tag{6.51}$$

Equations 6.49, 6.50 and 6.51 can be solved for Λ_α to give

$$\Lambda_y = \frac{E_{0,y}\int \Phi(z)e^{-\chi z}dz}{1-k_0^2 TL} \tag{6.52}$$

$$\Lambda_x = \frac{E_{0,x}\int \Phi(z)e^{-\chi z}dz}{1+k_0^2 T(\chi^2/k^2)L} \tag{6.53}$$

$$\Lambda_z = \frac{E_{0,z}\int \Phi(z)e^{-\chi z}dz}{1-(k_x^2/k^2)k_0^2 TL + (k_0^2/k^2)T\int [\Phi(z)]^2\,dz} \tag{6.54}$$

where L is defined as

$$L = \iint \Phi(z)\Phi(z')\bar{G}(z-z')\,dz\,dz' \tag{6.55}$$

In order to obtain the reflection coefficient, we must have the ratio of the amplitude of the left-decaying wave (coefficient of $e^{+\chi z}$) to the amplitude of the right-decaying wave (coefficient of $e^{-\chi z}$) at $z \to -\infty$. The transmission coefficient is similarly found from the ratios of the right-decaying waves (coefficients of $e^{-\chi z}$) at each side of the quantum well.

Inserting equation 6.52 for Λ_y into the expression for the electric field in the TE-polarisation

(equation 6.46) gives

$$E_y(z) = E_{0,y}e^{-\chi z} + \frac{k_0^2 T E_{0,y} \int \Phi(z)\, e^{-\chi z} dz \int \Phi(z')\, \bar{G}(z-z')\, dz'}{1 - k_0^2 TL} \tag{6.56}$$

As $z \to -\infty$,

$$\int \Phi(z')\, \bar{G}(z-z')\, dz' = \frac{1}{2\chi} e^{+\chi z} \int \Phi(z')\, e^{-\chi z'} dz' \tag{6.57}$$

$$\int \Phi(z') \frac{d}{dz} \bar{G}(z-z')\, dz' = \frac{1}{2} e^{+\chi z} \int \Phi(z')\, e^{-\chi z'} dz' \tag{6.58}$$

and the electric field far to the left of the quantum well is given by

$$E_y(z) = E_{0,y}e^{-\chi z} + \frac{k_0^2 T E_{0,y} \left(\int \Phi(z)\, e^{-\chi z} dz\right)^2}{2\chi(1 - k_0^2 TL)} e^{+\chi z} \tag{6.59}$$

for the TE-polarisation and

$$E_x(z) = E_{0,x}e^{-\chi z} + \frac{k_0^2 T}{2k^2} (ik_x \Lambda_z - \chi \Lambda_x) \int \Phi(z')\, e^{-\chi z'} dz' e^{+\chi z} \tag{6.60}$$

for the TM-polarisation. Either the x or the z-component of the electric field can be used to find the reflection and transmission in the TM-polarisation, so only the x-component is given here, for brevity.

As $z \to +\infty$,

$$\int \Phi(z')\, \bar{G}(z-z')\, dz' = \frac{1}{2\chi} e^{-\chi z} \int \Phi(z')\, e^{+\chi z'} dz' \tag{6.61}$$

$$\int \Phi(z') \frac{d}{dz} \bar{G}(z-z')\, dz' = \frac{1}{2} e^{-\chi z} \int \Phi(z')\, e^{+\chi z'} dz' \tag{6.62}$$

and the electric field far to the right of the quantum well is given by

$$E_y(z) = E_{0,y}e^{-\chi z} \left(1 + \frac{k_0^2 T \int \Phi(z)\, e^{-\chi z} dz \int \Phi(z')\, e^{+\chi z'} dz'}{2\chi(1 - k_0^2 TL)}\right) \tag{6.63}$$

for the TE-polarised light and

$$E_x(z) = E_{0,x} \left(1 - \frac{k_0^2 T}{2k^2} (ik_x \Lambda_z + \chi \Lambda_x) \int \Phi(z')\, e^{-\chi z'} dz'\right) e^{-\chi z} \tag{6.64}$$

for TM-polarised light.

The reflection coefficient for TE-polarised light is given as the ratio of the coefficients of $e^{+\chi z}$ and $e^{-\chi z}$ in equation 6.59 as

$$r_{qw} = \frac{k_0^2 T \left(\int \Phi(z)\, e^{-\chi z} dz\right)^2}{2\chi\left(1 - k_0^2 TL\right)} \tag{6.65}$$

The transmission coefficient for TE-polarised light is the ratio of the coefficients of $e^{-\chi z}$ in the expressions for the electric field far to the right (equation 6.63) and left (equation 6.59) of the quantum well

$$t_{qw} = 1 + \frac{k_0^2 T \int \Phi(z)\, e^{-\chi z} dz \int \Phi(z')\, e^{+\chi z'} dz'}{2\chi\left(1 - k_0^2 TL\right)} \tag{6.66}$$

Now, $e^{\pm\chi z} = \cosh(\chi z) \pm \sinh(\chi z)$, where $\cosh(\chi z)$ is an even function of z and $\sinh(\chi z)$ is an odd function of z. Since $\Phi(z)$ is an even function of z for an exciton in its ground state

$$\int \Phi(z)\, e^{\pm\chi z} dz = \int \Phi(z) \cosh(\chi z)\, dz \tag{6.67}$$

Thus the reflection and transmission coefficients are

$$r_{qw} = \frac{k_0^2 T \left(\int \Phi(z) \cosh(\chi z)\, dz\right)^2}{2\chi\left(1 - k_0^2 TL\right)} \tag{6.68}$$

$$t_{qw} = 1 + \frac{k_0^2 T \left(\int \Phi(z) \cosh(\chi z)\, dz\right)^2}{2\chi\left(1 - k_0^2 TL\right)} = 1 + r_{qw} \tag{6.69}$$

The quantity L defined in equation 6.55 can be found by performing the integrals directly

$$\begin{aligned} L = \frac{1}{2\chi}\left(\int \Phi(z) \cosh(\chi z)\, dz\right)^2 - \frac{1}{2\chi}\left(\int \Phi(z) \sinh(\chi z)\, dz\right)^2 \\ + \frac{1}{2\chi}\iint \Phi(z)\, \Phi(z') \sinh\left(\chi\left|z - z'\right|\right) dz\, dz' \end{aligned} \tag{6.70}$$

For an exciton in its ground state, the middle term on the right hand side of equation 6.70 will vanish, as $\Phi(z)$ is an even function of z while $\sinh(\chi z)$ is an odd function.

Defining (compare equation 6.37)

$$\Gamma_e = \frac{k}{2}\omega_{LT}\pi a_B^3 \left(\int \Phi(z) \cosh(\chi z)\, dz\right)^2 \tag{6.71}$$

the "reflection" and "transmission" coefficients for the TE polarisation can be expressed as

$$r_{qw} = \frac{\tilde{\Gamma}_e}{\tilde{\omega}_0 - \omega - \tilde{\Gamma}_e - i\Gamma} \tag{6.72}$$

$$t_{qw} = 1 + \frac{\tilde{\Gamma}_e}{\tilde{\omega}_0 - \omega - \tilde{\Gamma}_e - i\Gamma} = 1 + r_{qw} \tag{6.73}$$

respectively. Here

$$\tilde{\Gamma}_e = \frac{k}{\chi}\Gamma_e \tag{6.74}$$

and

$$\tilde{\omega}_0 = \omega_0 - \frac{k^2}{2\chi}\omega_{LT}\pi a_B^3 \iint \Phi(z)\,\Phi(z')\sinh(\chi|z - z'|)\,dz\,dz' \tag{6.75}$$

is the renormalisation of the exciton resonance frequency due to the polariton effect.

The reflection and transmission coefficients for the TM polarisation can be found in a similar manner. The reflection coefficient for TM-polarised light is given as the ratio of the coefficients of $e^{+\chi z}$ and $e^{-\chi z}$ in equation 6.60:

$$r_{qw} = \frac{k_0^2 T}{2k^2 E_{0,x}}(ik_x\Lambda_z - \chi\Lambda_x)\int \Phi(z')\,e^{-\chi z'}dz' \tag{6.76}$$

The transmission coefficient for TM-polarised light is the ratio of the coefficients of $e^{-\chi z}$ in the expressions for the electric field far to the right (equation 6.64) and left (equation 6.60) of the quantum well:

$$t_{qw} = 1 - \frac{k_0^2 T}{2k^2 E_{0,x}}(ik_x\Lambda_z + \chi\Lambda_x)\int \Phi(z')\,e^{-\chi z'}dz' \tag{6.77}$$

Again, for an exciton in the ground state we use equation 6.67, and for a plane wave $E_{0,z}/E_{0,x} = ik_x/\chi$, so the "reflection" and "transmission" coefficients for the TM polarisation can be expressed as

$$r_{qw} = -\frac{\tilde{\Gamma}'_e}{\tilde{\omega}'_0 - \tilde{\Gamma}'_0 - \omega - i\Gamma} - \frac{\tilde{\Gamma}''_e}{\tilde{\omega}''_0 - \tilde{\Gamma}''_e - \omega - i\Gamma} = r_1 - r_2 \tag{6.78}$$

$$t_{qw} = 1 - \frac{\tilde{\Gamma}'_e}{\tilde{\omega}'_0 - \tilde{\Gamma}'_0 - \omega - i\Gamma} + \frac{\tilde{\Gamma}''_e}{\tilde{\omega}''_0 - \tilde{\Gamma}''_e - \omega - i\Gamma} = 1 + r_1 + r_2 \tag{6.79}$$

where

$$\tilde{\Gamma}'_e = \frac{\chi}{k}\Gamma_e \tag{6.80}$$

$$\tilde{\omega}_0' = \omega_0 + \frac{\chi}{2}\omega_{LT}\pi a_B^3 \iint \Phi(z)\,\Phi(z')\sinh(\chi|z-z'|)\,dz\,dz' \tag{6.81}$$

$$\tilde{\Gamma}_e'' = \frac{k_x^2}{k\chi}\Gamma_e \tag{6.82}$$

$$\tilde{\omega}_0'' = \omega_0 - \frac{k_x^2}{2\chi}\omega_{LT}\pi a_B^3 \iint \Phi(z)\,\Phi(z')\sinh(\chi|z-z'|)\,dz\,dz' + \omega_{LT}\pi a_B^3 \int [\Phi(z)]^2\,dz \tag{6.83}$$

The exciton polariton eigenfrequencies are given by the poles of r_{qw} for the TE case (equation 6.72) and TM case (equation 6.78). Thus the transverse (T) polariton has a resonant frequency $\tilde{\omega}_0$, and a width given by the non-radiative damping Γ. Likewise, the L- and Z-polaritons have resonant frequencies of $\tilde{\omega}_0'$ and $\tilde{\omega}_0''$ respectively.

It is apparent from equation 6.72 and equation 6.78 that in the evanescent field case, there is no radiative damping of the exciton, in contrast to the case when a freely propagating wave is incident upon the quantum well. Mathematically, this is because in the denominator the quantity corresponding to the radiative exciton damping $\tilde{\Gamma}_0$ becomes imaginary in the case of evanescent waves and contributes only to the resonance frequency renormalisation.

This result can also be easily understood from a physical point of view. The radiative damping in the propagating wave case exists because the photons can propagate infinitely far away from the quantum well plane. However, in the evanescent wave case, light is no longer free to propagate in the direction out of the plane of the quantum well unless a suitable dielectric interface is encountered, and therefore the radiative exciton damping is zero. Consequently, exciton-polaritons are "dark" as they have an infinite radiative life-time [180].

Note that, if the angle of incidence corresponds to the critical angle of total internal reflection, (e.g. $k_z \to 0$ or $\chi \to 0$) so that the polariton state is at the edge of the light-cone, the reflection coefficients for the cases of propagating (equation 6.34) and evanescent (equation 6.72) waves coincide and are both equal to -1.

Note also that Γ_e in the expressions for the reflection and transmission in the evanescent field case are identical to the equivalent Γ_0 in the expressions for the reflection and transmission in the propagating wave case, as long as a complex angle of propagation is used to describe the electromagnetic fields in the evanescent wave case.

6.3 Interaction of quantum well excitons with evanescent plane electromagnetic waves

For the structure shown in figure 6.1, the amplitude reflection coefficient r can be expressed in terms of the amplitude reflection coefficients r_1 and r_{qw} of the interface between the media 1 and 2 and of the quantum well, respectively:

$$r = \frac{r_1 + r_{qw}e^{-\chi d}}{1 + r_1 r_{qw}e^{-\chi d}} \tag{6.84}$$

where d is the distance between the interface and the nearest edge of the quantum well.

Figure 6.2 shows some reflection spectra of TE-polarised light for the structure shown in figure 6.1. The parameters of the structure are chosen to correspond to an experimentally feasible III-V heterostructure. The refractive indices $n_1 = 3.7$ and $n_2 = 3.0$ correspond to GaAs and AlAs respectively and the critical angle of total internal reflection for the interface, given by equation 6.1, is $\theta_c = 54.176°$. The parameters of the quantum well are chosen to be those of an InGaAs quantum well of thickness 50 nm, with $\hbar\omega_0 = 0.9$ eV, $\hbar\Gamma_0 = 0.05$ meV, and $\hbar\Gamma = 1.0$ meV. The distance between the interface and quantum well is taken as $d = 100$ nm. Substantial angles of incidence on the GaAs/AlAs interface can be achieved by using a prism or diffraction grating on the external boundary of the sample. The reflection spectra of the dielectric interface with the quantum well place behind it are shown in figure 6.2 (a) are for a number of angles of incidence exceeding the critical angle for total internal reflection, and figure 6.2 (b) for angles below the critical angle.

It follows from equations 6.34 and 6.72 for the reflection of the quantum well near an exciton resonance that the interaction of light and the quantum well exciton is enhanced substantially if the angle of incidence on the dielectric interface θ_1 is close to the critical value θ_c. As $\theta_1 \to \theta_c$ from below θ_c, the angle of refraction $\theta_2 \to \pi/2$. Hence the exciton radiative broadening $\tilde{\Gamma}_0 = \Gamma_0/\cos\theta_2 \gg \Gamma$, where Γ is the non-radiative exciton damping. When $\theta_1 > \theta_c$, the angle of refraction is complex, where the real part of this angle is $\pi/2$. As $\theta_1 \to \theta_c$ from above θ_c, the imaginary part of the complex angle of refraction approaches zero, and $\tilde{\Gamma}_e$ in equation 6.72 becomes large. Figure 6.2 shows that if the incidence angle θ_1 is much less than θ_c, the reflection spectrum is represented by the usual type of resonant curve with a relatively small magnitude modulation. However, increase of θ_1 leads to a

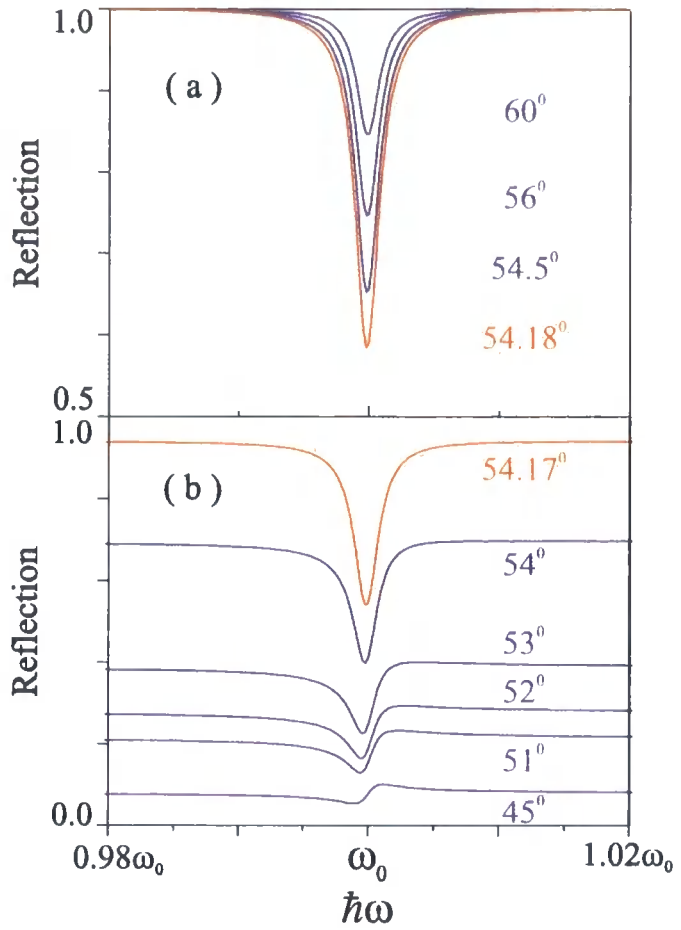

Figure 6.2 Reflection spectra of a dielectric interface with a quantum well placed behind it, as shown in figure 6.1, for various angles of incidence on the dielectric interface. The critical angle for total internal reflection at the interface is $\theta_c = 54.175$, and the red lines show spectra for angles of incidence close to θ_c. (a) Angles of incidence exceeding θ_c: 54.18°, 54.5°, 56°, 60°. (b) Angles of incidence below θ_c: 45°, 51°, 52°, 53°, 54° and 54.17°.

growth of the modulation, and the shape of the spectrum changes substantially. When θ_1 becomes close to θ_c the background reflectivity tends to unity and a Lorentzian dip appears at the frequency of the exciton resonance. Note that the position of the dip corresponds to the exciton resonance frequency ω_0, despite the fact that the pole in r_{qw} (equation 6.72) is shifted from ω_0 by $\tilde{\Gamma}_e$, which itself is quite large if the incidence angle is close to θ_c. Subsequent increase of the angle of incidence leads to a decrease of the depth of the excitonic dip.

Note that if θ_1 is exactly equal to the critical value θ_c, the relative depth of the excitonic dip exceeds 50% for the chosen parameters, despite the non-radiative damping of the exciton being 20 times stronger than its radiative counterpart. Such amplification of the excitonic modulation of reflection spectra makes the spectroscopy of quantum well excitons in the geometry of total internal reflection a promising tool for the precise determination of excitonic

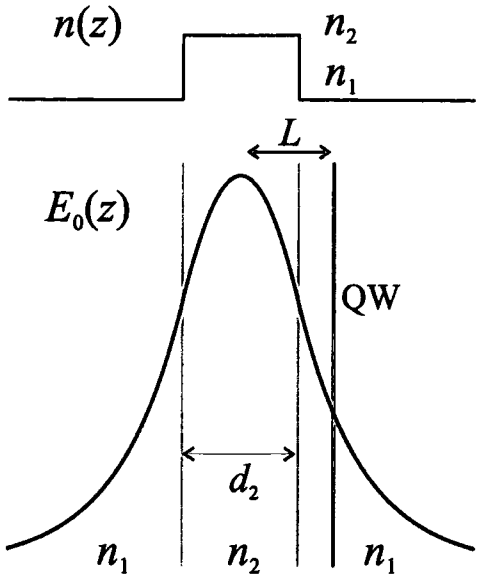

Figure 6.3 Top—the refractive index profile of the waveguide, $n\,(z)$. The parameters used in the numerical calculations were those appropriate for a AlAs:GaAs:AlAs waveguide ($n_1 = 3.0$ and $n_2 = 3.7$) with a thickness of $d_2 = 150\,\text{nm}$. Bottom—the electric field profile of the fundamental TE_0 mode of the waveguide. Vertical grey lines indicate the dielectric interfaces between the guiding layer and cladding of the waveguide. A quantum well can be embedded a distance L from the centre of the waveguide structure, as indicated.

parameters.

6.4 Dielectric slab waveguides

A dielectric slab waveguide is essentially a thin dielectric film of refractive index n_2 and thickness d_2, embedded in another dielectric material of refractive index $n_1 < n_2$, as shown in figure 6.3. It is also possible to construct non-symmetric waveguides, where the two semi-infinite cladding layers that surround the guiding layer are made of different materials.

The optical modes of a planar dielectric waveguide have an electric field of the form $E_m\,(z)\exp\left(ik_x x - i\omega t\right)$, where $E_m\,(z)$ is the electric field profile of the mode, found by solving the Maxwell equations in the three regions of the waveguide. For guided modes, the electric field decays exponentially into the cladding. The integer m is the mode number label, and gives the number of nodes in the field profile. Figure 6.3 shows the TE_0 mode of a planar dielectric waveguide with parameters of a AlAs:GaAs:AlAs structure ($n_1 = 3.0$ and $n_2 = 3.7$) and a guiding layer that is 150 nm thick.

For waveguiding, the propagation angle in the waveguide, θ_2, must exceed the critical

angle for total internal reflection

$$\sin\theta_2 > \frac{n_1}{n_2} \tag{6.85}$$

Therefore, using Snell's law $n_1 \sin\theta_1 = n_2 \sin\theta_2$, where θ_1 is the "angle of incidence" from the cladding to the guiding layer,

$$\sin\theta_1 > 1 \tag{6.86}$$

Thus the angle of incidence in the cladding layer is complex. It also follows that $\cos\theta_1$ is imaginary, and $\theta_1 = \pi/2 - i\ln\left(b \pm \sqrt{b^2-1}\right)$, where $b = \sin\theta_1 = (n_2/n_1)\sin\theta_2$.

The waveguide is also characterised by a cut-off frequency. This is the frequency for which the angle of propagation along the waveguide is $\theta_2 = \pi/2$, such that the wavevector in the guiding layer is directed along the waveguide axis. Thus for waveguiding, $k_1 < k_x < k_2$, where $k_1 = n_1\omega/c$, $k_2 = n_2\omega/c$ and $k_x = k_1 \sin\theta_1 = k_2 \sin\theta_2$. For any angle of propagation, when the frequency exceeds the cut-off frequency, optical confinement is lost, and the field spreads into the cladding of the waveguide.

6.4.1 Transfer matrix

The transfer matrix in a basis of tangential components of the electromagnetic fields (see section 2.1) across the guiding layer of the waveguide is

$$\hat{\mathrm{M}} = \begin{bmatrix} \cos(k_{2,z}d_2) & (i/p_2)\sin(k_{2,z}d_2) \\ ip_2 \sin(k_{2,z}d_2) & \cos(k_{2,z}d_2) \end{bmatrix} \tag{6.87}$$

where $p_2 = n_2\cos\theta_2$ for TE-polarised waves and $p_2 = \cos\theta_2/n_2$ for TM-polarised waves. $k_{2,z} = k_2\cos\theta_2$. To find the eigenmodes of the waveguide, the fields at the boundaries of the cladding and guiding layer are coupled by the transfer matrix, and outgoing wave boundary conditions are applied,

$$\hat{\mathrm{M}} \begin{bmatrix} 1 \\ -p_1 \end{bmatrix} = \mathcal{A} \begin{bmatrix} 1 \\ p_1 \end{bmatrix} \tag{6.88}$$

where $\mathcal{A}$ is a constant. In the waveguiding regime, the eigenfrequencies of the waveguide will be real, as the lifetimes of the guided modes in the waveguide are infinite.

For TE-polarised modes, eliminating $\mathcal{A}$ from the set of two coupled equations in equa-

tion 6.88 gives

$$M_{11} + M_{12}p_1 + M_{21}/p_1 + M_{22} = 0 \tag{6.89}$$

or

$$2\cos(k_{2,z}d_2) + i\left(\frac{p_1}{p_2} + \frac{p_2}{p_1}\right)\sin(k_{2,z}d_2) = 0 \tag{6.90}$$

Thus rearranging

$$\tan(k_{2,z}d_2) = \frac{2ip_1p_2}{p_1^2 + p_2^2} \tag{6.91}$$

or in terms of the wavevectors $k_{1,z} = i\chi$ and $k_{2,z}$, where χ is real, and

$$\tan(k_{2,z}d_2) = \frac{2\chi k_{2,z}}{k_{2,z}^2 - \chi^2} \tag{6.92}$$

which is the eigenvalue equation for the TE-polarised guided modes. Two different classes of solution leads to the symmetric and antisymmetric modes. The eigenvalues are

$$\omega = \frac{m\pi c}{n_2\cos\theta_2 d_2} + i\frac{c}{n_2\cos\theta_2 d_2}\ln r_1 \tag{6.93}$$

where odd values of the integer m give the frequencies of the antisymmetric modes and even values give the symmetric modes. r_1 is the value of the reflection coefficient at the dielectric interface between the guiding layer and the cladding of the waveguide, and is given by the Fresnel formula as

$$r_1 = \frac{p_2 - p_1}{p_2 + p_1} = \frac{p_2^2 + p_1^2 - 2p_1p_2}{p_2^2 - p_1^2} \tag{6.94}$$

where p_1 and p_2 are defined for the two polarisations as in chapter 2 (equation 2.3 and equation 2.4). In the waveguiding regime for TE-polarised light

$$p_1 = n_1\cos\theta_1 = in_2\sqrt{\sin^2\theta_2 - \sin^2\theta_c} \tag{6.95}$$

$$p_2 = n_2\cos\theta_1 \tag{6.96}$$

and for TM-polarised light

$$p_1 = \frac{\cos\theta_1}{n_1} = i\frac{1}{n_1}\sqrt{\frac{\sin^2\theta_2}{\sin^2\theta_c} - 1} \tag{6.97}$$

$$p_2 = \frac{\cos\theta_2}{n_2} \tag{6.98}$$

θ_c is the critical angle for total internal reflection at the interface of the guiding layer and cladding of the waveguide. Substitution of equation 6.95 and 6.96 into equation 6.94 gives the reflection coefficient for TE polarised light as

$$r_1 = \frac{1 - 2\sin^2\theta_2 + \sin^2\theta_c - 2i\cos\theta_2\sqrt{\sin^2\theta_2 - \sin^2\theta_c}}{1 - sin^2\theta_c} \tag{6.99}$$

and thus $|r_1| = 1$, as expected for total internal reflection. The phase of the reflection coefficient φ is given by

$$\tan\varphi = \frac{-2\cos\theta_2\sqrt{\sin^2\theta_2 - \sin^2\theta_c}}{1 - 2\sin^2\theta_2 + \sin^2\theta_c} \tag{6.100}$$

For TM polarised light, substitution of equation 6.97 and 6.98 into equation 6.94 gives the values of the reflection coefficient and its phase as

$$r_1 = \frac{\cos^2\theta_2 - \left(\frac{n_2}{n_1}\right)^2\left(\frac{\sin^2\theta_2}{\sin^2\theta_c} - 1\right) - 2i\frac{n_2}{n_1}\cos\theta_2\sqrt{\frac{\sin^2\theta_2}{\sin^2\theta_c} - 1}}{\cos^2\theta_2 + \left(\frac{n_2}{n_1}\right)^2\left(\frac{\sin^2\theta_2}{\sin^2\theta_c} - 1\right)} \tag{6.101}$$

$$\tan\varphi = \frac{-2\cos\theta_2\sqrt{\sin^2\theta_2 - \sin^2\theta_c}}{1 - 2\sin^2\theta_2 + \sin^2\theta_c} \tag{6.102}$$

Substituting $r_1 = e^{i\varphi}$ into equation 6.93 gives the eigenfrequencies of the guided modes as

$$\omega = \frac{c}{n_2\cos\theta_2 d_2}(m\pi - \varphi) \tag{6.103}$$

Thus the eigenfrequencies are purely real for the waveguiding regime reflecting their infinite lifetime. The eigenfrequencies are shifted from the frequencies of the corresponding Fabry-Perot modes in the structure by the value $c\varphi/n_2\cos\theta_2 d_2$. This shift of the eigenfrequencies is due to the phase shift of the light upon total internal reflection at either dielectric interface where the light undergoes total internal reflection. This phase shift is connected to the Goos-Hänchen shift [173], which is the lateral displacement that a light beam undergoes upon total internal reflection at a dielectric interface.

6.4.2 Numerical method of finding eigenfrequencies

To find the eigenfrequencies of a general planar layered structure, the transfer matrix must be calculated and the roots of equation 6.89 found. This can be done numerically by searching for the roots of the function in the complex angular frequency plane.

$$F(\omega) = M_{11} + M_{12}p_1 + M_{21}/p_1 + M_{22} = 0 \tag{6.104}$$

Since $F(\omega)$ is a complex function, the numerical search proceeds by finding the minimum in $|F(\omega)|$ and checking that the minimum are also the roots of $F(\omega)$ that are required. First the parameters of the search in the complex frequency plane are defined, and then the function $|F(\omega)|$ is minimised with respect to the real part of ω and then with respect to the imaginary part of ω. This procedure gives a value of ω in the vicinity of the root. For example, figure 6.4 shows the function $|F(\omega)|$ in the vicinity of a complex eigenfrequency of a guided mode of the waveguide structure shown in figure 6.3. Once in the vicinity of the root, the gradient of the function $|F(\omega)|$ can be evaluated, and a new estimate for the root found by moving in the direction of this gradient in the complex plane. After several iterations of this Newton-Raphson method, the minimum in the function $|F(\omega)|$ will be reached, and then it must be checked that this minimum is also a root by ensuring (to within numerical accuracy) that $|F(\omega)| = 0$ or $F(\omega) = 0$. As can be seen in figure 6.4, $|F(\omega)|$ is a smooth, well behaved function in the vicinity of the eigenfrequencies of the waveguide.

6.5 Waveguides with embedded quantum well

When a waveguide is embedded in a planar dielectric waveguide, there are two distinct choices of structure—either the quantum well can be placed in the guiding layer, where it will interact with the propagating field, or it can be placed in the cladding, where it will interact with the evanescent fields present there. The latter case is illustrated in figure 6.3.

6.5.1 Quantum well in the guiding layer

We consider the case of a quantum well placed at the centre of the guiding layer corresponding to $L = 0$ in figure 6.3 first. In the TE-polarisation, the transfer matrix across half

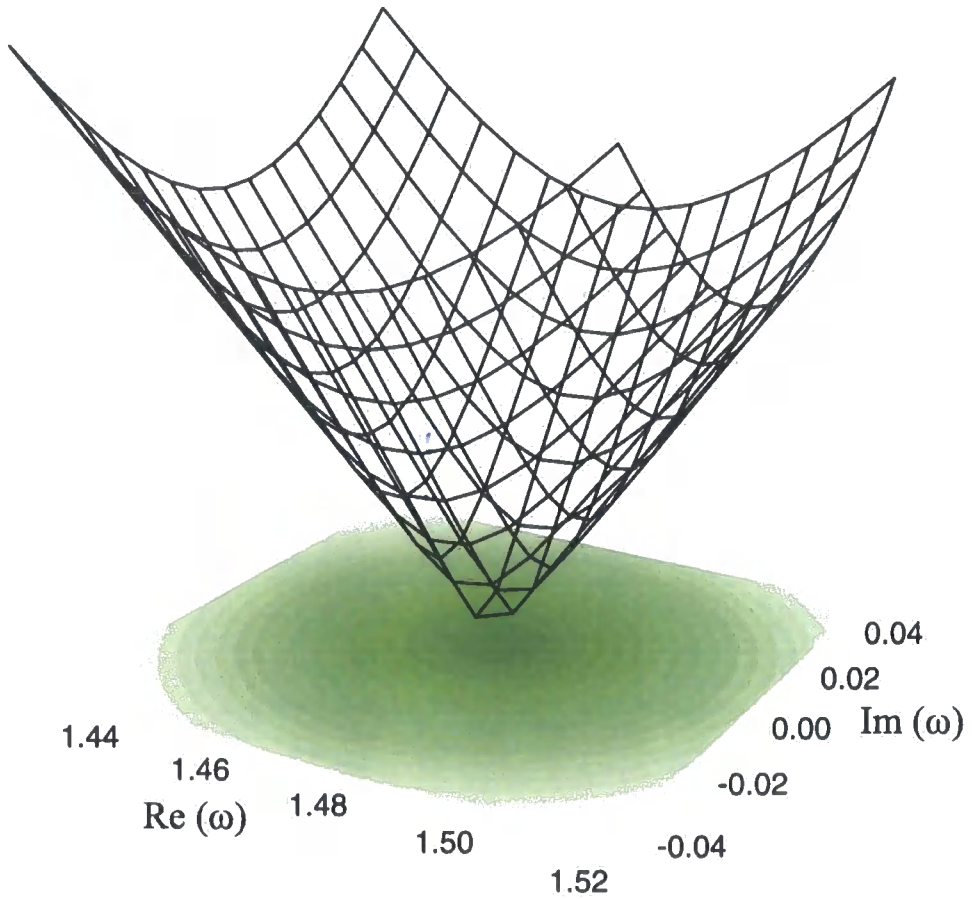

Figure 6.4 $|F(\omega)|$ for the waveguide structure in figure 6.3 in the vicinity of an eigenfrequency of a guided mode of the waveguide.

the waveguide is

$$\hat{\mathrm{M}}_{wg} = \begin{bmatrix} \cos(k_{2,z}d_2/2) & \frac{i}{p_2}\sin(k_{2,z}d_2/2) \\ ip_2\sin(k_{2,z}d_2/2) & \cos(k_{2,z}d_2/2) \end{bmatrix} \tag{6.105}$$

The transfer matrix across a structure can be expressed in terms of the reflection and transmission coefficients of the structure. For a symmetric structure in which the left and right bounding media are the same ($n_f = n_l$), such as for a quantum well embedded in a dielectric layer, then

$$\hat{\mathrm{M}} = \frac{1}{2t}\begin{bmatrix} t^2 - r^2 + 1 & -\left((1+r)^2 - t^2\right)/p \\ -p\left((1-r)^2 - t^2\right) & t^2 - r^2 + 1 \end{bmatrix} \tag{6.106}$$

In the case of a quantum well, $t_{qw} = 1 + r_{qw}$ and the transfer matrix for the quantum well is

$$\hat{\mathbf{M}}_{qw} = \begin{bmatrix} 1 & 0 \\ 2p_2 \dfrac{r_{qw}}{1 + r_{qw}} & 1 \end{bmatrix} \tag{6.107}$$

Therefore the transfer matrix for the structure when the quantum well is placed at the centre of the waveguide is

$$\hat{\mathbf{M}} = \hat{\mathbf{M}}_{wg}\hat{\mathbf{M}}_{qw}\hat{\mathbf{M}}_{wg} = \begin{bmatrix} M_{11} & M_{12} \\ M_{21} & M_{22} \end{bmatrix} \tag{6.108}$$

where

$$M_{11} = M_{22} = \cos\left(k_{2,z}d_2\right) - i\frac{r_{qw}}{1 + r_{qw}}\sin\left(k_{2,z}d_2\right) \tag{6.109}$$

$$M_{12} = \frac{i}{p_2}\sin\left(k_{2,z}d_2\right) + \frac{2}{p_2}\frac{r_{qw}}{1 + r_{qw}}\sin^2\left(k_{2,z}d_2/2\right) \tag{6.110}$$

$$M_{21} = ip_2\sin\left(k_{2,z}d_2\right) - 2p_2\frac{r_{qw}}{1 + r_{qw}}\cos^2\left(k_{2,z}d_2/2\right) \tag{6.111}$$

Now, from equation 6.34,

$$\frac{r_{qw}}{1 + r_{qw}} = \frac{i\tilde{\Gamma}_0}{\tilde{\omega}_0 - \omega - i\Gamma} \tag{6.112}$$

for TE-polarised waves. Far from the resonance frequency $\tilde{\omega}_0$, the quantity in equation 6.112 is small, and the transfer matrix elements in equation 6.109 to 6.111 have the same form as for a waveguide with no quantum well. However, as $\omega \to \tilde{\omega}_0$, the matrix elements depart significantly from the values in the absence of a quantum well, as shown in figure 6.5.

6.5.2 Dispersion relations

By adjusting value of the in-plane wavevector k_x and solving for the eigenvalues in the waveguide using equation 6.104, the dispersion relation $\omega\left(k_x\right)$ of the waveguide can be plotted. Figure 6.6 (a) shows the calculated dispersion relations for the cases $L = 0$ (quantum well in the centre of the waveguide, blue line), $L = 90\,\text{nm}$ (quantum well in the cladding, red line) and a bare waveguide with no quantum well (dashed line).

The dispersion of the bare waveguide is approximately linear, and is described by the

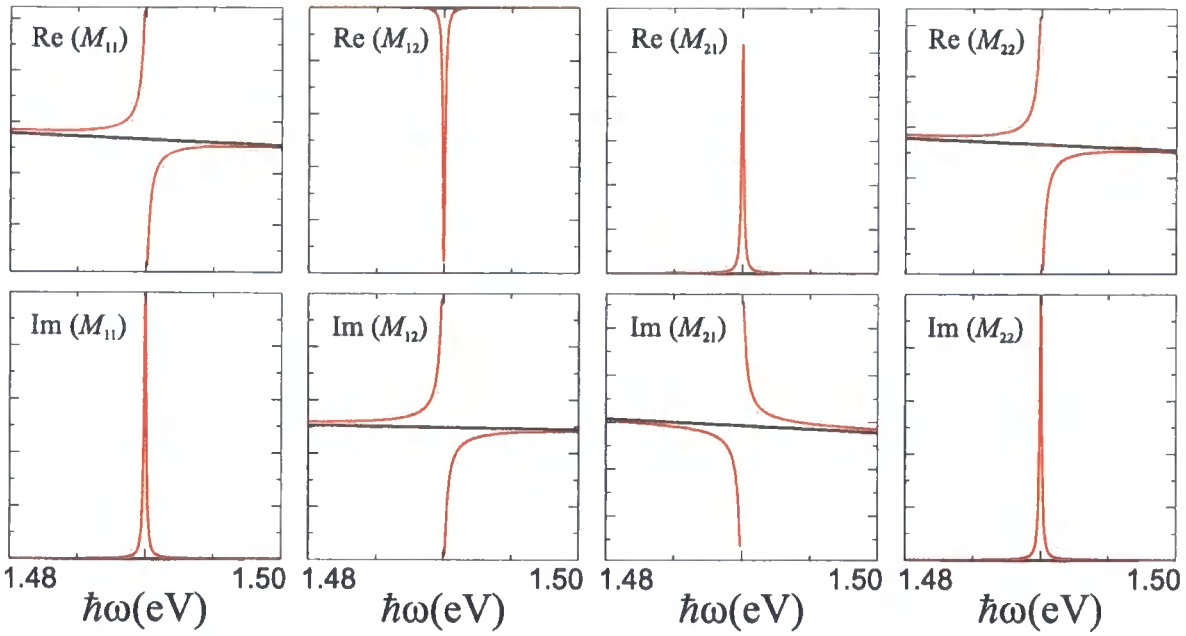

Figure 6.5 Transfer matrix elements as a function of the frequency ω for a dielectric waveguide (black) and a dielectric waveguide with a quantum well placed at the centre of the waveguide (red). The waveguide has parameters as shown in figure 6.3.

effective refractive index n_{eff} of the waveguide mode, where

$$k_x = n_{eff}\frac{\omega}{c} \tag{6.113}$$

The effective refractive index $n_{eff} = n_1 \sin\theta_1 = n_2 \sin\theta_2$ can take values between n_1 and n_2 for the waveguiding regime to be realised and is a measure of how much of the electric field of the mode is confined to the guiding layer.

When a quantum well is placed in the waveguide, a classic anti-crossing of the strongly coupled waveguide mode and exciton mode can be seen in figure 6.6 (a). This is the polariton effect, and the two branches of the dispersion relation are the upper and lower waveguide polariton modes. The imaginary parts of the complex eigenfrequencies (or mode damping coefficients) are shown in figure 6.6 (b). The solid lines are the mode damping coefficients of the lower polariton mode, and the dashed lines are for the upper mode. As a whole, figure 6.6 shows the transition between exciton-like modes, with no dispersion and finite lifetimes, to waveguide-like modes, with a linear dispersion relation and infinite lifetimes. The curves in between these two regions describe the waveguide polaritons modes.

The Rabi splitting of the upper and lower polariton modes is 6.6 meV for a quantum well at the centre of the waveguide, and 4.7 meV when the quantum well is placed in the cladding

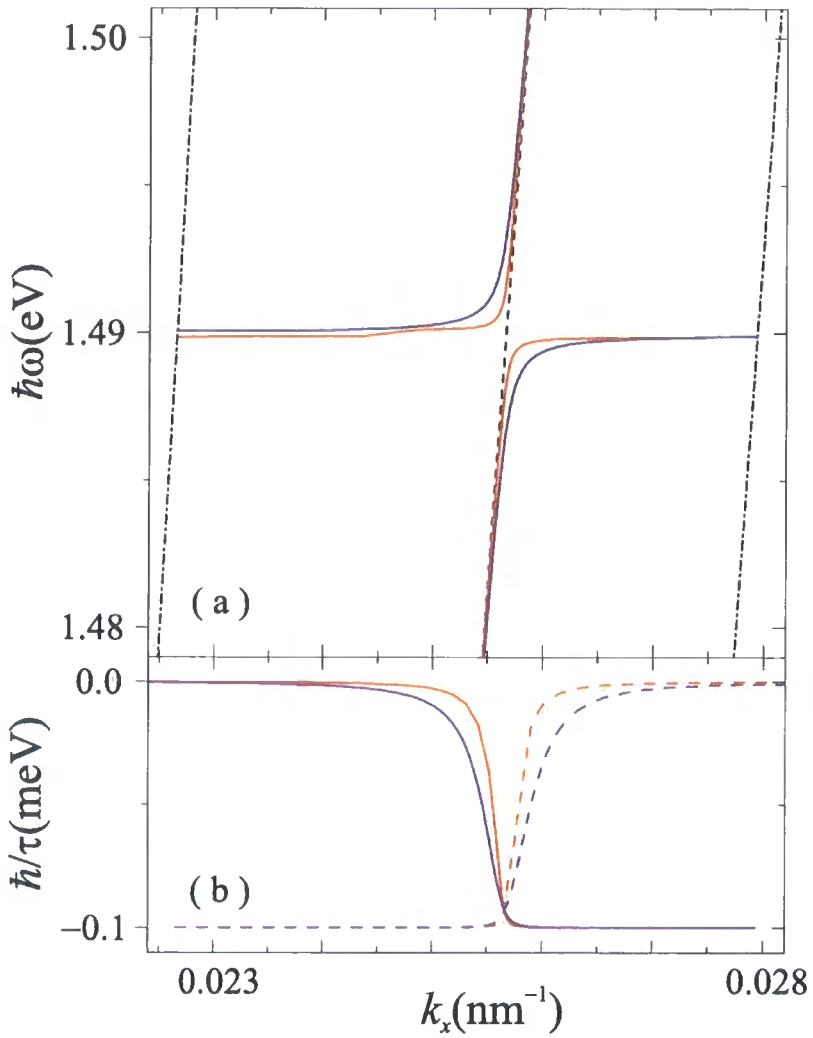

Figure 6.6 The dispersion relations for the TE_0 waveguide mode interacting with a quantum well exciton. The blue lines relate to the case of the quantum well at the centre of the waveguide ($L = 0$), whereas the red lines are for the quantum well in the cladding of the waveguide ($L = 90\,\text{nm}$). The complex eigenfrequencies of the waveguide polaritons have been calculated, with the real parts shown in (a), and the imaginary parts shown in (b) (the solid and dashed lines for the lower and upper waveguide polariton modes respectively). The dashed lines in (a) show the dispersion of the empty waveguide and the dash-dot lines show the cut-off frequencies for waveguiding. The quantum well exciton was modelled with the following parameters: $\hbar\omega_0 = 1.49\,\text{eV}$, $\hbar\Gamma_0 = 0.03\,\text{meV}$, $\hbar\Gamma = 0.1\,\text{meV}$.

at $L = 90\,\text{nm}$. The magnitude of the splitting is smaller in the $L = 90\,\text{nm}$ case than the $L = 0$ case due to the smaller electric field interacting with the quantum well exciton. In both cases, at the anti-crossing point the two polariton modes have lifetimes of $\tau = 7\,\text{ps}$ and a group velocity of $v_g = d\omega/dk_x = 0.14c$, which corresponds to a propagation distance along the waveguide of $v_g\tau = 0.3\,\text{mm}$.

6.6 Conclusions

This chapter has been concerned with the modelling of a structure in which waveguide polaritons occur. A semi-classical formalism based on non-local dielectric response theory has been developed to describe the interaction of a quantum well exciton with an evanescent plane wave, such as exists behind a dielectric interface where light undergoes total internal reflection as in the cladding of a dielectric waveguide in the guiding regime of light. Exact solutions of the Maxwell equations are obtained in a Green function method, for both the TE and TM-polarisations of light. Reflection and transmission coefficients for an evanescent plane wave interacting with a quantum well are shown to be identical to the case of propagating waves interacting with the quantum well, as long as a complex angle of incidence of the evanescent wave onto the quantum well, given by a generalised Snell's law, is used to describe the electromagnetic fields.

The excitonic response of a quantum well placed behind a dielectric interface has been modelled and it is found that if the angle of incidence of the light is equal to the critical angle for total internal reflection, the excitonic response in the reflection spectrum becomes significantly more pronounced and is an order of magnitude greater than in the normal incidence case.

A transfer matrix method has been applied to calculate the dispersion relation of a quantum well exciton interacting with the fundamental electromagnetic mode of a planar dielectric waveguide. Quantum wells in both the guiding layer and cladding of the waveguide have been modelled using experimentally feasible parameters for the waveguide and quantum well system. For the waveguide and quantum well parameters considered, strongly coupled waveguide polariton modes were apparent in the behaviour of the dispersion curves for both cases. At the anti-crossing point of the upper and lower polariton branches, the waveguide

polaritons are calculated to have lifetimes of around 7 ps, corresponding to a displacement along the waveguide axis of 0.3 mm. The Rabi-splitting of the two polariton branches of the dispersion relation is 6.6 meV when the quantum well is placed at the centre of the waveguide to interact with the anti-node of electric field of the fundamental waveguide mode. A smaller splitting of the polariton modes (4.7 meV) was found for the case of a quantum well placed in the cladding of the waveguide, where it interacts with the evanescent electromagnetic fields present there.

Chapter 7

Summary and Conclusions

This thesis has been concerned with the computational study of photonic crystals and other photonic microstructures, which have been the focus of world-wide research for the past 15 years owing to the potential for their use in a wide range of applications. Many of the proposed applications rely on the existence of a photonic band gap that can be formed using such structures; hence this thesis has chosen to concentrate on the photonic band gap. Theoretical methods for solving the Maxwell equations in one and two-dimensional dielectric structures are given (chapter 2 and chapter 3), and appropriate computational schemes are discussed. Novel designs for a 2D photonic crystal, based on an etched Bragg reflector (chapter 3) and an octagonal quasicrystalline unit cell (chapter 5), are proposed and shown to possess complete photonic band gaps for one polarisation of light. The parameters of the structures which optimise the properties (such as the width and isotropy) of the photonic band gap have been found. The controlled introduction of photonic modes with frequencies in the band gap via the introduction of microcavities into the photonic crystal has been discussed. The use of such modes is demonstrated in the design of a multilayered optical bandpass filter (chapter 2). The uncontrolled introduction of photonic modes into the band gap caused by disorder in the otherwise periodic relative permittivity in the photonic crystals is also investigated (chapter 4).

In chapter 2, it has been shown that a defect or microcavity layer can introduce a localised mode at a frequency that lies in the 1D photonic band gap of a periodic multilayer structure (a Bragg reflector). Such modes can be split in frequency by coupling together two or more microcavities, and it is shown that for a large number of coupled microcavities, a miniband

of allowed photonic states forms within the photonic band gap. A simple analytical approach has been developed to engineer the line shapes and tune the frequencies of the microcavity modes, and has been applied to design an optical passband filter based on coupled microcavities. It was found that the optimum square-shaped passband occurs at the transition between strong and weak coupling of the microcavity modes, and the parameters and properties of an optimal structure have been provided for a particular case.

The optical properties of a novel design for a 2D photonic crystal based on the deep etching of a Bragg reflector with air grooves parallel to the growth direction have been studied in chapter 3. The etched Bragg reflector was found to possess a wide complete photonic band gap for one polarisation of light for a large range of geometrical parameters of the structure, but only very narrow absolute photonic band gaps (where the complete band gaps of both polarisations overlap spectrally) were demonstrated, and then only for a very restrictive set of geometrical parameters. However, a wide spectral band where there is a significant reduction (up to a factor of 20) in the total density of photonic states as compared to a uniform medium characterised by the same mean relative permittivity is found for a large range of parameters of the etched Bragg reflector. These structures possess the ability to suppress strongly the spontaneous emission rate of an entity in the plane of the photonic crystal, and could also be used to provide effective optical confinement in two perpendicular directions. A systematic search of the geometrical parameter space of the etched Bragg reflector has been conducted, and the parameters of the structure which optimise the width of the complete band gap, and the spectral band of reduced density of states, are given. The calculated bandstructure, density of states and transmission spectra of the optimised structures have been presented.

The effect of disorder in an otherwise periodic modulation of the relative permittivity is investigated for both 1D and 2D photonic crystals in chapter 4. For disorder in 1D photonic crystals, the transfer matrix method was used to calculate directly the eigenfrequencies and lifetimes of modes in disordered Bragg reflectors. The photonic eigenmodes of an ensemble of 10^4 randomly disordered Bragg reflectors were investigated statistically for three models of disorder. By parameterising the level of disorder present in an ensemble of Bragg reflectors by the maximum deviation of the optical period away from that in the ideal structure, it is shown that the tail of the density of photonic states in the band gap is described by the tail

of a Gaussian function and is characterised by a penetration depth parameter. The relative penetration depth parameter is found to be directly proportional to the disorder parameter and the square root of the relative width of the photonic band gap. These dependences mean that the photonic band gap is resilient to disorder in 1D photonic crystals—it is apparent that there is a certain level of disorder below which the probability of finding disorder-induced states with eigenfrequencies at the centre of the photonic band gap is negligible. The effect of the mode structure on the transmission of an ensemble of 10^6 disordered structures was investigated, and it is shown that the penetration of photonic states into the band gap produces a threshold-like behaviour of the ensemble-averaged transmission at the centre of the band gap as a function of the disorder parameter. For small disorder below the threshold, perturbed edge states narrow the band gap, but transmission at the centre of the band gap increases slowly with increase of the disorder parameter. For disorder levels above the threshold, states have a significant probability of appearing throughout the band gap, and the ensemble-averaged transmission at the centre of the band gap increases rapidly with the disorder. For large disorder, states in the band gap are shown to have the characteristics of being localised on random microcavities, as well as perturbed edge states.

Two-dimensional hexagonal photonic crystals consisting of cylinders of air in a dielectric substrate, where the cylinders are randomly displaced from an ideal lattice, have been studied. The greater computational resources required to model 2D systems compared to 1D systems meant that a sample of only 10 disordered photonic crystals could be considered for each set of parameters. However, conclusions drawn from the statistical study of the eigenmodes of disordered 1D photonic crystals can be used to guide the interpretation of the results for disordered 2D photonic crystals. The transmission of both ballistic and scattered light have been modelled. A threshold behaviour of the ensemble-averaged ballistic transmission as a function of the disorder parameter is seen, similar to the case of transmission through disordered 1D photonic crystals, and this again is explained by the penetration of disorder-induced states into the photonic band gap. For large disorder, these states are shown to have the characteristics of states localised on random microcavities within the disordered 2D photonic crystal. However, the scattered transmission was shown to have a different dependence on the disorder parameter, and grows rapidly for small disorder.

The effect of disorder on a 2D photonic crystal with an incomplete band gap was also

considered. It was found that the closing of the band gap for certain directions allows the light to be scattered from evanescent states in the incident direction to propagating states in other directions in the crystal, and Fabry-Perot like modes are seen in the transmission spectra of the scattered light. The scattered transmission also becomes asymmetric due to the curvature of the allowed photonic bands above and below the incomplete band gap being different, so that the minimum in the transmission no longer coincides with the centre of the band gap.

The bandstructures of two-dimensional photonic crystals with octagonal quasicrystalline unit cells were calculated for a range of unit cells sizes and filling fractions in chapter 5. A complete 2D photonic band gap is found for one polarisation of light, and it is shown that the band gap becomes more isotropic as the size of the unit cell is increased. This is attributed to the increase in the range of the local quasicrystalline order in the unit cell of the crystal. For small filling fractions, a minimum size of the unit cell is needed for the formation of a complete photonic band gap, but the widest band gaps are found for unit cells of intermediate size. The formation of the photonic band gap is attributed to Bragg-like diffraction from certain planes in the quasicrystalline unit cell.

By considering the above photonic crystal with a quasicrystalline unit cell as a photonic quasicrystal in a supercell approximation, several microcavities at inequivalent sites in the photonic quasicrystal were considered. The eigenfrequencies of the microcavity modes as a function of the filling fraction were calculated, and the associated electromagnetic field profiles presented.

In chapter 6, a semi-classical formalism based on a non-local dielectric response theory is used to describe the interaction of a quantum well exciton with evanescent electromagnetic plane waves. Simplified expressions for the reflection and transmission of plane evanescent waves from a quantum well exciton are given, and it is shown that these are identical to the usual case of the interaction with propagating plane waves, as long as a complex angle of propagation found from a generalised Snell's law is used to describe the electromagnetic field of the evanescent plane wave.

The excitonic response of a quantum well placed behind a dielectric interface where total internal reflection can take place was calculated, and a large enhancement (by an order of magnitude) of the excitonic modulation of the reflection spectrum was demonstrated for

angles of incidence on the dielectric interface close to the critical angle for total internal reflection. A generalised transfer matrix method was then used to calculate the dispersion relations of waveguide polaritons. Two cases were considered—the quantum well embedded in the guiding layer of the waveguide, and the quantum well embedded in the cladding, where it interacts with the evanescent wave present there. For the parameters used for the waveguide and quantum well systems, an anti-crossing of the waveguide and exciton modes is seen for both cases, indicating that the strong coupling regime is realised. For the parameters used, the lifetimes of the upper and lower polaritons at the anti-crossing point were both close to 7 ps, corresponding to a displacement along the waveguide axis of 0.3 mm. The Rabi-splitting for a quantum well at the centre of the waveguide (6.6 meV) is larger than for the quantum well placed in the cladding (4.7 meV) due to the magnitude of the electric field in the centre of the waveguide being larger than that in the cladding.

7.1 Suggestions for further work

This section attempts to present some possible extensions to work in this thesis and also some other possible avenues of research along the same themes.

It was found in chapter 3 that the etched Bragg reflector structures can support a wide photonic band gap for one polarisation of light. The effect of disorder on the photonic band gap in this structure could be studied. The effect of a random displacement of the high relative permittivity "walls" in each unit cell would be especially interesting, as it would simulate the surface roughness that would surely result from any etching procedures on the scale required to fabricate a structure for use at visible frequencies. Also, defects or microcavities, and the field profiles of modes localised on them, could be studied, either by removing dielectric from the high relative permittivity walls or adding dielectric material to the air grooves. Such studies could be performed using similar methods to the study of disorder in 2D photonic crystals of chapter 4.

Photonic crystals with octagonal quasicrystalline unit cell were studied in chapter 5. Several different sized square unit cell can be chosen that are based on the octagonal quasicrystal. One possible extension of this work would be to repeat the study with a dodecagonal quasicrystal (with 12-fold rotational symmetry) where several different sized hexagonal unit

cells could be chosen. The methods used for such a study would be the same as in chapter 5, and it would be interesting to compare and contrast the results of such as a study with those already found here.

A major theme of this work has been the effects of disorder on the properties of photonic crystals. However, many facets of disorder are unexplored in the literature on photonic crystals, and could serve as the basis of future work. For example, an interface between photonic crystals or a surface of a photonic crystal is known to support localised interface/surface modes [181, 182]. For any photonic crystal to be technologically useful, we must be able to couple light into the photonic crystal at an interface or surface, and since all photonic crystals will be disordered to some extent, it would be interesting to know the effect of disorder on these interface/surface modes. The interface matching technique in ref. [59] could be used as a calculational basis for this investigation, but other methods of investigating interfaces or surfaces also exist, including supercell approximations in the plane wave method. Another extension would be to study disorder in 3D photonic crystals. As computers become more powerful, it will become feasible to study disorder in 3D photonic crystals using a supercell approach in a more systematic way than has currently been attempted.

Chapter 3 presented a transfer matrix method for the calculation of reflection and transmission coefficients of 2D structures by the solution of the Maxwell equations on a mesh. This method could be reformulated to include outgoing wave boundary conditions, similar to those used in the transfer matrix method for 1D multilayers in chapter 2, in order to calculate directly the frequencies and lifetimes of the eigenmodes of finite 2D photonic structures. Numerical routines contained in the publicly available code by Pendry *et al.* [20, 106, 107] could be modified once the form of the reformulation is known. However, this would be a far from trivial task, and the final success is in some doubt due to the numerical instabilities that the transfer matrix method suffers from. If successful, the new method would be a useful tool in the investigation of the properties of all 2D photonic structures. In particular, it could be used for the statistical study of the eigenmodes of disordered 2D photonic crystals similar to that carried out for 1D photonic crystals in chapter 4, although the sample size of disordered systems would still be limited by the available computational resources.

References

[1] P. A. Packan. *Pushing the limits.* Science **285** 2079–2081, 1999.

[2] J. D. Joannopoulos, R. D. Meade, and J. N. Winn. *Photonic Crystals: Molding the Flow of Light.* Princeton University Press, 1995.

[3] K. Sakoda. *Optical Properties of Photonic Crystals.* Springer, Berlin, 2001. ISBN: 3-540-41199-2.

[4] J. D. Joannopoulos, P. R. Villeneuve, and S. Fan. *Photonic crystals: putting a new twist on light.* Nature **386** 143–149, 1997.

[5] E. Yablonovitch. *Photonic band-gap crystals.* J. Phys.: Condens. Matter **5** 2443–2460, 1993.

[6] E. Yablonovitch. *Photonic band-gap structures.* J. Opt. Soc. Am. B **10** (2) 283–294, 1993.

[7] J. Pendry. *Playing tricks with light.* Science **285** 1687–1688, 1999.

[8] E. Yablonovitch. *Inhibited spontaneous emission in solid-state physics and electronics.* Phys. Rev. E **58** (20) 2059–2062, 1987.

[9] S. John. *Strong localization of photons in certain disordered dielectric superlattices.* Phys. Rev. Lett. **58** (23) 2486–2489, 1987.

[10] J. D. Joannopoulos. *Self assembly lights up.* Nature **414** 257–258, 2001.

[11] A. Blanco, E. Chomski, S. Grabtchak, M. Ibisate, S. John, S. W. Leonard, C. Lopez, F. Meseguer, H. Miguez, J. P. Mondia, G. A. Ozin, O. Toader, and H. M. van Driel.

Large-scale synthesis of a silicon photonic crystal with a complete three-dimensional bandgap near 1.5 micrometres. Nature **405** 437–440, 2000.

[12] K. Busch and S. John. *Photonic band gap formation in certain self-organizing systems.* Phys. Rev. E **58** (3) 3896–3908, 1998.

[13] E. Pavarini, L. C. Andreani, C. Soci, M. Galli, F. Marabelli, and D. Comoretto. *Band structure and optical properties of opal photonic crystals.* Phys. Rev. B **72** 045102, 2005.

[14] A. Rugge, J-S. Park, R. G. Gordon, and S. H. Tolbert. *Tantalum(v) nitride inverse opals as photonic structures for visible wavelengths.* J. Phys. Chem. B **109** 3764–3771, 2005.

[15] Y. A. Vlasov, X. Z. Bo, J. C. Sturm, and D. J. Norris. *On-chip natural assembly of silicon photonic bandgap crystals.* Nature **414** 289–293, 2001.

[16] J. E. G. J. Wijnhoven and W. L. Vos. *Preparation of photonic crystals made of air spheres in titania.* Science **281** 802–804, 1998.

[17] K. M. Ho, C. T. Chan, and C. M. Soukoulis. *Existence of a photonic gap in periodic dielectric structures.* Phys. Rev. Lett. **65** (25) 3152–3155, 1990.

[18] S. Fan, P. R. Villeneuve, R. D. Meade, and J. D. Joannopoulos. *Design of three-dimensional photonic crystals at submicron lengthscales.* Appl. Phys. Lett. **65** (11) 1466–1468, 1994.

[19] D. Cassagne, C. Jouanin, and D. Bertho. *Hexagonal photonic-band-gap structures.* Phys. Rev. B **53** (11) 7134–7142, 1996.

[20] J. B. Pendry and A. MacKinnon. *Calculation of photon dispersion-relations.* Phys. Rev. Lett. **69** (19) 2772–2275, 1992.

[21] M. Plihal and A. A. Maradudin. *Photonic band-structure of 2-dimensional systems - the triangular lattice.* Phys. Rev. B **44** (16) 8565, 1991.

[22] J. N. Winn, R. D. Meade, and J. D. Joannopoulos. *Two-dimensional photonic band-gap materials.* J. Mod. Optics **41** (2) 257–273, 1994.

[23] P. R. Villeneuve and M. Piché. *Photonic band gaps in two-dimensional square and hexagonal lattices.* Phys. Rev. B **46** (8) 4969–, 1992.

[24] R. D. Meade, K. D. Brommer, A. M. Rappe, and J. D. Joannopoulus. *Existence of a photonic band-gap in two dimensions.* Appl. Phys. Lett. **61** (4) 495–497, 1992.

[25] R. D. Meade, A. M. Rappe, K. D. Brommer, J. D. Joannopoulus, and O. L. Alerhand. *Accurate theoretical analysis of photonic band-gap materials.* Phys. Rev. B **48** (11) 8434–8437, 1993.

[26] R. Padjen, J. M. Gerard, and J. Y. Marzin. *Analysis of the filling pattern dependence of the photonic bandgap for two-dimensional systems.* J. Mod. Optics **41** (2) 295–310, 1994.

[27] Z. Zhang and S. Satpathy. *Electromagnetic wave propagation in periodic structures: Bloch wave solution of Maxwell's equations.* Phys. Rev. Lett. **65** (21) 2650–2653, 1990.

[28] K. M. Leung and Y. F. Liu. *Full vector wave calculation of photonic band structures in face-centred-cubic dielectric media.* Phys. Rev. Lett. **65** (21) 2646–2649, 1990.

[29] J. W. Haus. *A brief review of theoretical results for photonic band structures.* J. Mod. Optics **41** (2) 195–207, 1994.

[30] H. S. Sözüer and J. P. Dowling. *Photonic band calculations for woodpile structures.* J. Mod. Optics **41** (2) 231–239, 1994.

[31] T. F. Krauss, R. M. De La Rue, and S. Brand. *Two-dimensional photonic-bandgap structures operating at near infrared wavelengths.* Nature **383** 699–702, 1996.

[32] U. Grüning, V. Lehmann, S. Ottow, and K. Busch. *Macroporous silicon with a complete two-dimensional photonic band-gap centered at 5 μm.* Appl. Phys. Lett. **68** (6) 747–749, 1996.

[33] M. Zelsmann, E. Picard, T. Charvolin, E. Hadji, M. Heitzmann, B. Dal'zotto, M. E. Nier, C. Seassal, P. Rojo-Romeo, and X. Letartre. *Seventy-fold enhancement of light extraction from a defectless photonic crystal made on silicon-on-insulator.* Appl. Phys. Lett. **83** (13) 2542–2544, 2003.

[34] S. Noda, K. Tomoda, N. Yamamoto, and A. Chutinan. *Full three-dimensional photonic bandgap crystal at near-infrared wavelengths.* Science **289** 604–606, 2000.

[35] S. Y. Lin, J. G. Fleming, D. L. Hetherington, B. K. Smith, R. Biswas, K. M. Ho, M. M. Sigalas, W. Zubrzycki, S. R. Kurtz, and J. Bur. *A three-dimensional photonic crystal operating at infrared wavelengths.* Nature **394** 251–253, 1998.

[36] E. Pavarini and L. C. Andreani. *Etched distributed Bragg reflectors as three-dimensional photonic crystals: Photonic bands and density of states.* Phys. Rev. E **66** 036602, 2002.

[37] S. G. Johnson and J. D. Joannopoulos. *Three-dimensionally periodic dielectric layered structure with omnidirectional photonic band gap.* Appl. Phys. Lett. **77** (22) 3490–3492, 2000.

[38] S. G. Johnson, S. Fan, P. R. Villeneuve, and J. D. Joannopoulos. *Guided modes in photonic crystal slabs.* Phys. Rev. B **60** (8) 5751–5758, 1999.

[39] Y. Tsai, J. B. Pendry, and K. W.-K. Shung. *Absolute three-dimensional photonic band gap in the infrared regime in woven structures.* Phys. Rev. B **59** (16) R10401–R10404, 1999.

[40] R. D. Meade, K. D. Brommer, A. M. Rappe, and J. D. Joannopoulus. *Photonic bound states in periodic dielectric media.* Phys. Rev. B **44** (24) 13772–13774, 1991.

[41] P. R. Villeneuve, S. Fan, and J. D. Joannopoulos. *Microcavities in photonic crystals: mode symmetry, tunability, and coupling efficiency.* Phys. Rev. B **54** (11) 7837–7842, 1996.

[42] F. Jonsson, C. M. Sotomayor Torres, J. Seekamp, M. Schniedergers, A. Tiedemann, J. Ye, and R. Zentel. *Artificially inscribed defects in opal photonic crystals.* Microelectronic Engineering **78** (79) 429–435, 2005.

[43] M. A. Kaliteevski, J. Manzanares Martinez, D. Cassagne, J. P. Albert, S. Brand, and R. A. Abram. *Appearence of photonic minibands in disordered photonic crystal.* J. Phys.: Condens. Matter **15** 785–790, 2003.

[44] J. S. Foresi, P. R. Villeneuve, J. Ferrera, E. R. Thoen, G. Steinmeyer, S. Fan, J. D. Joannopoulos, L. C. Kimerling, H. I. Smith, and E. P. Ippen. *Photonic band-gap microcavities in optical waveguides.* Nature **390** 143–145, 1997.

[45] E. Özbay, G. Tuttle, M. Sigalas, C. M. Soukoulis, and K. M. Ho. *Defect structure in a layer-by-layer photonic band-gap crystal.* Phys. Rev. B **51** (20) 13961–13965, 1995.

[46] M. Qi, E. Lidorikis, P. T. Rakich, S. G. Johnson, J. D. Joannopoulos, E. P. Ippen, and H. I. Smith. *A three-dimensional optical photonic crystal with designed point defects.* Nature **429** 538–542, 2004.

[47] M. Bayindir, B. Temelkuran, and E. Ozbay. *Tight-binding description of the coupled defect modes in three-dimensional photonic crystals.* Phys. Rev. Lett. **84** (10) 2140–2143, 2000.

[48] S. G. Johnson, P. R. Villeneuve, S. Fan, and J. D. Joannopoulos. *Linear waveguides in photonic-crystal slabs.* Phys. Rev. B **62** (12) 8212–8222, 2000.

[49] S. Lan, S. Nishikawa, Y. Sugimoto, N. Ikeda, K. Asakawa, and H. Ishikawa. *Analysis of defect coupling in one- and two-dimensional photonic crystals.* Phys. Rev. B **65** 165208, 2002.

[50] M. F. Yanik and S. Fan. *Stopping light all optically.* Phys. Rev. Lett. **92** (8) 083901, 2004.

[51] A. Mekis, S. Fan, and J. D. Joannopoulos. *Bound states in photonic crystal waveguides and waveguide bends.* Phys. Rev. B **58** (8) 4809–4817, 1998.

[52] A. Mekis, J. C. Chen, I. Kurland, S. Fan, P. R. Villeneuve, and J. D. Joannopoulos. *High transmission through sharp bends in photonic crystal waveguides.* Phys. Rev. Lett. **77** (18) 3787–3790, 1996.

[53] G. Parker and M. Charlton. *Photonic crystals.* Physics World August 2000.

[54] J. C. Knight, J. Broeng, T. A. Birks, and P. St. J. Russell. *Photonic band gap guidance in optical fibers.* Science **282** 1476–1478, 1998.

[55] P. Russell. *Photonic crystal fibers.* Science **299** 358–362, 2003.

[56] P. Yeh. *Optical waves in layered media.* John Wiley & Sons, 1988.

[57] M. Born and E. Wolf. *Principles of Optics.* Cambridge University Press, sixth edition, 1980.

[58] H. Kosaka, T. Kawashima, A. Tomita, M. Notomi, T. Tamamura, T. Sato, and S. Kawakami. *Superprism phenomena in photonic crystals.* Phys. Rev. B **58**(16) R10096–R10099, 1998.

[59] A. A. Reeves. *Theoretical studies of one-dimensional and two-dimensional photonic structures.* PhD thesis, University of Durham, 2004.

[60] E. Cubukcu, K. Aydin, E. Ozbay, S. Foteinopoulou, and C. M. Soukoulis. *Negative refraction by photonic crystals.* Nature **423** 604–605, 2003.

[61] J. D. Jackson. *Classical electrodynamics.* John Wiley & Sons, third edition, 1999. ISBN 0-471-30932-X.

[62] J. R. Wendt, G. A. Vawter, P. L. Gourley, T. M. Brennan, and B. E. Hammons. *Nanofabrication of photonic lattice structures in GaAs/AlGaAs.* J. Vac. Sci. Technol. B **11** (6) 2637–2640, 1993.

[63] D. E. Wohlert, H. C. Lin, K. L. Chang, G. W. Pickrell Jr., J. H. Epple, K. C. Hsieh, and K. Y. Cheng. *Fabrication of a substrate-independent aluminum oxide-GaAs distributed Bragg reflector.* Appl. Phys. Lett. **75** (10) 13711373, 1999.

[64] M. V. Maximov, E. M. Ramushina, V. I. Skopina, E. M. Tanklevskaya, V. A. Solov'ev, Yu. M. Shernyakov, I. N. Kaiander, M. A. Kaliteevski, S. A. Gurevich, N. N. Ledentsov, V. M. Ustinov, Zh. I. Alferov, C. M. Sotomayor Torres, and D. Bimberg. *Edge-emitting InGaAs/GaAs lasers with deeply etched semiconductor/air distributed Bragg reflector mirrors.* Semicond. Sci. Technol. **17** L69–L71, 2002.

[65] V. Pacradouni, W. J. Mandeville, A. R. Cowan, P. Paddon, J. F. Young, and S. R. Johnson. *Photonic band structure of dielectric membranes periodically textured in two dimensions.* Phys. Rev. B **62** (7) 4204–4207, 2000.

[66] L. Dal Negro, C. J. Oton, Z. Gaburro, L. Pavesi, P. Johnson, A. Lagendijk, R. Righini, M. Colocci, and D. S. Wiersma. *Light transport through the band-edge states of Fibonacci quasicrystals.* Phys. Rev. Lett. **90** (5) 055501, 2003.

[67] L. Dal Negro, M. Stolfi, Y. Yi, J. Michel, X. Duan, L. C. Kimerling, J. LeBlanc, and J. Haavisto. *Photon band gap properties and omnidirectional reflectance in Si/SiO_2 Thue-Morse quasicrystals.* Appl. Phys. Lett. **84** (25) 5186–5188, 2004.

[68] V. Yannopapas, N. Stefanou, and A. Modinos. *Effect of stacking faults on the optical properties of inverted opals.* Phys. Rev. Lett. **86** (21) 4811–4814, 2001.

[69] Yu. A. Vlasov, M. A. Kaliteevski, and V. V. Nikolaev. *Different regimes of light localization in a disordered photonic crystal.* Phys. Rev. B **60** (3) 1555–1562, 1999.

[70] S. Wong, V. Kitaev, and G. A Ozin. *Colloidal crystal films: advances in universality and perfection.* J. Am. Chem. Soc. **125** 15589–15598, 2003.

[71] J. Broeng, S. E. Barkou, A. Bjarklev, J. C. Knight, T. A. Birks, and P. S. J. Russell. *Highly increased photonic band gaps in silica/air structures.* Optics Commun. **156** 240–244, 1998.

[72] A. Convertino, A. Valentini, P. V. Giugno, and R. Cingolani. *Infrared distributed Bragg reflectors based on amorphous SiC/SiO_2 heterostructures.* Appl. Phys. Lett. **70** (21) 2799–2800, 1997.

[73] C-C. Kao, Y. C. Peng, H. H. Yao, J. Y. Tsai, Y. H. Chang, J. T. Chu, H. W. Huang, T. T. Kao, T. C. Lu, H. C. Kuo, and S. C. Wang. *Fabrication and performance of blue GaN-based vertical-cavity surface emitting laser employing AlN/GaN and Ta_2O_5/SiO_2 distributed Bragg reflector.* Appl. Phys. Lett. **87** 081105, 2005.

[74] Yu. A. Vlasov, V. N. Astratov, O. Z. Karimov, A. A. Kaplianskii, V. N. Bogomolov, and A. V. Prokofiev. *Existence of a photonic pseudogap for visible light in synthetic opals.* Phys. Rev. B **55** (20) 13357–13360, 1997.

[75] J. Dorsaz, J. F. Charlin, S. Gradecak, and M. Ilegems. *Progess in AlInN–GaN Bragg reflectors: Application to a microcavity light emitting diode.* J. Appl. Phys. **97** 084505, 2005.

[76] M. E. Zoorob, M. D. B. Charlton, G. J. Parker, J. J. Baumberg, and M. C. Netti. *Complete photonic bandgaps in 12-fold symmetric quasicrystals.* Nature **404** 740–743, 2000.

[77] M. E. Zoorob, M. D. B. Charlton, G. J. Parker, J. J. Baumberg, and M. C. Netti. *Complete and absolute photonic bandgaps in highly symmetric photonic quasicrystals embedded in low refractive index materials.* Mat. Sci. B **74** 168–174, 2000.

[78] A. Convertino, A. Valentini, T. Ligonzo, and R. Cingolani. *Organic-inorganic dielectric multilayer systems as high reflectivity distributed Bragg reflectors.* Appl. Phys. Lett. **71** (6) 732–734, 1997.

[79] A. Convertino, A. Valentini, and R. Cingolani. *Organic multilayers as distributed Bragg reflectors.* Appl. Phys. Lett. **75** (3) 322–324, 1999.

[80] R. Sharma, E. D. Haberer, C. Meier, E. L. Hu, and S. Nakamura. *Vertically oriented GaN-based air-gap distributed Bragg reflector structure fabricated using band-gap-selective photoelectrochemical etching.* Appl. Phys. Lett. **87** 051107, 2005.

[81] C. Lei, T. J. Rogers, D. G. Deppe, and B. G. Streetman. *$ZnSe/CaF_2$ quarter-wave Bragg reflector for the vertical-cavity surface-emitting laser.* J. Appl. Phys. **69** (11) 74307434, 1991.

[82] R. C. Weast, D. R. Lide, M. J. Astle, and W. H. Beyer, editors. *Handbook of chemistry and physics.* CRC Press, Boca Raton, Florida, 70th edition, 1989.

[83] J. S. Blakemore. *Semiconducting and other major properties of gallium arsenide.* J. Appl. Phys. **53** (10) R123–R181, 1982.

[84] S. Adachi. *GaAs, AlAs and $Al_xGa_{1-x}As$: Material parameters for use in research and device applications.* J. Appl. Phys. **58** (3) R1–R29, 1985.

[85] M. Garriga, P. Lautenschlager, M. Cardona, and K. Ploog. *Optical properties of AlAs.* Solid State Commun. **61** (3) 157–160, 1987.

[86] S. Chao, W. H. Wang, M. Y. Hsu, and L. C. Wang. *Charateristics of ion-beam-sputtered high-refractive index TiO_2-SiO_2 mixed films.* J. Opt. Soc. Am. A **16** (6) 1477–1483, 1999.

[87] S. L. McCall, P. M. Platzman, R. Dalichaouch, D. Smith, and S. Schultz. *Microwave propagation in two-dimensional dielectric lattices.* Phys. Rev. Lett. **67** (15) 2017–2020, 1991.

[88] W. M. Robertson, G. Arjavalingam, R. D. Meade, K. D. Brommer, A. M. Rappe, and J. D. Joannopoulos. *Measurement of photonic band structure in a two-dimensional periodic dielectric array.* Phys. Rev. Lett. **68** (13) 2023–2026, 1992.

[89] E. Yablonovitch, T. J. Gritter, and K. M. Leung. *Photonic band structure: the face-centred-cubic case employing nonspherical atoms.* Phys. Rev. Lett. **67** (17) 2295–2298, 1991.

[90] E. Yablonovitch and T. J. Gritter. *Photonic band structure: the face-centred-cubic case.* Phys. Rev. Lett. **63** (18) 1950–1953, 1989.

[91] D. R. Smith, S. Schultz, S. L. McCall, and P. M. Platzmann. *Defect studies in a two-dimensional periodic photonic lattice.* J. Mod. Optics **41** (2) 395–404, 1994.

[92] D. R. Smith, R. Dalichaouch, N. Kroll, S. Schultz, S. L. McCall, and P. M. Platzmann. *Photonic band structure and defects in one and two dimensions.* J. Opt. Soc. Am. B **10** (2), 1993.

[93] S. Y. Lin, G. Arjavalingam, and W. M. Robertson. *Investigation of absolute photonic band gaps in two-dimensional dielectric structures.* J. Mod. Optics **41** (2) 385–393, 1994.

[94] C. Weisbuch, M. Nishioka, A. Ishikawa, and Y. Arakawa. *Observation of the coupled exciton-photon mode splitting in a semiconductor quantum microcavity.* Phys. Rev. Lett. **69** (23) 3314–3317, 1992.

[95] R. Houdré, R. P. Stanley, U. Oesterle, and C. Weisbuch. *Strong coupling regime in semiconductor microcavities.* C. R. Physique **3** 15–27, 2002.

[96] A. V. Kavokin and G. Malpuech. *Cavity Polaritons*, volume 32 of *Thin films and nanostructures*. Elsevier, 2003.

[97] J. A. Dobrowolski. Optical properties of films and coatings. In M. Bass, editor, *Handbook of optics: Fundamentals, techniques, & design*, volume 1, chapter 42. McGraw-Hill, 2nd edition, 1995.

[98] A. V. Kavokin and M. A. Kaliteevski. *Light-absorption effect on Bragg interference in multilayer semiconductor heterostructures.* J. Appl. Phys. **79** (2) 595–598, 1996.

[99] T. Someya, R. Werner, A. Forchel, M. Catalano, R. Cingolani, and Y. Arakawa. *Room temperature lasing at blue wavelengths in gallium nitride microcavities.* Science **285** 1905–1906, 1999.

[100] M. Kanzari and B. Rezig. *Optical polychromatic filter by the combination of periodic and quasi-periodic one-dimensional, dielectric photonic bandgap structures.* J. Opt. A:Pure Appl. Opt. **3** S201–S207, 2001.

[101] A. F. Turner. *Wide passband multilayer filters.* J. Opt. Soc. Am. **42** 878, 1952.

[102] S. D. Smith. *Design of multilayer filters by considering two effective interfaces.* J. Opt. Soc. Am. **48** 43–50, 1958.

[103] K. Sakoda. *Optical transmittance of a two-dimensional triangular photonic lattice.* Phys. Rev. B **51** (7) 4672–4675, 1995.

[104] R. Hillebrand and W. Hergert. *Band gap studies of triangular 2D photonic crystals with varying pore roundness.* Solid State Commun. **115** 227–232, 2000.

[105] H. S. Sözüer, J. W. Haus, and R. Inguva. *Photonic bands: convergence problems with the plane-wave method.* Phys. Rev. B **45** (24) 13962–13972, 1992.

[106] J. B. Pendry. *Photonic band structures.* J. Mod. Optics **41** (2) 209–229, 1994.

[107] P. M. Bell, J. B. Pendry, L. Martin Moreno, and A. J. Ward. *A program for calculating photonic band structures and transmission coefficients of complex structures.* Comp. Phys. Commun. **85** (2) 306–322, 1995.

[108] N. W. Ashcroft and N. D. Mermin. *Solid State Physics.* Saundrs College, Philadelphia, international edition, 1976. ISBN 0-03-049346-3.

[109] C. Kittel. *Introduction to solid state physics.* John Wiley & Sons, 6th edition, 1986. ISBN 0-471-87474-4.

[110] K. S. Krane. *Introductory nuclear physics.* John Wiley and Sons, New York, 1988. ISBN 0-471-80553-X.

[111] J. J. Sakurai. *Modern quantum mechanics.* Addison-Wesley, New York, 1985. ISBN 0-8053-7501-5.

[112] A. S. Davydov. *Quantum mechanics*, volume 1 of *International series in natural philosophy.* Pergamon Press, Oxford, 2nd edition, 1976. ISBN 0-08-020437-6.

[113] S. John. *Frozen light.* Nature **390** 661–662, 1997.

[114] A. A. Chabanov, M. Stoytchev, and A. Z. Genack. *Statistical signatures of photon localization.* Nature **404** 850–853, 2000.

[115] C. M. Soukoulis, editor. *Photonic Band Gap and Localization.* Number 308 in NATO ASI Series B. Plenum, New York, 1993.

[116] Y. A. Vlasov, V. N. Astratov, A. V. Baryshev, A. A. Kaplyanskii, O. Z. Karimov, and M. F. Limonov. *Manifestation of intrinsic defects in optical properties of self-organized opal photonic crystals.* Phys. Rev. E **61** (5) 5784–5793, 2000.

[117] V. D. Freilikher, B. A. Liansky, I. V. Yurkevich, A. A. Maradudin, and A. R. McGurn. *Enhanced transmission due to disorder.* Phys. Rev. E **51** (6) 6301–6304, 1995.

[118] R. C. McPhedran, L. C. Botten, A. A. Asatryan, N. A. Nicorovici, C. Martijn de Sterke, and P. A. Robinson. *Ordered and disordered photonic band gap materials.* Aust. J. Phys. **52** 791–809, 1999.

[119] R. C. McPhedran, L. C. Botten, A. A. Asatryan, N. A. Nicorovici, P. A. Robinson, and C. Martijn de Sterke. *Calculation of electromagnetic properties of regular and random arrays of metallic and dielectric cylinders.* Phys. Rev. E **52** (6) 791–809, 1999.

[120] W. R. Frei and H. T. Johnson. *Finite-element analysis of disorder effects in photonic crystals.* Phys. Rev. B **70** 165116, 2004.

[121] A. A. Asatryan, P. A. Robinson, L. C. Botten, R. C. McPhedran, N. A. Nicorovici, and C. Martijn de Sterke. *Effects of geometric and refractive index disorder on wave propagation in two-dimensional photonic crystals.* Phys. Rev. E **62** (4) 5711–5720, 2000.

[122] A. A. Asatryan, P. A. Robinson, L. C. Botten, R. C. McPhedran, N. A. Nicorovici, and C. Martijn de Sterke. *Effects of disorder on wave propagation in two-dimensional photonic crystals.* Phys. Rev. E **62** (4) 5711–5720, 2000.

[123] H. Y. Ryu, J. K. Hwang, and Y. H. Lee. *Effect of size nonuniformities on the band gap of two-dimensional photonic crystals.* Phys. Rev. B **59** (8) 5463–5469, 1999.

[124] E. Lidorikis, M. M. Sigalas, E. N. Economou, and C. M. Soukoulis. *Gap deformation and classical wave localization in disordered two-dimensional photonic-band-gap materials.* Phys. Rev. B **61** (20) 13458–13464, 2000.

[125] Z. Y. Li, X. Zhang, and Z. Q. Zhang. *Disordered photonic crystals understood by a perturbation formalism.* Phys. Rev. B **61** (23) 15738–15748, 2000.

[126] M. M. Sigalas, C. M. Soukoulis, C. T. Chan, and D. Turner. *Localization of electromagnetic waves in two-dimensional disorered systems.* Phys. Rev. B **53** (13) 8340–8348, 1996.

[127] N. A. Mortensen, M. D. Nielsen, J. R. Folkenberg, K. P. Hansen, and J. Laegsgaard. *Small-core photonic crystal fibres with weakly disordered air-hole claddings.* J. Opt. A: Pure Appl. Opt. **6** 221–223, 2004.

[128] M. A. Kaliteevski, J. M. Martinez, D. Cassagne, and J. P. Albert. *Disorder-induced modification of the transmission of light in a two-dimensional photonic crystal.* Phys. Rev. B **66** (11) 113101, 2002.

[129] M. A. Kaliteevski, J. Manzanarez Martinez, D. Cassagne, and J. P. Albert. *Disorder-induced modification of the attenuation of light in a two-dimensional photonic crystal with complete band gap.* Physica Status Solidi A **195** (3) 612–617, 2003.

[130] H. Li, B. Cheng, and D. Zhang. *Two-dimensional disordered photonic crystals with an average periodic lattice.* Phys. Rev. B **56** (17) 10734–10736, 1997.

[131] M. Bayindir, E. Cubukcu, I. Bulu, T. Tut, E. Ozbay, and C. M. Soukoulis. *Photonic band gaps, defect chacteristics, and waveguiding in two-dimensional disordered dielectric and mettallic photonic crystals.* Phys. Rev. B **64** (19) 195113, 2001.

[132] S. Fan, P. R. Villeneuve, and J. D. Joannopoulos. *Theoretical investigation of fabrication-related disorder on the properties of photonic crystals.* J. Appl. Phys. **78** (3) 1415–1418, 1995.

[133] M. M. Sigalas, C. M. Soukoulis, C. T. Chan, R. Biswas, and K. M. Ho. *Effect of disorder on photonic band gaps.* Phys. Rev. B **59** (20) 12767–12770, 1999.

[134] X. P. Feng and Y. Arakawa. *Defect modes in two-dimensional triangular photonic crystals.* Jpn. J. Appl. Phys. **36** L120–L123, 1997. Part 2.

[135] K. Sakoda. *Numerical study on localized defect modes in two-dimensional triangular photonic crystals.* J. Appl. Phys. **84** (3) 1210–1214, 1998.

[136] S. Noda, A. Chutinan, and M. Imada. *Trapping and emission of photons by a single defect in a photonic bandgap structure.* Nature **407** 608–610, 2000.

[137] S. Fan, P. R. Villeneuve, J. D. Joannopoulos, and H. A. Haus. *Channel drop tunneling through localized states.* Phys. Rev. Lett. **80** (5) 960–963, 1998.

[138] M. M. Sigalas, C. M. Soukoulis, E. N. Economou, C. T. Chan, and K. M. Ho. *Photonic band gaps and defects in two dimensions: studies of the transmission coefficient.* Phys. Rev. B **48** (19) 14121–14126, 1993.

[139] D. M. Beggs, M. A. Kaliteevski, S. Brand, and R. A. Abram. *Optimization of an optical filter with a square-shaped passband based on coupled microcavities.* J. Mod. Optics **51** (3) 437–446, 2004.

[140] T. N. Langtry, A. A. Asatryan, L. C. Botten, C. M. de Sterke, R. C. McPhedran, and P. A. Robinson. *Effects of disorder in two-dimensional photonic crystal waveguides.* Phys. Rev. E **68** 026611, 2003.

[141] W. T. Lau and S. Fan. *Creating large bandwidth line defects by embedding dielectric waveguides into photonic crystal slabs.* Appl. Phys. Lett. **81** (21) 3915–3917, 2002.

[142] K. Sakoda. *Symmetry, degeneracy, and uncoupled modes in two-dimensional photonic lattices.* Phys. Rev. B **52** (11) 7982–7986, 1995.

[143] C. Janot. *Quasicrystals: A Primer.* New York, Oxford University Press, second edition, 1994. ISBN 0-19-856551-8.

[144] J. B. Suck. *Prehistory of quasicrystals.* In J. B. Suck, M. Schreiber, and P. Häussler, editors, *Quasicrystals: an introduction to structure, physical properties, and applications*, number 55 in Material Science, chapter 1, pages 3–16. Springer, 2002.

[145] M. Baake. *Prehistory of quasicrystals.* In J. B. Suck, M. Schreiber, and P. Häussler, editors, *Quasicrystals: an introduction to structure, physical properties, and applications*, number 55 in Material Science, chapter 2, pages 17–48. Springer, 2002.

[146] U. Grimm and M. Schreiber. *Aperiodic tilings on the computer.* In J. B. Suck, M. Schreiber, and P. Häussler, editors, *Quasicrystals: an introduction to structure, physical properties, and applications*, number 55 in Material Science, chapter 3, pages 49–66. Springer, 2002.

[147] S. S. M. Cheng, L. M. Li, C. T. Chan, and Z. Q. Zhang. *Defect and transmission properties of two-dimensional quasiperiodic photonic band-gap systems.* Phys. Rev. B **59** (6) 4091–4099, 1999.

[148] Y. S. Chan, C. T. Chan, and Z.Y. Liu. *Photonic band gaps in two dimensional photonic quasicrystals.* Phys. Rev. Lett. **80** (5) 956–959, 1997.

[149] C. Jin, B. Cheng, B. Man, Z. Li, D. Zhang, S. Ban, and B. Sun. *Band gap and wave guiding effect in a quasiperiodic photonic crystal.* Appl. Phys. Lett. **75** (13) 1848–1850, 1999.

[150] C. Jin, B. Cheng, B. Man, Z. Li, and D. Zhang. *Two-dimensional dodecagonal and decagonal quasiperiodic photonic crystals in the microwave region.* Phys. Rev. B **61** (16) 10762–10767, 2000.

[151] M. A. Kaliteevski, S. Brand, R. A. Abram, T. F. Krauss, P. Millar, and R. M. De La Rue. *Diffraction and transmission of light in low-refractive index Penrose-tiled photonic quasicrystals.* J. Phys.: Condens. Matter **13** 10459–10470, 2001.

[152] M. A. Kaliteevski, S. Brand, and R. A. Abram. *Directionality of light transmission and reflection in two-dimensional Penrose tiled photonic quasicrystals.* J. Phys.: Condens. Matter **16** 1269–1278, 2004.

[153] J. Romero-Vivas, D. N. Chigrin, A. V. Lavrinenko, and C. M. Sotomayor Torres. *Photonic quasicrystals for application in WDM systems.* Phys. Stat. Sol. (a) **202** (6) 997–1001, 2005.

[154] M. A. Kaliteevski, S. Brand, R. A. Abram, T. F. Krauss, R. De La Rue, and P. Millar. *The design of two-dimensional photonic quasicrystals by means of a Fourier transform method.* J. Mod. Optics **48** (1) 9–14, 2001.

[155] M. A. Kaliteevski, S. Brand, R. A. Abram, T. F. Krauss, R. De La Rue, and P. Millar. *Two-dimensional Penrose-tiled photonic quasicrystals: from diffraction pattern to band structure.* Nanotechnology **11** 274–280, 2000.

[156] A. Della Villa, S. Enoch, G. Tayeb, V. Pierro, V. Galdi, and F. Capolino. *Band gap formation and multiple scattering in photonic quasicrystals with a Penrose-type lattice.* Phys. Rev. Lett. **94** 183903, 2005.

[157] W. Gellermann, M. Kohmoto, B. Sutherland, and P. C. Taylor. *Localization of light waves in Fibonacci dielectric multilayers.* Phys. Rev. Lett. **72** (5) 633–636, 1994.

[158] M. A. Kaliteevski, V. V. Nikolaev, R. A. Abram, and S. Brand. *Bandgap structure of optical Fibonacci lattices after light diffraction.* Optics and Spectroscopy **91** (1) 109–118, 2001.

[159] W. Man, M. Megens, P. J. Steinhardt, and P. M. Chaikin. *Experimental measurement of the photonic properties of icosahedral quasicrystals.* Nature **436** 993–996, 2005.

[160] D. T. Roper. *Photonic quasicrystals.* Master's thesis, University of Durham, 2005.

[161] E. L. Ivchenko and G. Pikus. *Superlattices and other heterostructure: symmetry and optical phenomena.* Number 110 in Solid State Sciences. Springer-Verlag, 1995. G. P. Skrebtsov (trans.).

[162] P. Harrison. *Quantum wells, wires and dots: Theoretical and computational physics.* John Wiley & Sons, 2000. ISBN 0 471 98495 7.

[163] A. Imamoğlu and R. J. Ram. *Quantum dynamics of exciton lasers.* Phys. Lett. A **214** 193–198, 1996.

[164] A. Imamoğlu, R. J. Ram, S. Pau, and Y. Yamamoto. *Nonequilibrium condensates and lasers without inversion: exciton-polariton lasers.* Phys. Rev. A **53** (6) 4250–4253, 1996.

[165] E. L. Ivchenko, M. A. Kaliteevski, A. V. Kavokin, and A. I. Nesvizhskii. *Reflection and absorption spectra from microcavities with resonant Bragg quantum wells.* J. Opt. Soc. Am. B **13** (5) 1061–1068, 1996.

[166] A. V. Kavokin and M. A. Kaliteevski. *Excitonic light reflection and absorption in semiconductor microcavities at oblique incidence.* Solid State Commun. **95** (12) 859–862, 1995.

[167] H. Deng, G. Weihs, C. Santori, J. Bloch, and Y. Yamamoto. *Condensation of semiconductor microcavity exciton polaritons.* Science **298**:199–202, 2002.

[168] F. Tassone, F. Bassani, and L. C. Andreani. *Quantum-well reflectivity and exciton-polariton dispersion.* Phys. Rev. B **45** (11) 6023–6030, 1992.

[169] V. V. Popov, T. V. Teperik, N. J. M. Horing, and T. Yu. Bagaeva. *Inhomogeneous radiative decay of polariton modes in a two-dimensional excitonic system.* Solid State Commun. **127** 589–594, 2003.

[170] R. Atanasov, F. Bassani, and V. M. Agranovich. *Mean-field polariton theory for asymmetric quantum wells.* Phys. Rev. B **49** (4) 2658–2666, 1994.

[171] D. S. Citrin. *Radiative lifetimes of excitons in quantum wells: localization and phase-coherence effects.* Phys. Rev. B **47** (7) 3832–3841, 1993.

[172] S. Jorda, U. Rössler, and D. Broido. *Fine structure of excitons and polariton dispersion in quantum wells.* Phys. Rev. B **48** (3) 1669–1677, 1993.

[173] M. J. Adams. *An introduction to optical waveguides.* John Wiley & Sons, 1981. ISBN 0 471 27969 2.

[174] E. L. Ivchenko. *Excitionic polaritons in periodic quantum-well structures.* Sov. Phys. Solid State **33** (8) 1344–1346, 1991.

[175] L. C. Andreani, F. Tassone, and F. Bassani. *Radiative lifetime of free excitons in quantum-wells.* Solid State Commun. **77** (9) 641–645, 1991.

[176] E. L. Ivchenko and A. V. Kavokin. *Reflection of light from structures with quantum wells, quantum wires, and quantum dots.* Sov. Phys. Solid State **34** (6) 968–971, 1992.

[177] M. A. Kaliteevski, S. Brand, R. A. Abram, V. V. Nikolaev, M. V. Maximov, C. M. Sotomayor Torres, and A. V. Kavokin. *Electromagnetic theory of the coupling of zero-dimensional exciton and photon states: a quantum dot in a spherical microcavity.* Phys. Rev. B **64** 115305, 2001.

[178] M. A. Kaliteevski, S. Brand, R. A. Abram, V. V. Nikolaev, M. V. Maximov, N. N. Ledentsov, C. M. Sotomayor Torres, and A. V. Kavokin. *Exciton polaritons in a cylindrical microcavity with an embedded quantum wire.* Phys. Rev. B **61** (20) 13791–13797, 2000.

[179] H. Haug and S. W. Koch. *Quantum theory of the optical and electronic properties of semiconductors.* World Scientific, 3rd edition, 1990.

[180] L. C. Andreani. *Optical transitions, excitons, and polaritons in bulk and low-dimensional semiconductor structures.* In E. Burstein and C. Weisbuch, editors, *Confined electrons and photons: New physics and applications*, volume 340 of *NATO ASI Series B: Physics*, pages 57–112. Plenum Press, 1995.

[181] L. L. Lin and Z. Y. Li. *Interface states in photonic crystal heterostructures.* Phys. Rev. B **63** 033310, 2001.

[182] R. D. Meade, K. D. Brommer, A. M. Rappe, and J. D. Joannopoulus. *Electromagnetic Bloch waves at the surface of a photonic crystal.* Phys. Rev. B **44** (19) 10961–10964, 1991.